Complexity

Dynamics of Piecewise Systems: Bifurcations, Chaos, and Applications in Science and Engineering

Lead Guest Editor: Eric Campos
Guest Editors: Jorge-Antonio Lopez-Renteria, Alexander N. Pisarchik, and Nohé Ramón Cázarez Castro

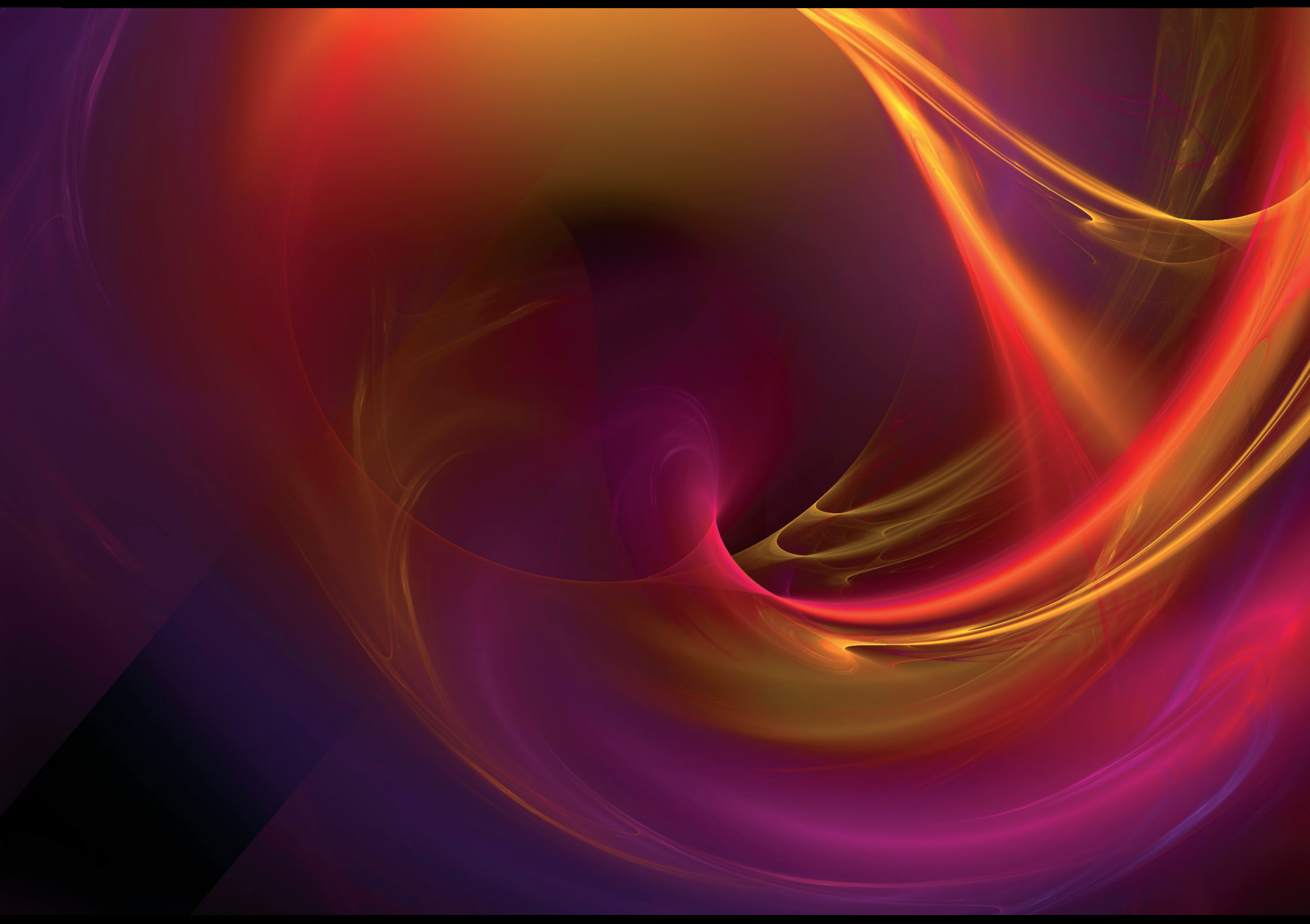

Dynamics of Piecewise Systems: Bifurcations, Chaos, and Applications in Science and Engineering

Complexity

Dynamics of Piecewise Systems: Bifurcations, Chaos, and Applications in Science and Engineering

Lead Guest Editor: Eric Campos
Guest Editors: Jorge-Antonio Lopez-Renteria, Alexander N. Pisarchik, and Nohé Ramón Cázarez Castro

Contents

Hindawi
Complexity
Volume 2021, Article ID 5623783, 24 pages
https://doi.org/10.1155/2021/5623783

WILEY | Hindawi

Research Article

Principle of Limiting Factors-Driven Piecewise Population Growth Model I: Qualitative Exploration and Study Cases on Continuous-Time Dynamics

Héctor A. Echavarria-Heras,[1] **Cecilia Leal-Ramírez**,[1] **Guillermo Gómez**,[2] **and Elia Montiel-Arzate**[3]

[1]*Departamento de Ecología, Centro de Investigación Científica y de Estudios Superiores de Ensenada, Carretera Ensenada-Tijuana No. 3918 Zona Playitas CP, Ensenada 22860, BC, Mexico*
[2]*Facultad de Ciencias, Universidad Nacional Autónoma de México, Avenida Universidad 3000 Circuito Exterior S/N, Delegación Coyoacán, CP Ciudad Universitaria, D.F.México 04510, Mexico*
[3]*Instituto Tecnológico de México, Boulevard Tecnológico #150, Ex Ejido Chapultepec, C.P, Ensenada 22780, BC, Mexico*

Correspondence should be addressed to Héctor A. Echavarria-Heras; heheras@icloud.com

Received 13 August 2021; Accepted 8 October 2021; Published 27 December 2021

Academic Editor: Jorge-Antonio Lopez-Renteria

We examine the comportment of the global trajectory of a piecewisely conceived single species population growth model. Formulation relies on what we develop as the principle of limiting factors for population growth, adapted from the law of the minimum of Liebig and the law of the tolerance of Shelford. The ensuing paradigm sets natality and mortality rates to express through extreme values of population growth determining factor. Dynamics through time occur over different growth phases. Transition points are interpreted as thresholds of viability, starvation, and intraspecific competition. In this delivery, we focus on the qualitative study of the global trajectory expressed on continuous time and on exploring the feasibility of analytical results against data on populations growing under experimental or natural conditions. All study cases sustained fittings of high reproducibility both at empirical and interpretative slants. Possible phase configurations include regimes with multiple stable equilibria, sigmoidal growth, extinction, or stationarity. Here, we also outline that the associating discrete-time piecewise model composes the logistic map applied over a particular region of the phase configuration. Preliminary exploratory analysis suggests that the logistic map's chaos onset could surpass once the orbit enters a contiguous phase region.

1. Introduction

As a rule, mathematical models that attempt to describe the dynamics of two or more populations, subject to a specific type of interaction in an ecosystem, are formulated based on too rigid hypotheses, resulting in poor concordance of the model's predictions with the natural process. The high degree of complexity of biological phenomena and their significant spatial-temporal variations do not assimilate by single-rule models, which are incapable of presenting the functional diversity required by levels of reliable prediction. However, when trying to include more biological information in the model hypotheses, it is often possible to fall into the opposite situation: creating models or techniques so complicated that they are also inoperative from an analytical standpoint.

From the traditional point of view, in building a model, it is necessary to include the most representative processes of the system that we are trying to describe to maintain simplicity as much as possible without losing relevant information. The problem reduces to a quest for those key processes that govern the interaction dynamics we are interested in studying. For example, in demographic ecology, the dynamics of a population depend on the correlation

between opposing influences such as birth generating and growth inhibitory processes. Each of these effects depends on a series of factors inherent to population growth. For example, births depend on age composition, sex proportion, fertility, available food, and so on. Correspondingly, the growth inhibition process may be set by population density, disease, abiotic factors such as temperature, humidity, pollution, and others. As the number of determining factors increases, the model's complexity affects tractability and interpretability. An alternative approach is considering a horizontal integration of complexity through a piecewise modeling strategy. While embracing this approach to gain interpretative strength, it would be desirable to imbue the construct of a mechanistic profile. This work explains how we build a piecewise population model (PPM) by following a systematic way, that is, creating a piecewise description of population growth by relying upon a logical deductive approach. An ad hoc logical system that could sustain such an enterprise is what we comprehend as a principle of limiting factors (PLF) for population growth. This paradigm entailed the derivation of a PPM as a collection of submodels called growth phases that continuously compose the global trend of population size. Each growth phase describes the dynamics over a specific time interval. The naming composite further refers to the principle of limiting factors-driven piecewise population model, which also represents utilizing the PLF-PPM acronym.

As we elucidate in what follows, the PLF-PPM can be arranged by following ideas in [1–3]. Mainly, the construct presented here reviews the approach in [3] to consider a modification taking into account the abatement effect that the population induces on an external resource necessary to guarantee its growth and permanence. The present PLF-PPM formulation also includes a specific scaling or weighting of population size to model the increase in mortality promoted by low population densities [4]. The resulting device allows meaningful ecological interpretation of consequential growth phases. Mainly for keeping this paper's extension manageable, we focus on the continuous-time form of the PLF-PPM. Nevertheless, we judged that it is pertinent to advance an outline of the next discrete-time version, whose detailed exploration will be addressed in the second part of this work. We include several study cases that show the empirical and interpretative adequacy of the present paradigm. The Appendix presents a qualitative study of associating continuous-time global trajectory.

2. Materials and Methods

2.1. The General Piecewise Population Growth Model Setup. Throughout this paper, symbol R stands for the set of real numbers and R^+ denotes the subset of R whose elements are positive. Correspondingly, the size of a population at a positive time t represents employing $x(t)$ and formally stands as a function having domain R^+ and range X_R, a proper subset of R^+, that is, $x(t)$: $R^+ \longrightarrow X_R \subseteq R^+$. For the case of an isolated population, a customary assumption establishes the existence of a function $G(x)$: $X_R \longrightarrow R$ such that

$$\dot{x}(t) = G(x(t)) \cdot x(t), \tag{1}$$

where $\dot{x}(t)$ stands for the rate of change of the number $x(t)$ of individuals in the population at time t. The function $G(x)$ is interpreted as an average estimate of the influence of all the processes that govern population growth. More specifically, this function embodies the average growth rate for each individual in the population. In the following, we will refer to $G(t)$ as the per capita growth rate or the intrinsic growth rate of $x(t)$.

Determining the function $G(x)$ in a closed form is usually impossible or very complicated. However, from an empirical perspective, it is possible to suppose that the function $G(x)$ admits expansion as a power series, with which we would obtain

$$G(x) = \sum_{i=0}^{\infty} a_i x^i. \tag{2}$$

Then, for example, neglecting the $a_n x^n$ terms with $n \geq 2$, we could consider the approximation

$$G(x) = r - kx. \tag{3}$$

The above characterization of the intrinsic growth rate $G(x)$ establishes the form of the differential equation (1) that leads to the identification of the so-called logistic curve, commonly adopted as a model of population growth in a limited environment. Although it is feasible to give a biological interpretation to equation (3) model, it shows the fragility inherent in all simplified models, which mainly relates to the lack of suitable complexity. Moreover, the variation of population size could compose an outstanding array of patterns. Then, maintaining a single association rule for $G(x)$, through the full extension of X_R, no matter how complex such a rule conceives, it could render insufficient to imbue a consistent reproducibility of observed population values. A traditional approach to adapt $G(x)$ is by considering a polynomial approximation of degree n derived from the infinite series of equation (2). Nevertheless, this approach bears a disadvantage since at gaining reproducibility strength, we could lose interpretability.

Before getting into matters on suitable complexity embedding of$G(x)$, we introduce some notation conventions. Given a function$S(t)$: $A \longrightarrow B$ and a subset $C \subseteq A$, the restriction of $S(t)$ to the set, C denotes $S(t)|_C$: $C \longrightarrow B$, it is formally defined by

$$S(t)|_C = S(t) \text{ for each } t \text{ in C}. \tag{4}$$

A second method of adapting the complexity attending to an optimal reproducibility criterion is conceiving $G(x)$ as a composite of m operating modes, each one characterized by a continuous and differentiable function $G_i(x) : \mathfrak{R}_i[x] \longrightarrow R$ being $\mathfrak{R}_i[x]$ a region defined through

$$\mathfrak{R}_i[x] = \{x | p_{i-1} < x \leq p_i\}, \tag{5}$$

for $i = 1, 2, \ldots, m$. The components of the vector $\mathbf{P} = (p_0, \ldots, p_m)$ represent breakpoints for transition among the operating modes $G_i(x)$. We also assume that the

collection of regions $\mathfrak{R}_i[x]$ provides a covering for the range of $x(t)$, that is, $X_R \subseteq \cup_1^m(\mathfrak{R}_i[x])$. We could formally set

$$G_i(x) = G(x)|_{\mathfrak{R}_i[x]}. \tag{6}$$

So, we can represent $G(x)$expanded by the $G_i(x)$ submodels for $i = 1, 2, \ldots, m$, namely,

$$G(x) = \sum_{i=1}^{m} \chi(\mathfrak{R}_i[x]) G_i(x), \tag{7}$$

with $\chi(\mathfrak{R}_i[x])$ representing the characteristic function of $\mathfrak{R}_i[x]$, namely,

$$\chi(\mathfrak{R}_i[x]) = \begin{cases} 1, & \text{if } x(t) \in \mathfrak{R}_i[x], \\ 0, & \text{if } x(t) \in \mathfrak{R}_i[x]^c, \end{cases} \quad 1. \tag{8}$$

Equation (7) intends to provide a piecewise description of the intrinsic population growth rate in the autonomous differential equation (1). Discretizing the resulting differential equation, we can identify the parameters defining the $G_i(x)$ submodels describing the phases of population growth, as well as the threshold parameters $p_0, p_1, \ldots, p_m$ that represent the transition points between the growth phases $G_i(x)$; given assumed continuity properties of $G(x)$, the phase changes must be set as continuous transitions between the submodels, that is, we have

$$G_i(p_i) = \lim_{x \longrightarrow p_i^-} G_{i+1}(x), \text{for } i = 1, 2, \ldots, m-1. \tag{9}$$

But, in the general settings, the transition between phases at breakpoints $p_0, p_1, \ldots, p_m$ can occur in a discontinuous way.

In the settings of the model of equation (1), the function $f(x) = G(x)x$ is interpreted as the natural growth rate of the population. Then, defining $f_i(x) = G_i(x)x$ for $i = 1, 2, \ldots, m$ and keeping the notation convention entailing the associated domain regions, according to equation (6), we set

$$f_i(x) = f(x)|_{\mathfrak{R}_i[x]}. \tag{10}$$

This way, we can propose a piecewise expanded form of equation (1), namely,

$$\dot{x}(t) = \sum_{i=1}^{m} \chi(\mathfrak{R}_i[x]) f_i(x), \text{for } x(0) = x_0, \tag{11}$$

where $\mathfrak{R}_i[x]$ and $\chi(\mathfrak{R}_i[x])$ are defined by equations (5) and (8) one to one.

The non-autonomous form of the dynamical system of equation (11) addresses similarly by replacing $f(x)$ by a continuous and differentiable function $f(x,t)$: $X_R \times R \longrightarrow R$ and interprets $x(t)$ and t as a forced form of the natural growth rate of the population. The extension of equation (11) to the non-autonomous case $f(x,t)$ follows by setting submodel $f_i(x,t)$:$\mathfrak{R}_i[x,t] \longrightarrow R$ being $\mathfrak{R}_i[x,t] = \mathfrak{R}_i[x] \times R$ for $i = 1, 2, \ldots, m$. This way, a piecewisely expanded non-autonomous form of equation (11) could be expressed by

$$\dot{x}(t) = \sum_{1=1}^{m} \chi(\mathfrak{R}_i[x,t]) f_i(x,t), \text{ with } x(0) = x_0, \tag{12}$$

where $\chi(\mathfrak{R}_i[x,t])$ symbolizes the characteristic function of the rectangle $\mathfrak{R}_i[x,t]$. Nevertheless, in this paper, we focus on the autonomous case.

To provide a piecewise representation of the solution $x(t)$ to the dynamical system of equation (11), we conceive trajectory sectors $x_i(t)$ for $i = 1, 2, \ldots, m$ defined by

$$x_i(t) = x(t)|_{T_i(t)}. \tag{13}$$

For $T_i(t) \subseteq R^+$, the interval $T_i(t) = x^{-1}(\mathfrak{R}_i[x])$. Since $x(t)$ varies continuously, we must set the consistency condition

$$x_i(t_i) = \lim_{t \longrightarrow t_i^-} x_{i+1}(t), \tag{14}$$

for $t_i = x^{-1}(p_i)$ being p_i the breakpoint for the transition from $f_i(x)$ to $f_{i+1}(x)$. Then, we arrange

$$x(t) = \sum_{i=1}^{m} \chi(T_i(t)) x_i(t), \text{for } x(0) = x_0, \tag{15}$$

with $\chi(T_i(t))$ being defined by

$$\chi(T_i(t)) = \begin{cases} 1, & \text{if } t \in T_i(t), \\ 0, & \text{if } t \in T_i(t)^c. \end{cases} \tag{16}$$

In any event, usually assembling equation (11) relies on an empirical description that abides by the highest reproducibility criterion. Regularly, such an approach disregards any phenomenological explanation of population growth. In this work, we explain a systematic way to obtain a collection of submodels that mimic the global trend of population size $x(t)$, where each one of them describes the dynamics over a specific time interval, that is, we build a piecewise description of both $\dot{x}(t)$ and $x(t)$ as given by equations (11) and (13) one to one by relying on a logical deductive approach. This can be obtained by following [1–3]. The corresponding derivation is based on the use of the ecological principle of limiting factors. The construct presented here corresponds to a modification of the slant in [3]. To consider the abatement effect that the population induces on an external resource necessary to guarantee its growth and permanence, the present formulation also includes a specific scaling or weighting of population size to model the increase in mortality promoted by low population densities [4].

2.2. The Principle of Limiting Factors. German Physiologist Justus Von Liebig [5], studying the growth of certain plants, realized that to guarantee their development, there had to be a set of essential nutrients. Some had to be abundant, and others were required only in small quantities. A significant discovery of Liebig was that the absence of some nutrient could not be replaced with any other that appeared in abundance. Moreover, a medium that contained all the nutrients in abundance except one of them, which appeared in insufficient quantity, would allow plant growth until the

nutrient was utterly depleted. The absence of some element limited growth. In addition, when growth occurred, the latter turned out to be controlled by the nutrient appearing in lesser proportion. Liebig called this regularity the law of the minimum. Later, in [6], the North American Ecologist V. E. Shelford extended the domain of Liebig's law to what is now known as the law of tolerance. Shelford pointed out that when there is an excess of a specific element, this can be as limiting as its deficiency. It follows that all the processes that determine the dynamics of a population will occur in intensities governed by the minima or maxima of the factors that nourish these processes. We refer to this notion as the principle of limiting factors (PLF) for simplicity and following the tradition. It intends to interpret the law that limits a process through the maximum and minimum of factors acting in the analyzed system.

2.3. The Principle of Limiting Factors-Driven Piecewise Population Growth Model. Considering the validity of the principle of limiting factors, let us construct a mathematical model to interpret the performance of a population whose size at time t is denoted by $x(t)$. We suppose that departing from a value $x(0) = x_0$, the population growth depends on an external resource whose availability at time t is modeled by a continuous and differentiable function $R(t)$ with rank in R^+. We will also assume that the natural growth rate of the population size $\dot{x}(t)$ as given by equation (2) expresses through a function $f(x) = G(x)x$ that determines on a first instance by the intensities of two opposing processes, one of birth $N(x)$ yielding offspring and another $M(x)$ determining the death of the individuals, that is,

$$f(x) = \beta N(x) - \mu M(x), \tag{17}$$

where β and μ are positive scaling parameters [2, 3], $N(x)$ stands for the strength of the process leading to increasing population size, that is, the rate at which the number of newborn in the population is generated, and $M(x)$ represents the intensity of the growth-inhibiting process, that is, the mortality rate. We assume that $N(x)$ and $M(x)$ both express through continuous and differentiable functions.

Then, according to the principle of limiting factors, we assume that $N(x)$ depends essentially on two factors: one being the size of the population $x(t)$ and the second one taken as the amount of feeding energy available; this symbolized employing $R(x)$. We suppose that before the population began exhausting the resource $R(x)$, this is kept at a constant value F_0. Additionally, we think through that the total weight of the population expresses in the same units of energy as $R(x)$. Let us also undertake that each individual in the $x(t)$ pool maintains an energy consumption equal to a proportion k of its weight. Then, we can assume in the first instance that $R(x)$ represents using the linear model

$$R(x) = F_0 - kx(t). \tag{18}$$

Then, resource availability $R(x_o)$ will plentifully suit feeding requirements of the initial population x_o whenever the condition $R(x_o) \gg kx_o$ satisfies or equivalently according to equation (18) whenever $F_0 \gg 2kx_0$ holds. We will then have that if the amount of energy consumed by the population at time t, i.e., $kx(t)$, is less than $R(x)$, there will be enough food for all individuals, that is, the availability of energy will guarantee that the population can participate in the reproduction process unrestrictedly, so we can establish the assumption that the birth rate will be proportional to the size of the population, that is, we can set the equality $N(x) = x(t)$. In the case in which $kx(t)$ exceeds $R(x)$, then only as many individuals of the population energetically equivalent to $R(x)$ will be able to feed. Therefore, the reproductive potential of the population will be limited. That is, according to Liebig's principle, energy availability will be a limiting factor for population growth. Then, $N(x) = R(x)$. Thus, we can define $N(x)$ by

$$N(x) = \min_t\{kx(t),\ R(x)\}. \tag{19}$$

Solving the inequality $kx(t) < F_0 - kx(t)$, we can express equation (19) in the equivalent form

$$N(x) = \min_t\{x(t),\ E\}, \tag{20}$$

where the constant $E = F_0/2k$ is interpreted as a starvation threshold since if $x(t)$ grows maintaining levels higher than E, the number of offspring will turn to be controlled by the external factor F_0 and the rate of individual energy consumption k that could eventually lead to the decline of the population.

Concerning the intensity of the natural death process $M(x)$, we will consider this, considering Shelford's law of tolerance based on population density as the critical factor. According to Allee's principle, reduced population levels will restrict the number of interactions between individuals, making mating difficult, implying decreasing recruitment, favoring even a lower number of individuals, and eventually leading to the total depletion of the population. In this circumstance, we will say that the strength of the mortality process will be proportional to the size of the population, that is, $M(x) = ax(t)$, where a is a positive constant. On the other hand, at high population sizes, density upsurges, the struggle for resources intensifies, and so does the transmission of diseases, thereby increasing mortality. In this case, we take the intensity of the mortality process as being proportional to the number of encounters between the individuals, that is, $M(x) = bx^2(t)$ where $b \in R^+$. Then, according to Shelford's law of tolerance, we can express $M(x)$ in the form

$$M(x) = \max_t\left\{ax(t), bx^2(t)\right\}. \tag{21}$$

In summary, the PLF and equations (11) and (17) imply the piecewise continuous form

$$\dot{x}(t) = \sum_{i=1}^{m} \chi\left(\mathfrak{R}_i[x]\right) f_i(x), \text{for } x(0) = x_0, \tag{22}$$

where $f_i(x)$ and $\mathfrak{R}_i[x] i = 1, 2, 3, 4$ are given by

$$\left.\begin{array}{ll} f_1(x) = \beta E - \mu b x(t)^2 & \Re_1[x] = \left\{x(t) \middle| (x(t) > E) \wedge \left(x(t) > \dfrac{a}{b}\right)\right\} \\ f_2(x) = \beta x(t) - \mu b x(t)^2 & \Re_2[x] = \left\{x(t) \middle| (x(t) < E) \wedge \left(x(t) > \dfrac{a}{b}\right)\right\} \\ f_3(x) = (\beta - \mu a) x(t) & \Re_3[x] = \left\{x(t) \middle| (x(t) < E) \wedge \left(x(t) < \dfrac{a}{b}\right)\right\} \\ f_4(x) = \beta E - \mu a x(t) & \Re_4[x] = \left\{x(t) \middle| (x(t) > E) \wedge \left(x(t) < \dfrac{a}{b}\right)\right\} \end{array}\right\}, \tag{23}$$

with $\chi(\Re_i[x])$ representing the characteristic function of $\Re_i[x]$ for $i = 1, 2, 3, 4$ (cf. equation (8)). In what follows, the principle of limiting factors-driven piecewise population growth model of equations (22) and (23) will be referred to as PLF-PPM for short.

Since $x(t)$ stands for the solution to equation (22), then according to equation (15), we have that $x_i(t) = x(t)|_{T_i(t)}$ for $i = 1, 2, 3, 4$, stands for the ith sector of the PLF driven trajectory $x(t)$ having range in $\Re_i[x]$, and correspondingly, this sets $T_i(t) = x^{-1}(\Re_i[x])$. Then, $x_i(t)$ solves the differential equation $\dot{x}_i(t) = f_i(x(t))$ with $x_i(t)$ satisfying $x_i(0) = x_{i0} \in \Re_i[x]$ and the restriction $t \in T_i(t)$. Therefore, we have

$$\left.\begin{array}{llll} x_1(t) = \dfrac{\lambda_1\left(C - e^{-2t\sqrt{\beta\mu b E}}\right)}{C + e^{-2t\sqrt{\beta\mu b E}}} & x(t) \in \Re_1[x], t \in T_1(t) & x_{10} = \dfrac{\lambda_1(C-1)}{C+1} & \lambda_1 = \sqrt{\dfrac{\beta E}{\mu b}} \\ x_2(t) = \dfrac{C\lambda_2}{\lambda_2 e^{-\beta t} + C} & x(t) \in \Re_2[x], t \in T_2(t) & x_{20} = \dfrac{\beta C}{\beta + \mu b C} & \lambda_2 = \dfrac{\beta}{\mu b} \\ x_3(t) = C e^{(\beta - \mu a)t} & x(t) \in \Re_3[x], t \in T_3(t) & x_{30} = C & \\ x_4(t) = C e^{-\mu a t} + \lambda_4\left(1 - e^{-\mu a t}\right) & x(t) \in \Re_4[x], t \in T_4(t) & x_{40} = C & \lambda_4 = \dfrac{\beta E}{\mu a} \end{array}\right\}, \tag{24}$$

with λ_i being the equilibrium solutions as determined by the natural growth rates $f_i(x(t))$ (cf. equation (24)). Additionally, the submodels $x_i(t)$ composing the solution $x(t)$ as given by equation (15) determine by the order relationship that E and a/b satisfy. Accordingly, the global trajectory $x(t)$could fit to three possible topologies, one type M_1 associating to the statement M_1: $(E > a/b)$, another form M_2 consistent to M_2: $(E > a/b)$; and a third form M_3 associating to M_3: $(E > a/b)$ the phase composite $P_1(t, x(t))$ for M_1 models will include regions $\Re_1[x], \Re_2[x]$, and $\Re_3[x]$, that is, $P_1(t, x(t)) = \cup_{i\neq 4}\{\Re_i[x]\} \bigcup (0, \infty)$. Correspondingly, for models M_2, phase arrangement becomes $P_2(t, x(t)) = \cup_{i\neq 2}\{\Re_i[x]\} \bigcup (0, \infty)$. In turn, phase portrait for models M_2 and the regions $\Re_2[x]$ and $\Re_4[x]$ is mutually exclusive. For models M_3, the phase combination turns to $P_3(t, x(t)) = \cup_{i\neq 2,4}\{\Re_i[x]\} \bigcup (0, \infty)$. The Appendix presents a qualitative study of trajectories resulting from equation (22).

3. Results

3.1. Analytic Exploration. To study the varied forms of the global trajectory $x(t)$ derived from the PLF-PM, we begin by setting the array of possible phase configurations associated with the basic parameters a, b, E, β, and μ (cf. equations (22) and (23)). We depart from the ordering relationship for the external energy E and the ratio of mortality from population density proportions, a/b, that yields a first model type classification $(M_i, i = 1, 2, 3)$. We have to consider models M_1 associated to the inequality $E > a/b$, where the range of $x(t)$ composes the regions: $\Re_1[x] = \{a/b < E < x\}$, $\Re_2[x] = \{a/b < x < E\}$, and $\Re_3[x] = \{x < a/b < E\}$ (cf. equation (23)). For model type M_2 where the relationship $E > a/b$ holds, the range of $x(t)$ will be divided into the regions $\Re_1[x]$, $\Re_3[x]$, and $\Re_4[x] = \{x < a/b < E\}$ (cf. equation (23)). For model type M_3 linking to the ordering $E = a/b$, the range of $x(t)$ will be divided into the regions $\Re_1[x]$ and $\Re_3[x]$. We can be aware that regions $\Re_2[x]$ and

$\mathfrak{R}_4[x]$ are mutually excluding. Besides, it also requires classifying possible phase arrangements according to a Birth to Mortality Scaled Ordering (BMS_i, $i = 1, 2, 3$), namely, BMS_1: when $(\beta < \mu a)$, BMS_2: if $(\beta > \mu a)$, and BMS_3: whenever $(\beta = \mu a)$. Additionally, each model type M_i with $i = 1, 2$ determines possible placements of the initial condition, and each one associated to composing phase regions $\mathfrak{R}_i[x]$ with $i = 1, 2, 3, 4$ determines an initial condition ordering ($IC_{ik(i)}$ with $i = 1, 2$ and $k(i) = 1, 2, \ldots, 5$), namely, IC_{11}: for $(E < x_o)$, IC_{12}: whenever $(a/b < x_o < E)$, IC_{13}: when $(x_o < a/b)$, IC_{14}: if $(x_o = E)$, and IC_{15}: whenever $(x_o = a/b)$. Correspondingly, IC_{21}: for $(x_o < E)$, IC_{22}: whenever $(E < x_o < a/b)$, IC_{23}: when $(x_o > a/b)$,IC_{24}: if $(x_o = E)$, and IC_{25}: whenever $(x_o > a/b)$. The possible phase arrangements typify according to a three-dimensional conjunction operator $\mathscr{H}[\mathbf{i}, \mathbf{j}, \mathbf{k}(\mathbf{i})] = (M_i \wedge BMS_j \wedge IC_{ik(i)})$ for i and $k(i)$ as specified. Table 1 summarizes phase arrangements for model type M_1, and Table 2 summarizes those corresponding to model type M_2. In addition to the $\mathscr{H}[\mathbf{i}, \mathbf{j}, \mathbf{k}(\mathbf{i})]$ conjunctions, we must consider the positioning of the equilibrium solutions inside their associated regions. For this reason, in the presentation of results, we could use the $O\lambda(i, j)$ indicator for $i = 1, 2, 4$ designating equilibrium λ_i and $j = 1, 2, 4$ describing region $\mathfrak{R}_i[x]$. Then, for instance, $O\lambda(1, 1)$ identifies the placement of equilibrium λ_1 inside region $\mathfrak{R}_1[x]$; correspondingly, $O\lambda(2, 3)$ labels positioning of λ_2 inside region $\mathfrak{R}_3[x]$ and so on. Yet given $O\lambda(i, j)$, this relates to distinguishing how the initial condition is positioned relative to the equilibrium solution λ_i. Resulting orderings generically symbolize through $IC\lambda(i, j)$ for $i = 1, 2, 4$ associated to the equilibrium solution λ_i and $j = 1, 2$ labeling the ordering of x_0 relative to λ_i. This way, $IC\lambda(i, 1)$ stands for $(x_0 < \lambda_i)$ and $IC\lambda(i, 2)$ stands for $(x_0 > \lambda_i)$. Besides described symbols, we could refer to direct inequalities that a given equilibrium satisfies relative to thresholds defining regions.

Then, for instance, the statement $(\mathscr{H}[\mathbf{2}, \mathbf{2}, \mathbf{1}] \wedge IC\lambda(i, j) \wedge IC\lambda(1, 1)) \equiv 1$ signifies that we have a model type M_1 with $\beta > \mu a$ and that the initial condition satisfies $a/b < x_o$, the λ_1 equilibrium in region $\mathfrak{R}_1[x]$, that is, $\lambda_1 > a/b$, and finally that $a/b < x_o < \lambda_1$. In the Appendix, we present an extended qualitative study of the performance of the global trajectory $x(t)$ under conjunctions $\mathscr{H}[\mathbf{i}, \mathbf{j}, \mathbf{k}(\mathbf{i})] \wedge O\lambda(i, j) \wedge IC\lambda(i, j)$.

Figure 1(a) shows the performance of the PLF-PM composite trajectory $x(t)$ for the $\mathscr{H}[\mathbf{1}, \mathbf{1}, \mathbf{1}]$ configuration. Particularly, shown placement $a/b < \lambda_1 < E$ derives from the auxiliary ordering $E > \mu a^2/\beta b$. The global trajectory $x(t)$ initiates in a region $\mathfrak{R}_1[x]$ according to the $x_1(t)$ rule. Then, since for $\beta < \mu a$ population size decreases, continuity of linked trajectory projects a time t_1 such that $x(t)$ reaches the E threshold, that is, $x(t_1) = E$, and then $x(t)$ enters into the region $\mathfrak{R}_2[x]$ switching to the $x_2(t)$ rule. The settings imply the existence of a second time t_2 so that $x(t)$ touches the a/b frontier, thereby getting into the region $\mathfrak{R}_3[x]$ and following according to the $x_3(t)$ rule. But, since $\beta < \mu a$, eventually $x(t)$ vanishes. $\mathscr{H}[\mathbf{1}, \mathbf{1}, \mathbf{2}]$ and $\mathscr{H}[\mathbf{1}, \mathbf{1}, \mathbf{3}]$ configurations similarly tied to the $\beta < \mu a$ ordering also drive population size to vanish Figure 1(b) pertains to the $\mathscr{H}[\mathbf{2}, \mathbf{1}, \mathbf{1}]$ arrangement. Composite trajectory $x(t)$ begins in the region $\mathfrak{R}_1[x]$ according to the $x_1(t)$ rule, but $\beta < \mu a$, and then population size decreases, so at a time t_1, it reaches the a/b threshold, that is, $x(t_1) = a/b$, entering into the region $\mathfrak{R}_4[x]$ and subsequently abiding by the rule $x_4(t)$. The decreasing trend implies population size touching the E boundary at a second time t_2, thereby placing within the region $\mathfrak{R}_3[x]$ and then switching again, this time to the $x_4(t)$ rule. Afterward, population size keeps decreasing following an asymptotic trend to extinction. The faith of the PLF-PM composite trajectory $x(t)$ for $\mathscr{H}[\mathbf{2}, \mathbf{1}, \mathbf{2}]$ and $\mathscr{H}[\mathbf{2}, \mathbf{1}, \mathbf{3}]$ is extinction equally. Figure 1(c) pertains to the $\mathscr{H}[\mathbf{3}, \mathbf{1}, \mathbf{1}]$ conjunction corresponding to the $x_o > E$ ordering. Then, in the beginning, population size $x(t)$ places in the region $\mathfrak{R}_1[x]$ and decreases according to the $x_1(t)$ rule. Subsequently, it asymptotically approaches the value $\lambda_1 < E$, but on its trend, it hits the E boundary at time t_1 switching to rule $x_3(t)$ holding in region $\mathfrak{R}_3[x]$. The condition $\beta < \mu a$ drives population to extinction. For $\mathscr{H}[\mathbf{3}, \mathbf{1}, \mathbf{2}]$ conjunction, the initial condition placement $x(0) < E$ keeps the population size within region $\mathfrak{R}_3[x]$ where it progresses to extinction according to the $x_3(t)$ trajectory.

Table 1: Basic phase arrangements $\mathscr{H}[1, \mathbf{j}, \mathbf{k}(\mathbf{i})]$ determined by the PLF-PM and phase arrangements for model type M_1 associated to the $E > a/b$ ordering.

$\mathscr{H}[i, j, k(i)]$	M_1	BMS_i	BMS_i	$IC_{ik(i)}$	$IC_{ik(i)}$
$\mathscr{H}[1, 1, 1]$	$E > a/b$	BMS_1	$\beta < \mu a$	IC_{11}	$E < x_o$
$\mathscr{H}[1, 1, 2]$	$E > a/b$	BMS_1	$\beta < \mu a$	IC_{12}	$a/b < x_o < E$
$\mathscr{H}[1, 1, 3]$	$E > a/b$	BMS_1	$\beta < \mu a$	IC_{13}	$x_o < a/b < E$
$\mathscr{H}[1, 1, 4]$	$E > a/b$	BMS_1	$\beta < \mu a$	IC_{14}	$x_o = E$
$\mathscr{H}[1, 1, 5]$	$E > a/b$	BMS_1	$\beta < \mu a$	IC_{15}	$x_o = a/b$
$\mathscr{H}[1, 2, 1]$	$E > a/b$	BMS_2	$\beta > \mu a$	IC_{21}	$E < x_o$
$\mathscr{H}[1, 2, 2]$	$E > a/b$	BMS_2	$\beta > \mu a$	C_{22}	$a/b < x_o < E$
$\mathscr{H}[1, 2, 3]$	$E > a/b$	BMS_2	$\beta > \mu a$	IC_{23}	$x_o < a/b < E$
$\mathscr{H}[1, 2, 4]$	$E > a/b$	BMS_2	$\beta > \mu a$	IC_{24}	$x_o = E$
$\mathscr{H}[2, 2, 5]$	$E > a/b$	BMS_2	$\beta > \mu a$	IC_{25}	$x_o = a/b$

$j = 1, 2$ sign discriminates ordering between β and μa, and the composing index $k(i)$ differentiates the position of the initial condition among the phase regions constituting a model type M_1.

Assume $(O\lambda(2, 1) \wedge \mathscr{H}[\mathbf{1}, \mathbf{2}, \mathbf{1}]) \equiv 1$; then, the condition BMS_1: $(\beta < \mu a)$ holds; additionally, the λ_2 equilibrium localizes above E, that is, $O\lambda(2, 1)$: $(\lambda_2 > E)$, and these orderings appear in conjunction with M_1: $(E > a/b)$ and IC_{11}: $(E < x_o)$. Particularly, $\lambda_2 > E$ implies $\lambda_1 > E$ so the initial condition placement $E < x_o < \lambda_1$ sets the $x(t)$ trajectory to increase according to the $x_1(t)$ rule, approaching the asymptotic limit λ_1 and staying within region $\mathfrak{R}_1[x]$. On the other hand, whenever we have $E < \lambda_1 < x_o$, population size $x(t)$ decreases asymptotically towards λ_1. This establishes λ_1 as a stable equilibrium in region $\mathfrak{R}_1[x]$ (see Figure 2(a)). Alternatively, under the statement $(O\lambda(2, 2) \wedge \mathscr{H}[\mathbf{1}, \mathbf{2}, \mathbf{2}]) \equiv 1$, since we have $\beta > \mu a$, the ordering $\lambda_2 > a/b$; then, since $O\lambda(2, 2)$ implies $\lambda_2 < E$, we could have $a/b < x_o < \lambda_2 < E$ or $a/b < \lambda_2 < x_o < E$. If $a/b < x_o < \lambda_2 < E$ gets true, $x(t)$ will behave according to the $x_2(t)$ law, and then it will decrease from x_o and approach the asymptotic limit λ_2. For $a/b < \lambda_2 < x_o < E$, the population size $x(t)$ still conforming to the $x_2(t)$ growth law will increase from x_o and approach λ_2. Thus, λ_2 stands for a stable

Table 2: Basic phase arrangements $\mathscr{H}[2, j, k(i)]$ determined by the PLF-PM and phase arrangements for model type M_2 associated to the $E < a/b$) ordering.

$\mathscr{H}[i, j, k(i)]$	M_2	BMS_i	BMS_i	$\text{IC}_{ik(i)}$	$\text{IC}_{ik(i)}$
$\mathscr{H}[2, 1, 1]$	$E < a/b$	BMS_1	$\beta < \mu a$	IC_{11}	$E < x_o$
$\mathscr{H}[2, 1, 2]$	$E < a/b$	BMS_1	$\beta < \mu a$	IC_{12}	$a/b < x_o < E$
$\mathscr{H}[2, 1, 3]$	$E < a/b$	BMS_1	$\beta < \mu a$	IC_{13}	$x_o < a/b < E$
$\mathscr{H}[2, 1, 4]$	$E < a/b$	BMS_1	$\beta < \mu a$	IC_{14}	$x_o = E$
$\mathscr{H}[2, 1, 5]$	$E < a/b$	BMS_1	$\beta < \mu a$	IC_{15}	$x_o = a/b$
$\mathscr{H}[2, 2, 1]$	$E < a/b$	BMS_2	$\beta > \mu a$	IC_{21}	$E < x_o$
$\mathscr{H}[2, 2, 2]$	$E < a/b$	BMS_2	$\beta > \mu a$	C_{22}	$a/b < x_o < E$
$\mathscr{H}[2, 2, 3]$	$E < a/b$	BMS_2	$\beta > \mu a$	IC_{23}	$x_o < a/b < E$
$\mathscr{H}[2, 2, 4]$	$E < a/b$	BMS_2	$\beta > \mu a$	IC_{24}	$x_o = E$
$\mathscr{H}[2, 2, 5]$	$E < a/b$	BMS_2	$\beta > \mu a$	IC_{25}	$x_o = a/b$

$j = 1, 2$ sign discriminates ordering between β and μa, and the composing index $k(i)$ differentiates the position of the initial condition among the phase regions constituting a model type M_2

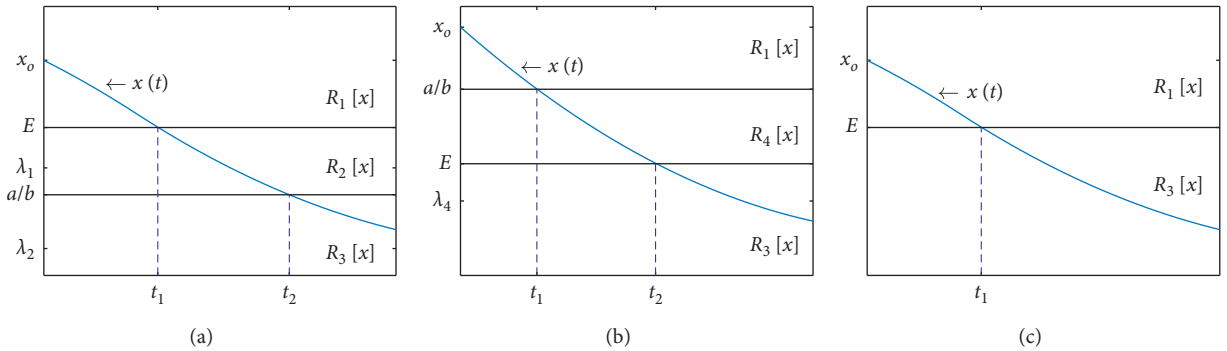

Figure 1: Examples of the construction of the PLF-PM composite trajectory $x(t)$ for $\mathscr{H}[\mathbf{i}, \mathbf{1}, \mathbf{1}]$ for $i = 1, 2, 3$; these configurations include a BMS_1: ($\beta < \mu a$) condition. (a) Composite trajectory $x(t)$ for $\mathscr{H}[\mathbf{1}, \mathbf{1}, \mathbf{1}]$. (b) Composite trajectory $x(t)$ for $\mathscr{H}[\mathbf{2}, \mathbf{1}, \mathbf{1}]$. (c) Composite trajectory $x(t)$ for $\mathscr{H}[\mathbf{3}, \mathbf{1}, \mathbf{1}]$.

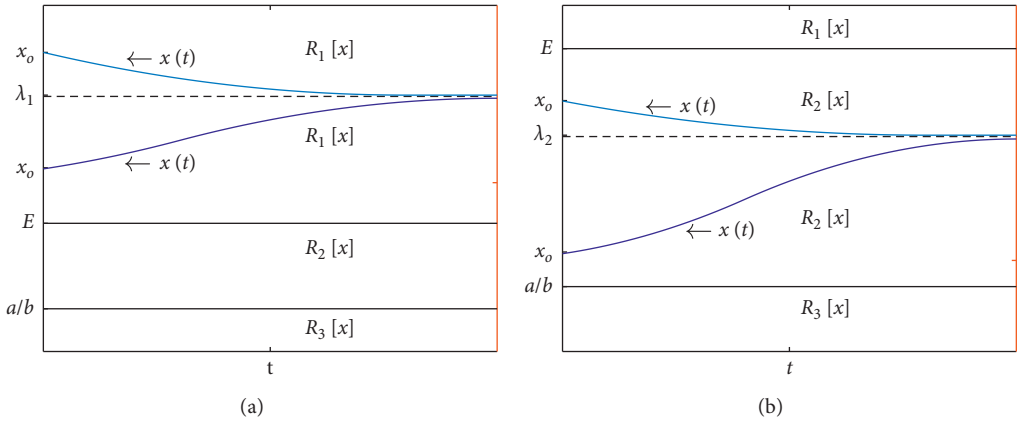

Figure 2: Continued.

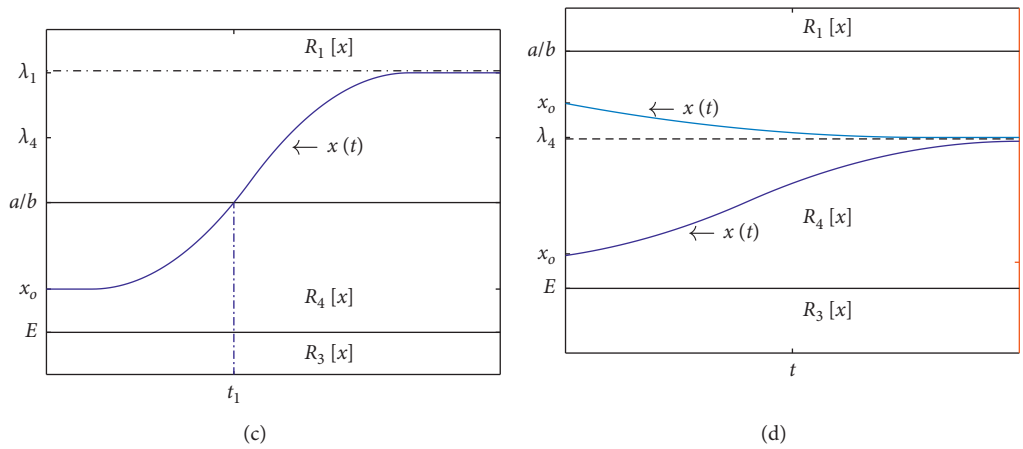

FIGURE 2: Examples of the construction of the PLF-PM composite trajectory $x(t)$ for $\mathscr{H}[i,2,k]$ for $i=1,2$, and $k=1,2,3$; referred configuration entitles the BMS_2: $(\beta>\mu a)$ condition. (a) The statement $((\lambda_2>E)\wedge\mathscr{H}[\mathbf{1},\mathbf{2},\mathbf{1}])\equiv 1$ holds, λ_1 is a stable equilibrium in the region $\mathfrak{R}_1[x]$. (b) Under the $((\lambda_2<E)\wedge\mathscr{H}[\mathbf{1},\mathbf{2},\mathbf{2}])\equiv 1$ statement, λ_2 places in region $\mathfrak{R}_2[x]$ and becomes a stable equilibrium solution. (c) Whenever $((E<\lambda_4<a/b)\wedge\mathscr{H}[\mathbf{2},\mathbf{2},\mathbf{2}])\equiv 1$, the λ_4 equilibrium places in $\mathfrak{R}_4[x]$; since $E<x_o<a/b$, $x(t)$ increases, reaching the a/b boundary at time t_1, and switches to rule $x_1(t)$ but since $\lambda_1>a/b$, $x(t)$ increases asymptotically towards λ_1 staying within region $\mathfrak{R}_1[x]$. (d) In turn, if $((E<\lambda_4<a/b)\wedge\mathscr{H}[\mathbf{2},\mathbf{2},\mathbf{2}])\equiv 1$, then λ_4 stands for a stable equilibrium solution in the region $\mathfrak{R}_4[x]$.

equilibrium in the region $\mathfrak{R}_2[x]$ (see Figure 2(b)). Under the $\mathscr{H}[\mathbf{2},\mathbf{2},\mathbf{2}]$ arrangement, population size $x(t)$ begins in the region $\mathfrak{R}_4[x]$ following the $x_4(t)$ rule with $\lambda_4>E$. If $E<x_0<\lambda_4<a/b, x(t)$ increases as it asymptotically approaches λ_4. On the other hand, if $E<\lambda_4<x_0<a/b$, $x(t)$ decreases while asymptotically approaching λ_4. Therefore, the condition $((E<\lambda_4<a/b)\wedge\mathscr{H}[\mathbf{2},\mathbf{2},\mathbf{2}])\equiv 1$ bears a stable equilibrium at λ_4 (see Figure 2(c)). Whenever $\lambda_4>a/b$, the λ_4 equilibrium lies within region $\mathfrak{R}_1[x]$. Since $E<x_o<a/b$, population size increases according to rule $x_4(t)$ approaching λ_4 reaching the a/b boundary at time t_1 switching to rule $x_1(t)$, since $\lambda_1>a/b$ population size increases asymptotically towards λ_1 staying within region $\mathfrak{R}_1[x]$ (see Figure 2(d)). $\mathscr{H}[\mathbf{1},\mathbf{2},\mathbf{3}]$ and $\mathscr{H}[\mathbf{2},\mathbf{2},\mathbf{3}]$ bear $x(t)$ increasing from $E<x_o$ and could approach asymptotically λ_4 whenever this equilibrium solution lies within region $\mathfrak{R}_4[x]$ or λ_1 if $\lambda_4>a/b$.

For $\mathscr{H}[\mathbf{1},\mathbf{3},\mathbf{1}]$, population size $x(t)$ starts in the region $\mathfrak{R}_1[x]$ and controls by $x_1(t)$ with equilibrium solution λ_1 satisfying $a/b<\lambda_1<E<x_0$. Hence, $x(t)$ decreases and attains the E threshold at a time t_1, transferring to rule $x_2(t)$ and then asymptotically approaching the equilibrium solution $\lambda_2=a/b$ (see Figure 3(a)). For the arrangement $\mathscr{H}[\mathbf{1},\mathbf{3},\mathbf{2}]$, the initial condition sets $x(t)$ to acquire the $x_2(t)$ law in $\mathfrak{R}_2[x]$ and then it approaches the equilibrium solution λ_2. Correspondingly, the $\mathscr{H}[\mathbf{1},\mathbf{3},\mathbf{3}]$ composite $x(t)$ obeys the $x_3(t)$ rule in region $\mathfrak{R}_3[x]$, but since $\beta=\mu a$, it remains stationary at x_o. These configurations suggest a maximum limiting effect of resource scarcity. For $\mathscr{H}[\mathbf{2},\mathbf{3},\mathbf{1}]$, population size $x(t)$ begins within the region $\mathfrak{R}_1[x]$ and since $\lambda_1<a/b$ places in region $\mathfrak{R}_4[x]$, then $x_1(t)$ decreases, intersecting a/b at a time t_1 where it switches to rule $x_4(t)$, ultimately approaching the equilibrium solution $\lambda_4=E$. A $\mathscr{H}[\mathbf{2},\mathbf{3},\mathbf{2}]$ arrangement sets $E<x_0<a/b$, and population size starts within the region $\mathfrak{R}_4[x]$ and sets by $x_4(t)$ approaching the $\lambda_4=E$ equilibrium (see Figure 3(b)). For $\mathscr{H}[\mathbf{2},\mathbf{3},\mathbf{3}]$, the conditions $x_0<E$ and $\beta=\mu a$ set population size beginning within the region $\mathfrak{R}_3[x]$, following $x_3(t)$ that remains stationary at x_0. For $\mathscr{H}[\mathbf{3},\mathbf{3},\mathbf{1}]$, initial condition sets population size $x(t)$ within the region $\mathfrak{R}_1[x]$, following $x_1(t)$. Since $\beta=\mu a$ and $E=a/b$ implies $\lambda_1=E$, then $x(t)$ decreases to λ_1 (see Figure 3(c)). For $\mathscr{H}[\mathbf{3},\mathbf{3},\mathbf{2}]$, we have $x_0<E$, and population size starts within the region $\mathfrak{R}_3[x]$ and follows to growth law $x_3(t)$ but since $\beta=\mu a$, it remains stationary at x_0 (see Figure 3(d)). Configurations in Figure 3 suggest a maximum limiting effect of resource scarcity on population growth; even a BMS_1: $(\beta<\mu a)$ condition does not perform.

In summary, the PLF-PPM's continuous-time global population size trajectory can stand an outstanding array of different performances. It could model population decline whenever the ordering $\beta<\mu a$ holds (see Figure 1). Alternatively, $\beta>\mu a$ could induce conditional stability depending on the achieved parametric arrangement (e.g., Figure 2). Also, the statement $\beta>\mu a$ could entail a purely growing regime for population size $x(t)$ (e.g. $((E<\lambda_4<a/b)\wedge\mathscr{H}[\mathbf{2},\mathbf{2},\mathbf{2}]\equiv 1)$ shown in Figure 2(d). Furthermore, $\beta=\mu a$ circumstance signposts a maximum effect of resource abatement on population growth (e.g., $\mathscr{H}[\mathbf{3},\mathbf{3},\mathbf{1}]$ shown in Figure 3(c)). Moreover, for critical values of E threshold, this configuration could exacerbate Allee effects, and this is due to random influences which could promote vanishing of population size. Furthermore, the ratio a/b in the settings of the PLF-PPM is interpreted as an Allee threshold since $x(t)<a/b$ implies $ax(t)>bx^2(t)$, so population size below a/b controls the mortality process as entailed by the $M(x)$ setup (cf. equation (21)). It is also pertinent to emphasize that for model type M_1, even though population size places below the starvation threshold E, its dynamics could take place under an Allee effect regime. Correspondingly, for M_2 type models, population could evolve in a regime combining both

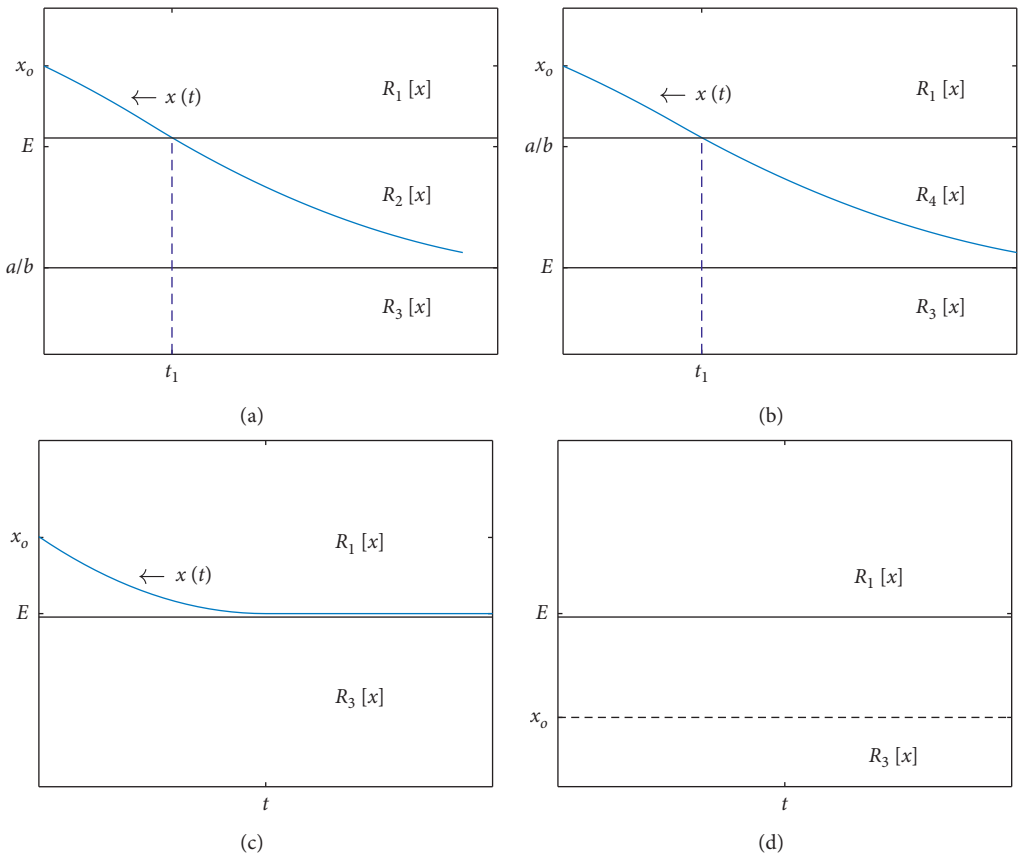

Figure 3: Examples of the shape of the global trajectory $x(t)$ for $\mathscr{H}[i, 3, k(i)]$configuration. (a) The $x(t)$ path for the $\mathscr{H}[\mathbf{1}, \mathbf{3}, \mathbf{1}]$ conjunction population size $x(t)$ starts in the region $\mathfrak{R}_1[x]$ and approaches asymptotically the equilibrium solution $\lambda_2 = a/b$. (b) For $\mathscr{H}[\mathbf{2}, \mathbf{3}, \mathbf{2}]$, population size $x(t)$ begins in the region $\mathfrak{R}_1[x]$ according to $x_1(t)$ and decreases and then switches to rule $x_4(t)$ to approach asymptotically $\lambda_4 = E$. (c) $\mathscr{H}[\mathbf{3}, \mathbf{3}, \mathbf{1}]$ ordering sets $x(t)$ initially within the region $\mathfrak{R}_1[x]$ and then $x(t)$ decreases to $\lambda_1 = E$. (d) For $\mathscr{H}[\mathbf{3}, \mathbf{3}, \mathbf{2}]$, we have $x_0 < E$, and population size starts within the region $\mathfrak{R}_3[x]$ and follows growth law $x_3(t)$ but since $\beta = \mu a$, it remains stationary at x_0.

starvation and Allee effects. Consequently, by adapting the number of factors defining $N(x)$ and $M(x)$ in equation (17) so as to suit specific modeling aims, we could endure the PLF-PPM suitable predictive strength. In what follows, we explain the performance of the PLF-PPM model of equation (22) as an exploratory tool given different datasets.

4. Study Cases

In what follows, we explain the performance of the PLF-PPM model of equation (22) as an exploratory tool given different datasets. We address data of Armstrong [7] on the growth of populations of asexual *Dugesia tigrina*, data reported by Huisman [8] on developing experimental populations of the unicellular green algae *Chlorella vulgaris*, a study by Davidson [9] on a sheep population introduced in Tasmania, data by Pearl [10] on the growth of *Drosophila melanogaster*, and data reported by Hughes and Tanner [11] on the slow decline of an *Agaricia agaricites* population on Jamaican reefs. Fitted parameters, associated standard deviations, and concordance correlation coefficient values [12] are given in Table 3. All required PLF-PPM fits were achieved by using the Berkeley Madonna Software Version 8.3.18. Besides, acquiring the resource abatement function $R(x)$ relied on using equation (18) setting $E = F_0/2k$ for $k = 1$, which assures getting a proxy for the maximum depletion rate.

Armstrong [7] maintained populations of asexual *Dugesia tigrina*, in an arrangement of finger bowls. Bowls contained 120 ccs of water each and were kept at a temperature of 25°C. Every other day, each population received 0.1 ccs of freshly killed brine shrimp. The bowls were cleaned at the end of the feeding period. The initial population size in every bowl amounted to 35 worms. Reproduction occurred only by transverse fission, with each worm dividing to produce a tail that developed into a new individual. For data assembly, a tail was any recent fission product not adequately developed to consume food. In the experiment, tails were added to the population's artificially increasing reproductive efficiency. Because this method amounts to exogenous addition of biomass, we focused on data of population control named 1–0 without tails added to fit the PLF-PM. The plot of the CCC = 0.9920 global trajectory is shown in Figure 4(a). Associated estimated parameter values are presented in Table 3. Acquired orderings were $\beta > \mu a$ and $x_o < a/b < \lambda_1 < \lambda_2 < E < \lambda_4$ corresponding to a $\mathscr{H}[\mathbf{1}, \mathbf{2}, \mathbf{3}]$ arrangement composing regions

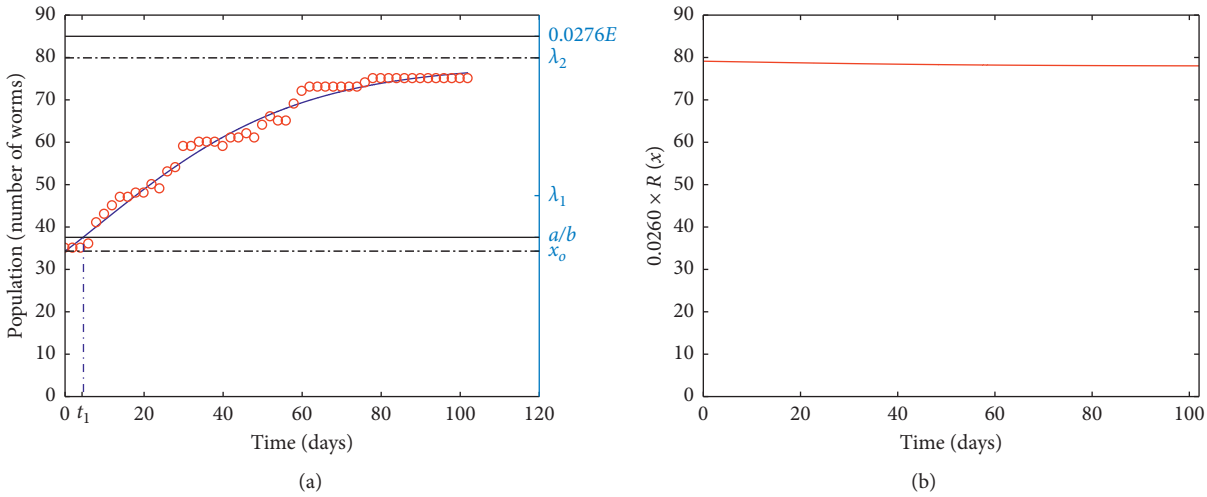

Figure 4: Fit of the PLF-PPM to data of Armstrong [7] relates to the growth of an experimental population of planarian *Dugesia tigrina*. (a) Fitted trajectory lines. (b) Proportion $(0.0260 \times R(x))$ of resource abatement function.

$\mathfrak{R}_1[x], \mathfrak{R}_2[x]$, and $\mathfrak{R}_3[x]$. Population size places initially within the region $\mathfrak{R}_3[x]$ and acquires the form $x_3(t)$ until it reaches the upper boundary at a/b at time $t_1 = 4.43$ where it gets into the region $\mathfrak{R}_2[x]$ switching to rule $x_2(t)$, approaching the asymptotic limit λ_2. Since dynamics mainly describe the region $\mathfrak{R}_2[x]$, mortality could perhaps be explained by cannibalism induced by high intraspecific competition. The author inferred about food scarcity for population levels near the equilibrium. Nevertheless, the PLF-PM identifies an energy threshold E well above the equilibrium level, which explains the shape of the resource depletion trajectory proxy shown in Figure 4(b). Therefore, population regulation is solely controlled by density-dependent mortality.

Huisman [8] studied the growth of experimental populations of the unicellular green algae *Chlorella vulgaris*. Populations were raised in continuous cultures incubated at 20°C and administered with plentiful nutrients and O_2. Thus, growth limitation is exclusively associated with incident light energy. We handpicked data on population G. Figure 5(a) shows the global trajectory associated with the CCC = 0.9946 fit of the PLF-PM. The values of estimated parameters are presented in Table 3. Acquired parametric orderings were $\beta > \mu a$ and $x_o < a/b < \lambda_2 < E$ conforming to $\mathscr{H}[\mathbf{1}, \mathbf{2}, \mathbf{3}]$ composing regions $\mathfrak{R}_1[x], \mathfrak{R}_2[x]$, and $\mathfrak{R}_3[x]$. Population size places initially within the region $\mathfrak{R}_3[x]$ and rules by $x_3(t)$ until it reaches the upper boundary at a/b at time $t_1 = 3.7$ where it goes into the region $\mathfrak{R}_2[x]$ switching to rule $x_2(t)$, approaching the asymptotic limit λ_2. The equilibrium value λ_2 was practically attained at the end of the 18^{th} day, with regulation by recruitment of new individuals and mortality dominated by individual properties. This photosynthetic organism synthesizes biomass based on a combination of factors like light, CO_2, and nutrients. The threshold **E** could be conceived as the biomass size such that the aggregated life enduring factors become limiting factors. Because there were sufficient CO_2 and nutrients in this case, the E threshold could be interpreted as the level of available light energy. Our analysis sustains the assumption in [8] that population growth in *Chlorella vulgaris* is limited exclusively by incident light. Therefore, the value of the E threshold estimated by the fit of the PLF-PPM determines a resource abatement function that suggests that the amount of incident light for the G-labeled population in Huisman's experiment was not limiting (see Figure 5(b)); this is because the equivalent of E in biomass units lies well above the equilibrium level λ_2.

Davidson [9] studied a sheep population introduced in Tasmania. We acquired related proxy data from [13] representing the averages of the number of individuals taken on periods of 5 years. The recorded data span a total of 120 years. The first average corresponds to 1814–1819, and we arranged for 1819 to stand for year zero. The global trajectory acquired from the CCC = 0.9484 fit of the PLF-PM is shown in Figure 6(a). The obtained parametric orderings were $\beta > \mu a$ and $x_o < a/b < \lambda_1 < \lambda_2 < E < \lambda_4$, associated to a $\mathscr{H}[\mathbf{1}, \mathbf{2}, \mathbf{3}]$ arrangement that composes regions $\mathfrak{R}_1[x], \mathfrak{R}_2[x]$, and $\mathfrak{R}_3[x]$. Population size places initially within the region $\mathfrak{R}_3[x]$ and progressed according to rule $x_3(t)$. The fit points out that within the region $\mathfrak{R}_3[x]$, population growth was slow at the beginning, which suggests that reproduction was limited by a reduced number of individuals. Population size crossed the a/b threshold at the beginning of year 6 (1825). Population growth switched to rule $x_2(t)$, associated with recruitment and mortality controlled by population size. Thus, fitted trajectory increased approaching the equilibrium λ_2 placing inside $\mathfrak{R}_2[x]$ (see Figure 6(a)). Besides, it can be learned from Figure 6(b) that in spite of surpassing two records and another two almost reaching the E threshold, their influence was not strong enough so as to change the damped oscillating trend about λ_2 imposed by rule $x_2(t)$. Indeed, the dominance of the dynamic arrangement endured by the $x_2(t)$ rule stayed over some

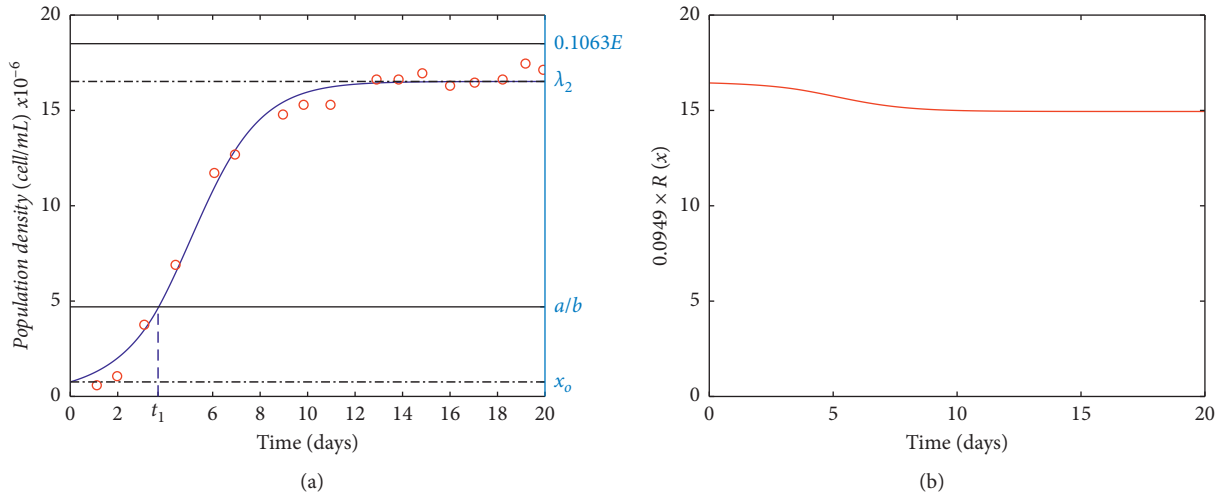

Figure 5: Fit of the PLF-PPM to data taken from Huisman [8] relates to the growth of an experimental population of the unicellular green algae, *Chlorella vulgaris*. (a) Fitted trajectory lines. (b) Proportion $(0.0949 \times R(x))$ of resource abatement function.

Table 3: Estimated values of initial population size x_9 and basic parameter a, b, β, μ, E, produced by fitting the PLF-PPM of equation (22) to the listed datasets.

Dataset	Fitted parameters										
	x_o	A	b	B	μ	E	a/b	λ_1	λ_2	λ_4	CCC
Armstrong [7]	34.31	3.59	0.09	0.03	0.0050	3077.43	39.88	47.4100	79.91	6.5e+03	0.9920
	0.06	0.38	0.06	0.00	0.0003	625.18	—	—	—	—	—
Huisman [8]	0.75	186.53	39.71	0.68	0.0010	174	4.69	2.12e+3	16.51	2.1e+3	0.9946
	0.11	49.65	15.31	0.02	0.0002	84.56	—	—	—	—	—
Pearl [10]	3.96	1.89	0.08	0.25	0.0092	628.30	22.18	38.27	318.28	9.0e−3	0.9913
	1.15	0.48	0.00	0.01	0.0001	37.48	—	—	—	—	—
Davidson [9]	85.73	146	0.56	0.18	1.94e+4	1974	260.71	1.02e+3	1.69e+3	1.2e+4	0.9484
	58.10	41.79	1.75	0.02	0.0000	178.63	—	—	—	—	—
Hughes and Tanner [11]	213.42	1186.56	1.57	0.09	1.64e+4	376.55	755.77	180.74	360.98	752.05	0.9340
	1.5153	309.59	1.95	0.05	9.49e−5	104.61	—	—	—	—	—

Records right below parameter estimates correspond to associated standard errors. Calculated a/b ratio, equilibria $\lambda_1, \lambda_2, \lambda_4$, and concordance correlation coefficient (CCC) values are also displayed.

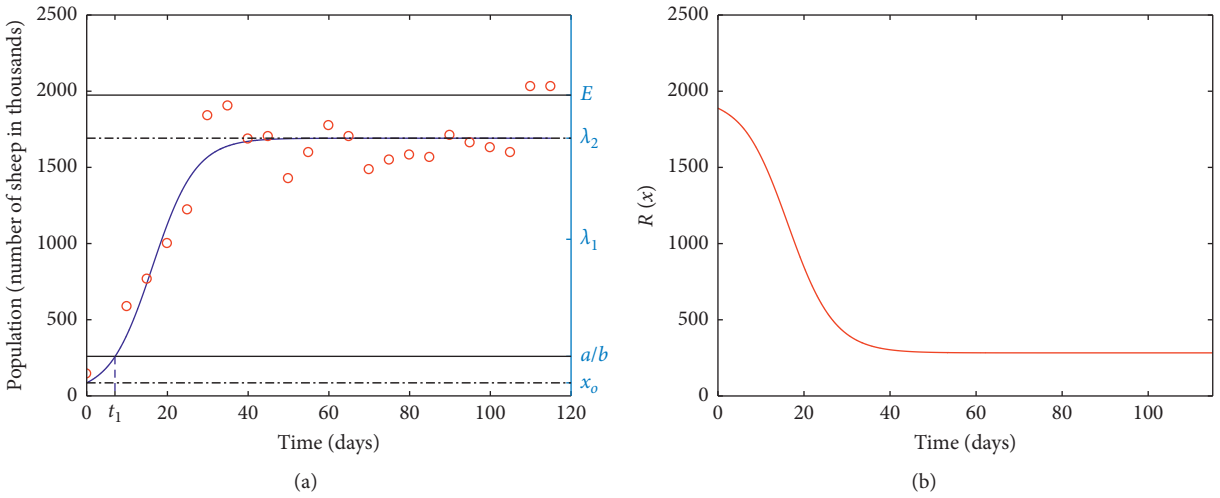

Figure 6: Fit of the PLF-PPM to data of Davidson [9] relates to the growth of a sheep population introduced in Tasmania. (a) Fitted trajectory lines. (b) Resource abatement function $R(x)$.

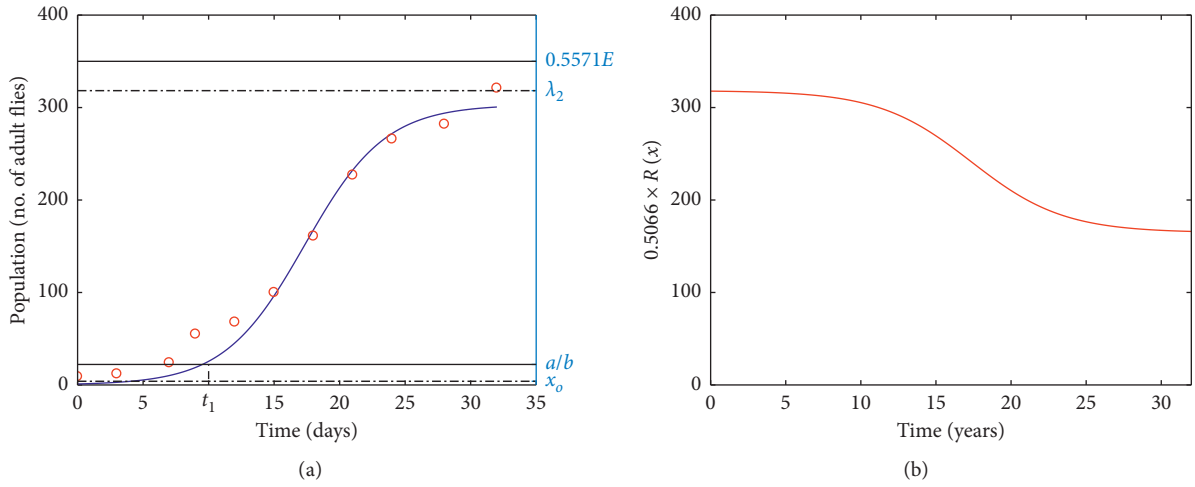

Figure 7: Fit of the PLF-PPM to data of Pearl [10] relates to the growth of an experimental population of the fruit fly *Drosophila melanogaster*. (a) Fitted trajectory lines. (b) Proportion $(0.5066 \times R(x))$ of resource abatement function $R(x)$.

time long enough to induce the trend to equilibrium suggested by the PLF-PPM fit.

We now consider the construction of the global trajectory $x(t)$ associated with a fit of the PLF-PM to data of [10], taken from [14]. Pearl [10] maintained populations of *Drosophila melanogaster* in bottles using yeast as food and fitted a logistic curve to the associated data expressed as the counted number of adult flies in a particular day. Sang [15] criticized the procedure, quarreling that the experiments did not keep the yeast constant but as a growing population on its own. The plots associated with the PLF-PPM fit displayed in Figure 7(a) produced the parameter orderings $\beta > \mu a$ and $x_0 < a/b < E < \lambda_2$ that conform to a $\mathscr{H}[\mathbf{1}, \mathbf{2}, \mathbf{3}]$ arrangement, that is, a model type M_1 with BMS_2: $(\beta > \mu a)$ and IC_{13}: $(x_o < a/b)$. Phase arrangement includes regions $\mathfrak{R}_1[x], \mathfrak{R}_2[x]$, and $\mathfrak{R}_3[x]$. At the beginning of the growth process, $x(t)$ stays in the region $\mathfrak{R}_3[x]$ but the statement BMS_2: $(\beta > \mu a) \equiv 1$, forces associating a rule $x_3(t)$ to increase, and then it reaches the a/b boundary at $t_1 = 10$, thereby entering the region $\mathfrak{R}_2[x]$ and then progressing asymptotically to λ_2 following rule $x_2(t)$. The fit shows that the fly population is entirely controlled by density-dependent mortality. In contrast to Sang [15], the PLF-PPM fit demonstrates that energy did not play a decisive role $((E > \lambda_2)$; also, see Figure 7(b)), so we can close that variations in feeding energy did not determine the dynamics since otherwise $x_1(t)$ would compose the global trajectory $x(t)$. The application of the FDM sustains the assumption that in Pearl's experiment, energy does not provide a criterion to define a carrying capacity. Furthermore, the equilibrium λ_2 is not expressed in terms of E but solely as a function of the scaling parameters β, μ, and b.

Hughes and Tanner [11] reported a slow decline of the coral population on Jamaican reefs over 16 years. We fitted the PLF-PM to data on *Agaricia agaricites* colonies recorded during 1977–1993. The authors established that local extinction is explained by increased mortality rates plus the adverse effects of two hurricanes, Allen (in 1980) and Gilberto (in 1988). Also relevant in explaining the decline was the impossibility of recovery because of a recruitment failure. Figure 8(a) shows the global trajectory associated with the fit CCC = 0.9340 of the PLF-PM. The values of the parameter estimates are given in Table 3. Acquired parametric orderings were $\beta < \mu a$ and $x_o < \lambda_2 < E < \lambda_1 < a/b$ conforming to a $\mathscr{H}[\mathbf{2}, \mathbf{1}, \mathbf{3}]$ arrangement and composing regions $\mathfrak{R}_1[x], \mathfrak{R}_2[x]$, and $\mathfrak{R}_3[x]$. Population size places initially within the region $\mathfrak{R}_3[x]$ and rules by $x_3(t)$. Food was not limiting. Perhaps perturbation set its level under the upper boundary of the $\mathfrak{R}_3[x]$ region where Allee effects dominate mortality. Then, possibly a recruitment failure impeded compensation to the abatement effects linked to the $\beta < \mu a$ ordering. Then, our analysis corroborates the assumption of Hughes and Tanner [11]. In any event, recruitment failure could not associate with resource reduction (see Figure 8(b)).

The PLF-PPM displayed high reproducibility strength in all performed fits, as it derives from the high CCC values included in Table 3. Moreover, parallel plots of resource abatement explain that fitted values of initial resource availability thresholds E explain the occurrence of recorded equilibrium levels. Results point towards the consistency of the PLF-PPM as an exploratory tool. Nevertheless, the direct fitting procedure endured by the Berkeley Madonna software relied upon apportioning initial values of

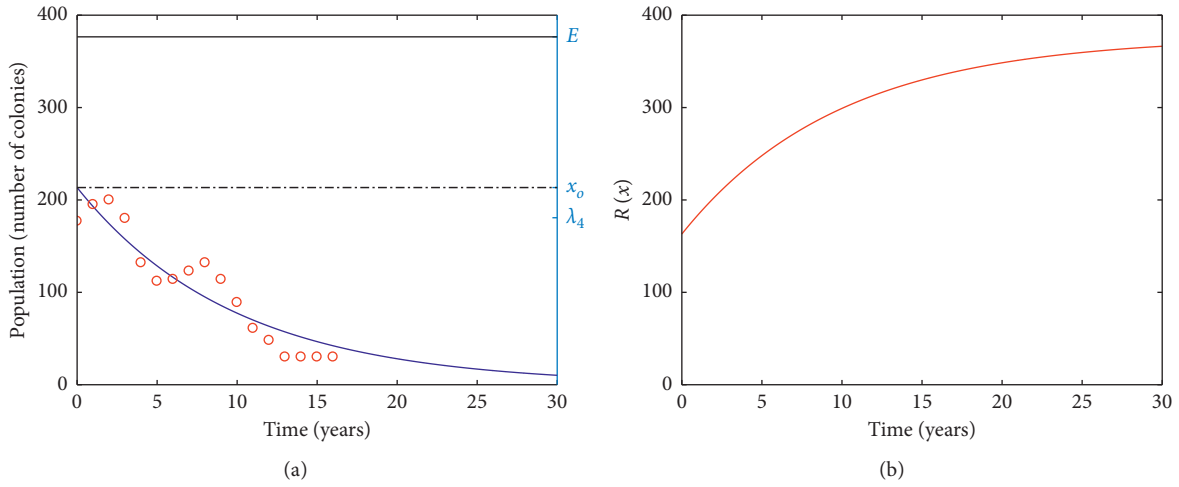

FIGURE 8: Fit of the PLF-PM to data of Hughes and Tanner [11] relates to the decline of *Agaricia agaricites* coral population on Jamaican reefs. (a) Fitted trajectory lines. (b) Resource abatement function $R(x)$.

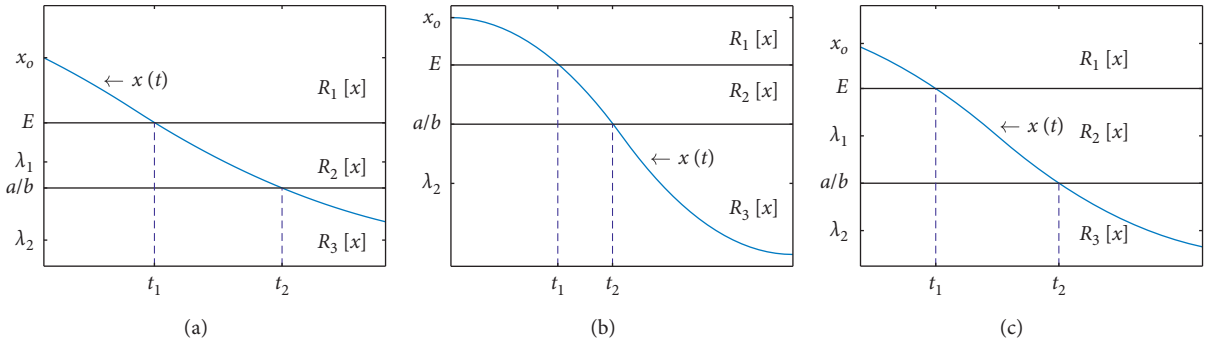

FIGURE 9: The PLF-PPM composite trajectory $x(t)$ for the $\mathscr{H}[\mathbf{1},\mathbf{1},\mathbf{1}]$ configuration. (a) $a/b < \sqrt{\beta E/\mu b} < E$ derived from the auxiliary ordering $E > \mu a^2/\beta b$. This panel shows that the global trajectory $x(t)$ reaches the E threshold at a time t_1. (b) Population size keeps decreasing, so it touches the a/b frontier. (c) Since $\beta < \mu a$, the population becomes extinct.

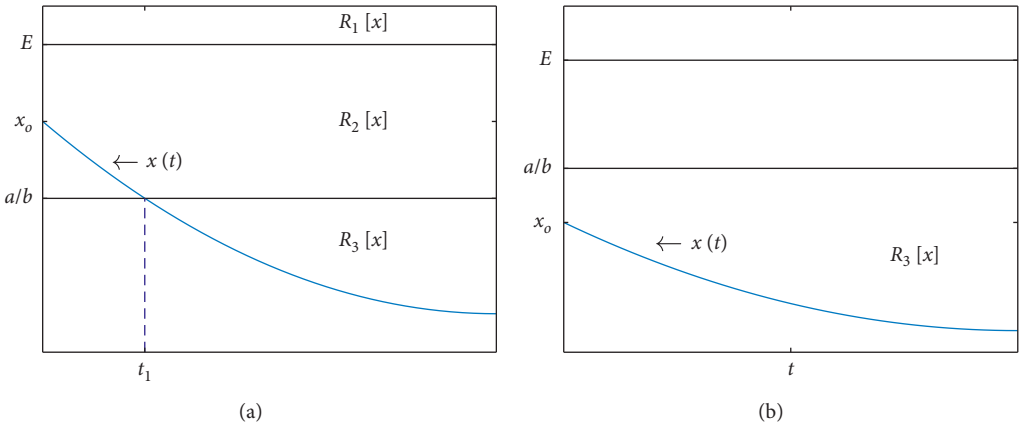

FIGURE 10: The PLF composite trajectory $x(t)$ for the $\mathscr{H}[\mathbf{1},\mathbf{1},\mathbf{2}]$ configuration. (a) The global trajectory $x(t)$ decreases from x_o until it reaches the a/b threshold at time t_1. Since $\beta < \mu a$, population size keeps decreasing until it becomes extinct. (b) Extinction as determined by the $\mathscr{H}[\mathbf{1},\mathbf{1},\mathbf{3}]$ arrangement.

parameter estimates. Necessarily, this brought about high sensibility associated to local minimum problems at the non-linear acquisition of final estimates. Detected inconveniences suggest revision aimed at adapting techniques that could lessen the experienced parameter estimation burden.

4.1. Outline of the Discrete-Time Setup of the PLF-PPM. Although this paper focuses on addressing the analysis of the PLF-PPM arrangement trajectories on continuous time, we consider it pertinent at this setting to outline the associated discrete-time form. For this reason, we let $f_i(x_n)$ denote the discrete-time form of the phase model $f_i(x)$ as given by equation (22) for $i = 1, 2, 3, 4$. Also, let $\mathfrak{R}_i[x_n]$ be the corresponding range of application of the rule $f_i(x_n)$. Then, if $\chi(\mathfrak{R}_1[x_n])$ stands for the characteristic function of $\mathfrak{R}_1[x_n]$, we get

$$x_{n+1} = x_n + \sum_{i=1}^{4} \chi(\mathfrak{R}_i[x_n]) f_i(x_n), \tag{25}$$

for $n = 0, 1, 2, \ldots$, with x_0 being placed on one of the regions $\mathfrak{R}_i[x_n]$. Then,

$$\left.\begin{array}{ll} f_1(x_n) = \beta E - \mu b x_n^2 & \mathfrak{R}_1[x_n] = \left\{x_n \middle| (x_n > E) \wedge \left(x_n > \dfrac{a}{b}\right)\right\} \\ f_2(x_n) = \beta x_n - \mu b x_n^2 & \mathfrak{R}_2[x_n] = \left\{x_n \middle| (x_n < E) \wedge \left(x_n > \dfrac{a}{b}\right)\right\} \\ f_3(x_n) = (\beta - \mu a) x_n & \mathfrak{R}_3[x_n] = \left\{x_n \middle| (x_n < E) \wedge \left(x_n < \dfrac{a}{b}\right)\right\} \\ f_4(x_n) = \beta E - \mu a x_n & \mathfrak{R}_4[x_n] = \left\{x_n \middle| (x_n > E) \wedge \left(x_n < \dfrac{a}{b}\right)\right\} \end{array}\right\}. \tag{26}$$

The parametrization $r = 1 + \beta$ and $s = \mu b$ and then the change of variable $(r/s)z_n = x_n$ will bring the logistic map as a submodel composing the seek for discrete-time formulation. Concomitantly, equation (25) transforms into

$$z_{n+1} = \sum_{1=1}^{m} \chi(\mathfrak{R}_i[z_n]) \theta_i(z_n), \tag{27}$$

where

$$\left.\begin{array}{ll} \theta_1(z_n) = \dfrac{s(1-r)E}{r} + z_n(1 - r z_n), & \mathfrak{R}_1[z_n] = \left\{z_n \middle| \left(z_n > \dfrac{sE}{r}\right) \wedge \left(z_n > \dfrac{sa}{rb}\right)\right\} \\ \theta_2(z_n) = r z_n (1 - z_n) & \mathfrak{R}_2[z_n] = \left\{z_n \middle| \left(z_n < \dfrac{sE}{r}\right) \wedge \left(z_n > \dfrac{sa}{rb}\right)\right\} \\ \theta_3(z_n) = \left(r - \dfrac{sa}{b}\right) z_n & \mathfrak{R}_3[z_n] = \left\{z_n \middle| \left(z_n < \dfrac{sE}{r}\right) \wedge \left(z_n < \dfrac{sa}{rb}\right)\right\} \\ \theta_4(z_n) = \dfrac{s(r-1)E}{r} + \left(1 - \dfrac{sa}{b}\right) z_n & \mathfrak{R}_4[z_n] = \left\{z_n \middle| \left(z_n > \dfrac{sE}{r}\right) \wedge \left(z_n < \dfrac{sa}{rb}\right)\right\} \end{array}\right\}. \tag{28}$$

Equivalently,

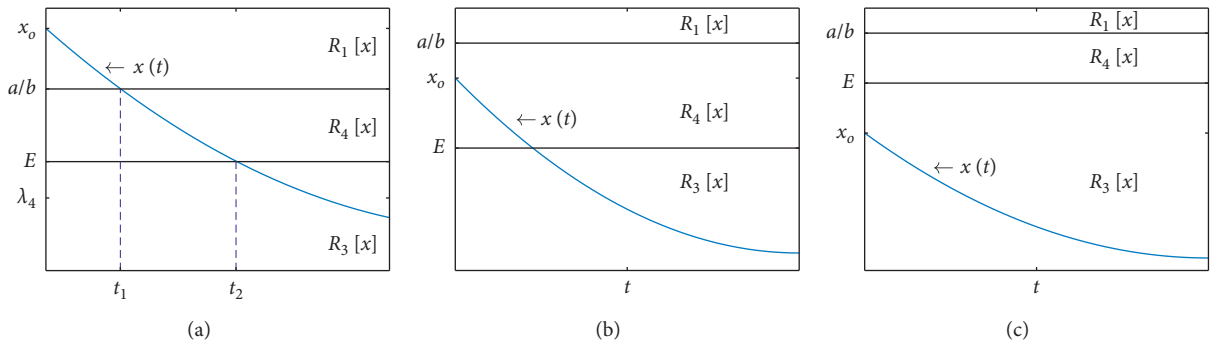

FIGURE 11: The shape of the PLF composite trajectory $x(t)$ under an extinction configuration. (a) The global trajectory $x(t)$ for the $\mathscr{H}[\mathbf{2},\mathbf{1},\mathbf{1}]$ decreases from $x_o > a/b > E$ until it reaches the a/b threshold at time t_1. The $x(t)$ trajectory keeps decreasing, and it hits the E threshold at a particular time t_2. Later, since $\beta < \mu a$, population size keeps decreasing until it becomes extinct. (b) Case $\mathscr{H}[\mathbf{2},\mathbf{1},\mathbf{2}]$ where population size decreases from $E < x_o < a/b$ and reaches the E boundary at a time t_1 and then it progresses to extinction. (c) $\mathscr{H}[\mathbf{2},\mathbf{1},\mathbf{3}]$configuration, where departing from $x_o < E < a/b$, the population becomes extinct.

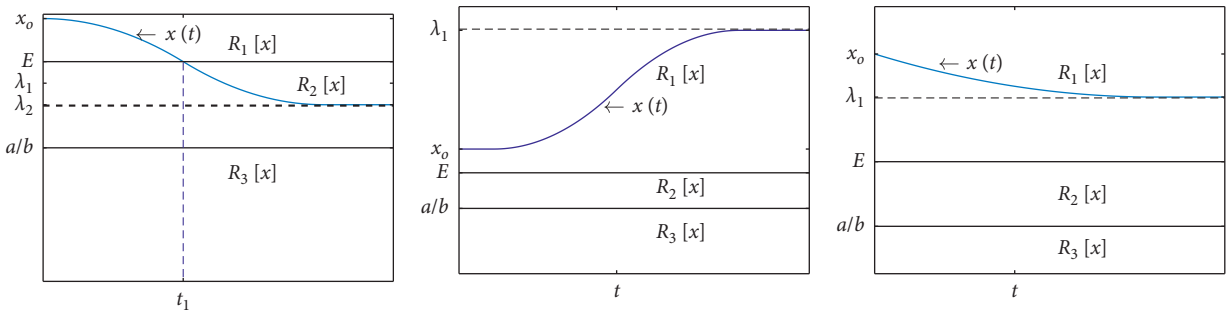

FIGURE 12: The shape of the PLF composite trajectory $x(t)$ for the $\mathscr{H}[\mathbf{1},\mathbf{2},\mathbf{1}]$ configuration. (a) The condition $((\lambda_2 < E) \wedge \mathscr{H}[\mathbf{1},\mathbf{2},\mathbf{1}]) \equiv 1$, where the trajectory departs from $x_o > E > a/b$ and decreases as it approaches asymptotically the equilibrium solution λ_2 placed in region $\mathfrak{R}_2[x]$. (b) In the case $((\lambda_2 > E) \wedge \mathscr{H}[\mathbf{1},\mathbf{2},\mathbf{1}]) \equiv 1$, departing from $E < x_o < \lambda_1$, the trajectory increases and asymptotically approaches λ_1. (c) $E < \lambda_1 < x_o$, where population size decreases to λ_1, which establishes λ_1 as a stable equilibrium in the region $\mathfrak{R}_1[x]$.

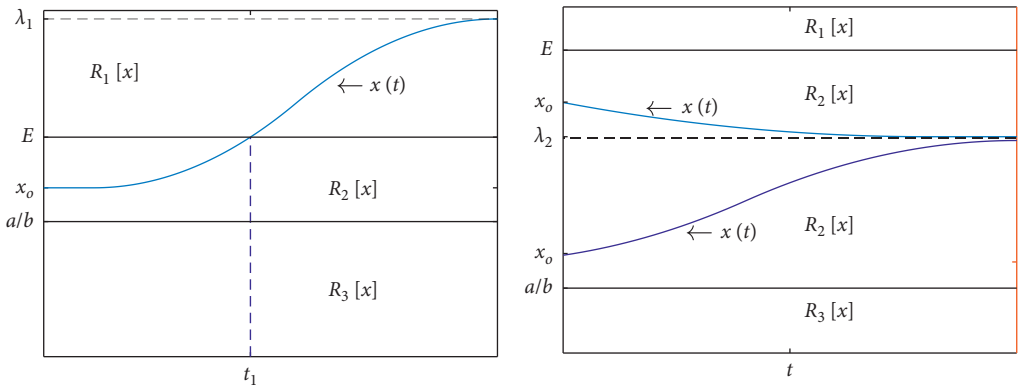

FIGURE 13: The shape of the PLF composite trajectory $x(t)$ for the $\mathscr{H}[\mathbf{1},\mathbf{2},\mathbf{2}]$ configuration. (a) The case $((\lambda_2 > E) \wedge \mathscr{H}[\mathbf{1},\mathbf{2},\mathbf{2}]) \equiv 1$ where the trajectory departs from $a/b < x_o < E < \lambda_2$ and increases through the $\mathfrak{R}_2[x]$ region as it approaches asymptotically the equilibrium solution λ_2 placed in region $\mathfrak{R}_1[x]$, so it will switch at a time t_1 to rule $x_1(t)$ approaching λ_1. (b) The case $((\lambda_2 < E) \wedge \mathscr{H}[\mathbf{1},\mathbf{2},\mathbf{2}]) \equiv 1$. The population size approaches the stable equilibrium λ_2 placed inside $\mathfrak{R}_2[x]$.

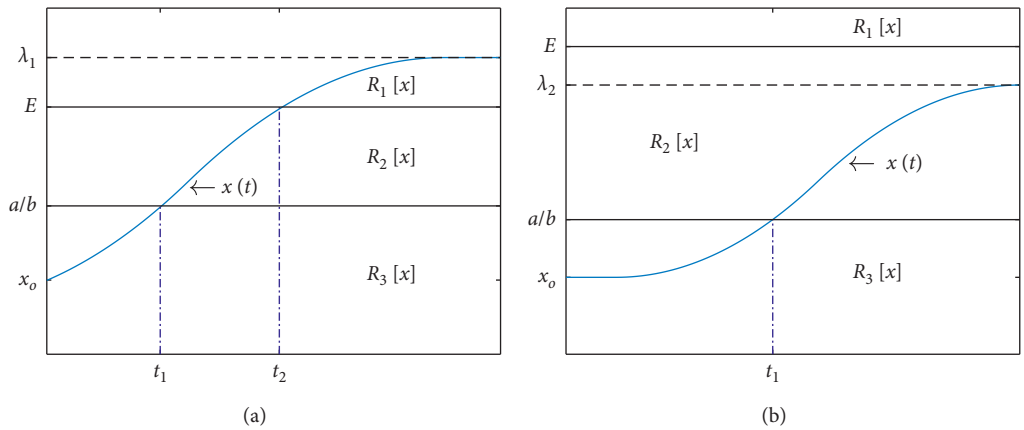

FIGURE 14: The comportment of the PLF composite trajectory $x(t)$ for the $\mathscr{H}[\mathbf{1},\mathbf{2},\mathbf{2}]$configuration. (a) The case $((\lambda_2 > E) \wedge \mathscr{H}[\mathbf{1},\mathbf{2},\mathbf{2}]) \equiv 1$; the relationship $x_o < a/b < E < \lambda_2$ holds, so the population size $x(t)$ places initially within the region $\mathfrak{R}_3[x]$ and grows according to the $x_3(t)$ trajectory; then, at a time t_1,$x(t)$ reaches E, so dynamics are now controlled by $x_1(t)$ and consequently will asymptotically approach the λ_1 threshold placed in $\mathfrak{R}_1[x]$. (b) $((\lambda_2 < E) \wedge \mathscr{H}[\mathbf{1},\mathbf{2},\mathbf{3}]) \equiv 1$; the inequality $x_0 < a/b < \lambda_2 < E$ holds, and population size is ruled by $x_3(t)$ until it reaches a/b and switches to $x_2(t)$, and then it remains in $\mathfrak{R}_2[x]$ approaching the asymptotic limit λ_2.

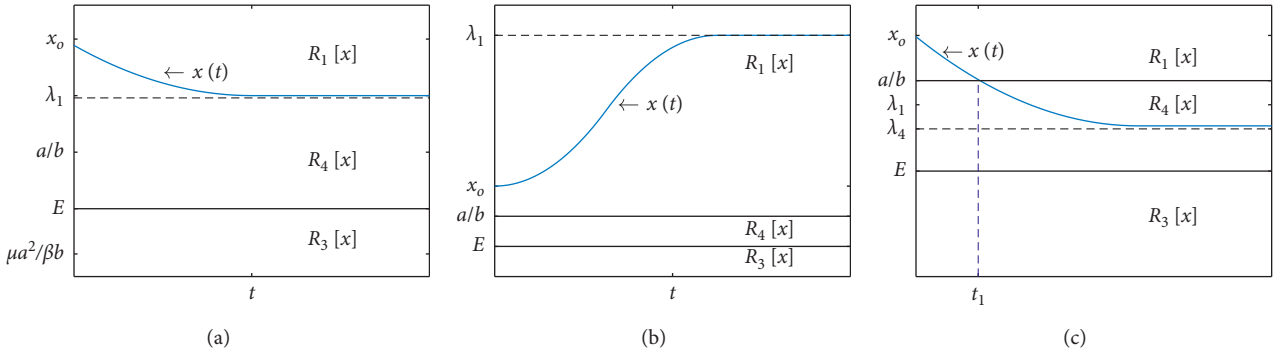

FIGURE 15: The construction of the global trajectory $x(t)$ under the $\mathscr{H}[2,2,1]$ arrangement. (a) Since $x_o > a/b$, population size initiates dynamics within the region $\mathfrak{R}_1[x]$ according to the $x_1(t)$rule that bears the equilibrium solution $\lambda_1 > E$. If $E < a/b < \lambda_1 < x_0$, population size decreases as it approaches λ_1. (b) If $E < a/b < x_0 < \lambda_1$, population size increases approaching λ_1 asymptotically. (c) Whenever $E < \lambda_1 < a/b < x_0$, population size initiates within the region $\mathfrak{R}_1[x]$ and decreases towards λ_1, entering into the region $\mathfrak{R}_4[x]$ at a time t_1 and then switching to rule $x_4(t)$, but $\beta/\mu a > 1$, and then $E < \lambda_4 < a/b < x_o$, so $x(t)$ keeps decreasing as it approaches asymptotically λ_4.

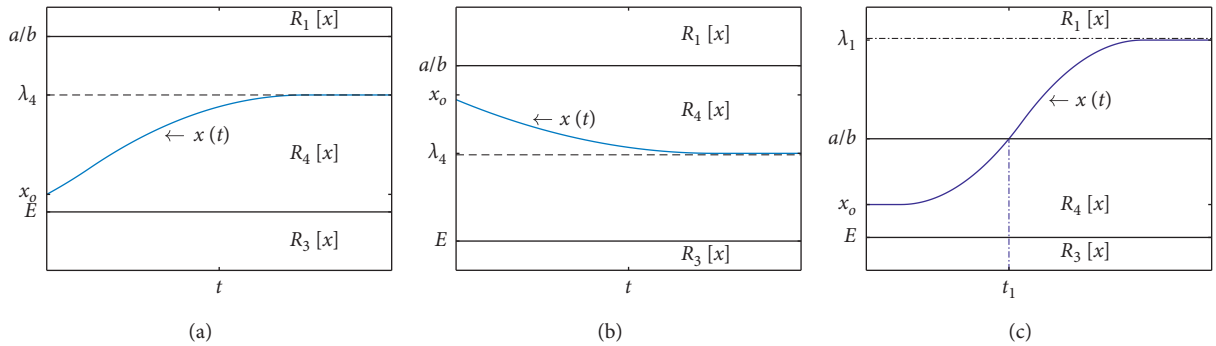

FIGURE 16: The behavior of the global trajectory $x(t)$ under the $\mathscr{H}[\mathbf{2},\mathbf{2},\mathbf{2}]$ arrangement. (a) Population size begins in the region $\mathfrak{R}_4[x]$ following $x_4(t)$ with $\lambda_4 > E$; if $E < x_0 < \lambda_4 < a/b$, population size increases as it approaches λ_4. (b) On the other hand, if $E < \lambda_4 < x_0 < a/b$, population size decreases approaching λ_4 asymptotically. (c) Whenever $\lambda_4 > a/b$, λ_4 equilibrium lies within the region $\mathfrak{R}_1[x]$, and then, since $E < x_o < a/b$, population size increases according to rule $x_4(t)$ approaching λ_4 reaching the a/b boundary at time t_1 switching to rule $x_1(t)$; then, since $\lambda_1 > a/b$, population size increases asymptotically towards λ_1 staying within region $\mathfrak{R}_1[x]$.

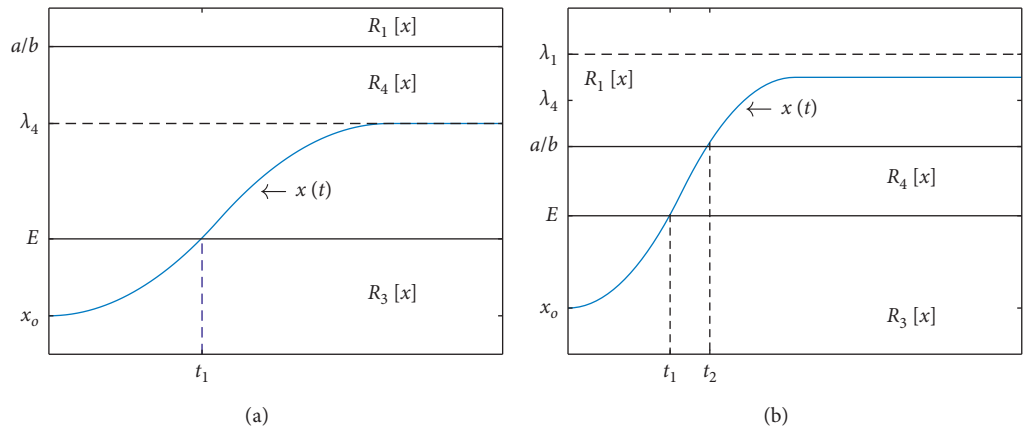

FIGURE 17: The form of the global trajectory $x(t)$ for the $\mathscr{H}[\mathbf{2},\mathbf{2},\mathbf{3}]$ composite. (a) The initial condition $x_o < E$ sets population size $x(t)$ within the region $\mathfrak{R}_3[x]$ ruled by $x_3(t)$; continuity implies $x_3(t_1) = E$; then, for $t > t_1$, $x(t)$ increases according to $x_4(t)$ approaching λ_4 whenever this places in $\mathfrak{R}_4[x]$. (b) Whenever λ_4 places within region $\mathfrak{R}_1[x]$, by continuity, $x_3(t)$ reaches the a/b boundary at a time t_2 switching to rule $x_1(t)$ satisfying $f_1(a/b) > 0$ implying $\lambda_1 > a/b$; therefore, $x(t)$ approaches λ_1 asymptotically.

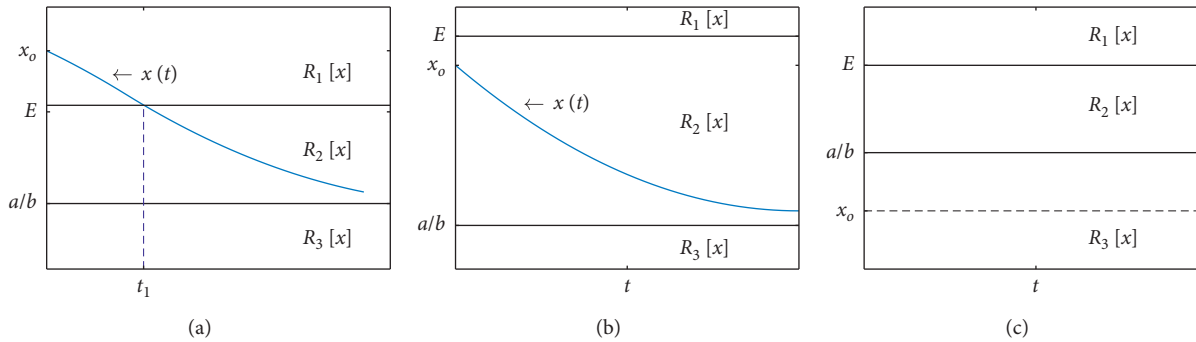

FIGURE 18: The construction of the global trajectory $x(t)$ for the $\mathscr{H}[1,3,\mathbf{k}]$ composite $(k = 1, 2, 3)$. (a) For $\mathscr{H}[\mathbf{1},\mathbf{3},\mathbf{1}]$, population size starts at $x_o > E$ in region $\mathfrak{R}_1[x]$ and is controlled by $x_1(t)$ that bears the asymptotic limit $\lambda_1 = \sqrt{aE/b}$ satisfying $a/b < \lambda_1 < E < x_0$, and population size decreases reaching the E threshold at a certain time t_1 switching to growing rule $x_2(t)$ and will asymptotically approach the equilibrium solution $\lambda_2 = a/b$. (b) For the arrangement $\mathscr{H}[\mathbf{1},\mathbf{3},\mathbf{2}]$, the initial condition placement $a/b < x_o < E$ sets population size behaving according to the $x_2(t)$ law in $\mathfrak{R}_2[x]$, and population size approaches the equilibrium solution $\lambda_2 = a/b$. (c) Correspondingly, the $\mathscr{H}[\mathbf{1},\mathbf{3},\mathbf{3}]$ composite sets $x_o < E$, and population size obeys the $x_3(t)$ rule in region $\mathfrak{R}_3[x]$, but since $\beta = \mu a$, it remains stationary at the x_o value.

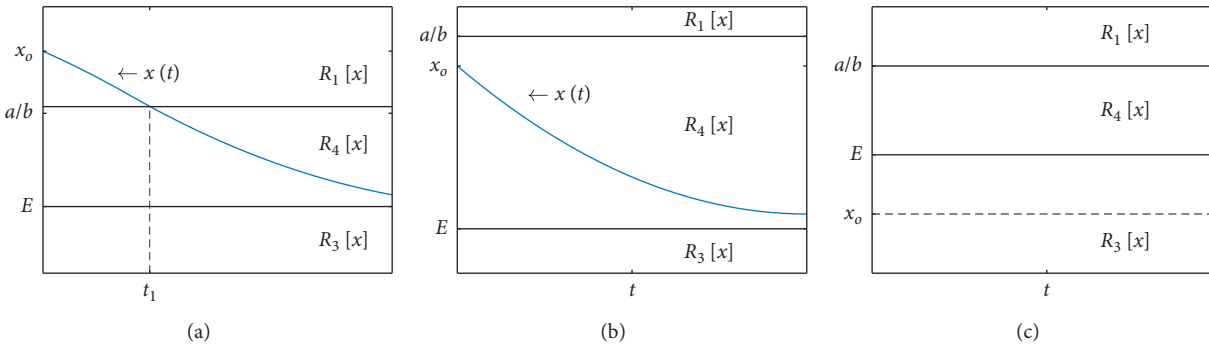

FIGURE 19: The assemblage of the global trajectory $x(t)$ for the $\mathscr{H}[2,3,\mathbf{k}]$ composite $(k = 1, 2, 3)$. (a) For the $\mathscr{H}[\mathbf{2},\mathbf{3},\mathbf{1}]$ arrangement, population size $x(t)$ begins at $x_o > a/b$ within region $\mathfrak{R}_1[x]$ then $\lambda_1 < a/b$ places in region $\mathfrak{R}_4[x]$, $x(t)$ decreases, and intersects a/b at a time t_1. Then switches to rule $x_4(t)$ which decreases and approaches the equilibrium solution $\lambda_4 = E$. (b) For the case $\mathscr{H}[\mathbf{2},\mathbf{3},\mathbf{2}]$, we have $E < x_0 < a/b$, population size starts within the region $\mathfrak{R}_4[x]$ and sets by $x_4(t)$ approaching the $\lambda_4 = E$ equilibrium. (c) For $\mathscr{H}[\mathbf{2},\mathbf{3},\mathbf{3}]$, the condition $x_0 < E$ and $\beta = \mu a$ set population size beginning within the region $\mathfrak{R}_3[x]$ and following $x_3(t)$ that remains stationary at x_0.

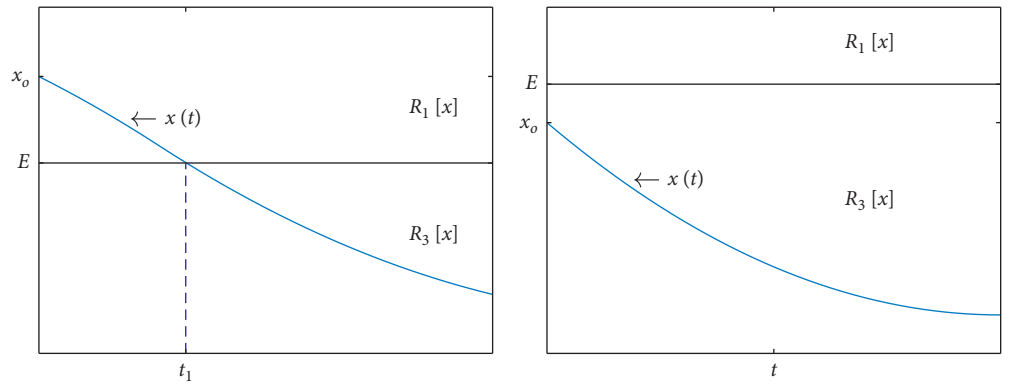

FIGURE 20: The form of the global trajectory $x(t)$ for the $\mathscr{H}[3,1,\mathbf{k}]$ composite $(k = 1,2,3)$. (a) The case $\mathscr{H}[3,1,1]$ is associated to $x_o > E$; then, at the beginning, dynamics are set by the path $x_1(t)$ prevalent in region $\mathfrak{R}_1[x]$ that asymptotically approaches the value $\lambda_1 < E$; then, population size decreases and hits the E boundary at the time t_1 switching to $x_3(t)$ holding in region $\mathfrak{R}_3[x]$ which drives the population to extinction. (b) For the case $\mathscr{H}[\mathbf{3},\mathbf{1},\mathbf{2}]$, the initial condition placement $x(0) < E$ keeps the population size within the region $\mathfrak{R}_3[x]$ as it progresses to extinction according to the $x_3(t)$ trajectory.

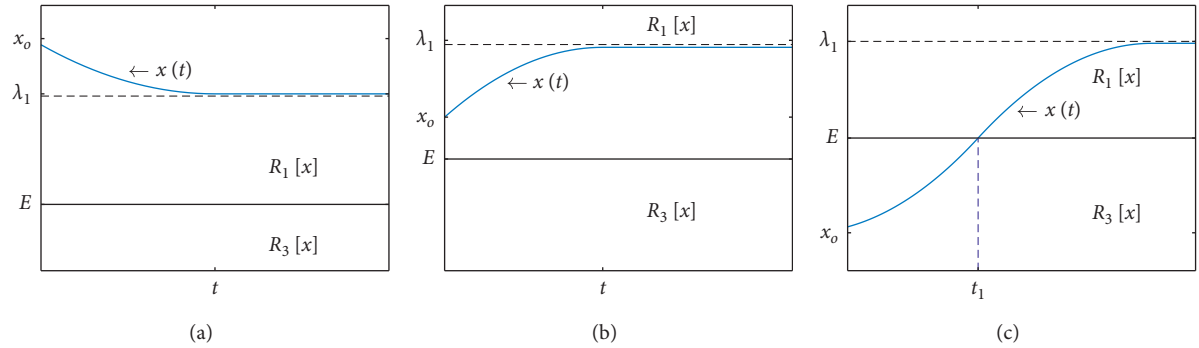

FIGURE 21: The global trajectory $x(t)$ for the $\mathscr{H}[3,2,\mathbf{k}]$ composite $(k = 1,2,3)$. (a) For $\mathscr{H}[\mathbf{3},\mathbf{2},\mathbf{1}]$, we have $x_o > E$, so $x(t)$ begins in region $\mathfrak{R}_3[x]$, according to the $x_1(t)$ rule, so if $E < \lambda_1 < x_0$, it asymptotically decreases approaching $\lambda_1 > E$. (b) Alternatively, the $E < x_0 < \lambda_1$ ordering sets population size increasing to λ_1. (c) For $\mathscr{H}[\mathbf{3},\mathbf{2},\mathbf{2}]$, conditions $x(0) < E$ and $\beta > \mu a$ place $x(t)$ inside region $\mathfrak{R}_3[x]$ increasing according to $x_3(t)$ until it hits the E boundary at a time t_1, and then it switches to the $x_1(t)$ rule progressing towards the equilibrium solution λ_1 in $\mathfrak{R}_1[x]$.

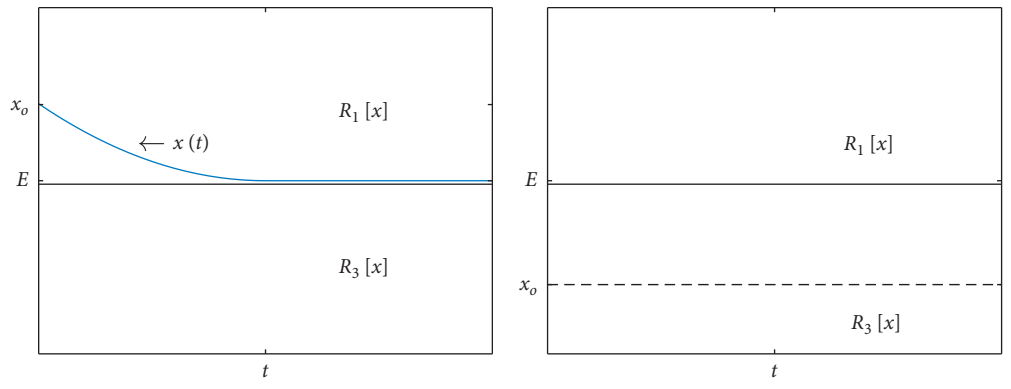

FIGURE 22: The comportment of the global trajectory $x(t)$ for the $\mathscr{H}[3,3,\mathbf{k}]$ composite $k = 1,2,3)$. (a) For $\mathscr{H}[\mathbf{3},\mathbf{3},\mathbf{1}]$ condition, $x_0 > E$ sets population size $x(t)$ to begin within the region $\mathfrak{R}_1[x]$ following $x_1(t)$. Since $\beta = ua$ and $E = a/b$ imply $\lambda_1 = E$, then $x(t)$ decreases to λ_1 (b) For $\mathscr{H}[\mathbf{3},\mathbf{3},\mathbf{2}]$, we have $x_o < E$, and population size starts within the region $\mathfrak{R}_3[x]$ and follows to growth law $x_3(t)$ but since $\beta = ua$, it remains stationary at x_o.

$$z_{n+1} = \begin{cases} \dfrac{s(1-r)E}{r} + z_n(1 - rz_n), & \mathfrak{R}_1[z_n] = \left[\left(z_n > \dfrac{sE}{r}\right) \wedge \left(z_n > \dfrac{sa}{rb}\right)\right], \\ rz_n(1 - z_n), & \mathfrak{R}_2[z_n] = \left[\left(z_n < \dfrac{sE}{r}\right) \wedge \left(z_n > \dfrac{sa}{rb}\right)\right], \\ \left(r - \dfrac{sa}{b}\right)z_n, & \mathfrak{R}_3[z_n] = \left[\left(z_n < \dfrac{sE}{r}\right) \wedge \left(z_n < \dfrac{sa}{rb}\right)\right], \\ \dfrac{s(r-1)E}{r} + \left(1 - \dfrac{sa}{b}\right)z_n, & \mathfrak{R}_4[z_n] = \left[\left(z_n > \dfrac{sE}{r}\right) \wedge \left(z_n < \dfrac{sa}{rb}\right)\right]. \end{cases} \tag{29}$$

For the sake of conciseness, we avert a detailed study of the performance of the discrete-time form of the PLF-PPM to an upcoming second part of this work. In the meantime, the parametrization of equation (25) given by equation (29) bears insight since it suggests that given the condition on the parameter r that renders upset of chaos in the logistic map submodel $\theta_2(z_n)$, once the resulting orbit crosses the upper boundary of the region $\mathfrak{R}_2[z_n]$, dynamics will be set by the $\theta_1(z_n)$ submodel so the system will escape the chaotic regime and approach an equilibrium point in the region $\mathfrak{R}_1[z_n]$ or the $\theta_1(z_n)$ orbit could get back again to the chaotic regime determined by the logistic map $\theta_2(z_n)$. Alternatively, the $\theta_2(z_n)$ orbit could reach the lower boundary of the region $\mathfrak{R}_2[z_n]$ then switching to the $\theta_3(z_n)$ dynamics ruling in $\mathfrak{R}_3[z_n]$. Then depending in the paramter odering z_n could decrease steadily and eventually vanish, or else wander aound in region $R_3[z_n]$ before getting back to the chaotic regime.

5. Discussion

Regulation by extreme value is observed in a plentiful of biological processes covering varied scales. It manifests on cellular structures such as mitochondria, where the maxima or minima of a periodical chemical reaction rule the formation of observed patterns [16]. Also, in the ecological settings, variables such as physical stress due to high or low temperatures, salinity, soil water content, wind velocities, and long or short exposures to air express better through extreme values than standard measures of central tendency [17, 18]. The notion of biological control by extreme values dates back to Justus Von Liebig, who established the law of the minimum. It states that an organism's growth rate is regulated by the nutrient present in the minimum [5]. Generally, any factor that slows down potential growth in an ecosystem is described as a limiting factor. Acknowledgment of lower-upper tolerance limits for a process drove generalization of the law of the minimum into the law of the tolerance of Shelford [6].

Furthermore, the interaction of limiting factors can indirectly influence the effect of other factors not in themselves limiting. This paradigm, known as the principle of limiting factors, has proven to be very useful in studying whole or parts of ecosystems [13, 19]. The joint Liebig–Shelford paradigm adopted here bears that population growth control occurs by balancing birth and mortality processes, the first determined by factor inducing the minimum offspring and the second by forcing the maximum number of deaths among individuals. This notion sustains the formal piecewise setup expressed by equation (22) and refers to PLF-PPM. Such a paradigm could allow a piecewise account of population dynamics composing growth phases delimited by density dependence cooperation and competition [20–23], thresholds of starvation, and critical density or extinction [20, 24]. The present PLF-PPM conceives growth phases controlled by limiting factors acting over domains bounded by population size thresholds. The first version of a PLF-PPM addressed a predator-prey model where Liebig's law governs the natality process of the prey population [1]. Echavarría and Gomez [25] and Echavarría et al. [26] extended these ideas to formulate models in which the mortality rate is set by the maximum value of factors that depend on population size. Montiel-Arzate et al. [3] adopted the referred Liebig–Shelford principle of limiting factors to formulate a functionally diverse population growth model. The approach in [3] relied on a parametrization of the birth process that rendered qualitative exploration burdensome, explaining why it is missing. Besides, Montiel-Arzate et al. [3] did not include a specific parametrization of mortality due to Allee effects which we incorporate here represented by the term $ax(t)$ as described by equation (21). Present settings allowed exhaustive qualitative exploration of the PLF-PPM global trajectory $x(t)$ presented in the Appendix. Even considering only population size and an external resource as limiting factors, the present formulation ensures a set of 20 basic orderings, each one associated to a different distribution of phases, which conform to an outstanding array of varying operation modes for the PLF-PPM. Such a flexible structure endures a sound interpretative strength displayed in the fitting results of the addressed study cases. Particularly, present settings allow visualization of abatement of resources controlling the birth process.

Nevertheless, a direct fitting procedure that relies on estimates' initial values brought high sensibility associated with local minimum problems at the non-linear acquisition of final values. These inconveniences suggest revision aimed to adapt a maximization of reproducibility strength criterion and simulation techniques that could lessen the parameter estimation burden experienced. Another point concerns adaptation of a symbolic manipulation code aimed at

automatically exploring phase arrangement and their implications for stability. Yet another essential issue left untouched here concerns exploring the outlined discrete-time version of the PLF-PPM of equation (25) and its alternate form (29). In the meantime, the parametrization of equation (29) already suggests that even conditions on the parameter r rendering upset of chaos in the logistic map submodel $\theta_2(z_n)$ once the resulting orbit crosses the upper boundary of the region $\mathfrak{R}_2[z_n]$ dynamics will be set by the $\theta_1(z_n)$ submodel, so the system will escape chaos before the orbit gets back again to the chaotic regime determined by the logistic map $\theta_2(z_n)$. Given the present results, no doubt that the suggested adaptation of codes to enhance both qualitative exploration and parameter fitting procedures will strengthen the applicability of offered PLF-PPM. Meanwhile, its present form already provides an outstanding research tool through which critical ecological parameters can be identified and be meaningfully interpreted.

6. Conclusions

This paper elucidates a logical deductive approach to establishing a piecewise structured model to interpret the growth of a single species population. The offered PLF-PPM derives as a logical consequence of what we coined as a principle of limiting factors for population growth, a paradigm adapted by merging Liebig's law of the minimum and the tolerance law of Shelford. The formal approach explains by the extreme value characterization of the birth $N(x(t))$ and mortality $M(x(t))$ processes in equation (15). Conceived forms allow the selection of the factors that play the decisive role in controlling population growth at a given time. The flexibility from a piecewise structure imbues the PLF-PPM with a noticeable reproducibility strength. Considered study cases briefly elaborate on this. The PLF-PPM bears as well an outstanding interpretative advantage. Such a feature infuses our construct with the capability of identifying different growth phases. These associate with regions of the dominance of crucial factors determining population dynamics such as a starvation regime, population size viability, or regimes of high population density effects. We only contemplated one external factor, E, and population size itself to describe $N(x(t))$ and $M(x(t))$. Concomitantly, the number of possible phase configurations was over ten times the number of parameters involved, which is the reason why ensuing parametrization proved to be seemingly adequate given addressed datasets. Nevertheless, as the number of explaining factors increases, more parameters are required. Then, the tied analytical exploration becomes complicated. Then particularly, acquiring suitable complexity could lead to local minimum difficulties connected to non-linear estimation. In this order of ideas, a quest for efficient parameter estimation methods that enhance the practical advantages derived from the PLF-PPM seems necessary. Such an endeavor concerns the research aims to pursue in a further paper. Another relevant research subject is pending, which is exhaustively exploring the discrete-time PLF-PPM construct outlined by equation (25).

Appendix

To study the diverse configurations of the phase portrait associated with the model of equation (22), we depart from the fundamental order relationship for the external energy E and the ratio of mortality from population density proportions, a/b, that yields a first model type classification (M_i, $i = 1, 2$). We have to consider model type M_1 associated to the inequality $E > a/b$, where the range of $x(t)$ composes the regions: $\mathfrak{R}_1[x] = \{a/b < E < x\}$, $\mathfrak{R}_2[x] = \{a/b < x < E\}$, and $\mathfrak{R}_3[x] = \{x < a/b < E\}$. For model type M_2, where the relationship $E < a/b$ holds, the range of $x(t)$ will be divided into the regions $\mathfrak{R}_1[x]$, $\mathfrak{R}_3[x]$, and $\mathfrak{R}_4[x] = \{a/b < x < E\}$. For model type M_3 linking to the ordering $E = a/b$, the range of $x(t)$ will be divided into the regions $\mathfrak{R}_1[x]$ and $\mathfrak{R}_3[x]$. Besides, it is also required to classify possible phase portrait arrangements according to the Birth to Mortality a–Scaled Ordering (BMS_i, $i = 1, 2, 3$), namely, BMS_1: when ($\beta < \mu a$), BMS_2: if ($\beta > \mu a$), and BMS_3: whenever ($\beta = \mu a$). Finally, the placement of the initial condition placement determines a third classification pointer ($\mathrm{IC}_{\mathrm{ik}(i)}$ with $i = 1, 2$ and $k(i) = 1, 2, \ldots, 5$), namely, IC_{11} for ($E < x_o$), IC_{12}: whenever ($a/b < x_o < E$), IC_{13}: whenever ($x_o < a/b$), IC_{14}: if ($x_o = E$), and IC_{15}: whenever ($x_o = a/b$). Correspondingly, IC_{21}: for ($x_o < E$), IC_{22}: whenever ($E < x_o < a/b$), IC_{23}: when ($x_o > a/b$),IC_{24}: if ($x_o = E$), and IC_{25}: whenever ($x_o = a/b$). The possible phase portrait arrangements typify according to a three-dimensional conjunction operator $\mathfrak{R}[i, j, k(i)] = (M_i \wedge \mathrm{BMS}_j \wedge \mathrm{IC}_{\mathrm{ik}(i)})$ for i and $k(i)$ as specified. Tables 1 and 2 summarizes phase arrangements and corresponding parameter orderings.

(A). Analysis of Trajectories for Orderings of the $\mathscr{H}[1, 1, \mathbf{k}]$ Type

We begin by analyzing case $\mathscr{H}[1, 1, 1]$ associated to conjunction ($M_1 \wedge \mathrm{BMS}_1 \wedge \mathrm{IC}_{11}$): model type M_1: ($E > a/b$)), Birth to Mortality Scaled Order (BMS_1): ($\beta < \mu a$), and initial condition ordering (IC_{11}): ($x_o > E$). Given this parametric arrangement, the range $X_R = \cup_{i=1,2,3} \mathfrak{R}_i[x]$ is associated. Then, since $x_o > E$, at the beginning of the growth process, population size departs from a value $x(0) > E$ and its dynamics are set by the path $x_1(t)$ prevailing in region $\mathfrak{R}_1[x]$.

$$x_1(t) = \frac{\lambda_1\left(C - e^{-2t\sqrt{\beta\mu b E}}\right)}{C + e^{-2t\sqrt{\beta\mu b E}}}, \quad \lim_{t \longrightarrow \infty} x_1(t) = \lambda_1, \tag{A.1}$$

where $\lambda_1 = \sqrt{\beta E/\mu b}$ and C can be determined from the condition $x(0) = x_o$.

Besides, in $\mathfrak{R}_1[x]$, the growth law, $\dot{x}(t) = \beta E - \mu b x^2(t)$, applies; therefore, $\dot{x}(t) < 0$ whenever $x(t) > \sqrt{\beta E/\mu b}$ and the trajectory $x(t)$ will monotonically decrease towards $\sqrt{\beta E/\mu b}$. Since we also have $\beta < \mu a$, then $\beta/\mu b < a/b < E$ which implies $\beta E/\mu b < E^2$, and thus the equilibrium placement $\sqrt{\beta E/\mu b} < E < x_0$ holds. Then, departing from x_0, the trajectory asymptotically decreases towards $\sqrt{\beta E/\mu b} < E$. But, by continuity, while $x_1(t)$ approaches $\sqrt{\beta E/\mu b} < E$, it will first hit the E value at a particular time t_1, that is, $x_1(t_1) = E$

(see Figure 9(a))). Then, it keeps forward entering into the region $\mathfrak{R}_2[x]$ with dynamics switching to $x_2(t)$, namely,

$$x_2(t) = \frac{\beta}{Ce^{-\beta t} + \mu b}, \text{with}, \quad \lim_{t\longrightarrow\infty} x(t) = \frac{\beta}{\mu b}, \tag{A.2}$$

where C can be determined from the condition $x(t_1) = E$.

Since $\dot{x}(t)$ is continuous, it turns out that $x(t)$ will keep decreasing. But, since $\beta < \mu a$, we have $\beta/\mu b < a/b < E$; besides, in region $\mathfrak{R}_2[x]$, we have $\dot{x}(t) = (\beta - \mu b x)x$; then, $\dot{x}(t) < 0$ for $x > \beta/\mu b$. Therefore, population size will decrease asymptotically approaching the value $\beta/\mu b$. But under the inequality $\beta/\mu b < a/b$ and given the continuity of x(t), there is a real number t_2 such that $x(t_2) = a/b$ (see Figure 9(b)). Next, $x(t)$ switches to the growth form $x_3(t)$ holding in region $\mathfrak{R}_3[x]$, namely,

$$x_3(t) = x_o e^{(\beta-\mu a)t}, \text{with}, \quad \lim_{t\longrightarrow\infty} x(t) = 0, \tag{A.3}$$

and since $\beta < \mu a$, the population size decreases until it eventually becomes extinct. So, for the phase portrait arrangement $\mathscr{H}[\mathbf{1},\mathbf{1},\mathbf{1}]$, population size displays the global path shown in Figure 9(c).

We now undertake case $\mathscr{H}[\mathbf{1},\mathbf{1},\mathbf{2}]$: $(M_1 \wedge \text{BSM}_1 \wedge \text{IC}_{12})$: model type M_1: $(E > a/b)$, Birth to Mortality Scaled Order 1 (BMS_1): $(\beta < \mu a)$, and initial condition ordering (IC_{12}): $(a/b < x_o < E)$. Based on the previous analysis, we obtain that whenever $a/b < x_o < E$, population size $x(t)$ places initially within the region $\mathfrak{R}_2[x]$ according to the $x_2(t)$ law approaching the asymptotic limit $\beta/\mu b$. Since for the case $\mathscr{H}[\mathbf{1},\mathbf{1},\mathbf{2}]$, the inequality $\beta/\mu b < a/b$ holds, population size decreases, so it eventually reaches the a/b threshold at a time t_1 (see Figure 10(a)). After that, it enters the region $\mathfrak{R}_3[x]$ and again since $\beta < \mu a$, it will keep decreasing now according to the $x_3(t)$ law, thereby becoming extinct (see Figure 10(a)).

We now explain the performance of $x(t)$ in the case $\mathscr{H}[\mathbf{1},\mathbf{1},\mathbf{3}]$: $(M_1 \wedge \text{BMS}_1 \wedge \text{IC}_{13})$: model type M_1: $(E > a/b)$ and Birth to Mortality Scaled Order 1 (BMS_1): $(\beta < \mu a)$ and initial condition ordering (IC_{13}): $(x_o < a/b < E)$. For this arrangement, population size initially is placed within the region $\mathfrak{R}_3[x]$ and then evolves according to growth law $x_3(t)$, but since we have $\beta < \mu a$, it keeps decreasing until it eventually vanishes (see Figure 10(b)).

(B). Analysis of Trajectories for Orderings of the $\mathscr{H}[\mathbf{2},\mathbf{1},\mathbf{k}]$ Type

Let us now analyze the global trajectory $x(t)$ for an $\mathscr{H}[\mathbf{2},\mathbf{1},\mathbf{1}]$ arrangement. We have that the initial condition placement $x_o > a/b > E$ applies. At the beginning of the growth process, population size $x(t)$ will take on a $x_1(t)$ form as given by equation (A.1) which decreases for $t \geq 0$ and asymptotically approaches a value $\sqrt{\beta E/\mu b}$. Now, for $\mathscr{H}[\mathbf{2},\mathbf{1},\mathbf{1}]$, the statement $\beta < \mu a$ is true. Then, $\mu a/\beta > 1$ implying $\mu a^2/\beta b > a/b$ and since parameters satisfy the condition defining model type M_2, we have $\mu a^2/\beta b > a/b > E$ and consequently $a^2/b > \beta E/\mu$, namely, $(a/b)^2 > \beta E/\mu b$.Taking also into account that $\beta E/\mu b > 0$, it follows that $a/b > \sqrt{\beta E/\mu b}$. Then, due to the continuity of $x(t)$ while approaching $\sqrt{\beta E/\mu b}$, there must be a real number t_1 such that $x(t_1) = a/b$ (see Figure 11(a)). Then, for $t \geq t_1$, dynamics will take place in the region $\mathfrak{R}_4[x]$, where population size behaves according to the $x_4(t)$ rule, namely,

$$x_4(t) = x_o e^{-\mu a t} + \frac{\beta E}{\mu a}\left(1 - e^{-\mu a t}\right), \text{ with } \quad \lim_{t\longrightarrow\infty} x(t) = \lambda_4, \tag{A.4}$$

where $\lambda_4 = \beta E/\mu a$. Since the condition $\beta < \mu a$ implies $\beta/\mu a < 1$, then $\lambda_4 < E$.

Inside $\mathfrak{R}_4[x]$, the dynamical system shapes $\dot{x} = \beta E - \mu a x$, and then $\dot{x}(t) < 0$ for $x(t) > \beta E/\mu a$ and population size will decrease while asymptotically approaching the equilibrium solution $\beta E/\mu a$ placing below E, but on its way to reach $\beta E/\mu a$, by continuity, the $x(t)$ trajectory will necessarily cross the E threshold at a specific time t_2. Once entering the region $\mathfrak{R}_3[x]$, population size will be controlled by $x_3(t)$ but since $\beta < \mu a$, the population eventually vanishes (see Figure 11(a)).

Considering the analysis above, the construction of the $x(t)$ path in the case $\mathscr{H}[\mathbf{2},\mathbf{1},\mathbf{2}]$ follows through. The initial condition placement $E < x_o < a/b$ implies population entering the region $\mathfrak{R}_3[x]$ and again population becomes extinct (see Figure 11(b)). The $\mathscr{H}[\mathbf{2},\mathbf{1},\mathbf{3}]$ case encompasses the statement $(M_2 \wedge \text{BMS}_1 \wedge \text{IC}_{23}) \equiv 1$, so we have that the initial condition satisfies $x_o < E < a/b$. Therefore, population size starts within the region $\mathfrak{R}_3[x]$ and behaves according to rule $x_3(t)$, but again, since $\beta < \mu a$, the trend will be decreasing, and eventually, the population will become extinct (see Figure 11(c)). In summary, the $\mathscr{H}[\mathbf{i},1,\mathbf{k}]$ arrangements for $i = 1,2$ and $k = 1,2,\ldots,5$ imply the population's extinction.

(C). Analysis of Trajectories for Orderings of the $\mathscr{H}[1,2,\mathbf{k}]$ Type

We address the case $\mathscr{H}[\mathbf{1},\mathbf{2},\mathbf{1}]$: $(M_1 \wedge \text{BMS}_2 \wedge \text{IC}_{21})$: model type M_1: $(E > a/b)$, Birth to Mortality Scaled Order (BMS_2): $(\beta > \mu a)$, and initial condition ordering (IC_{11}): $(x_o > E)$. Two additional orderings determine the phase arrangement. They are associated to the placement relative to E of the equilibrium solution $\lambda_2 = \beta/\mu b$ associated to the dynamical system prevailing in the region $\mathfrak{R}_2[x]$. We have to take into account the additional $(\beta/\mu b < E))$ and $(\lambda_2 > E))$ orderings.

Assume $((\lambda_2 < E) \wedge \mathscr{H}[\mathbf{1},\mathbf{2},\mathbf{1}]) \equiv 1$. Since $x_o > E$, at the beginning of the process, population size will be set by $x_1(t)$ (see equation A.1), the law that prevails in $\mathfrak{R}_1[x]$, where $\lambda_1 = \sqrt{\beta E/\mu b}$ and C can be determined from the condition $x(0) = x_o$. Besides, in $\mathfrak{R}_1[x]$, the dynamical system takes on the form, $\dot{x}(t) = \beta E - \mu b x^2$, that is associated to the equilibrium solution $\lambda_1 = \sqrt{\beta E/\mu b} = \sqrt{\lambda_2 E}$, and as we explained $\dot{x}(t) < 0$ for $x(t) > \lambda_1$. Besides, the $\beta > \mu a$ ordering implies $\lambda_2 > a/b$ or equivalently $\lambda_2 E > aE/b > a^2/b^2$; then, $\lambda_1 > a/b$. Since the additional ordering condition $\lambda_2 < E$ applies, we would have $\lambda_2 E < E^2$ which implies $E > \lambda_1 > a/b$. Then, in its approach to λ_1, the $x_1(t)$ trajectory will hit the E threshold, i.e., there exists a real number t_1 such that $x_1(t_1) = E$, and then for $t > t_1$, population size $x(t)$ turns to be controlled by

$x_2(t)$ (see equation (A.2)). Therefore, the trajectory approaches asymptotically the equilibrium solution λ_2. But since we established $\lambda_2 > a/b$, then $x_2(t)$ remains in region $\Re_2[x]$ (see Figure 12(a)).

If $((\lambda_2 > E) \wedge \mathscr{H}[\mathbf{1},\mathbf{2},\mathbf{1}]) \equiv 1$, then $\beta E/\mu b > E^2$ holds, implying $\lambda_1 > E$; then, the condition $E < x_o < \lambda_1$ will set the $x(t)$ trajectory to increase according to the $x_1(t)$ rule, and it will approach the asymptotic limit λ_1 while staying within the region $\Re_1[x]$ (see Figure 12(b)). On the other hand, whenever we have $E < \lambda_1 < x_o$, the population size $x(t)$ will decrease asymptotically towards λ_1 (see Figure 12(c)). Therefore, this establishes λ_1 as a stable equilibrium in the region $\Re_1[x]$.

We now consider case $\mathscr{H}[\mathbf{1},\mathbf{2},\mathbf{2}]$: $(M_1 \wedge \mathrm{BMS}_2 \wedge \mathrm{IC}_{12})$: model type M_1: $(E > a/b)$), Birth to Mortality Scaled order (BMS_2): $(\beta > \mu a)$, and initial condition placing (IC_{12}): $(a/b < x_o < E)$). Assume $((\lambda_2 > E) \wedge \mathscr{H}[\mathbf{1},\mathbf{2},\mathbf{2}]) \equiv 1$. Under this conjunction, the $\beta > \mu a$ ordering implies $\lambda_2 > a/b$, so we have $a/b < x_o < E < \lambda_2$. On the other hand, $\lambda_2 E > aE/b$, and since $E > a/b$ implies $aE/b > a^2/b^2$, then we have $\lambda_2 E > a^2/b^2$ or equivalently $\lambda_1 > a/b$. Now since $\lambda_2 > E$ applies, we would have $\lambda_2 E > E^2$ which implies $a/b < E < \lambda_1$. Therefore, at the beginning of the growth process, population size places inside $\Re_2[x]$ and for $t > 0$, it behaves according to the law $x_2(t)$(see equation (A.2)).

For $x(t) < \lambda_2$, $\dot{x}(t) > 0$, so population size will grow logistically in region $\Re_2[x]$ approaching the limit λ_2 that places in the region $\Re_1[x]$; therefore, for a specific value t_1, the statement $x(t_1) = E$ fulfills, and from that moment the population will grow logistically, according to growth law $x_1(t)$ approaching asymptotically to the λ_1 equilibrium (see Figure 13(a)).

Assume now that $((\lambda_2 > E) \wedge \mathscr{H}[\mathbf{1},\mathbf{2},\mathbf{2}]) \equiv 1$. Since $\beta > \mu a$, the ordering $\lambda_2 > a/b$ maintains; then, since $\lambda_2 < E$, we could have $a/b < x_o < \lambda_2 < E$ or $a/b < \lambda_2 < x_o < E$. If the ordering $a/b < x_o < \lambda_2 < E$ is true, the population size $x(t)$ will behave according to the $x_2(t)$ law, and then it will decrease from x_o and approach the asymptotic limit λ_2. For $a/b < \lambda_2 < x_o < E$, the population size $x(t)$ is still clinching to the $x_2(t)$ law and then will increase from x_o and approach λ_2. Then, λ_2 shows a stable equilibrium (see Figure 13(b)).

We now consider case $\mathscr{H}[\mathbf{1},\mathbf{2},\mathbf{3}]$: $(M_1 \wedge \mathrm{BMS}_2 \wedge \mathrm{IC}_{13})$: model type M_1: $(E > a/b)$) and Birth to Mortality Scaled order (BMS_2):$(\beta > \mu a)$ and initial condition placing (IC_{12}): $(x_o < a/b < E)$. Assume also that $((\lambda_2 > E) \wedge \mathscr{H}[\mathbf{1},\mathbf{2},\mathbf{3}]) \equiv 1$. Then, as we have explained the order relationship $x_o < a/b < E < \lambda_2$, the population size $x(t)$ places initially within the region $\Re_3[x]$ and grows according to the $x_3(t)$ trajectory (see equation (A.3)), which is the reason why the population will initiate an increasing exponential growth. When crossing by the value $x(t) = a/b$, the population will stop growing exponentially and will be governed by $x_2(t)$, the logistic law in $\Re_2[x]$, and will asymptotically approach the equilibrium solution λ_2. But since $E < \lambda_2$, eventually, population size will reach the level E so dynamics will turn to be set by the $x_1(t)$ growing pattern, and it consequently will asymptotically approach the λ_1 threshold placed in the $\Re_1[x]$ region (see Figure 14(a)).

Similarly, the analysis of the conjunction $((\lambda_2 < E) \wedge \mathscr{H}[\mathbf{1},\mathbf{2},\mathbf{3}])$ is true. As the inequality $x_0 < a/b < \lambda_2 < E$ holds, once the population size reaches the a/b boundary, it switches from the rule $x_3(t)$ to $x_2(t)$ and remains in region $\Re_2[x]$ approaching the asymptotic limit λ_2 (see Figure 14(b)).

(D). Analysis of Trajectories for Orderings of the $\mathscr{H}[2,2,\mathbf{k}]$ Type

We now consider the arrangement $\mathscr{H}[\mathbf{2},\mathbf{2},\mathbf{1}]$: $(M_2 \wedge \mathrm{BMS}_2 \wedge \mathrm{IC}_{21})$: model type $(M_2$: $E < a/b)$, Birth to Mortality Scaled order (BMS_2): $(\beta > \mu a)$, and initial condition placing (IC_{21}): $(x_o > a/b)$. The range of $x(t)$ will compose the regions $\Re_3[x]$, $\Re_4[x]$, and $\Re_1[x]$. Then, $\beta > \mu a$ which leads to $\beta E/\mu b > bE/a$ but $E^2 < aE/b$implying $\lambda_1 > E$. Then, since $x_o > a/b$, population size $x(t)$ begins within the region $\Re_1[x]$. If $E < a/b < \lambda_1 < x_0$, population size decreases as it approaches λ_1 (see Figure 15(a)). On the other hand, if $E < a/b < x_0 < \lambda_1$, population size increases approaching λ_1 asymptotically (see Figure 15(b)).

Now, since $\lambda_1 > E$, this equilibrium solution could place such that $E < \lambda_1 < a/b < x_0$. Again population size initiates dynamics within the region $\Re_1[x]$ and models according to the $x_1(t)$rule. Therefore, population size $x(t)$ decreases towards λ_1, but since the whole trajectory $x(t)$ is continuous, there exists a real number t_1 such that $(t_1) = a/b$, so for $t > t_1$, the population now places within the region $\Re_4[x]$ and behaves according to rule $x_4(t)$ (see equation (A.4)), where $\lambda_4 = \beta E/\mu a$. Moreover, $x_4(t)$ decreases whenever it attains values above λ_4 and increases if it places below λ_4. We have $\beta/\mu a > 1$, and then $\lambda_4 > E$. Therefore, $E < \lambda_4 < a/b < x_o$ holds, and then $x(t)$ decreases as it approaches asymptotically λ_4 (see Figure 15(c)).

Assume that the $\mathscr{H}[\mathbf{2},\mathbf{2},\mathbf{2}]$ arrangement holds. Then, we have $E < a/b$, so the range of $x(t)$ composes regions $\Re_3[x]$,$\Re_4[x]$, and $\Re_1[x]$. Since $E < x_o < a/b$, population size $x(t)$ initially places within the region $\Re_4[x]$ following the $x_4(t)$ law. But $\beta > \mu a$ implies $\beta E/\mu a > E$; therefore, $\lambda_4 > E$. We have two possible orderings for the placement of λ_4 relative to a/b, namely, $O_1(\lambda_4, a/b)$: $(E < \lambda_4 < a/b)$ and $O_2(\lambda_4, a/b)$: $(E < a/b < \lambda_4)$. Additionally, conditioned on $O_1(\lambda_4, a/b) \equiv 1$, we have to take into account the location of x_o comparative to λ_4. That is, $O_{11}(\lambda_4, x_o)$: $(E < x_o < \lambda_4 < a/b))$ or $O_{12}(\lambda_4, x_o)$: $(E < \lambda_4 < x_o < a/b))$. Assume $(O_{11}(\lambda_4, x_o) \wedge \mathscr{H}[\mathbf{2},\mathbf{2},\mathbf{2}]) \equiv 1$. Thus, $x(t)$ increases and approaches λ_4 staying within $\Re_4[x]$ (see Figure 16(a)). Undertake now $(O_{12}(\lambda_4, x_o) \wedge \mathscr{H}[\mathbf{2},\mathbf{2},\mathbf{2}]) \equiv 1$; accordingly, $x(t)$ starts above λ_4, so for $t > 0$, population size will decrease while approaching asymptotically this value, again staying within $\Re_4[x]$ (see Figure 16(b)).

Whenever $((\lambda_4, < a/b) \wedge \mathscr{H}[\mathbf{2},\mathbf{2},\mathbf{2}]) \equiv 1$, the λ_4 equilibrium lies within the region $\Re_1[x]$. Then, since $E < x_o < a/b$, population size increases according to rule $x_4(t)$ approaching λ_4. Continuity of $x(t)$ implies the existence of a real number $t_1 > 0$ such that $x_4(t_1) = a/b$, so for $t > t_1$, population size models by rule $x_1(t)$. Now, we have $f_4(x) = \beta E - \mu a x(t)$; then, $f_1(a/b) = \beta E - \mu b(a/b)^2$. Additionally, by continuity of $f(x)$, it follows that

$f_1(a/b) = f_4(a/b)$ and since we assumed $a/b < \lambda_4$, necessarily $f_4(a/b) > 0$. Therefore, $f_1(a/b) > 0$, that is, we also have $\beta E - \mu b(a/b)^2 > 0$ which in turn sets $\beta E > \mu b(a/b)^2$ or equivalently $\sqrt{\beta E/\mu b} > a/b$, that is, $\lambda_1 > a/b$. Therefore, population size increases asymptotically towards λ_1 staying within region $\Re_1[x]$ for $t > t_1$ (see Figure 16(c)).

Whenever we have the $\mathscr{H}[\mathbf{2},\mathbf{2},\mathbf{3}]$ composite statement, the initial condition $x_o < E$ places population size $x(t)$ within the region $\Re_3[x]$ obeying the exponential growth law $x_3(t)$, and since $\beta > \mu a$, it will increase for $t > 0$. This way, continuity of $x_3(t)$ implies the existence of a time t_1 such that $x_3(t_1) = E$. Then, for $t > t_1$, the behavior of $x(t)$ sets through $x_4(t)$. Again the statement $\beta > \mu a$ implies $\lambda_4 > E$, so we could have $((E < \lambda_4 < a/b)$ or $(E < a/b < \lambda_4)$ orderings. Assume $((E < \lambda_4 < a/b) \wedge \mathscr{H}[\mathbf{2},\mathbf{2},\mathbf{2}]) \equiv 1$. Then, $x(t)$ initiates in $\Re_3[x]$ and increases as it approaches λ_4 staying within $\Re_4[x]$. (see Figure 17(a)). Undertake now $((E < a/b < \lambda_4) \wedge \mathscr{H}[\mathbf{2},\mathbf{2},\mathbf{2}]) \equiv 1$. Then, the λ_4 equilibrium places within the region $\Re_1[x]$ so by continuity, population size reaches the a/b boundary switching to rule $x_1(t)$ and satisfying $f_1(a/b) > 0$ which implies $\lambda_1 > a/b$. Therefore, $x(t)$ approaches λ_1 asymptotically (see Figure 17(b)).

(E). Analysis of Trajectories for Orderings of the $\mathscr{H}[1,3,\mathbf{k}]$ Type

We begin by analyzing case $\mathscr{H}[\mathbf{1},\mathbf{3},\mathbf{1}]$ associated to conjunction $(M_1 \wedge \mathrm{BMS}_1 \wedge \mathrm{IC}_{11})$: model type M_1: $(E > a/b)$ and Birth to Mortality Scaled Order (BMS_3): $(\beta = \mu a)$ and initial condition ordering (IC_{11}): $(x_o > E)$. Given this parametric arrangement, at the beginning of the growth process, population size departs from a value $x(0) > E$, and its dynamics are set by the path $x_1(t)$ (see equation (A.1)) prevailing in region $\Re_1[x]$, with $\lambda_1 = \sqrt{\beta E/\mu b}$. Since $\beta = \mu a$, we have $\lambda_1 = \sqrt{aE/b}$, but we also have $E > a/b$; then, $E^2 > aE/b$, and therefore we obtain $\lambda_1 < E$. On the other hand, if $E > a/b$, we also have $aE/b > (a/b)^2$ and consequently $\lambda_1 > a/b$. Therefore, $a/b < \lambda_1 < E < x_0$, and population size $x(t)$ decreases approaching λ_1. But since λ_1 lies in region $\Re_2[x]$, eventually population size will cross the E threshold at a particular time t_1 and will switch to growing rule $x_2(t)$. This law is associated with the equilibrium solution $\lambda_2 = a/b$, so population asymptotically approaches this value (see Figure 18(a)).

For the arrangement $\mathscr{H}[\mathbf{1},\mathbf{3},\mathbf{2}]$, we have the initial condition placement $a/b < x_o < E$. Then, population size begins within the region $\Re_2[x]$ and behaves according to the $x_2(t)$ law. Therefore, population size approaches the equilibrium solution $\lambda_2 = \beta/\mu b$, but since $\beta = \mu a$, we have $\lambda_2 = a/b$. Then, population size approaches asymptotically the a/b boundary (see Figure 18(b)). In turn, the $\mathscr{H}[\mathbf{1},\mathbf{3},\mathbf{3}]$ composite encompasses the initial condition placement $x_o < E$; therefore, population size obeys the $x_3(t)$ rule, and since $\beta = \mu a$, it remains stationary at the x_o value (see Figure 18(c)).

(F). Analysis of Trajectories for Orderings of the $\mathscr{H}[2,3,\mathbf{k}]$ Type

We now consider the arrangement $\mathscr{H}[\mathbf{2},\mathbf{3},\mathbf{1}]$: $(M_2 \wedge \mathrm{BMS}_3 \wedge \mathrm{IC}_{21})$: model type M_2: $(E < a/b)$, Birth to Mortality Scaled order (BMS_3): $(\beta = \mu a)$, and initial condition placing (IC_{21}): $x_o > a/b)$. The range of $x(t)$ will compose the regions $\Re_3[x]$, $\Re_4[x]$, and $\Re_1[x]$ Then, since $x_o > a/b$, population size $x(t)$ begins within the region $\Re_1[x]$ and hangs onto the $x_1(t)$ trajectory. Now, the $E < a/b$implies $aE/b < a^2/b^2$ and since $\beta = \mu a$, we have $\lambda_1 = \sqrt{aE/b}$; therefore, $\lambda_1 < a/b$. Consequently, λ_1 places in region $\Re_4[x]$, and the $x_1(t)$ trajectory decreases, so on its approach to λ_1, it will intersect the a/b boundary at a time t_1. Subsequently, $x(t)$ switches to the rule $x_4(t)$ valid in $\Re_4[x]$. Now, the $\beta = \mu a$ setting implies $\lambda_4 = E$, so since by continuity, we have $x_4(t_1) = a/b$, and population size decreases and approaches the equilibrium solution λ_4 matching the E threshold (see Figure 19(a)). The case $\mathscr{H}[\mathbf{2},\mathbf{3},\mathbf{2}]$ is associated to the conjunction $(M_2 \wedge \mathrm{BMS}_3 \wedge \mathrm{IC}_{22})$, so initial value x_o fulfils $E < x_0 < a/b$, and then population size starts within the region $\Re_4[x]$ and holds to growth law $x_4(t)$ approaching the $\lambda_4 = \beta E/\mu a$ equilibrium which under the condition $\beta = \mu a$ satisfies $\lambda_4 = E$. Therefore, $x(t)$ decreases asymptotically to E (see Figure 19(b)). Finally, for $\mathscr{H}[\mathbf{2},\mathbf{3},\mathbf{3}]$, the condition $x_0 < E$ sets population size beginning within the region $\Re_3[x]$ following the $x_3(t)$ growth law. Again, the condition $\beta = \mu a$ sets $x_3(t)$ to remain stationary at x_0 (see Figure 19(c)).

(G). Analysis of Trajectories for Orderings of the $\mathscr{H}[3,1,\mathbf{k}]$ Type

We begin by analyzing case $\mathscr{H}[\mathbf{3},\mathbf{1},\mathbf{1}]$ associated to conjunction $(M_3 \wedge \mathrm{BMS}_1 \wedge \mathrm{IC}_{31})$: model type M_3: $(E = a/b)$ and Birth to Mortality Scaled Order (BMS_1): $(\beta < \mu a)$ and initial condition ordering IC_{31}: $(x_o > E)$. Given this parametric ordering, population size confines only to regions $\Re_1[x]$ and $\Re_3[x]$. At the beginning of the growth process, population size departs from a value $x(0) > E$ and its dynamics are set by the path $x_1(t)$ prevalent in region $\Re_1[x]$, so it asymptotically approaches the value $\lambda_1 = \sqrt{\beta E/\mu b}$. Again, the $\beta < \mu a$ ordering implies $\sqrt{\beta E/\mu b} < E$, and then population size decreases and eventually hits the E boundary following the $x_3(t)$ rule holding in the region $\Re_3[x]$ which since $\beta < \mu a$ drives the population to extinction (see Figure 20(a)). The analysis of the case $\mathscr{H}[\mathbf{3},\mathbf{1},\mathbf{2}]$ is straightforward since the initial condition placement $x(0) < E$ keeps the population size cling to region $\Re_3[x]$ where it progresses to extinction according to the $x_3(t)$ trajectory (see Figure 20(b)).

(H). Analysis of Trajectories for Orderings of the $\mathscr{H}[3,2,\mathbf{k}]$ Type

Whenever the $\mathscr{H}[3,2,1]$ ordering achieves, we have to consider the conjunction $(M_3 \wedge \mathrm{BMS}_2 \wedge \mathrm{IC}_{31})$: model type M_3: $(E = a/b)$, Birth to Mortality Scaled Order (BMS_1): $(\beta > \mu a)$, and initial condition ordering (IC_{31}): $(x_o > E)$. This way, population size $x(t)$ begins in region $\Re_1[x]$, and thus it obeys $x_1(t)$ rule, so it asymptotically approaches the value $\lambda_1 = \sqrt{\beta E/\mu b}$. Correspondingly, the $\beta > \mu a$ ordering implies $\lambda_1 > E$, and then population size decreases to $\lambda_1$whenever $E < \lambda_1 < x_o$ (see Figure 21(a)). On the other hand, whenever $E < x_0 < \lambda_1$, population size increases to λ_1 (see Figure 21(b)).

Similarly, for the case $\mathscr{H}[\mathbf{3},\mathbf{2},\mathbf{2}]$, the range of $x(t)$ composes the regions $\mathfrak{R}_3[x]$and $\mathfrak{R}_1[x]$. The initial condition $x(0) < E$ places population size initially inside the region $\mathfrak{R}_3[x]$. The ordering $\beta > \mu a$ sets population size $x(t)$ to increase according to the $x_3(t)$ trajectory keeping inside the region $\mathfrak{R}_3[x]$ until it hits the E boundary at a time t_1. Later, it switches to the $x_3(t)$ rule progressing towards the equilibrium solution λ_1 (see Figure 21(c)).

(I). Analysis of Trajectories for Orderings of the $\mathscr{H}[3,3,\mathbf{k}]$ Type

The $\mathscr{H}[\mathbf{3},\mathbf{3},\mathbf{1}]$ ordering links to conjunction $(M_3 \wedge \mathrm{BMS}_2 \wedge \mathrm{IC}_{31})$: model type M_3: $(E = a/b)$ and Birth to Mortality Scaled Order (BMS_3): $(\beta = \mu a)$ and initial condition ordering (IC_{31}): $(x_o > E)$ The range of $x(t)$ will compose the regions $\mathfrak{R}_3[x]$and $\mathfrak{R}_1[x]$. Then, population size $x(t)$ begins within the region $\mathfrak{R}_1[x]$ and follows the $x_1(t)$ trajectory. Now, $\beta = \mu a$ and $E = a/b$ imply $\lambda_1 = E$. Consequently, if $E = a/b = \lambda_1 < x_0$, then $x(t)$ decreases as it approaches λ_1 (see Figure 22(a)).

The case $\mathscr{H}[\mathbf{3},\mathbf{3},\mathbf{2}]$ is associated to the conjunction $M_3 \wedge \mathrm{BMS}_3 \wedge \mathrm{IC}_{32}$ so initial population size x_o satisfies $x_o < E$. Then, population size starts within the region $\mathfrak{R}_3[x]$ and embraces to growth law $x_3(t)$ which under the condition $\beta = ua$ remains stationary at x_o. Therefore, $x(t)$ decreases asymptotically to E (see Figure 22(b)). Similarly, the $\mathscr{H}[\mathbf{3},\mathbf{3},\mathbf{3}]$ arrangement corresponds to the case $\mathscr{H}[\mathbf{3},\mathbf{3},\mathbf{2}]$.

Data Availability

Data sources are referenced in the text.

Conflicts of Interest

The authors declare that there are no conflicts of interest regarding the publication of this paper.

Acknowledgments

This research was supported solely on institutional funding (CICESE).

References

[1] I. A. Polyetayev, "Modeli volterra, jishnir-zhertva y nekotorye ij obobschenyas ispolzovainien printsipa liebija," *Zhurnal Obshchei Biologii*, vol. 34, no. 1, p. 43, 1971.

[2] H. A. Echavarría and A. G. Gómez, "Modelos tipo volterra y el principio ecológico de los factores limitantes," *Comunicaciones Internas, Facultad de Ciencias UNAM*, vol. 6, pp. 1–25, 1975.

[3] E. Montiel-Arzate, H. Echavarría-Heras, and C. Leal-Ramírez, "A functionally diverse population growth model," *Mathematical Biosciences*, vol. 187, no. 1, pp. 21–51, 2004.

[4] W. C. Allee, *Animal Aggregations*, The University of Chicago Press, Chicago, IL, USA, 1931.

[5] L. Von and L. R. Pomeroy, "Principles of agricultural chemistry with special reference to the late researches made in England," in *Cycles of Essential Elements (Benchmark papers in Ecology), vol. I*p. 11, Dowwden, Hutchison & Ross, Stroudsburg, PA, USA, 1974.

[6] V. E. Shelford, *Animal Communities in Temperate North America*, The University of Chicago Press, Chicago, IL, USA, 1913.

[7] J. T. Armstrong, "The population dynamics of the planarian, Dugesia Tigrina," *Ecology*, vol. 45, no. 2, pp. 361–365, 1964.

[8] J. Huisman, "Population dynamics of light-limited phytoplankton: microcosm experiments," *Ecology*, vol. 80, no. 1, pp. 202–210, 1999.

[9] J. Davidson, "On the growth of the sheep population in Tasmania," *Transactions of the Royal Society of South Australia*, vol. 62, pp. 342–346, 1938.

[10] R. Pearl, "The growth of populations," *The Quarterly Review of Biology*, vol. 2, no. 4, pp. 532–548, 1927.

[11] T. P. Hughes and J. E. Tanner, "Recruitment failure, life histories, and long-term decline of caribbean corals," *Ecology*, vol. 81, no. 8, pp. 2250–2263, 2000.

[12] L. I.-K. Lin, "A concordance correlation coefficient to evaluate reproducibility," *Biometrics*, vol. 45, no. 1, pp. 255–268, 1989.

[13] E. P. Odum, *Fundamentals of Ecology*, W.B. Saunders Co, Philadelphia, PA, USA, 3rd edition, 1971.

[14] C. J. Krebs, *Ecology: The Experimental Analysis of Distribution and Abundance*, Addison-Wesley, New York, NY, USA, 4th edition, 1994.

[15] J. H. Sang, "Population growth in Drosophila cultures," *Biological Reviews*, vol. 25, no. 2, pp. 188–219, 1950.

[16] A. E. R. Woodcock and M. Davis, *Catastrophe Theory*, E. P. Dutton, New York, USA, 1978.

[17] S. D. Gaines and M. W. Denny, "The largest, smallest, highest, lowest, longest, and shortest: extremes in ecology," *Ecology*, vol. 74, no. 6, pp. 1677–1692, 1993.

[18] M. W. Denny and S. O. Deines, "On the prediction of maximal intertidal wave forces," *Limnology & Oceanography*, vol. 35, no. 1, pp. 1–15, 1990.

[19] E. P. Odum, *Ecology*, Holt Rinehart & Winston, New York, NY, USA, 1963.

[20] H. T. Odum and W. C. Allee, "A note on the stable point of populations showing both intraspecific cooperation and disoperation," *Ecology*, vol. 35, no. 1, pp. 95–97, 1954.

[21] A. Nicholson, "An outline of the dynamics of animal populations," *Australian Journal of Zoology*, vol. 2, no. 1, pp. 9–65, 1954.

[22] W. M. Getz, "Population dynamics: a per capita resource approach," *Journal of Theoretical Biology*, vol. 108, no. 4, pp. 623–643, 1984.

[23] W. M. Getz, "A hypothesis regarding the abruptness of density dependence and the growth rate of populations," *Ecology*, vol. 77, no. 7, pp. 2014–2026, 1996.

[24] B. Dennis, "Allee effects: population growth, critical density, and the chance of extinction," *Natural Resource Modeling*, vol. 3, no. 4, pp. 481–538, 1989.

[25] H. A. Echavarría and A. G. Gómez, "El principio de los factores limitantes y el crecimiento de poblaciones," *Comunicaciones Internas, Departamento de Matemáticas, UNAM*, vol. 13, pp. 1–36, 1979.

[26] H. A. Echavarría, E. Solana, and H. Madrid, "A functionally diverse model for predator prey systems Lamberson," in *Natural Resource Modeling and Management I, International Workshop for Natural Resource Modeling and Analysis*, H. Echavarría and R. H. Lamberson, Eds., p. 47, Department of Ecology CICESE, Ensenada, Mexico, 1994.

Hindawi
Complexity
Volume 2021, Article ID 4249106, 16 pages
https://doi.org/10.1155/2021/4249106

Research Article

Cooperation-Based Modeling of Sustainable Development: An Approach from Filippov's Systems

Jorge A. Amador,[1] **Johan Manuel Redondo**,[2] **Gerard Olivar-Tost**,[3] **and Christian Erazo**[4]

[1]*Instituto de Investigación de Recursos Biológicos Alexander von Humboldt, Bogota, DC, Colombia*
[2]*Facultad de Ciencias Económicas y Administrativas, Universidad Católica de Colombia, Bogota, DC, Colombia*
[3]*Departamento de Ciencias Naturales y Tecnología, Universidad de Aysén, Aysen, Chile*
[4]*Facultad de Ingeniería Mecánica, Electrónica y Biomédica, Universidad Antonio Nariño, Bogota, DC, Colombia*

Correspondence should be addressed to Gerard Olivar-Tost; gerard.olivar@uaysen.cl

Received 28 April 2021; Revised 4 August 2021; Accepted 9 August 2021; Published 27 September 2021

Academic Editor: Jorge-Antonio Lopez-Renteria

The concept of Sustainable Development has given rise to multiple interpretations. In this article, it is proposed that Sustainable Development should be interpreted as the capacity of territory, community, or landscape to conserve the notion of well-being that its population has agreed upon. To see the implications of this interpretation, a Brander and Taylor model, to evaluate the implications that extractivist policies have over an isolated community and cooperating communities, is proposed. For an isolated community and through a bifurcation analysis in which the Hopf bifurcation and the heteroclinic cycle bifurcation are detected, 4 prospective scenarios are found, but only one is sustainable under different extraction policies. In the case of cooperation, the exchange between communities is considered by coupling two models such as the one defined for the isolated community, with the condition that their transfers of renewable resources involve conservation policies. Since human decisions do not occur in a continuum, but rather through jumps, the mathematical model of cooperation used is a Filippov System, in which the dynamics could involve two switching manifolds of codimension one and one switching manifold of codimension two. The exchange in the cooperation model, for specific parameter arrangements, exhibits n-periodic orbits and chaos. It is notable that, in the cases in which the system shows sliding, it could be interpreted as a recovery delay related to the time needed by the deficit community to recover, until its dependence on the other community stops. It is concluded (1) that a sustainability analysis depends on the way well-being is defined because every definition of well-being is not necessarily sustainable, (2) that sustainability can be visualized as invariant sets in the nonzero region of the space of states (equilibrium points, n-periodic orbits, and strange attractors), and (3) that exchange is key to the prevalence of the human being in time. The results question us on whether Sustainable Development is only to keep us alive or if it also implies doing it with dignity.

1. Introduction

Sustainable Development is a concept that has become relevant [1] since due to the series of criticisms that had been made regarding the global model of economic growth, which put the survival of all living species on the planet at risk, including the human being. Reports such as "Limits to Growth" [2] warned about the capacity of the planet in the face of the dynamics proposed from the socioeconomic point of view to generate growth.

The global impact of the concept did not lead to a homogeneous school of thought on Sustainable Development, but to the establishment of families of conceptual positions that tried to adapt the concept to their interpretations, as in the case of corporate sustainability and environmental sustainability, which made the word sustainability a suffix or the Latin American case in which the language allowed the differentiation between "sostenible" and "sustentable," to eradicate the economic character that the concept was taking on political agendas or its interpretations that gave rise to

weak/strong sustainability [3], to sustainable landscapes [4] and to the widely recognized approach of Elkington [5], and the triple bottom line is sustainability from social, economic, and environmental dimensions.

The interpretation made in this article of the definition of Sustainable Development proposed by [1]: "satisfying present needs without compromising the satisfaction of the needs of future generations," assumes (1) that the system of needs is not a unique set, but is defined according to the territory, landscape, or community and the ways of life in them, (2) that the system of needs does not have important changes from one generation to another, (3) that satisfying needs has the purpose of generating well-being, and (4) that this well-being must exist for this generation and any future generation. In this sense, sustainability is an emerging expression of the territory, landscape, or community, which results from the interactions of its socio-ecological components, so its analysis must be carried out according to systemic and dynamic form [6]. In this article, then, it will be said that a territory, landscape, or community is sustainable if the notion of well-being that its population has agreed upon is a conservation law and symmetry of time, in the nonnegative region of the space of states.

This interpretation has different implications: (1) if the system of needs depends on the territory, landscape, or community and their ways of life, there cannot be a single sustainability, but there are sustainabilities, (2) if the system of needs can go from one generation to another without important changes, it is because the way in which it is defined has prioritized what is really important, whatever that means, (3) the set of all definitions that could be proposed for well-being would not necessarily lead to Sustainable Development because many of them will only be valid in the short term, and (4) restricting sustainability to the economic, social, and environmental dimensions is insufficient to capture the complexity of a definition of well-being that can be perpetuated over time as well as fallacious environmental, social, and economic sustainability considerations that ignore the interdependence that exists between these dimensions and others to make socio-ecological systems viable in the long term.

But the most important implication about well-being, as a conservation law, is that in Sustainable Development well-being cannot increase or decrease, unless there are exchanges of information, matter, and energy from one territory, landscape, or community to another, which is completely contrary to the case in which a territory is eroded to guarantee the well-being of another, without compensation for the resources taken being sufficient for its recovery.

Here we study the case in which two socio-ecological systems have exchanges, constituting a new socio-ecological system on which it is not clear how these exchanges will determine their sustainability. In this sense, the purpose of this article is to present the first approach to the study of exchanges between territories, landscapes, and communities within the framework of Sustainable Development from discontinuous piecewise smooth systems and explain the implications of this approach for two communities, based on the analysis of their dynamic behavior.

Due to it is the first approximation, the mathematical model has variables that define a very simple notion of well-being, based on populations and available renewable resources, with which it will seek to demonstrate the conservation of well-being.

The mathematical model used for this purpose is a Filippov system [7, 8]. The choice of this type of system resides in the fact that human decisions do not necessarily occur continuously, but rather through jumps defined by ranges of tolerance to events.

For an introduction to Filippov's systems, see [9–13]. An equivalent formulation in part is found in [14]. For a review of piecewise linear systems, it can be reviewed [15–18]. Regarding the limit cycles in Filippov's systems, it is recommended to review [19]. On the bifurcations of these systems, there are articles from [20–26], together with more specialized articles such as [27–29] for periodic orbits, [30, 31] for sliding bifurcations or the Hopf bifurcation compendium of [32]. Other topics that may be of interest are the numerical aspects of the solution of these differential systems [33, 34] or stochastic perturbations to periodic orbits with sliding [35, 36].

On the applications of Filippov systems, the works have been mainly oriented to friction oscillators [31, 37–41], neural networks activated by discontinuous functions [42–46], memristor-based neural networks [47–53], neural networks with switching control using the Filippov system with delay [54–57], and electronic converters [58]. On issues related to Sustainable Development, the number of papers is much more limited, with approaches from the analysis of communities [59], from the analysis of companies [60] and others that touch on close issues such as energy systems [61–64], pest or disease control [65–67], HIV behavior [68, 69], behavior longterm communities [70], or communications security [71]. It is also worth mentioning a novel approach to the study of systems using multiple switching regions that have been proposed in [72].

For the simulation, tools such as SLIDECONT [73] or smooth solvers [74] have been developed for the analysis of sliding bifurcation of Filippov systems. Numerical continuation methods of these systems have also been proposed [41]. More recently there is the TC-hat software from [75], COCO [76], and MAMBO [77].

The rest of the paper is structured as follows. After this introductory section, two sections are presented in which (1) the effect of the variation of the extraction capacities in an isolated community is modeled and simulated, using a two-dimensional continuous model, see Section 2, and (2) the effect of the exchange of resources between two communities, based on a Filippov system, see Section 3. In these models, seeking to have a first approximation of sustainability as conservation of the well-being of territory, landscape, or community, it is assumed that well-being is having renewable resources, which oversimplifies a plausible definition of well-being, but allows the presentation of the possibilities of this interpretation of sustainability, as will be seen in the discussion of results' sections, see Section 4, and of conclusions, see Section 5. The article ends with the proposal for future research in this line of work, see Section 6.

2. Effect of the Variation of the Extraction Capacities in a Community

The mathematical model on which this article is based is the one developed by Brander and Taylor [78], who presented a general equilibrium model to represent the dynamic interaction between renewable resources and population, seeking to explain the case of Easter Island.

The Brander and Taylor model has been modified by authors to achieve a better approximation to modern systems of extraction and use of renewable resources, obtaining differential systems of greater dimension and elaboration. For example, multiple economic activities have been incorporated, adding to the extraction of resources and the production of manufactured goods [79] or proposing agriculture as a parallel and different activity to extraction [80]. Institutional adjustments and some economic structures of property rights have also been included, which restrict the conditions of extraction and consumption that could mitigate or dampen the cycles of abundance and famine [81, 82] or the consideration of conservation policies that were based on resource extraction charges [83].

Most of the models based on differential equations emerged from the Brander and Taylor model as well as other models of the same type that study the dynamic relationship between population and resources and contemplated isolated societies, without considering migrations or exchanges of information, matter, or energy. However, one can find models with differential equations that somehow incorporate this coupling between societies. For example, in [84], a model is presented that tries to capture the effect that migration has on the degradation of natural resources; in [85], a model is used to investigate the emergent effects of the movement of people, goods, and natural resources, between two societies that have characteristics similar to those of Easter Island; a different coupling method is used in [86], where two new state variables are proposed: the capital inventory and a social development index, for the construction of a dynamic migration network between municipalities of a region in Colombia; finally, in [87], a socio-ecological model of multiple human populations is proposed, which exploit their natural resources or that of another population when their own are scarce, finding that the increase in interacting communities accelerates and aggravates the collapse.

This article, in contrast to [87], studies the long-term effect of economic cooperation between two communities, for which a simplified version of [80] of the Brander and Taylor model was used so that the extraction of resources is considered as the only economic activity developed.

The system of differential equations for the representation of the dynamics of an isolated community considers that the population change is given by the extraction speed that the population L has of its available renewable resources S, from a per-capita extraction rate ϵ [85] and the minimum per-capita caloric requirements σ of its population, in consideration of a conversion factor from mass units of the extracted resource to caloric units ϕ, while for the change in available renewable resources S, it is assumed that the renewable resource is regenerated if it is above the T limit (strong growth effect), at a rate of ρ up to that reaches its carrying capacity K (growth limit of the renewable resources) and that depends on the mentioned extraction that the population makes of the resources, as shown in the following equation:

$$\begin{aligned}\frac{\mathrm{d}L}{\mathrm{d}t} &= \phi\varepsilon LS - \sigma L,\\ \frac{\mathrm{d}S}{\mathrm{d}t} &= \rho S\left(\frac{S}{T} - 1\right)\left(1 - \frac{S}{K}\right) - \varepsilon LS.\end{aligned} \tag{1}$$

System (1) has 4 equilibrium points:

$$\begin{aligned}P_1 &= (0, 0),\\ P_2 &= (0, T),\\ P_3 &= (0, K),\\ P_4 &= \left(-\frac{\rho\left(KT\epsilon^2\phi^2 - K\epsilon\phi\sigma - T\epsilon\phi\sigma + \sigma^2\right)}{KT\phi^2\epsilon^3}, \frac{\sigma}{\epsilon\phi}\right).\end{aligned} \tag{2}$$

Following Figure 1, equilibrium P_1 is always a stable node, and P_2 is always an unstable saddle-type node, making the Allee effect considered for the resources in the model remarkable. The Allee effect occurs when the regeneration rate slows down at low resource density [88].

When ε gradually increases, P_3 and P_4 collide in what is called a branch point BP. In this collision, $K = \sigma/K\phi$ and $-\rho\,(KT\phi^2\epsilon^2 - K\phi\sigma\epsilon - T\phi\sigma\epsilon + \sigma^2)/\phi^2\epsilon^3 KT = 0$. When solving for ε, we found that BP occurs at $\varepsilon^{\mathrm{BP}} = \sigma/K\phi$, and if $\varepsilon < \varepsilon^{\mathrm{BP}}$ population is negative and P_4 is unstable while P_3 is stable, equilibrium population is positive and P_4 becomes a stable focus if $\varepsilon > \varepsilon^{\mathrm{BP}}$ until the Hopf bifurcation H is reached, see Figure 1. To prove the existence of a Hopf bifurcation, we define the Jacobian matrix as

$$J = \begin{bmatrix} \phi\varepsilon S - \sigma & \phi\varepsilon L \\ -\varepsilon S & -\dfrac{KT\varepsilon L - 2\rho KS + KT\rho + 3\rho S^2 - 2\rho TS}{KT} \end{bmatrix}, \tag{3}$$

whose eigenvalues are

$$\lambda_{1,2} = \frac{1}{2}\left(\mathrm{Tr}J \pm \sqrt{\mathrm{Tr}J^2 - 4\mathrm{Det}J}\right). \tag{4}$$

$\mathrm{Tr}J$ corresponds to the trace of J and $\mathrm{Det}J$ to its determinant. When solving for ϵ, the trace evaluated at P_4, we find that a Hopf bifurcation occurs at $\epsilon^H = 2\sigma/(K + T)\phi$ since P_4 has a pair of pure imaginary eigenvalues, satisfying the equilibrium condition, giving rise to the instability of the P_4 focus. Furthermore, the system undergoes the Hopf bifurcation as long as the real part of eigenvalues really change sign by crossing zero. The previous condition can be proved by demonstrating that the cross speed of the real part with respect to the control parameter is nonzero. Since

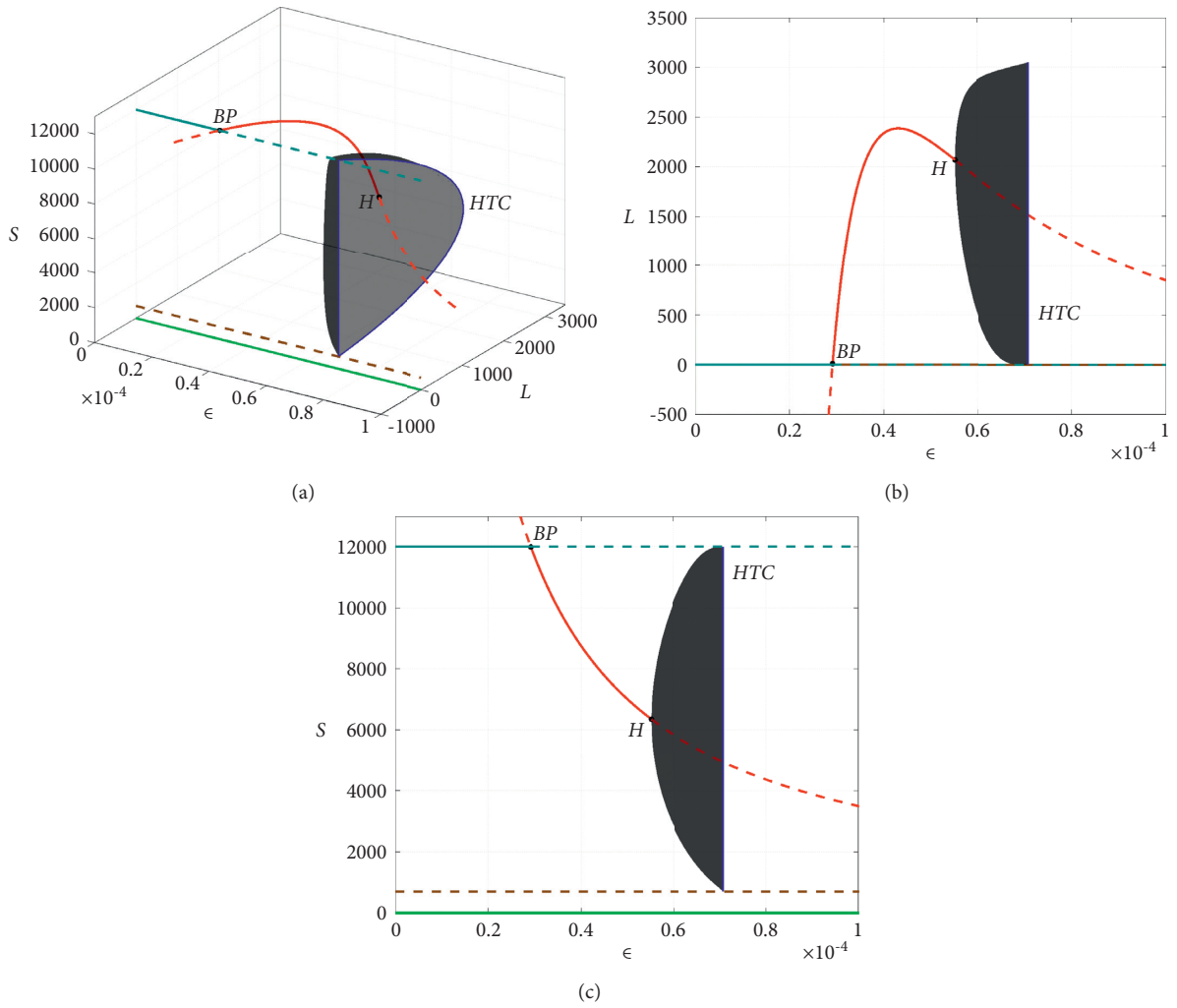

Figure 1: Steady-state change for an isolated community when the per-capita extraction rate ϵ is taken as the control parameter. The solid line represents stable equilibrium points, and the dashed line represents unstable equilibrium points. The shaded area represents limit cycles. (a) Bifurcation diagram, (b) projection on ϵ-L plane, and (c) projection on ϵ-S plane. Parameter values for this simulation are $\sigma = 0.14$, $\phi = 0.4$, $K = 12000$, $T = 700$, and $\rho = 0.03$.

$(1/2)\mathrm{Tr}J$ is the real part of the eigenvalues, the cross speed is given by

$$\frac{\mathrm{d}}{\mathrm{d}\epsilon}[\mathrm{Re}(\lambda(\epsilon))]_{\epsilon=\epsilon^H} = \frac{\phi\rho(K+T)^3}{8\sigma KT} \neq 0, \tag{5}$$

so that the transversality condition is satisfied. Finally, according to the sign of the first Lyapunov coefficient, $l_1 = -1.675825e-07$, and the Hopf bifurcation is supercritical giving rise to a stable limit cycle [89]. Numerical continuation of periodic orbits and detection of heteroclinic bifurcation HTC were developed using MATCONT [90].

On the contrary, the nodes P_3 and P_4 collide at $\varepsilon \approx 0.3$, making the node P_3, related to load capacity, go from stable to unstable (chair type), while node P_4 makes it from unstable to stable, for a positive increment of ϵ.

At $\varepsilon \approx 0.55$ a Hopf bifurcation occurs, giving rise to the instability of the P_4 node, which becomes a repulsive node, while an attractor limit cycle emerges, that becomes large, for positive increases of ϵ, until in $\epsilon \approx 0.7$, it gives rise to heteroclinic orbits between the nodes P_2 and P_3, forming a heteroclinic cycle, from which the limit cycle disappears.

Note that, before the branch point BP, the amount of resources extracted does not meet the population's need, leading to its disappearance. From BP and up to the Hopf bifurcation H, the resources extracted are sufficient to sustain a specific amount of population, gradually decreasing the support capacity of the system. Between H and the heteroclinic bifurcation HTC, the population-resources relationship enters into a dynamic of oscillation between scarcity and abundance, which becomes critical when the HTC is exceeded, at which time, followed by a moment at maximum abundance, the population will grow so large that it will critically deplete resources, leading to the collapse of the population and its resources.

3. Effect of Resource Exchange between Two Communities

In this section, the dynamics of exchange between two communities for the supply of their population's needs are considered, in which decision-makers are willing to enforce rules on resource extraction, have a conservation policy, and have a complete understanding of the socio-ecological system that allows them to define clear extraction limits.

3.1. Exchange with Continuous Coupling. The model for two communities, see system (6), assumes that each population keeps the proportion C_i, $i = 1, 2$, while exchanging the proportion $(1 - C_i)$ of the resources that produces but also protects an amount equal to its unextracted resources to the amount received by the exchange $S_{i\longrightarrow j}$, $i = 1, 2$, $i \neq j$, in caloric units:

$$\begin{aligned}
\frac{dL_1}{dt} &= C_1\phi_1\varepsilon_1 L_1 S_1 + (1 - C_2)\phi_2\varepsilon_2 L_2 S_2 - \sigma_1 L_1,\\
\frac{dS_1}{dt} &= \rho_1 S_1\left(\frac{S_1}{T_1} - 1\right)\left(1 - \frac{S_1}{K_1}\right) - \varepsilon_1 L_1 (S_1 - S_{2\longrightarrow 1}),\\
\frac{dL_2}{dt} &= C_2\phi_2\varepsilon_2 L_2 S_2 + (1 - C_1)\phi_1\varepsilon_1 L_1 S_1 - \sigma_2 L_2,\\
\frac{dS_2}{dt} &= \rho_2 S_2\left(\frac{S_2}{T_2} - 1\right)\left(1 - \frac{S_2}{K_2}\right) - \varepsilon_2 L_2 (S_2 - S_{1\longrightarrow 2}).
\end{aligned} \tag{6}$$

The resource conservation policy is given by equation (7), which is a conversion factor between the resources of the two communities:

$$S_{i\longrightarrow j} = \frac{(1 - C_i)\phi_i\epsilon_i S_i}{\phi_j\epsilon_j}. \tag{7}$$

For simplicity, simulations have been carried out with normalized S_i, considering $s_i = S_i/K_i$.

3.2. Exchange Rules between Communities. For the representation of resources' exchange rules between communities, it was considered that the exchange proportions C_i depend on levels of resources that are defined for each community, understanding that a level is a set of states of available renewable resources, such that, if the level between the communities is different, there is an exchange from the community with greater resources to the community with fewer resources, and if the level is the same, no exchanges are made. This representation implies that the exchange rates C_i change according to the available level of resources that the two communities have at each instant of time.

In this way, it is assumed that cooperation is a decision that is made mutually under certain considerations related to resource stocks, whose main objective is to mitigate the overexploitation of natural resources of the needy community (understand a needy community as one that has brought its available renewable resources to a deficit threshold).

The 4-dimensional space of states has two switching regions Σ_i, $i = 1, 2$, each of which defines the decision change limits, also defining two levels of available renewable resources by community: deficit and surplus. Considering that the communities would not be willing to have their levels defined differently to avoid exposing their resources in the exchange measures, it has been considered that the levels of each community have the same thresholds.

3.3. Behavior with Exchange Rules through Filippov Systems. To represent the rules defined above and taking into account that they define a discontinuous system, we will now present the formalism of Filippov's systems [8] required to obtain the differential system that models the exchange between two communities.

3.3.1. Formalism of Filippov's Systems. In Filippov systems with a commutation surface, the state space is divided into two regions R_1 and R_2 through a surface Σ, defined as the set 0 of a smooth scalar function h. Thus, we have

$$\dot{x} = f(x) = \begin{cases} f_1(x), & x \in R_1,\\ f_2(x), & x \in R_2, \end{cases}, x(0) = x_0 \in \mathbb{R}^n, \tag{8}$$

where f_1 and f_2 are smooth vector fields. The regions R_1 and R_2 and the surface Σ are defined as

$$\begin{aligned}
R_1 &= \{x \in \mathbb{R}^n \colon h(x) > 0\},\\
R_2 &= \{x \in \mathbb{R}^n \colon h(x) < 0\},\\
\Sigma &= \{x \in \mathbb{R}^n \colon h(x) = 0\}.
\end{aligned} \tag{9}$$

In this case, the dynamics on Σ are classified in

(i) *Sliding Region.* $\hat{\Sigma} = \{x \in \mathbb{R}^n \colon \mathscr{L}_{f_1}h(x) \cdot \mathscr{L}_{f_2}h(x) < 0, \mathscr{L}_{f_1}h(x) < 0\}$, $\hat{\Sigma} \subset \Sigma$, when both vector fields $f_1(x)$ and $f_2(x)$ point to Σ

(ii) *Escaping Region.* $\Sigma_e = \{x \in \mathbb{R}^n \colon \mathscr{L}_{f_1}h(x) \cdot \mathscr{L}_{f_2}h(x) < 0, \mathscr{L}_{f_1}h(x) > 0\}$, $\Sigma_e \subset \Sigma$

(iii) *Crossing Region.* $\Sigma_c = \{x \in \mathbb{R}^n \colon \mathscr{L}_{f_1}h(x) \cdot \mathscr{L}_{f_2}h(x) > 0\}$, $\Sigma_c \subset \Sigma$

Here, $\mathscr{L}_{f_{1,2}}h(x) \colon = \nabla h(x) \cdot f_{1,2}(x)$ is defined as the Lie derivative of $h(x)$ with respect to the vector field $f_{1,2}$. Once the evolution of the system reaches the sliding surface, the dynamics can be defined as a linear combination of the vector fields (f_1 and f_2) through the Filippov formalism [8], namely,

$$\dot{x} = f_\Sigma(x), \quad x \in \hat{\Sigma}, \tag{10}$$

where

$$f_\Sigma = (1 - \lambda)f_1(x) + \lambda f_2(x), \tag{11}$$

and λ is the solution of

$$\begin{cases} 0 = \nabla h(x)^T \cdot f_\Sigma(x),\\ 0 = h(x). \end{cases} \tag{12}$$

On the contrary, the trajectory of the system leaves the sliding region as soon as the vector fields $f_{1,2}$ become tangent to Σ, that is, making $\lambda = 0$ and $\lambda = 1$, and we obtain $\mathscr{L}_{f_1} h(x) = 0$ or $\mathscr{L}_{f_2} h(x) = 0$.

Now, if we consider a system with two commutation surfaces Σ_1 and Σ_2, according to Filippov's formalism, the state space will be divided into four regions R_1, R_2, R_3, and R_4:

$$\begin{aligned} R_1&: f_1 \text{ for } \quad h_1 > 0, h_2 > 0, \\ R_2&: f_2 \text{ for } \quad h_1 < 0, h_2 > 0, \\ R_3&: f_3 \text{ for } \quad h_1 < 0, h_2 < 0, \\ R_4&: f_4 \text{ for } \quad h_1 > 0, h_2 < 0. \end{aligned} \tag{13}$$

In this case, the trajectories of the system can evolve in any of the mentioned regions as well as on the regions Σ_1 and Σ_2. Additionally, the system can evolve on the commutation surface of codimension two, defined by the intersection of the two commutation surfaces of codimension one (i.e., $\Sigma = \Sigma_1 \cap \Sigma_2$):

$$\Sigma = \left\{ x \in \mathbb{R}^n : h(x) = 0, h(x) = \begin{bmatrix} h_1(x) \\ h_2(x) \end{bmatrix} \right\}. \tag{14}$$

Now, the codimension 1 sliding vector fields are defined as $f_\Sigma^\pm$ with respect to each switching surface $\Sigma_{1,2}^\pm$, i.e.,

$$\begin{aligned} \dot{x} &= f_{\Sigma_1^+} = (1-\lambda_1) f_1(x) + \lambda_1 f_4(x), \lambda_1 = \frac{\mathscr{L}_{f_1} h_1(x)}{\mathscr{L}_{f_1 - f_4} h_1(x)}, \\ \dot{x} &= f_{\Sigma_1^-} = (1-\lambda_2) f_2(x) + \lambda_2 f_3(x), \lambda_2 = \frac{\mathscr{L}_{f_2} h_1(x)}{\mathscr{L}_{f_2 - f_3} h_1(x)}, \\ \dot{x} &= f_{\Sigma_2^+} = (1-\lambda_3) f_1(x) + \lambda_3 f_2(x), \lambda_3 = \frac{\mathscr{L}_{f_1} h_2(x)}{\mathscr{L}_{f_1 - f_2} h_2(x)}, \\ \dot{x} &= f_{\Sigma_2^-} = (1-\lambda_4) f_3(x) + \lambda_4 f_4(x), \lambda_4 = \frac{\mathscr{L}_{f_3} h_2(x)}{\mathscr{L}_{f_3 - f_4} h_2(x)}. \end{aligned} \tag{15}$$

If a path is followed on one of the sliding surfaces $\sum_{1,2}^\pm$, the attractiveness can be characterized according to the first-order output conditions (tangency conditions). Whenever $\lambda_{1,2,3,4} = 0$ and $\lambda_{1,2,3,4} = 1$, the exit conditions of the first order are expressed by

$$\begin{aligned} &\mathscr{L}_{f_1} h_1(x) = 0, \\ &\mathscr{L}_{f_2} h_1(x) = 0, \\ &\mathscr{L}_{f_1} h_2(x) = 0, \\ &\mathscr{L}_{f_2} h_2(x) = 0, \\ &\mathscr{L}_{f_3} h_1(x) = 0, \\ &\mathscr{L}_{f_4} h_1(x) = 0, \\ &\mathscr{L}_{f_3} h_2(x) = 0, \\ &\mathscr{L}_{f_4} h_2(x) = 0. \end{aligned} \tag{16}$$

The vector field of sliding on the commutation surface Σ can be defined through the convex method of Filippov [8]. In this way, the dynamics on Σ are

$$F_\Sigma(x) = \sum_{i=1}^{4} \lambda_i(x) f_i(x), \tag{17}$$

where

$$\lambda_i(x) \geq 0 \wedge \sum_{i=1}^{4} \lambda_i(x) = 1, \tag{18}$$

taking into account that $F_\Sigma(x)$ must be tangent to Σ, that is, $\mathscr{L}_{F_\Sigma} h_i(x) = 0, i = 1, 2$. Clearly, it can be seen from the above that there is no single solution for the coefficients $\lambda_i(x)$ since we now have a system of three equations with four unknowns. In the literature, two systematic methods allow defining the codimension 2 sliding vector field under certain conditions, the *bilinear combination* [91] and the method called *moments of solutions* [92] although the ambiguity that arises when considering multiple switching surfaces remains a problem under study. A nonlinear formulation of the sliding vector field called *hidden dynamics* is proposed in [93], which has been effective in modeling real mechanical phenomena such as friction.

The bilinear interpolation method was originally introduced by Seidman [91] and further studied in [92]. The idea is to obtain a vector field on the intersection by forming a bilinear interpolation among the four vector fields:

$$f_B := (1-\hat{\alpha})(1-\hat{\beta}) f_1 + (1-\hat{\alpha})\hat{\beta} f_2 + \hat{\alpha}(1-\hat{\beta}) f_3 + \hat{\alpha}\hat{\beta} f_4, \tag{19}$$

where $\hat{\alpha}$ and $\hat{\beta}$ are smooth functions of $x \in \Sigma$, between $[0, 1]$. Under the orthogonality conditions ($\mathscr{L}_{F_B}(h_1)(x) = \mathscr{L}_{F_B}(h_2)(x) = 0$), $\hat{\alpha}$ and $\hat{\beta}$ can be found by solving the following nonlinear system equations:

$$\begin{aligned} &(1-\hat{\alpha})(1-\hat{\beta}) \begin{bmatrix} \mathscr{L}_{f_1} h_1 \\ \mathscr{L}_{f_1} h_2 \end{bmatrix} + (1-\hat{\alpha})\hat{\beta} \begin{bmatrix} \mathscr{L}_{f_2} h_1 \\ \mathscr{L}_{f_2} h_2 \end{bmatrix} \\ &+ \hat{\alpha}(1-\hat{\beta}) \begin{bmatrix} \mathscr{L}_{f_3} h_1 \\ \mathscr{L}_{f_3} h_2 \end{bmatrix} + \hat{\alpha}\hat{\beta} \begin{bmatrix} \mathscr{L}_{f_4} h_1 \\ \mathscr{L}_{f_4} h_2 \end{bmatrix} = 0. \end{aligned} \tag{20}$$

Assuming that we are following a trajectory on Σ, the second-order conditions are defined by

$$\begin{aligned} &\mathscr{L}_{f_{\sum_1^+}} h_1(x) = 0, \\ &\mathscr{L}_{f_{\sum_1^-}} h_1(x) = 0, \\ &\mathscr{L}_{f_{\sum_2^+}} h_2(x) = 0, \\ &\mathscr{L}_{f_{\sum_2^-}} h_2(x) = 0. \end{aligned} \tag{21}$$

3.3.2. Filippov System Model. The variation in the exchange rates of each community is assumed according to the following rule:

$$C_1 = \begin{cases} C_1^+, & \text{if } h_1 > 0, \\ C_1^-, & \text{if } h_1 < 0, \end{cases}$$
$$C_2 = \begin{cases} C_2^+, & \text{if } h_2 > 0, \\ C_2^-, & \text{if } h_2 < 0. \end{cases} \tag{22}$$

Based on the Filippov formalism, the dynamics of resource exchange between two communities can be rewritten in state space by making $x = [L_1, S_1, L_2, S_2]^T$, $h_1 = S_1 - \alpha_T$, and $h_2 = S_2 - \alpha_T$, α_T being the decision threshold for both communities, that is,

$$\dot{x} = f(x) = \begin{cases} f_1(x), & x \in R_1 \\ f_2(x), & x \in R_2 \\ f_3(x), & x \in R_3 \\ f_4(x), & x \in R_4 \end{cases}, \quad x(0) = x_0 \in \mathbb{R}^4, \tag{23}$$

where

$$f_1(x) = \begin{pmatrix} C_1^+\phi_1\epsilon_1 L_1 S_1 - \sigma_1 L_1 + (1 - C_2^+)\phi_2\epsilon_2 L_2 S_2 \\ \rho_1 S_1\left(\frac{S_1}{T_1} - 1\right)\left(1 - \frac{S_1}{K_1}\right) - \epsilon_1 L_1 (S_1 - S_{2\longrightarrow 1}) \\ C_2^+\phi_2\epsilon_2 L_2 S_2 - \sigma_2 L_2 + (1 - C_1^+)\phi_1\epsilon_1 L_1 S_1 \\ \rho_2\left(\frac{S_2}{T_2} - 1\right)\left(1 - \frac{S_2}{K_2}\right)S_2 - \epsilon_2 L_2 (S_2 - S_{1\longrightarrow 2}) \end{pmatrix}, \tag{24}$$

$$f_2(x) = \begin{pmatrix} C_1^-\phi_1\epsilon_1 L_1 S_1 + (1 - C_2^+)\phi_2\epsilon_2 L_2 S_2 - \sigma_1 L_1 \\ \rho_1 S_1\left(\frac{S_1}{T_1} - 1\right)\left(1 - \frac{S_1}{K_1}\right) - \epsilon_1 L_1 (S_1 - S_{2\longrightarrow 1}) \\ C_2^+\phi_2\epsilon_2 L_2 S_2 + (1 - C_1^-)\phi_1\epsilon_1 L_1 S_1 - \sigma_2 L_2 \\ \rho_2 S_2\left(\frac{S_2}{T_2} - 1\right)\left(1 - \frac{S_2}{K_2}\right) - \epsilon_2 L_2 (S_2 - S_{1\longrightarrow 2}) \end{pmatrix}, \tag{25}$$

$$f_3(x) = \begin{pmatrix} C_1^-\phi_1\epsilon_1 L_1 S_1 + (1 - C_2^-)\phi_2\epsilon_2 L_2 S_2 - \sigma_1 L_1 \\ \rho_1 S_1\left(\frac{S_1}{T_1} - 1\right)\left(1 - \frac{S_1}{K_1}\right) - \epsilon_1 L_1 (S_1 - S_{2\longrightarrow 1}) \\ C_2^-\phi_2\epsilon_2 L_2 S_2 + (1 - C_1^-)\phi_1\epsilon_1 L_1 S_1 - \sigma_2 L_2 \\ \rho_2 S_2\left(\frac{S_2}{T_2} - 1\right)\left(1 - \frac{S_2}{K_2}\right) - \epsilon_2 L_2 (S_2 - S_{1\longrightarrow 2}) \end{pmatrix}, \tag{26}$$

$$f_4(x) = \begin{pmatrix} C_1^+\phi_1\epsilon_1 L_1 S_1 + (1 - C_2^-)\phi_2\epsilon_2 L_2 S_2 - \sigma_1 L_1 \\ \rho_1 S_1\left(\frac{S_1}{T_1} - 1\right)\left(1 - \frac{S_1}{K_1}\right) - \epsilon_1 L_1 (S_1 - S_{2\longrightarrow 1}) \\ C_2^-\phi_2\epsilon_2 L_2 S_2 + (1 - C_1^+)\phi_1\epsilon_1 L_1 S_1 - \sigma_2 L_2 \\ \rho_2 S_2\left(\frac{S_2}{T_2} - 1\right)\left(1 - \frac{S_2}{K_2}\right) - \epsilon_2 L_2 (S_2 - S_{1\longrightarrow 2}) \end{pmatrix}. \tag{27}$$

Furthermore, the switching manifold is defined as

$$\Sigma_1 = \{x \in \mathbb{R}^4 : S_1 - \alpha_T = 0\},$$
$$\Sigma_2 = \{x \in \mathbb{R}^4 : S_2 - \alpha_T = 0\}. \tag{28}$$

It is worth to mention that, due to parameter configuration, the flow does not enter into switching manifold of codimension two, and it can be seen in Section 3.4.1 for more details. By solving $f^{\pm}_{\Sigma_{1,2}} = 0$, we found that there exists an equilibrium point outside the sliding region, and thus, the system does not have pseudoequilibrium points. Analytical expressions of tangency points are

$$\mathscr{L}_{f_1} h_1(x) = \rho_1 S_1\left(\frac{S_1}{T_1} - 1\right)\left(1 - \frac{S_1}{K_1}\right) - \epsilon_1 L_1\left(S_2 - \frac{(1 - C_2^+)\phi_2\epsilon_2 S_2}{\phi_1\epsilon_1}\right) = 0,$$
$$\mathscr{L}_{f_4} h_1(x) = \rho_1 S_1\left(\frac{S_1}{T_1} - 1\right)\left(1 - \frac{S_1}{K_1}\right) - \epsilon_1 L_1\left(S_2 - \frac{(1 - C_2^-)\phi_2\epsilon_2 S_2}{\phi_1\epsilon_1}\right) = 0,$$
$$\mathscr{L}_{f_1} h_2(x) = \rho_2 S_2\left(\frac{S_2}{T_2} - 1\right)\left(1 - \frac{S_2}{K_2}\right) - \epsilon_2 L_2\left(S_2 - \frac{(1 - C_1^+)\phi_1\epsilon_1 S_1}{\phi_2\epsilon_2}\right) = 0,$$
$$\mathscr{L}_{f_2} h_2(x) = \rho_2 S_2\left(\frac{S_2}{T_2} - 1\right)\left(1 - \frac{S_2}{K_2}\right) - \epsilon_2 L_2\left(S_2 - \frac{(1 - C_1^-)\phi_1\epsilon_1 S_1}{\phi_2\epsilon_2}\right) = 0. \tag{29}$$

Because α_T is the decision threshold for both communities, then we can replace S_1 and S_2 in the above equations since it is supposed that the decision-making threshold is equal in both communities. Next, we can solve for L_1 and L_2 to graph sliding regions, see the yellow región in Figure 2.

3.4. Dynamics of Exchange between Communities with One Decision Level. From the system defined by the vector fields presented in equations (24)–(27), we will present the results of the simulations carried out under the following conditions, which represent the exchange policy between the two communities:

(i) Similar parameter configurations are considered between the two communities that exchange their resources, except in the case of the effective extraction rate and regeneration rate of renewable resources of each community

(ii) It is assumed that the effective rate of extraction of the second community ϵ_2 is high in consideration of that defined for the first community so that, by depleting its resources more quickly, it does not count on the cooperation of the community one, and it will collapse and disappear (as in the case of high extraction of resources from the isolated community presented in Section 2).

(iii) It is assumed that the renewable resources of each community are regenerated at different rates, that is, $\rho_1 \neq \rho_2$. This is to suggest that the physiographic, climatic, and productive conditions of the two communities are not necessarily the same, and each one has its complexity.

(iv) It is assumed that the switching regions that define the decision thresholds of the communities are in the same percentage value of resources since they are

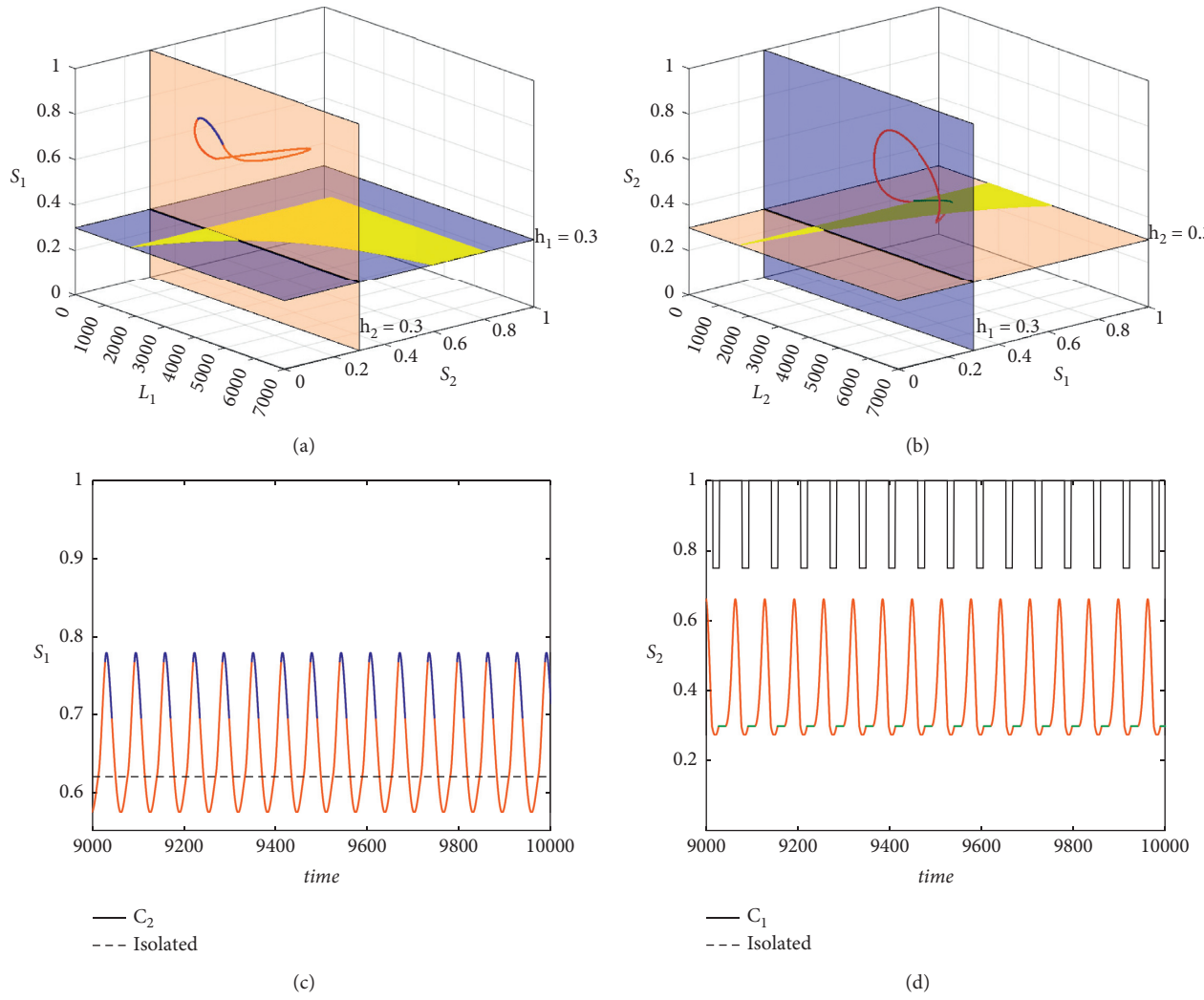

Figure 2: Periodic behavior induced by switching regions for $\epsilon_1 = 4.7e^{-5}$.

framed in the same collaboration policy, guaranteeing that their exchanges occur under equal conditions.

(v) Whenever a community is at the deficit threshold, the collaboration policy says that the community at the surplus threshold will cooperate with up to a certain percentage of its resources, indicating that cooperation only occurs in one direction.

(vi) If the two communities are at the same threshold, the exchanges $C_1 = C_2 = 1$ are closed, leaving them as if they were isolated communities. In the case where they are at the surplus threshold, the exchange would not be necessary, while in the case where they are at the deficit threshold, the exchange would not be probable since the communities would be putting at risk the little resource that they have left to sustain their populations.

The initial condition of the simulations is found in the surplus thresholds for the two communities so that there is room to show resource management errors, represented in their extraction measures in contrast to the resource regeneration capacity and how a policy of cooperation based on exchange becomes an alternative for the community on the threshold of deficit.

The simulations presented show the results for parameter arrangements that led to obtaining periodic and chaotic behaviors (see Section 3.4.2), which are verified in the projections of the steady-state diagram presented in Section 3.4.3.

The general parameter values used in these simulations are $\sigma_i = 0.14$, $\rho_1 = 0.03$, $\rho_2 = 0.04$, $T_i = 700$, $K_i = 12000$, $\epsilon_2 = 7e^{-5}$, and $\phi_i = 0.4$. The initial condition considered was $(L_1, S_1, L_2, S_2) = (2000, 10400, 2500, 8600)$, the values for the exchange decision through the switching regions were set at 30%, and the exchange rate defined when the community i cooperates with the other was 25% (i.e., $1 - C_i = 0.25$, $i = 1.2$).

The effective extraction rate ϵ_1 is taken as a control parameter to perform the steady-state analysis presented in Section 3.4.3. With this configuration, it is avoided to reach the switching manifold of codimension two, which corresponds to the intersection between the two switching manifolds Σ_i of codimension one, described in equation (14).

To present the simulations of this 4-dimensional system, 3-dimensional projections were used to allow the switching manifolds to be adequately visualized. It should be understood then that the switching regions will appear with a smaller dimension than they have. This was achieved by using the spaces $s_1 - L_1 - s_2$ and $s_2 - L_2 - s_1$. Also, it was considered that the colors facilitate the reading of the simulations. The three-dimensional projection of the switching region Σ_1 at $h_1 = 0.3$ is colored blue, while the region Σ_2 at $h_2 = 0.3$ is colored orange. The sliding regions were drawn in yellow. The trajectory in orange corresponds to that defined by the vector fields f_i, in what we have called the "thresholds," while in blue and green, to contrast with the colors of the switching regions and the projections of the landslide trajectories.

The corresponding time series of the resource variables s_i and the signal of the exchange variable C_i were added to the three-dimensional projections, considering that (1) the solution for the case of communities is drawn on a continuous line coupled, (2) the dotted line shows the trajectory of the case of communities that evolve in isolation $C_i = 1$, and (3) the colors correspond to the colors used in the three-dimensional projection.

3.4.1. Periodic Behavior. For the first simulation, it has been considered to compare the behavior between two communities under the effects of two scenarios: (1) noncooperation and (2) cooperation, considering a relatively low extraction rate from community one ϵ_1, see Figure 2.

In the noncooperation scenario, presented through dotted lines in the time series of Figures 2(c) and 2(d), it is shown how the first community has reached a nonzero equilibrium value of its resources, while the second has disappeared.

In the cooperation scenario, a 1-periodic behavior is obtained with sliding over the switching manifold of community two Σ_2, which means that, through the exchange of resources, community two no longer disappears, achieving that the two communities are preserved in time, through a periodic cycle, see Figures 2(a) and 2(b).

The black signal, in Figures 2(c) and 2(d), shows the behavior of exchanges between communities; while community 1 does not receive resources ($C_2 = 1$), community two does through periodic pulses that satisfy their noncontinuous needs $(0.75 < C_1 < 1)$.

In this way, due to the configuration of the system, we see that the management of the socio-ecological system shown by community one, in scenarios of cooperation or noncooperation, allows it to be maintained over time, while community two only achieves it through cooperation.

The exchange avoids collapse and leads to a process of recovery of the community in deficit, which is not immediate, since it must overcome a delay that occurs while sliding over the switching manifold, possibly related to the recovery of its resources and education for cultural transformation and sustainable management, to finally appreciate recovery and stop dependence on the other community.

3.4.2. Chaotic Behavior. For the second simulation, again, it has been considered to compare the behavior between the two communities under the scenarios of (1) noncooperation and (2) cooperation, but now a relative extraction rate of the one ϵ_1 community has been considered high, see Figure 3.

In the noncooperation scenario, which is shown through dotted lines in the time series of Figures 3(c) and 3(d), isolated communities obtain opposite effects; the first community reaches the equilibrium of its resources despite having considerably increased its resource extraction rate ϵ_1, while the second community disappears.

In the cooperation scenario, chaotic behavior is obtained with sliding over the switching manifold of community two Σ_2, which means that, through the exchange of resources, community two no longer disappears, achieving that the two communities are preserved in time, with their trajectory confined to a region of state space, see Figures 3(a) and 3(b).

The black signal, in Figures 3(c) and 3(d), shows the behavior of exchanges between communities; while community 1 remains without receiving resources ($C_2 = 1$), community two continues depending on the other community, but now, through irregular pulses that satisfy their noncontinuous needs $(0.75 < C_1 < 1)$.

Under this system configuration, the management of the socio-ecological system shown by community one, in scenarios of cooperation or noncooperation, again allows it to be maintained over time, while community two only achieves it through cooperation.

In the cooperation scenario, for the extraction value relatively higher than the one used in the periodic system configuration of Section 3.4.1, the exchange once again avoids collapse and leads to a process of recovery of the community in deficit but this implies that the contributing community enters into a chaotic behavior confined to states that do not expose their resources and that the receiving community oscillates between the thresholds of surplus and deficit, achieving this long in the first. It draws the attention of community two that, leaving the deficit threshold, they must slide in the switching manifold during irregular (chaotic) periods that perhaps express different levels of consciousness, although their extraction policy is the same.

3.4.3. Steady-State Analysis. In this final simulation, a set of diagrams containing the steady-state mappings are presented, obtained for each of the state variables by the variation of the parameter ϵ_1 in the range of values where resource exchanges occur between the communities, involving sliding over the switching manifold Σ_2.

For the elaboration of this diagram, a total of 3000 simulations were carried out from an initial condition centered on $(L_1, S_1, L_2, S_2) = (2000, 10400, 2500, 8600)$, in which each simulation took a value of the ϵ_1 parameter in the range of 4.6×10^{-5} to 5.5×10^{-5}. This range of the control parameter was chosen for convenience, for two reasons: (1) it is the range in which sliding occurs over the switching manifold Σ_2, giving rise to the periodic and chaotic behaviors that were already mentioned in Sections 3.4.1 and 3.4.2, and (2) in this range, the system does not reach the

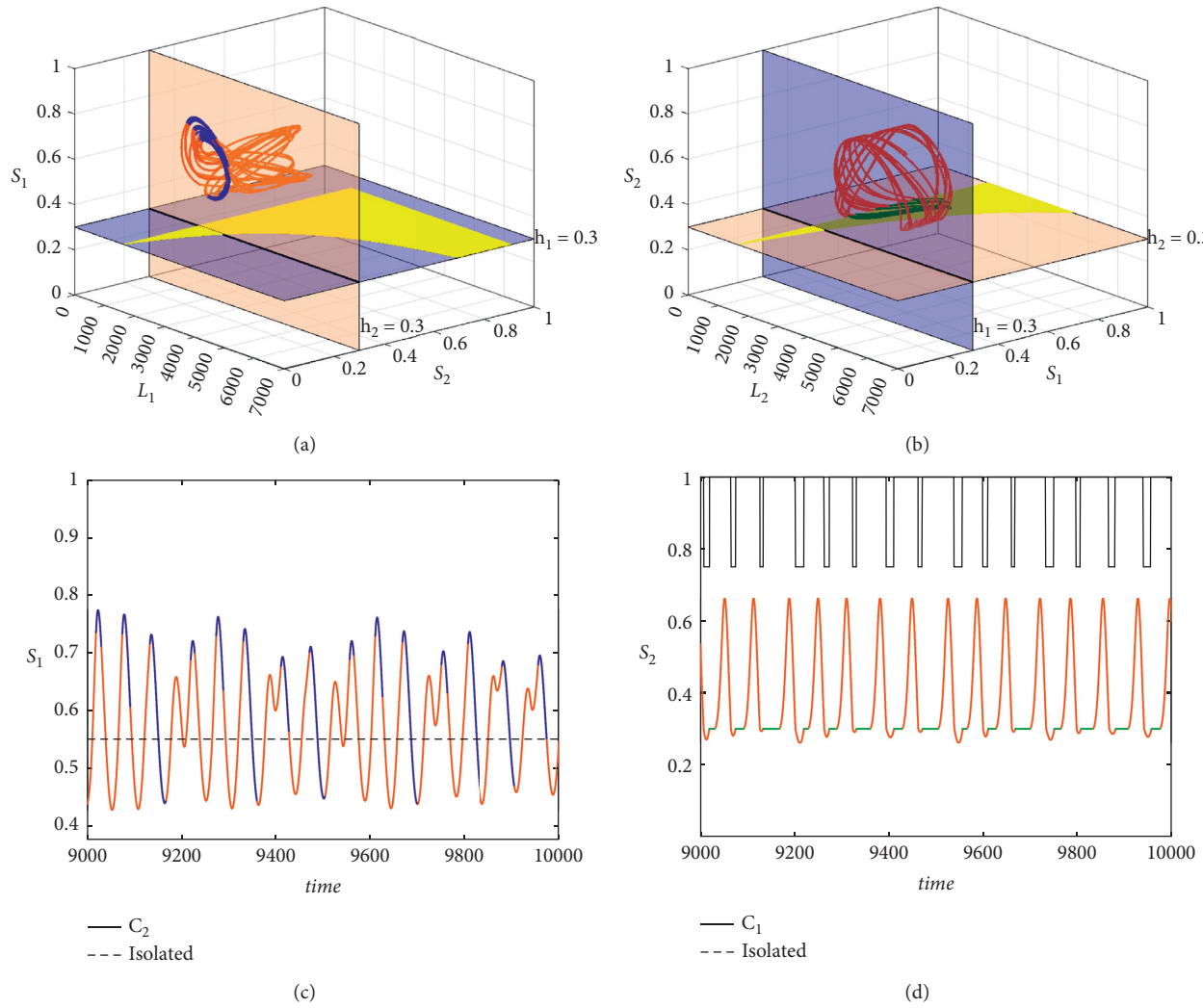

Figure 3: Chaotic behavior induced by switching regions for $\epsilon_1 = 5.3e^{-5}$.

codimension two switching region. The simulations were carried out until reaching the time $t = 10,000$, sampling the maximum and minimum values of the last 1000 units of time, in consideration of the changes in the behavior that the switching manifold makes on the periodic behavior of the orbits, as shown in Figure 3(d). In this way, the simulations presented in Figure 4 were obtained, where the representations of the upper steady-state, in green, map the maximums of the solution, while those of the lower part, in red, map their minima.

In this analysis, as ϵ_1 increases in the selected range, the system shows changes in periodicity and chaos in the dynamics of the behavior of community one (population and resources), without deviating it from the surplus threshold, see Figures 4(a) and 4(c), while community two exhibits behaviors of period one for the population and periodicity and chaos for resources when they are at the deficit threshold, see Figures 4(b) and 4(d). For the final interval of the analysis, the exchange was found to occur without sliding, through orbits of period one.

4. Discussion of Results

In this section, the results obtained will be discussed to understand (1) the effect of the variation of the extraction capacities in an isolated community, using a two-dimensional continuous model, see Section 2, and (2) the effect of the exchange of resources between two communities, based on a Filippov system, see Section 3, considering that, to have a first approximation of sustainability as conservation of well-being in a territory, landscape, or community, it is assumed that well-being is having renewable resources, which, as mentioned in the introduction, oversimplifies a plausible definition of well-being, but allows the presentation of the possibilities of the interpretation proposed in this article for sustainability.

In the first place, regarding the effect of the variation in extraction capacities in an isolated community, it is notable that, following the bifurcation diagram in Figure 1, the dynamics of the system involves four prospective scenarios: (1) *negligence*: in which the extraction is insufficient to sustain the population, (2) *harmony*: in which the extraction

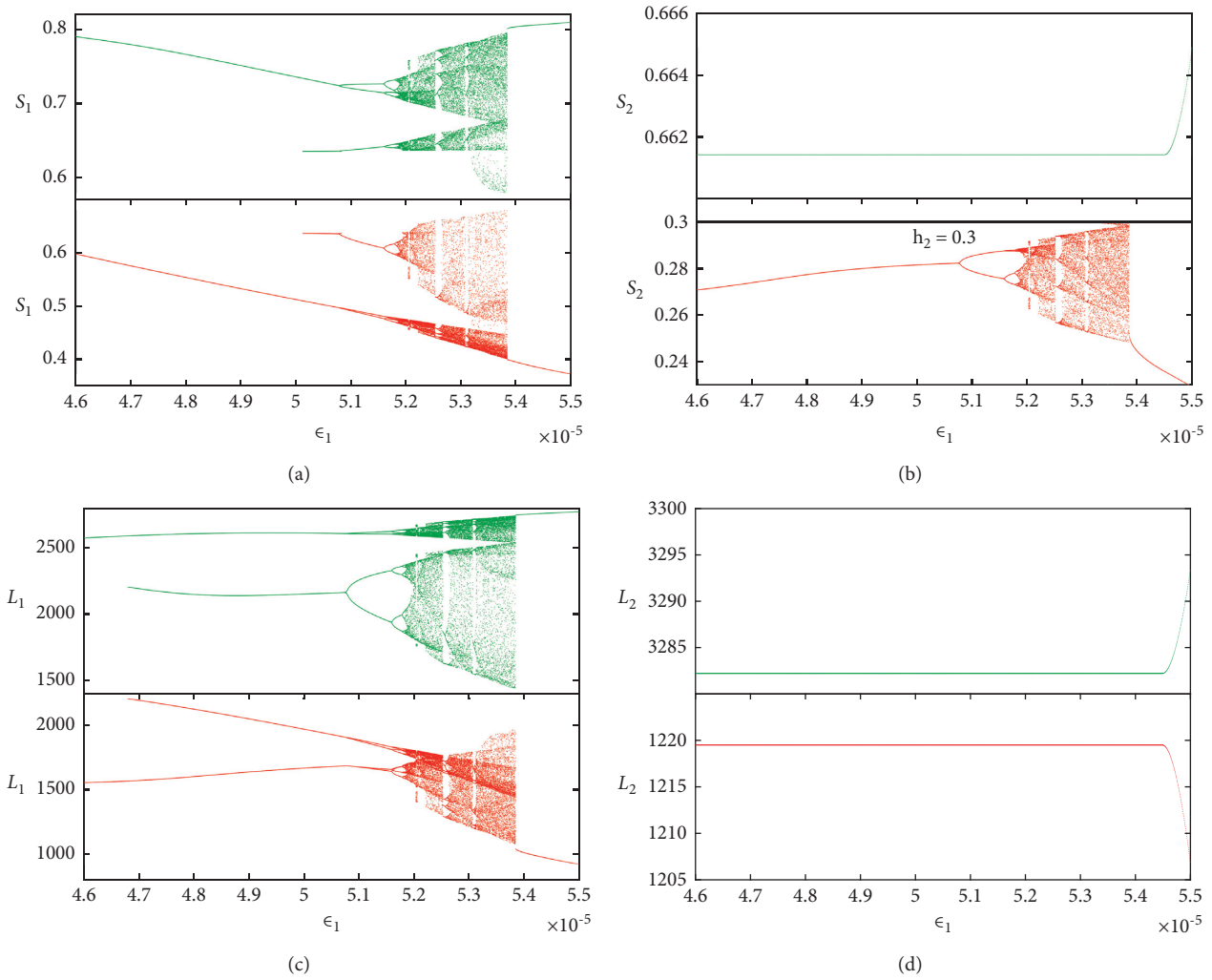

Figure 4: Steady state maps.

and recovery of resources are in equilibrium, (3) *instability*: in which there are continuous oscillations between scarcity and abundance, and (4) *collapse*: in which the excess in the extraction of resources leads to the disappearance of the population and the resources.

In this case, the conservation of well-being could only be appreciated in the harmony scenario, through the invariant set of equilibrium point type that the system defines for a certain level of extraction, so it is concluded that a territory, community, or landscape isolated, and it is only sustainable if it finds the balance between its population and the extraction of resources that it does for its maintenance, in consideration of the regenerative capacity of the resources.

This result, and its corresponding scenarios, can be compared with the current situation of humanity as a large community in a space with limited resources: planet Earth, with only the scenario that we call harmony being sustainable.

Second, on the effect of the exchange of resources between two communities based on a Filippov system, the results have allowed us to see through simulations and the dynamics emerging from the interaction between two communities that share their resources in pursuit of well-being, through invariant sets such as periodic orbits and strange attractors, who allow us to conclude that sustainability can take different invariant forms within the notion of well-being, in addition to the equilibrium form shown for an isolated community.

The reason why the exchange between the two communities reaches sustainability under these multiple geometries (equilibrium point, periodic orbit, or strange attractor), although one of the communities has been configured not to be sustainable without the exchange, is as follows: (1) there were clear conservation policies (represented through the switching manifolds) and (2) the policies had perfect control (the system was programmed deterministically). However, achieving sustainability through exchange makes the consuming community stabilize while the resource-rich community becomes unstable.

This is where an interpretation of well-being as several renewable resources fails because the instability of the stock reflects the socio-ecological instability of the one who contributes the resources to ensure that the community at the threshold of deficit can satisfy its demands for resources,

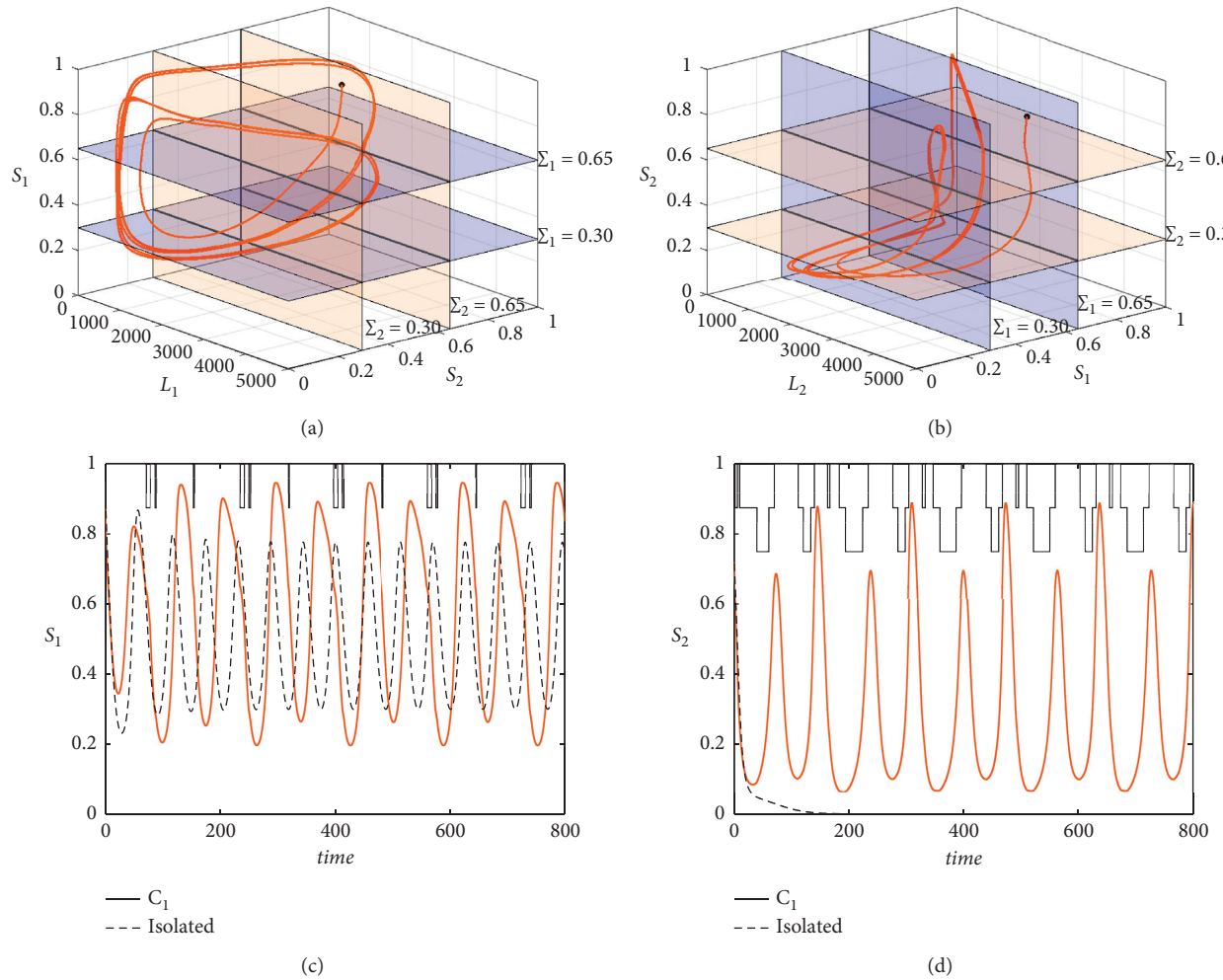

Figure 5: Steady state for economic cooperation between two communities when you have two switching regions. Parameter setting is $C_i = 0.75$, $\sigma_i = 0.14$, $\rho_1 = 0.03$, $\rho_2 = 0.04$, $T_i = 700$, $K_i = 12000$, $\beta_1 = 5.8e^{-5}$, $\epsilon_2 = 7e^{-5}$, and $y\phi_i = 0.4$.

without questioning or regulating the needs of the extractivist community, meaning that the contributing community maintains the stability of the relationship, despite the stability of its other socio-ecological dimensions. In other words, satisfying the needs of an extractive community despite another community can generate socio-ecological instabilities in the community that it contributes (violence, tyrannies, wage abuses, inhumane living conditions, etc.?). So, speaking of sustainability, the definition of what is well-being must be multidimensional, involving at least people, animals (domestic or livestock), and ecosystems.

About sliding, it shows how a community is trapped in a set of transition states between one threshold and another while regulating the population. This can be derived from a biological impulse of humanity that, without clear controls, tends to deteriorate its well-being, falling into the tragedy of commons ground.

The values of the exchange constants, together with the values of the extraction rates, proved to be conditioning factors for the development or deterioration of the communities, suggesting that they should be careful with their definition, before proclaiming a national or international exchange policy.

5. Conclusions

The exchange avoids collapse and leads to a process of recovery of the community in deficit, which is not immediate, since it must overcome a delay that occurs while sliding over the switching manifold, possibly related to the recovery of its resources and education for cultural transformation and sustainable management, to finally appreciate recovery and stop dependence on the other community.

The approach made in this paper from mathematical modeling for the analysis of the sustainability of territories, communities, and landscapes, between which there may or may not be exchanges, understanding that sustainability occurs when well-being is a law of conservation of the spatial unit of analysis, allows to understand that

(i) Without exchange possibilities, a population will depend on the extraction rate and the regeneration capacity of its resources, to prevail or disappear.

(ii) The exchange of resources is key to the survival of the human species, without this implying sustainability. This cooperation uses redundancy in the other to maintain itself.

(iii) A definition of well-being limited to the number of resources as a need can generate undesirable instabilities in the contributing socio-ecological systems unless that is the sustainability that we wish to establish.

(iv) Sustainability can be visualized in the attraction basins of the invariant sets of socio-ecological systems whose states do not include null values, so it can be said that there are sustainabilities and that sustainability analyzes have many opportunities from modeling and analysis with Filippov systems and bifurcation theory.

6. Future Research

The coupling introduces two new parameters into the system, h_i and C_i. As future work, it is proposed to evaluate the effect that varying one of the two has on the exchange dynamics, given that the change of the switching manifold or the exchange values, would allow evaluating which would be the threshold that leads to the best performance of the system, even if those values are not equal.

It is also proposed to consider the existence of more than one switching region for the definition of the decision levels of the system, as proposed in Figure 5.

Finally, it is proposed to establish sets of needs that allow defining in a multidimensional way the well-being of the territory, community, or landscape and promoting socio-ecological arrangements that allow us not only to have life but to have it with dignity.

Data Availability

The data used to support the findings of the study are available from the corresponding author upon request.

Conflicts of Interest

The authors declare that there are no conflicts of interest regarding the study of this paper.

Acknowledgments

Christian Erazo acknowledges support from University Antonio Nariño through the Research Project 2018216.

References

[1] G. H. Brundtland, *Our Common Future*Oxford University Press, Oxford, UK, 1987.

[2] D. Meadows, "Limits to growth, a report for the club of Rome's project on the predicament of mankind," *Universe Books*, Chelsea Green Publishing, Hartford, VT, USA, 1972.

[3] R. K. Turner, "Sustainability: principles and practice," in *Sustainable Environmental Economics and Management: Principles and Practice*, R. K. Turner, Ed., pp. 3–36, Belhaven Press, London, UK, 1993.

[4] J. Wu, "Landscape sustainability science: ecosystem services and human well-being in changing landscapes," *Landscape Ecology*, vol. 28, no. 6, pp. 999–1023, 2013.

[5] J. Elkington, "Enter the triple bottom line," in *The Triple Bottom Line: Does it All Add up? Assessing the Sustainability of Business and CSR*, A. Henriques and J. Richardson, Eds., pp. 1–186, Earthscan, London, UK, 2004.

[6] J. M. Redondo, "Landscape sustainability analysis: methodological approach from dynamical systems," in *Journal of Physics: Conference Series*IOP Publishing, Bristol, UK, 2019.

[7] A. F. Filippov, "Differential equations with discontinuous right-hand side," *American Mathematical Society Translations*, vol. 42, no. 2, pp. 354–362, 1964.

[8] A. F. Filippov, "Equations with the right-hand side continuous in x and discontinuous in t," in *Differential Equations with Discontinuous Righthand Sides*, pp. 3–47, Springer, Berlin, Germany, 1988.

[9] M. A. Teixeira, "Stability conditions for discontinuous vector fields," *Journal of Differential Equations*, vol. 88, no. 1, pp. 15–29, 1990.

[10] Y. A. Kuznetsov, S. Rinaldi, and A. Gragnani, "One-parameter bifurcations in planar Filippov systems," *International Journal of Bifurcation and Chaos*, vol. 13, no. 8, pp. 2157–2188, 2003.

[11] M. Guardia, T. M. Seara, and M. A. Teixeira, "Generic bifurcations of low codimension of planar Filippov systems," *Journal of Differential Equations*, vol. 250, no. 4, pp. 1967–2023, 2011.

[12] I. Remco, H. Nijmeijer, *Dynamics and Bifurcations of Nonsmooth Mechanical Systems*, Vol. 18, Springer Science & Business Media, Berlin, Germany, 2013.

[13] M. Di Bernardo, C. J. Budd, A. R. Champneys et al., "Bifurcations in nonsmooth dynamical systems," *SIAM Review*, vol. 50, no. 4, pp. 629–701, 2008.

[14] V. Utkin, "Variable structure systems with sliding modes," *IEEE Transactions on Automatic Control*, vol. 22, no. 2, pp. 212–222, 1977.

[15] E. Freire, E. Ponce, F. Rodrigo, and F. Torres, "Bifurcation sets of continuous piecewise linear systems with two zones," *International Journal of Bifurcation and Chaos*, vol. 8, no. 11, pp. 2073–2097, 1998.

[16] V. Carmona, E. Freire, E. Ponce, and F. Torres, "On simplifying and classifying piecewise-linear systems," *IEEE Transactions on Circuits and Systems I: Fundamental Theory and Applications*, vol. 49, no. 5, pp. 609–620, 2002.

[17] E. Ponce, J. Ros, and E. Vela, "Limit cycle and boundary equilibrium bifurcations in continuous planar piecewise linear systems," *International Journal of Bifurcation and Chaos*, vol. 25, no. 3, Article ID 1530008, 2015.

[18] J. Llibre, E. Ponce, and J. Ros, "Algebraic determination of limit cycles in a family of three-dimensional piecewise linear differential systems," *Nonlinear Analysis: Theory, Methods & Applications*, vol. 74, no. 17, pp. 6712–6727, 2011.

[19] B. R. de Freitas, J. Llibre, and J. C. Medrado, "Limit cycles of continuous and discontinuous piecewise-linear differential systems in R3," *Journal of Computational and Applied Mathematics*, vol. 338, pp. 311–323, 2018.

[20] R. Cristiano and D. J. Pagano, "Two-parameter boundary equilibrium bifurcations in 3D-filippov systems," *Journal of Nonlinear Science*, vol. 29, no. 6, pp. 2845–2875, 2019.

[21] O. Makarenkov and J. S. W. Lamb, "Dynamics and bifurcations of nonsmooth systems: a survey," *Physica D: Nonlinear Phenomena*, vol. 241, no. 22, pp. 1826–1844, 2012.

[22] A. Colombo, M. di Bernardo, S. J. Hogan, and M. R. Jeffrey, "Bifurcations of piecewise smooth flows: perspectives, methodologies and open problems," *Physica D: Nonlinear Phenomena*, vol. 241, no. 22, pp. 1845–1860, 2012.

[23] F. Dercole, F. Della Rossa, A. Colombo, and Y. A. Kuznetsov, "Two degenerate boundary equilibrium bifurcations in planar Filippov systems," *SIAM Journal on Applied Dynamical Systems*, vol. 10, no. 4, pp. 1525–1553, 2011.

[24] M. R. Jeffrey and A. Colombo, "The two-fold singularity of discontinuous vector fields," *SIAM Journal on Applied Dynamical Systems*, vol. 8, no. 2, pp. 624–640, 2009.

[25] M. R. Jeffrey and S. J. Hogan, "The geometry of generic sliding bifurcations," *SIAM Review*, vol. 53, no. 3, pp. 505–525, 2011.

[26] M. R. Jeffrey, "Nondeterminism in the limit of nonsmooth dynamics," *Physical Review Letters*, vol. 106, no. 25, Article ID 254103, 2011.

[27] Z. Du, Y. Li, and W. Zhang, "Bifurcation of periodic orbits in a class of planar Filippov systems," *Nonlinear Analysis: Theory, Methods & Applications*, vol. 69, no. 10, pp. 3610–3628, 2008.

[28] Z. Du and Y. Li, "Bifurcation of periodic orbits with multiple crossings in a class of planar Filippov systems," *Mathematical and Computer Modelling*, vol. 55, no. 3-4, pp. 1072–1082, 2012.

[29] B. N. Arne, "Non-periodic motion caused by grazing incidence in an impact oscillator," *Journal of Sound and Vibration*, vol. 145, pp. 279–297, 1991.

[30] M. Di Bernardo, P. Kowalczyk, and A. Nordmark, "Bifurcations of dynamical systems with sliding: derivation of normal-form mappings," *Physica D: Nonlinear Phenomena*, vol. 170, no. 3-4, pp. 175–205, 2002.

[31] M. Di Bernardo, P. Kowalczyk, and A. Nordmark, "Sliding bifurcations: a novel mechanism for the sudden onset of chaos in dry friction oscillators," *International Journal of Bifurcation and Chaos*, vol. 13, no. 10, pp. 2935–2948, 2003.

[32] D. J. W. Simpson, "A compendium of Hopf-like bifurcations in piecewise-smooth dynamical systems," *Physics Letters A*, vol. 382, no. 35, pp. 2439–2444, 2018.

[33] L. Dieci and L. Lopez, "Sliding motion in Filippov differential systems: theoretical results and a computational approach," *SIAM Journal on Numerical Analysis*, vol. 47, no. 3, pp. 2023–2051, 2009.

[34] L. Dieci and L. Lopez, "A survey of numerical methods for IVPs of ODEs with discontinuous right-hand side," *Journal of Computational and Applied Mathematics*, vol. 236, no. 16, pp. 3967–3991, 2012.

[35] D. J. W. Simpson, "On resolving singularities of piecewise-smooth discontinuous vector fields via small perturbations," *Discrete & Continuous Dynamical Systems-A*, vol. 34, no. 9, pp. 3803–3830, 2014.

[36] D. J. W. Simpson and R. Kuske, "Stochastic perturbations of periodic orbits with sliding," *Journal of Nonlinear Science*, vol. 25, no. 4, pp. 967–1014, 2015.

[37] C. Erazo, M. E. Homer, P. T. Piiroinen, and M. Di Bernardo, "Dynamic cell mapping algorithm for computing basins of attraction in planar Filippov systems," *International Journal of Bifurcation and Chaos*, vol. 27, no. 12, Article ID 1730041, 2017.

[38] E. Bossolini, M. Brns, and K. U. Kristiansen, "Canards in stiction: on solutions of a friction oscillator by regularization," *SIAM Journal on Applied Dynamical Systems*, vol. 16, no. 4, pp. 2233–2258, 2017.

[39] E. Blokhina, D. Galayko, D. Fournier-Prunaret, and O. Feely, "Sliding in a piecewise-smooth dynamical system with a hold-on effect," *Physics Letters A*, vol. 378, no. 42, pp. 3085–3092, 2014.

[40] M. Guardia, S. J. Hogan, and T. M. Seara, "An analytical approach to codimension-2 sliding bifurcations in the dry-friction oscillator," *SIAM Journal on Applied Dynamical Systems*, vol. 9, no. 3, pp. 769–798, 2010.

[41] P. Kowalczyk and P. T. Piiroinen, "Two-parameter sliding bifurcations of periodic solutions in a dry-friction oscillator," *Physica D: Nonlinear Phenomena*, vol. 237, no. 8, pp. 1053–1073, 2008.

[42] A. Pratap, "Finite-time synchronization criterion of graph theory perspective fractional-order coupled discontinuous neural networks," *Advances in Difference Equations*, vol. 2020, p. 1, 2020.

[43] A. Pratap, "Quasi-pinning synchronization and stabilization of fractional order BAM neural networks with delays and discontinuous neuron activations," *Chaos, Solitons and Fractals*, vol. 131, 2020.

[44] A. Pratap, R. Raja, J. Cao, C. P. Lim, and O. Bagdasar, "Stability and pinning synchronization analysis of fractional order delayed Cohen-Grossberg neural networks with discontinuous activations," *Applied Mathematics and Computation*, vol. 359, pp. 241–260, 2019.

[45] X. Yang, Q. Song, J. Liang, and B. He, "Finite-time synchronization of coupled discontinuous neural networks with mixed delays and nonidentical perturbations," *Journal of the Franklin Institute*, vol. 352, no. 10, pp. 4382–4406, 2015.

[46] M. Forti and P. Nistri, "Global convergence of neural networks with discontinuous neuron activations," *IEEE Transactions on Circuits and Systems I: Fundamental Theory and Applications*, vol. 50, no. 11, pp. 1421–1435, 2003.

[47] C. Chen, "Finite-time Mittag-Leffler synchronization of fractional-order delayed memristive neural networks with parameters uncertainty and discontinuous activation functions," *Chinese Physics B*, vol. 29, p. 4, 2020.

[48] S. Liu, Y. Yu, S. Zhang, and Y. Zhang, "Robust stability of fractional-order memristor-based Hopfield neural networks with parameter disturbances," *Physica A: Statistical Mechanics and Its Applications*, vol. 9, pp. 845–854, 2018.

[49] A. Abdurahman, H. Jiang, and C. Hu, "General decay synchronization of memristor-based Cohen-Grossberg neural networks with mixed time-delays and discontinuous activations," *Journal of the Franklin Institute*, vol. 354, no. 15, pp. 7028–7052, 2017.

[50] Z. Cai, L. Huang, M. Zhu, and D. Wang, "Finite-time stabilization control of memristor-based neural networks," *Nonlinear Analysis: Hybrid Systems*, vol. 20, no. 37, pp. 37–54, 2016.

[51] Y. Gu, Y. Yu, and H. Wang, "Synchronization for fractional-order time-delayed memristor-based neural networks with parameter uncertainty," *Journal of the Franklin Institute*, vol. 353, no. 15, pp. 3657–3684, 2016.

[52] H. Bao, J. H. Park, and J. Cao, "Matrix measure strategies for exponential synchronization and anti-synchronization of memristor-based neural networks with time-varying delays," *Applied Mathematics and Computation*, vol. 270, pp. 543–556, 2015.

[53] H. Wu, R. Li, S. Ding, X. Zhang, and R. Yao, "Complete periodic adaptive antisynchronization of memristor-based neural networks with mixed time-varying delays," *Canadian Journal of Physics*, vol. 92, no. 11, pp. 1337–1349, 2014.

[54] Z. Cai and L. Huang, "Lyapunov-Krasovskii stability analysis of delayed Filippov system: applications to neural networks with switching control," *International Journal of Robust and Nonlinear Control*, vol. 30, no. 2, pp. 699–718, 2020.

[55] Z. Cai, L. Huang, and L. Zhang, "Improved switching controllers for finite-time synchronization of delayed neural networks with discontinuous activations," *Journal of the Franklin Institute*, vol. 354, no. 15, pp. 6692–6723, 2017.

[56] Z. Cai, L. Huang, D. Wang, and L. Zhang, "Periodic synchronization in delayed memristive neural networks based on Filippov systems," *Journal of the Franklin Institute*, vol. 352, no. 10, pp. 4638–4663, 2015.

[57] H. Wu, "Robust almost periodic dynamics for interval neural networks with mixed time-varying delays and discontinuous activation functions," *Abstract and Applied Analysis*, vol. 2013, Article ID 630623, 13 pages, 2013.

[58] J. A. Taborda, F. Angulo, and G. Olivar, "Bifurcation analysis on nonsmooth torus destruction scenario of delayed-pwm switched buck converter," *International Journal of Bifurcation and Chaos*, vol. 19, no. 7, pp. 2193–2212, 2009.

[59] A. Jorge, G. Olivar, and F. Angulo, "Smooth and Filippov models of sustainable development: bifurcations and numerical computations," *Differential Equations and Dynamical Systems*, vol. 21, pp. 173–184, 2013.

[60] O. Valencia-Rodríguez, G. Olivar-Tost, and J. M. Redondo, "Modeling a productive system incorporating elements of business sustainability," *Dyna*, vol. 85, no. 207, pp. 113–122, 2018.

[61] J. Valencia-Calvo, G. Olivar-Tost, J. D. Morcillo-Bastidas, C. J. Franco-Cardona, and I. Dyner, "Non-smooth dynamics in energy market models: a complex approximation from system dynamics and dynamical systems approach," *IEEE Access*, vol. 8, pp. 128877–128896, 2020.

[62] J. M. Redondo, "Making decisions in national energy markets with bifurcation analysis," in *Journal of Physics: Conference Series*Institute of Physics Publishing, Bristol, UK, 2019.

[63] J. M. Redondo, "Modeling for the regional integration of electricity markets," *Energy for Sustainable Development*, vol. 43, pp. 100–113, 2018.

[64] J. Valencia-Calvo, C. J. Franco-Cardona, G. Olivar-Tost, and I. Dyner-Rezonzew, "Enfoque metodológico para el estudio y representación de comportamientos complejos en mercados de electricidad," *Ingeniería y Ciencia*, vol. 12, no. 24, pp. 195–220, 2016.

[65] C. Chen, C. Li, and Y. Kang, "Modelling the effects of cutting off infected branches and replanting on fire-blight transmission using Filippov systems," *Journal of Theoretical Biology*, vol. 439, pp. 127–140, 2018.

[66] G. Tang, W. Qin, and S. Tang, "Complex dynamics and switching transients in periodically forced Filippov prey-predator system," *Chaos, Solitons & Fractals*, vol. 61, pp. 13–23, 2014.

[67] S. Tang, J. Liang, Y. Xiao, and R. A. Cheke, "Sliding bifurcations of Filippov two stage pest control models with economic thresholds," *SIAM Journal on Applied Mathematics*, vol. 72, no. 4, pp. 1061–1080, 2012.

[68] B. Tang, Y. Xiao, R. A. Cheke, and N. Wang, "Piecewise virus-immune dynamic model with HIV-1 RNA-guided therapy," *Journal of Theoretical Biology*, vol. 377, pp. 36–46, 2015.

[69] B. Tang, Y. Xiao, S. Sivaloganathan, and J. Wu, "A piecewise model of virus-immune system with effector cell-guided therapy," *Applied Mathematical Modelling*, vol. 47, pp. 227–248, 2017.

[70] F. Dercole, A. Gragnani, and S. Rinaldi, "Bifurcation analysis of piecewise smooth ecological models," *Theoretical Population Biology*, vol. 72, no. 2, pp. 197–213, 2007.

[71] X. Yang, Z. Yang, and X. Nie, "Exponential synchronization of discontinuous chaotic systems via delayed impulsive control and its application to secure communication," *Communications in Nonlinear Science and Numerical Simulation*, vol. 19, no. 5, pp. 1529–1543, 2014.

[72] J. Amador-Moncada, "Dinámicas no-lineales y no-suaves en procesos estrés-enfermedad/nonlinear and nonsmooth dynamics in stress-sickness processes," *Ciencia en Desarrollo*, vol. 8, no. 1, pp. 9–19, 2017.

[73] F. Dercole and Y. A. Kuznetsov, "SlideCont: an auto 97 driver for bifurcation analysis of Filippov systems," *ACM Transactions on Mathematical Software*, vol. 1, no. 1, pp. 95–119, 2005.

[74] P. T. Piiroinen and Y. A. Kuznetsov, "An event-driven method to simulate Filippov systems with accurate computing of sliding motions," *ACM Transactions on Mathematical Software*, vol. 34, no. 3, 2008.

[75] P. Thota and H. Dankowicz, "TC-HAT (widehat): a novel toolbox for the continuation of periodic trajectories in hybrid dynamical systems," *SIAM Journal on Applied Dynamical Systems*, vol. 7, no. 4, pp. 1283–1322, 2008.

[76] G. Formica, "Coupling FEM with parameter continuation for analysis of bifurcations of periodic responses in nonlinear structures," *Journal of Computational and Nonlinear Dynamics*, vol. 8, no. 2, 2013.

[77] H. Dankowicz, *Multibody Mechanics and Visualization*, Springer Science & Business Media, Berlin, Germany, 2005.

[78] J. Brander and M. Scott Taylor, "The simple economics of Easter island: a Ricardo-Malthus model of renewable resource use," *American Economic Review*, vol. 88, no. 1, pp. 119–138, 1998.

[79] R. Reuveny and C. S. Decker, "Easter island: historical anecdote or warning for the future?" *Ecological Economics*, vol. 35, no. 2, pp. 271–287, 2000.

[80] S. D'Alessandro, "Non-linear dynamics of population and natural resources: the emergence of different patterns of development," *Ecological Economics*, vol. 62, no. 3, pp. 473–481, 2007.

[81] T. R. Dalton and R. Morris Coats, "Could institutional reform have saved Easter island?" *Journal of Evolutionary Economics*, vol. 10, no. 5, pp. 489–505, 2000.

[82] T. R. Dalton, R. M. Coats, and B. R. Asrabadi, "Renewable resources, property-rights regimes and endogenous growth," *Ecological Economics*, vol. 52, no. 1, pp. 31–41, 2005.

[83] J. C. V. Pezzey and J. M. Anderies, "The effect of subsistence on collapse and institutional adaptation in population-resource societies," *Journal of Development Economics*, vol. 72, no. 1, pp. 299–320, 2003.

[84] J. M. Anderies and M. Hegmon, "Robustness and resilience across scales: migration and resource degradation in the prehistoric U.S. southwest," *Ecology and Society*, vol. 16, no. 2, pp. 1708–3087, 2011.

[85] S. Roman, S. Bullock, and M. Brede, "Coupled societies are more robust against collapse: a hypothetical look at Easter island," *Ecological Economics*, vol. 132, pp. 264–278, 2017.

[86] D. Angulo, F. Angulo, and G. Olivar, "Dynamics and forecast in a simple model of sustainable development for rural

populations," *Bulletin of Mathematical Biology*, vol. 77, no. 2, pp. 368–389, 2015.

[87] Z. Dockstader, C. T. Bauch, and M. Anand, "Interconnections accelerate collapse in a socio-ecological metapopulation," *Sustainability*, vol. 11, pp. 2071–1050, 2019.

[88] M. B. Eppinga, K. Siteur, M. Baudena et al., "Long-term transients help explain regime shifts in consumer-renewable resource systems," *Communications Earth & Environment*, vol. 2, no. 1, 2021.

[89] Y. A. Kuznetsov, *Elements of Applied Bifurcation Theory*, Vol. 112, Springer Science & Business Media, Berlin, Germany, 2013.

[90] A. Dhooge, W. Govaerts, and Y. A. Kuznetsov, "Matcont," *ACM Transactions on Mathematical Software*, vol. 29, no. 2, pp. 141–164, 2003.

[91] J. C. Alexander and I. S. Thomas, "Sliding modes in intersecting switching surfaces, I: blending," *Houston Journal of Mathematics*, vol. 24, no. 3, pp. 545–569, 1998.

[92] L. Dieci and F. Difonzo, "The moments sliding vector field on the intersection of two manifolds," *Journal of Dynamics and Differential Equations*, vol. 29, no. 1, pp. 169–201, 2017.

[93] M. R. Jeffrey, "Hidden dynamics in models of discontinuity and switching," *Physica D: Nonlinear Phenomena*, vol. 273-274, pp. 34–45, 2014.

Hindawi
Complexity
Volume 2021, Article ID 5559913, 24 pages
https://doi.org/10.1155/2021/5559913

Research Article

Emergence of Hidden Attractors through the Rupture of Heteroclinic-Like Orbits of Switched Systems with Self-Excited Attractors

R. J. Escalante-González[1] **and Eric Campos**[2]

[1]*Electrical, Electronic and Mechatronics Department, Technological Institute of San Luis Potosí, Tecnológico Avenue, Soledad de Graciano Sánchez, San Luis Potosí 78437, Mexico*
[2]*División de Control y Sistemas Dinámicos, Instituto Potosino de Investigación Científica y Tecnológica (IPICYT), Camino a La Presa San José 2055, Lomas 4 Sección 78216, San Luis Potosí, S.L.P., Mexico*

Correspondence should be addressed to R. J. Escalante-González; rodolfo.escalante@outlook.com

Received 10 February 2021; Revised 6 July 2021; Accepted 15 August 2021; Published 6 September 2021

Academic Editor: Xianggui Guo

This work is dedicated to the study of an approach that allows the generation of hidden attractors based on a class of piecewise-linear (PWL) systems. The systems produced with the approach present the coexistence of self-excited attractors and hidden attractors such that hidden attractors surround the self-excited attractors. The first part of the approach consists of the generation of self-excited attractors based on pairs of equilibria with heteroclinic orbits. Then, additional equilibria are added to the system to obtain a bistable system with a second self-excited attractor with the same characteristics. It is conjectured that a necessary condition for the existence of the hidden attractor in this class of systems is the rupture of the trajectories that resemble heteroclinic orbits that join the two regions of space that surround the pairs of equilibria; these regions resemble equilibria when seen on a larger scale. With the appearance of a hidden attractor, the system presents a multistable behavior with hidden and self-excited attractors.

1. Introduction

There are two classes of attractors according to [1], which are defined as follows: the first class is given by those classical attractors excited from unstable equilibria called self-excited attractors whose basin of attraction intersects at least a neighborhood of an equilibrium point [2], and they are not difficult to find via numerical methods, and the second class is called hidden attractors whose basin of attraction does not contain neighborhoods of equilibria. The localization of this last class represents a more difficult task which has led to interesting approaches as the analytical-numerical algorithm suggested in [1] for the localization of hidden attractors of Chua's circuit.

Definition 1 (see [2])."An attractor is called a self-excited attractor if its basin of attraction intersects with any open neighborhood of an unstable fixed point. Otherwise, it is called a hidden attractor."

A hidden attractor is commonly observed in systems without equilibria or systems with a stable equilibrium point. Therefore, these classes of systems could serve as a starting point in the search for hidden attractors. However, according to the definition, a hidden attractor could be found in a system with any type and number of equilibria as well as any kind of attractors. Multistability is usually related to the existence of more than one attractor. Different scenarios of multistability are reported in [3].

Arnold Sommerfeld worked with one of the first dynamical systems with oscillating behavior but no equilibria [4]. In 1994, a conservative system without equilibria that presents a chaotic flow was reported in [5]. This system, known as Sprott case A, presents two quadratic nonlinearities, and it is a particular case of the Nose-Hoover system [6]. After this work, several three-dimensional systems without equilibria with chaotic attractors have been reported, like the one in [7] with two quadratic nonlinearities based on the Sprott system case *D*, the one in [8] with three quadratic nonlinearities, or the piecewise-linear system reported in [9]. In [10], three methods are used to produce seventeen three-dimensional systems without equilibria with chaotic flows, which present only quadratic nonlinearities.

Four-dimensional systems without equilibria with chaotic or hyperchaotic attractors have also been reported. For instance, systems with quadratic and cubic nonlinearities with hyperchaotic attractors are reported in [11, 12]. The first piecewise-linear system without equilibria that exhibits a hyperchaotic attractor is reported in [13]. It is the result of the approximation made to the quadratic nonlinearities of an extended diffusionless Lorenz system. In [14], a four-dimensional system without equilibria with chaotic multiwing butterfly attractors is presented.

Since the double-scroll attractor in Chua's circuit, there exists an interest to generate double-scroll and multiscroll attractors. In circuits based on Chua's circuit, the implementation of piecewise-linear resistors with multiple segments is not an easy task due to their irregular breakpoints and slopes. Some approaches for self-excited scroll attractors have been reported in [15–19]. Recently, in [20], an approach for the generation of multiscroll hidden attractors with any number of scrolls in a system without equilibria was introduced. In [21], two systems with multiscroll hidden attractors are constructed by introducing nonlinear functions into Sprott system case A. In [22], a no-equilibrium system with a multiscroll hidden chaotic sea is introduced. In [23], a memristive system with chaotic attractors is presented. The multiscroll hidden attractors and multiwing hidden attractors exhibited by the system are sensitive to the transient simulation.

In [24], the widening of the basins of attraction of a class of piecewise-linear systems is studied. Also, a system with a double-scroll hidden attractor along with two double-scroll self-excited attractors is introduced. Based on this result, it is natural to think about the possibility of generating hidden attractors via multistable systems with double-scroll self-excited attractors.

An approach that allows the generation of hidden attractors based on a kind of piecewise-linear (PWL) system is studied in this work. The study reveals a relationship between the emergence of a hidden attractor and the existence of trajectories that, when are seen on a larger scale, resemble heteroclinic orbits joining the self-excited attractors.

The study performed in this work suggests that some classes of systems with a multistable behavior could be designed geometrically to exhibit hidden and self-excited attractors. Chaotic scroll attractors have been widely studied and have been found useful in the design of pseudorandom number generation [25]. It has been demonstrated that the number of scrolls on some classes of systems affects the properties of the generated sequences determining if they fulfill the statistical test of the NIST and affecting the stream ciphering of images [26]. Some chaotic systems can be restored by reconstructing the attractor, which is not desirable in an encryption algorithm since it would reduce the security [27]. In a hidden scroll attractor, the restoration of the system is harder [27]. Thus, the class of systems discussed in this work could lead to the development of new cryptographic algorithms with more complex multistable systems with self-excited and hidden scroll attractors.

The structure of the article is as follows: In Section 2, a class of piecewise-linear systems with double-scroll self-excited chaotic attractors is introduced. In Section 3, additional equilibria are considered to generate two self-excited attractors. In Section 4, the transitory behavior of the trajectories surrounding the self-excited attractors of the system is studied. In Section 5, the relation between the emergence of a hidden attractor and the existence of trajectories that, when are seen on a larger scale, resemble heteroclinic orbits joining the self-excited attractors is discussed. Finally, conclusions are given in Section 6.

2. Heteroclinic Chaos

To introduce the approach, let us first consider a partition P of the metric space $X \subset \mathbb{R}^3$, endowed with the Euclidean metric d. Let $P = \{P_1, \ldots, P_\eta\}$ $(\eta > 1)$ be a finite partition of X, that is, $X = \cup_{1 \le i \le \eta} P_i$, and $P_i \cap P_j = \varnothing$ for $i \neq j$. Each element of the set P is called an atom and each atom contains a saddle equilibrium point. Due to these atoms, P_i have a saddle equilibrium point, then within each atom there is a stable manifold and also an unstable manifold. These stable manifolds W^s and unstable manifolds W^u are necessary for the mechanism of expansion and contraction present in chaotic dynamics.

Let $T\colon X \longrightarrow X$, with $X \subset \mathbb{R}^3$, be a piecewise-linear dynamical system whose dynamics is given by a family of subsystems of the form

$$\dot{x} = A\mathbf{x} + f(\mathbf{x})B, \tag{1}$$

where $\mathbf{x} = (x_1, x_2, x_3)^T \in \mathbb{R}^3$ is the state vector, and $A = \{\alpha_{ij}\} \in \mathbb{R}^{3\times 3}$ is a linear operator, $B = (\beta_1, \beta_2, \beta_3)^T$ is a constant vector, and f is a functional. The vector $f(\mathbf{x})B$ is a constant vector in each atom P_i such that the equilibria are given by $\mathbf{x}^*_{\mathrm{eq}_i} = (x^*_{1_{\mathrm{eq}_i}}, x^*_{2_{\mathrm{eq}_i}}, x^*_{3_{\mathrm{eq}_i}})^T = -f(\mathbf{x})A^{-1}B \in P_i$, with $i = 1, \ldots, \eta$.

Oscillations of the flow around the equilibria $\mathbf{x}^*_{\mathrm{eq}_i}$ are desired. Let us assign a negative real eigenvalue $\lambda_1 = c$ to the complexification of the operator $A(A_{\mathbb{C}})$ with the corresponding eigenvector v_1, and a pair of complex conjugate eigenvalues with positive real part $\lambda_2 = a + ib$ and $\lambda_3 = a - ib$ with the corresponding eigenvectors v_2 and v_3. Additionally, we restrict $b/a \ge 10$. Thus the stable and unstable manifolds are given by $W^s_{\mathbf{x}^*_{\mathrm{eq}_i}} = \{\mathbf{x} + \mathbf{x}^*_{\mathrm{eq}_i} \colon \mathbf{x} \in \mathrm{span}\{v_1\}\}$ and $W^u_{\mathbf{x}^*_{\mathrm{eq}_i}} =$

$\{\mathbf{x} + \mathbf{x}^*_{\text{eq}_i} : \mathbf{x} \in \text{span}\{v_2, v_3\}\}$, where v_1, v_2 and v_3 are given as follows:

$$v_1 = \begin{pmatrix} 1 \\ 0 \\ \frac{1}{2} \end{pmatrix}, \quad v_2 = \begin{pmatrix} 0 \\ -1 \\ 0 \end{pmatrix}, \quad v_3 = \begin{pmatrix} -1 \\ 0 \\ 1 \end{pmatrix}. \tag{2}$$

The matrix of the linear operator A is defined as follows:

$$A = \begin{pmatrix} \frac{a}{3} + \frac{2c}{3} & b & \frac{2c}{3} - \frac{2a}{3} \\ -\frac{b}{3} & a & \frac{2b}{3} \\ \frac{c}{3} - \frac{a}{3} & -b & \frac{2a}{3} + \frac{c}{3} \end{pmatrix}. \tag{3}$$

In this work, we denote the local stable and unstable manifolds of an equilibrium point $\mathbf{x}^*_{\text{eq}}$ as $W^s_{\mathbf{x}^*_{\text{eq}}}$ and $W^u_{\mathbf{x}^*_{\text{eq}}}$, respectively, and they are responsible for connecting the equilibria of a dynamical system. Recall that a heteroclinic orbit is a path that joins two equilibrium points in the phase space. Similarly, a homoclinic orbit is a path that starts and ends at the same equilibrium point.

We also denoted the closure of a set P_i as $\text{cl}(P_i)$. Thus, for each pair of atoms P_i and P_j, $i \neq j$, if $\text{cl}(P_i) \cap \text{cl}(P_j) \neq \emptyset$, then these atoms are adjacent and the switching surface between them is given by the intersection, i.e., $SW_{ij} = \text{cl}(P_i) \cap \text{cl}(P_j)$.

Each SW_{ij} has associated an equation of the form $\widehat{A}x_1 + \widehat{B}x_2 + \widehat{C}x_3 + D = \mathbf{N}_{12} \cdot \mathbf{x}^T + D = 0$, with $\widehat{A} > 0$ where $\mathbf{N}_{12} = (\widehat{A}, \widehat{B}, \widehat{C})$ is the normal vector. Then the atoms P_i, $i = 1, 2$ are defined as follows:

$$\begin{aligned} P_1 &= \{\mathbf{x} \in \mathbb{R}^3 : x_3 > 0, \mathbf{N}_{12} \cdot \mathbf{x}^T \leq -D\} \\ &\cup \{\mathbf{x} \in \mathbb{R}^3 : x_3 \leq 0, \mathbf{N}_{12} \cdot \mathbf{x}^T < -D\}, \\ P_2 &= \{\mathbf{x} \in \mathbb{R}^3 : x_3 > 0, \mathbf{N}_{12} \cdot \mathbf{x}^T > -D\} \\ &\cup \{\mathbf{x} \in \mathbb{R}^3 : x_3 \leq 0, \mathbf{N}_{12} \cdot \mathbf{x}^T \geq -D\}. \end{aligned} \tag{4}$$

Remark 1. The divergence of the PWL system (1) considering the linear operator A given by (3) is $\nabla = 2a + c$, so the system is dissipative in each atom of the partition P if $2a < |c|$.

With the atoms of a P partition containing a saddle equilibrium point in each of them as defined above, it is possible to generate heteroclinic orbits. To generate a heteroclinic orbit, at least two equilibria are required. Therefore, consider a partition with two atoms $P = \{P_1, P_2\}$, the constant vector $B \in \mathbb{R}^3$ is defined as follows:

$$B = \begin{pmatrix} -\frac{a}{3} - \frac{2c}{3} \\ \frac{b}{3} \\ \frac{a}{3} - \frac{c}{3} \end{pmatrix}, \tag{5}$$

and the functional f is given by

$$f(\mathbf{x}) = \begin{cases} -\alpha, & \mathbf{x} \in P_1, \\ \alpha, & \mathbf{x} \in P_2, \end{cases} \tag{6}$$

with $\alpha > 0$. So the equilibria are at $\mathbf{x}^*_{\text{eq}_1} = (-\alpha, 0, 0)^T \in P_1$ and $\mathbf{x}^*_{\text{eq}_2} = (\alpha, 0, 0)^T \in P_2$, and the stable and the unstable manifolds are given by

$$\begin{aligned} W^s_{\mathbf{x}^*_{\text{eq}_1}} &= \{\mathbf{x} \in \mathbb{R}^3 : \mid x_1 + \alpha = 2x_3, x_2 = 0\}, \\ W^u_{\mathbf{x}^*_{\text{eq}_1}} &= \{\mathbf{x} \in \mathbb{R}^3 : \mid x_1 + x_3 = -\alpha\}, \\ W^s_{\mathbf{x}^*_{\text{eq}_2}} &= \{\mathbf{x} \in \mathbb{R}^3 : \mid x_1 - \alpha = 2x_3, x_2 = 0\}, \\ W^u_{\mathbf{x}^*_{\text{eq}_2}} &= \{\mathbf{x} \in \mathbb{R}^3 : \mid x_1 + x_3 = \alpha\}. \end{aligned} \tag{7}$$

Proposition 1 (see [28, 29]). *"The hyperbolic system given by (1), (3), (5), and (6) generates a pair of heteroclinic orbits if the switching surface between the atoms P_1 and P_2 is given by the plane $SW_{12} = \{\mathbf{x} \in \mathbb{R}^3 : 2x_1 - x_3 = 0\}$."*

The points where the stable and unstable manifolds intersect at SW are given by

$$\begin{aligned} \mathbf{x}_{in_1} &= \text{cl}\left(W^s_{\mathbf{x}^*_{\text{eq}_1}}\right) \cap \text{cl}\left(W^u_{\mathbf{x}^*_{\text{eq}_2}}\right) = \left(\frac{\alpha}{3}, 0, \frac{2\alpha}{3}\right)^T, \\ \mathbf{x}_{in_2} &= \text{cl}\left(W^s_{\mathbf{x}^*_{\text{eq}_2}}\right) \cap \text{cl}\left(W^u_{\mathbf{x}^*_{\text{eq}_1}}\right) = \left(-\frac{\alpha}{3}, 0, -\frac{2\alpha}{3}\right)^T. \end{aligned} \tag{8}$$

These points $\mathbf{x}_{\text{in}_1}$ and $\mathbf{x}_{\text{in}_2}$ belong to SW_{12} and $\mathbf{x}_{\text{in}_1} \in P_1$ and $\mathbf{x}_{\text{in}_2} = P_2$. Because these points $\mathbf{x}_{\text{in}_1}$ and $\mathbf{x}_{\text{in}_2}$ belong to the stable manifolds $W^s_{\mathbf{x}^*_{\text{eq}_1}}$ and $W^s_{\mathbf{x}^*_{\text{eq}_2}}$, respectively, they are points whose trajectories remain in atoms P_1 and P_2, respectively. Thus, the heteroclinic orbits are defined as follows:

$$\begin{aligned} \text{HO}_1 &= \{\mathbf{x} \in \varphi(\mathbf{x}_{in_1}, t) : t \in (-\infty, \infty)\}, \\ \text{HO}_2 &= \{\mathbf{x} \in \varphi(\mathbf{x}_{in_2}, t) : t \in (-\infty, \infty)\}. \end{aligned} \tag{9}$$

For the system given by (1), (3), (5), and (6), it is possible to find several points $\mathbf{x}_0 \in \mathrm{HO}_i$ such that $|\mathbf{x}_{\mathrm{eq}_i} - \mathbf{x}_0| < \varepsilon$ with ε arbitrarily small and $i = 1, 2$. Thus, one can find initial conditions for the simulation of the heteroclinic orbits as close to the equilibria as desired. One example of the initial condition formula for P_1 is as follows:

$$\mathbf{x}_0^1 = \begin{pmatrix} \frac{2}{3}\alpha e^{-(2ka\pi/b)} - \alpha \\ 0 \\ -\frac{2}{3}\alpha e^{-(2ka\pi/b)} \end{pmatrix}, \tag{10}$$

and for P_2

$$\mathbf{x}_0^2 = \begin{pmatrix} -\frac{2}{3}\alpha e^{-(2ka\pi/b)} + \alpha \\ 0 \\ \frac{2}{3}\alpha e^{-(2ka\pi/b)} \end{pmatrix}, \tag{11}$$

with $k \in \mathbb{Z}^+$.

Example 1. Consider the system (1), (3), (5), and (6) with $\mathrm{SW}_{12} = \{\mathbf{x} \in \mathbb{R}^3 \colon 2x_1 - x_3 = 0\}$ and the parameters $a = 0.2, b = 5, c = -3, \alpha = 1$.

The above-defined system fulfills Proposition 1, so it presents a heteroclinic orbit. From (10) and (11), two initial conditions,

$$\begin{aligned} \mathbf{x}_{01} &= (-0.9999976751050959, 0, -2.3248949041393315e-6)^T, \\ \mathbf{x}_{02} &= (0.9999976751050959, 0, 2.3248949041393315e-6)^T, \end{aligned} \tag{12}$$

are chosen with $k = 50$ to simulate the two heteroclinic orbits shown in Figure 1(a). A double-scroll attractor with heteroclinic chaos is generated, and it is shown in Figure 1(a) for the initial condition $\mathbf{x}_0 = (0, 0, 0)^T$.

The unstable manifolds $W^u_{\mathbf{x}^*_{\mathrm{eq}_1}} = \{\mathbf{x} \in \mathbb{R}^3 \colon x_1 + x_3 + 1 = 0\}$ and $W^u_{\mathbf{x}^*_{\mathrm{eq}_2}} = \{\mathbf{x} \in \mathbb{R}^3 \colon x_1 + x_3 - 1 = 0\}$ and the stable manifolds $W^s_{\mathbf{x}^*_{\mathrm{eq}_1}} = \{\mathbf{x} \in \mathbb{R}^3 \colon (x_1 + 1)/2 = x_3; x_2 = 0\}$ and $W^s_{\mathbf{x}^*_{\mathrm{eq}_2}} = \{\mathbf{x} \in \mathbb{R}^3 \colon (x_1 - 1)/2 = x_3; x_2 = 0\}$. The intersection points are given by $\mathrm{cl}(W^s_{\mathbf{x}^*_{\mathrm{eq}_2}}) \cap \mathrm{cl}(W^u_{\mathbf{x}^*_{\mathrm{eq}_1}}) = (-(1/3), 0, -(2/3))^T$, $\mathrm{cl}(W^s_{\mathbf{x}^*_{\mathrm{eq}_1}}) \cap \mathrm{cl}(W^u_{\mathbf{x}^*_{\mathrm{eq}_2}}) = ((1/3), 0, (2/3))^T$.

Proposition 2 (see [29]). *"If the partition P contains more than two atoms $\{P_1, P_2, \ldots, P_k\}$, with $2 < k \in \mathbb{Z}^+$, and each atom is a hyperbolic set defined as above. Furthermore, the atoms by pairs P_i and P_{i+1} fulfill Proposition 1. Then, the system generates $2(k-1)$ heteroclinic orbits."*

Proof. A direct consequence of Proposition 1. □

3. Emergence of Multiscroll Attractors through Multiple Heteroclinic Orbits

According to the Proposition 2, it is possible to generate multiscroll attractors based on multiple heteroclinic orbits. So in this Section, we consider more than two hyperbolic sets in the partition with the aim of studying the existence of heterocyclic cycles and the attractors exhibited by the system when varying the location of the equilibria.

Consider the partition $P = \{P_1, P_2, P_3, P_4\}$ along with the piecewise-linear dynamical system (1), with A and B given by (3) and (5), respectively. Thus the function $f(\mathbf{x})$ is defined in the four atoms as follows:

$$f(\mathbf{x}) = \begin{cases} -\alpha - \gamma, & \mathbf{x} \in P_1, \\ \alpha - \gamma, & \mathbf{x} \in P_2, \\ -\alpha + \gamma, & \mathbf{x} \in P_3, \\ \alpha + \gamma, & \mathbf{x} \in P_4, \end{cases} \tag{13}$$

where $\alpha, \gamma > 0$. The equilibria are at

$$\begin{aligned} \mathbf{x}^*_{\mathrm{eq}_1} &= \begin{bmatrix} -(\gamma + \alpha) \\ 0 \\ 0 \end{bmatrix}, \\ \mathbf{x}^*_{\mathrm{eq}_2} &= \begin{bmatrix} -(\gamma - \alpha) \\ 0 \\ 0 \end{bmatrix}, \\ \mathbf{x}^*_{\mathrm{eq}_3} &= \begin{bmatrix} (\gamma - \alpha) \\ 0 \\ 0 \end{bmatrix}, \\ \mathbf{x}^*_{\mathrm{eq}_4} &= \begin{bmatrix} (\gamma + \alpha) \\ 0 \\ 0 \end{bmatrix}, \end{aligned} \tag{14}$$

so $\mathbf{x}^*_{\mathrm{eq}_1} \in P_1$, $\mathbf{x}^*_{\mathrm{eq}_2} \in P_2$, $\mathbf{x}^*_{\mathrm{eq}_3} \in P_3$ and $\mathbf{x}^*_{\mathrm{eq}_4} \in P_4$. The location of the equilibria according to the parameters $0 < \alpha$ and $0 < \gamma$ is as follows:

(i) The equilibria are on the x_1 axis and for $\alpha = \gamma$ the system only have three equilibria. Otherwise, it has four equilibria.

(ii) For $\alpha < \gamma$ the distance of the equilibria $\mathbf{x}^*_{\mathrm{eq}_1}$ and $\mathbf{x}^*_{\mathrm{eq}_4}$ to the origin $O = (0, 0, 0)^T$ are the same $d(\mathbf{x}^*_{\mathrm{eq}_1}, O) = d(\mathbf{x}^*_{\mathrm{eq}_4}, O)$ and also for $d(\mathbf{x}^*_{\mathrm{eq}_2}, O) = d(\mathbf{x}^*_{\mathrm{eq}_3}, O)$.

(iii) For $\gamma = 2\alpha$, all equilibria are at the same distance $d(\mathbf{x}^*_{\mathrm{eq}_1}, \mathbf{x}^*_{\mathrm{eq}_2}) = d(\mathbf{x}^*_{\mathrm{eq}_2}, \mathbf{x}^*_{\mathrm{eq}_3}) = d(\mathbf{x}^*_{\mathrm{eq}_3}, \mathbf{x}^*_{\mathrm{eq}_4}) = 2\alpha$.

(iv) The other case is when $\gamma \neq 2\alpha$, and $d(\mathbf{x}^*_{\mathrm{eq}_1}, \mathbf{x}^*_{\mathrm{eq}_2}) = d(\mathbf{x}^*_{\mathrm{eq}_3}, \mathbf{x}^*_{\mathrm{eq}_4}) = 2\alpha$, but $d(\mathbf{x}^*_{\mathrm{eq}_2}, \mathbf{x}^*_{\mathrm{eq}_3}) \neq 2\alpha$.

In this section, we are especially interested in the case of $\gamma \neq 2\alpha$ such that $\gamma > \alpha$ with switching surfaces given by

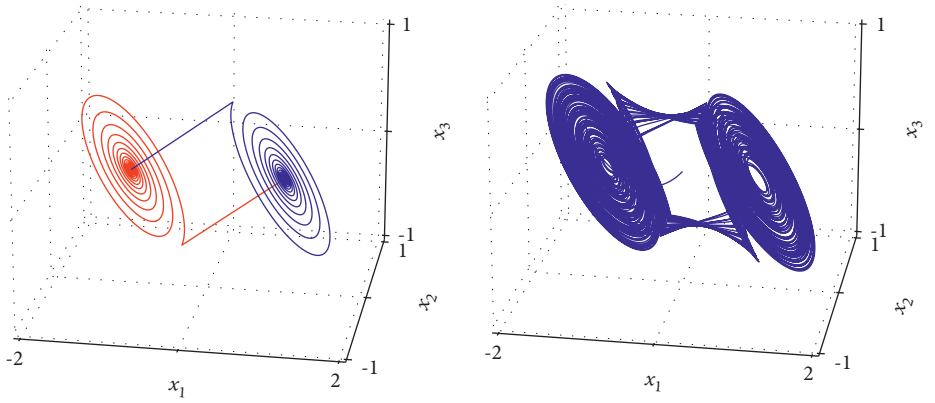

FIGURE 1: In (a) the heteroclinic loop of the system (1), (3), (5), and (6) with the switching surface $\{x \in \mathbb{R}^3 : 2x_1 - x_3 = 0\}$, the parameters $a = 0.2, b = 5, c = -3, \alpha = 1$, and the initial conditions $\mathbf{x}_{01} = (-0.9999976751050959, 0, -2.3248949041393315e-6)^T$ (red) and $\mathbf{x}_{02} = (0.9999976751050959, 0, 2.3248949041393315e-6)^T$ (blue), and in (b) a double-scroll attractor that emerges from a heteroclinic orbit using the following initial condition $\mathbf{x}_0 = (0, 0, 0)^T$ and the same parameters.

$$\begin{aligned} SW_{12} &= \mathrm{cl}(P_1) \cap \mathrm{cl}(P_2) = \{\mathbf{x} \in \mathbb{R}^3 : 2x_1 - x_3 = -2\gamma\}, \\ SW_{23} &= \mathrm{cl}(P_2) \cap \mathrm{cl}(P_3) = \{\mathbf{x} \in \mathbb{R}^3 : 2x_1 - x_3 = 0\}, \\ SW_{34} &= \mathrm{cl}(P_3) \cap \mathrm{cl}(P_4) = \{\mathbf{x} \in \mathbb{R}^3 : 2x_1 - x_3 = 2\gamma\}, \end{aligned} \tag{15}$$

which fulfill that

$$\begin{aligned} \mathrm{SW}_{i(i+1)} \cap \{\mathbf{x} \in \mathbb{R}^3 : x_3 > 0\} &\in P_i, \\ \mathrm{SW}_{i(i+1)} \cap \{\mathbf{x} \in \mathbb{R}^3 : x_3 \leq 0\} &\in P_{i+1}. \end{aligned} \tag{16}$$

This way of defining the switching surfaces provokes that the intersections between them and the stable manifolds contain a point, and the intersections between them and the unstable manifolds are the empty set, i.e., $W^u_{\mathbf{x}^*_{\mathrm{eq}_1}} \cap \mathrm{SW}_{12} = \varnothing$ and $W^s_{\mathbf{x}^*_{\mathrm{eq}_1}} \cap \mathrm{SW}_{12} \neq \varnothing$.

Let us define two points, $pb = W^s_{\mathbf{x}^*_{\mathrm{eq}_1}} \cap SW_{12}$ and $pa = W^s_{\mathbf{x}^*_{\mathrm{eq}_3}} \cap SW_{23}$ as shown in Figure 2. Then pa and pb are given as follows:

$$\begin{aligned} pa &= \begin{pmatrix} -\dfrac{(\gamma - \alpha)}{3} \\ 0 \\ -\dfrac{2(\gamma - \alpha)}{3} \end{pmatrix}, \\ pb &= \begin{pmatrix} \dfrac{\alpha}{3} - \gamma \\ 0 \\ \dfrac{2\alpha}{3} \end{pmatrix}. \end{aligned} \tag{17}$$

The set $\mathrm{cl}(W^u_{\mathbf{x}^*_{\mathrm{eq}_2}}) \cap \mathrm{SW}_{12}$ can be written as follows:

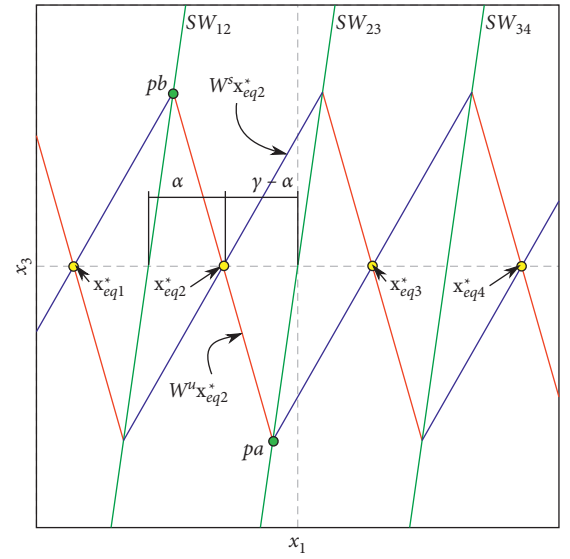

FIGURE 2: Projection of the stable and unstable manifolds and switching planes onto the $x_1 - x_3$ plane. The diagram shows the location of the unstable manifold marked with red lines, the stable manifold marked with blue lines, and switching planes marked with green lines.

$$\{\mathbf{x} \in \mathbb{R}^3 : \mathbf{x} = (0, \varepsilon, 0)^T + pb, \varepsilon \in \mathbb{R}\}, \tag{18}$$

and the set $\mathrm{cl}(W^u_{\mathbf{x}^*_{\mathrm{eq}_2}}) \cap \mathrm{SW}_{23}$ can be written as follows:

$$\{\mathbf{x} \in \mathbb{R}^3 : \mathbf{x} = (0, \varepsilon, 0)^T + pa, \varepsilon \in \mathbb{R}\}. \tag{19}$$

Consider the transformation $\mathbf{z}^{(2)} = Q^{-1}(\mathbf{x} - \mathbf{x}^*_{\mathrm{eq}_2})$, since $Q^{-1}(0, \varepsilon, 0)^T = (0, -\varepsilon, 0)^T$, so $\mathbf{z}^{(2)} = (0, \varepsilon, 0)^T + Q^{-1}(pb - \mathbf{x}^*_{\mathrm{eq}_2})$, where $Q^{-1}(pb - \mathbf{x}^*_{\mathrm{eq}_2})$ is a point on the plane $z_2^{(2)} - z_3^{(2)}$. And $\mathbf{z}^{(2)} = (0, \varepsilon, 0)^T + Q^{-1}(pa - \mathbf{x}^*_{\mathrm{eq}_2})$, where $Q^{-1}(pa - \mathbf{x}^*_{\mathrm{eq}_2})$ is also a point on the plane $z_2^{(2)} - z_3^{(2)}$. Then, the set (18) in $\mathbf{z}^{(2)}$ coordinates is given by

$$\left\{\mathbf{z}^{(2)} \in \mathbb{R}^3 \colon \mathbf{z}^{(2)} = \left(0, \varepsilon, \frac{2\alpha}{3}\right)^T, \varepsilon \in \mathbb{R}\right\}, \tag{20}$$

and the set (19) in $\mathbf{z}^{(2)}$ coordinates is given by

$$\left\{\mathbf{z}^{(2)} \in \mathbb{R}^3 \colon \mathbf{z}^{(2)} = \left(0, \varepsilon, \frac{2(\alpha-\gamma)}{3}\right)^T, \varepsilon \in \mathbb{R}\right\}. \tag{21}$$

Thus, the sets (20) and (21) are orthogonal lines to the $z_3^{(2)}$ axis. The points pa and pb in $\mathbf{z}^{(2)}$ coordinates will be denoted as follows:

$$\begin{aligned} pa_z &= \begin{pmatrix} 0 \\ 0 \\ \dfrac{2(\alpha-\gamma)}{3} \end{pmatrix}, \\ pb_z &= \begin{pmatrix} 0 \\ 0 \\ \dfrac{2\alpha}{3} \end{pmatrix}. \end{aligned} \tag{22}$$

With the uncoupled system in $\mathbf{z}^{(2)}$ coordinates, we can analyze the flow on the plane $z_2^{(2)} - z_3^{(2)}$ close to $\mathbf{z}_{\mathrm{eq}_2}^{*(2)}$.

$$\begin{aligned} \dot{z}_2^{(2)} &= a z_2^{(2)} - b z_3^{(2)}, \\ \dot{z}_3 &= b z_2^{(2)} + a z_3^{(2)}, \end{aligned} \tag{23}$$

$$r\dot{r} = z_2^{(2)} \dot{z}_2^{\ (2)} + z_3^{(2)} \dot{z}_3^{\ (2)} = a r^2, \tag{24}$$

$$\dot{r} = ar, \tag{25}$$

$$r = r_0 e^{at}. \tag{26}$$

It follows from (22) that if $\alpha = \gamma - \alpha$, then the points pa_z and pb_z are at the same distance from $\mathbf{z}_{\mathrm{eq}_2}^{*(2)} = (0,0,0)^T$. Thus, from (26), it follows that the trajectories with initial conditions pa_z and pb_z remain in P_2 for all $t < 0$.

Our case study is $\gamma - \alpha \neq \alpha$, such that $\gamma > \alpha$. Let us consider the case $\gamma - \alpha > \alpha$, and it can be seen from (22) that pb_z is closer to $\mathbf{z}_{\mathrm{eq}_2}^{(2)}$ than pa_z, this is, $d(pb_z, \mathbf{z}_{\mathrm{eq}_2}^{(2)}) < d(pa_z, \mathbf{z}_{\mathrm{eq}_2}^{(2)})$. Then, if γ is sufficiently big with respect to α, the trajectory with the initial condition pa_z will eventually reach the set given by (20) for $t < 0$; i.e., the trajectory of the initial condition $pa \in \mathrm{SW}_{23}$ reaches the switching plane SW_{12} and not the equilibrium point $\mathbf{x}_{\mathrm{eq}_2}^*$. This means that in $\mathbf{x}$ coordinates, the heteroclinic orbit from $\mathbf{x}_{\mathrm{eq}_2}^*$ to $\mathbf{x}_{\mathrm{eq}_3}^*$ does not exist. Similarly, when pb_z is further than pa_z from $\mathbf{z}_{\mathrm{eq}_2}^{*(2)}$, this is, $d(pa_z, \mathbf{z}_{\mathrm{eq}_2}^{(2)}) < d(pb_z, \mathbf{z}_{\mathrm{eq}_2}^{(2)})$, for γ sufficiently small, the trajectory with the initial condition pb_z will eventually reach the set given by (21) for $t < 0$, i.e., the trajectory of the initial condition $pb \in \mathrm{SW}_{12}$ reaches the switching plane SW_{23} and not the equilibrium point $\mathbf{x}_{\mathrm{eq}_2}^*$. This means that in $\mathbf{x}$ coordinates, the heteroclinic orbit from $\mathbf{x}_{\mathrm{eq}_2}^*$ to $\mathbf{x}_{\mathrm{eq}_1}^*$ does not exist.

The next proposition warranty the existence of heteroclinic orbits when γ belongs to an interval of real numbers where the case $\gamma - \alpha \neq \alpha$ is considered, such that $\gamma > \alpha$.

Proposition 3. *The hyperbolic system given by (1), (3), (5), and (13) with the switching surfaces given in (15) generates six heteroclinic orbits if*

$$\frac{\alpha\left(e^{-a\tau}\cos(b\tau) - 1\right)}{e^{-a\tau}\cos(b\tau)} > \gamma > \alpha\left(1 - e^{-a\tau}\cos(b\tau)\right), \tag{27}$$

where

$$\tau = \frac{\arctan(b/a) + \pi/2}{b}. \tag{28}$$

Proof. To find the values of γ for which these heteroclinic orbits exist, let us assume pa is a point of the heteroclinic orbit joining $\mathbf{x}_{\mathrm{eq}_2}^*$ and $\mathbf{x}_{\mathrm{eq}_3}^*$, i.e.,

$$\begin{aligned} \lim_{t \longrightarrow -\infty} \varphi(pa, t) &= \mathbf{x}_{\mathrm{eq}_2}^*, \\ \lim_{t \longrightarrow \infty} \varphi(pa, t) &= \mathbf{x}_{\mathrm{eq}_3}^*. \end{aligned} \tag{29}$$

Because $pa \in W^s_{\mathbf{x}^*_{\mathrm{eq}_3}}$ then $\lim_{t \longrightarrow \infty} \varphi(pa, t) = \mathbf{x}_{\mathrm{eq}_3}^*$. For the other part of the heteroclinic orbit, we analyze the system in $\mathbf{z}^{(2)}$ coordinates, we have pa_z, pb_z, $\mathbf{z}_{\mathrm{eq}_2}^{*(2)}$, and the orbit is given by $\mathbf{z}^{(2)}(t)$. We assume that $\mathbf{z}^{(2)}(0) = pa_z$, so we want that $\mathbf{z}^{(2)}(t)$ remains in P_2 for all $t < 0$. Thus, we need to find the first maximum in the component $z_3^{(2)}$ of the trajectory whose initial condition is pa_z for $t < 0$. According to (22), the third component of pa_z and pb_z are $(2(\alpha - \gamma)/3) < 0$ and $0 < (2\alpha/3)$, respectively. This maximum gives us the intersection point between the trajectory $\mathbf{z}^{(2)}(t)$ and the axis $z_3^{(2)}$. Then we can compare the third component of the trajectory $\mathbf{z}^{(2)}(t)$ and the point pb_z, in terms of α and γ to ensure that $\mathbf{z}^{(2)}(t)$ remains in P_2 for all $t < 0$.

The trajectory $\mathbf{z}^{(2)}(t)$ for the initial condition $\mathbf{z}_0^{(2)} = (z_{10}^{(2)}, z_{20}^{(2)}, z_{30}^{(2)})^T$ is as follows:

$$\begin{aligned} z_1^{(2)}(t) &= z_{10}^{(2)} e^{-ct}, \\ z_2^{(2)}(t) &= z_{20}^{(2)} e^{at}\cos(bt) - z_{30}^{(2)} e^{at}\sin(bt), \\ z_3^{(2)}(t) &= z_{20}^{(2)} e^{at}\sin(bt) + z_{30}^{(2)} e^{at}\cos(bt). \end{aligned} \tag{30}$$

This set of equations is analyzed for $t < 0$. The same analysis can be done for $0 < t$ by using the following set of equations:

$$z_1^{(2)}(t) = z_{10}^{(2)} e^{ct}, \tag{31}$$

$$z_2^{(2)}(t) = z_{20}^{(2)} e^{-at}\cos(bt) + z_{30}^{(2)} e^{-at}\sin(bt), \tag{32}$$

$$z_3^{(2)}(t) = -z_{20}^{(2)} e^{-at}\sin(bt) + z_{30}^{(2)} e^{-at}\cos(bt). \tag{33}$$

Since we are looking for the first maximum in $z_3^{(2)}(t)$ for $0 < t$.

Then from (33) with the initial condition pa_z given in (22),

$$z_3^{(2)}(t) = \frac{2(\alpha-\gamma)}{3}e^{-at}\cos(bt), \tag{34}$$

$$\dot{z}_3^{(2)}(t) = -\frac{2(\alpha-\gamma)}{3}e^{-at}(b\,\sin(bt) + a\,\cos(bt)), \tag{35}$$

$$\dot{z}_3^{(2)}(t) = -\frac{2(\alpha-\gamma)}{3}e^{-at}\left(\sqrt{a^2+b^2}\,\cos\left(bt - \arctan\left(\frac{b}{a}\right)\right)\right), \tag{36}$$

to find the maximum, we equate to zero

$$0 = -\frac{2(\alpha-\gamma)}{3}e^{-at}\left(\sqrt{a^2+b^2}\,\cos\left(bt - \arctan\left(\frac{b}{a}\right)\right)\right). \tag{37}$$

Thus, it turns out that

$$bt - \arctan\left(\frac{b}{a}\right) = \frac{\pi}{2} + n\pi, \quad \text{with } n \in \mathbb{Z},$$

$$t = \frac{\arctan(b/a)}{b} + \frac{\pi}{2b} + \frac{n\pi}{b}, \quad \text{with } n \in \mathbb{Z}. \tag{38}$$

We will call $t_{\max}$ the time for the first maximum. Thus, it follows that

$$t_{\max} = \frac{\arctan(b/a) + \pi/2}{b} \tag{39}$$

then from (34),

$$z_3^{(2)}(t_{\max}) = \frac{2(\alpha-\gamma)}{3}e^{-at_{\max}}\cos(bt_{\max}). \tag{40}$$

This maximum $z_3^{(2)}$ must be part of P_2, since pb_z belongs to P_1 it follows from (22) that

$$\frac{2\alpha}{3} > \frac{2(\alpha-\gamma)}{3}e^{-at_{\max}}\cos(bt_{\max}),$$

$$\frac{\alpha\left(e^{-at_{\max}}\cos(bt_{\max}) - 1\right)}{e^{-at_{\max}}\cos(bt_{\max})} > \gamma. \tag{41}$$

Now, let us assume pb is a point of the heteroclinic orbit joining $\mathbf{x}^*_{\text{eq}_2}$ and $\mathbf{x}^*_{\text{eq}_1}$, i.e.,

$$\lim_{t\longrightarrow-\infty}\varphi(pb,t) = \mathbf{x}^*_{\text{eq}_2},$$
$$\lim_{t\longrightarrow\infty}\varphi(pb,t) = \mathbf{x}^*_{\text{eq}_1}. \tag{42}$$

Because $pb \in W^s_{\mathbf{x}^*_{\text{eq}_1}}$ then $\lim_{t\longrightarrow\infty}\varphi(pb,t) = \mathbf{x}^*_{\text{eq}_1}$.

Following the same procedure described above but looking for a minimum, due to the third component of pb_z is $0 < (2\alpha/3)$. It is found that

$$t_{\min} = \frac{\arctan(b/a) + \pi/2}{b}. \tag{43}$$

Then from (33) and the point pb_z given in (22),

$$z_3^{(2)}(t_{\min}) = \frac{2\alpha}{3}e^{-at_{\min}}\cos(bt_{\min}). \tag{44}$$

This minimum $z_3^{(2)}$ must be part of P_2, since pa_z belongs to P_3 it follows from (22) that

$$\frac{2(\alpha-\gamma)}{3} < \frac{2\alpha}{3}e^{-at_{\min}}\cos(bt_{\min}),$$
$$\gamma > \alpha\left(1 - e^{-at_{\min}}\cos(bt_{\min})\right). \tag{45}$$

Then defining $\tau = t_{\max} = t_{\min}$

$$\frac{\alpha\left(e^{-a\tau}\cos(b\tau) - 1\right)}{e^{-a\tau}\cos(b\tau)} > \gamma > \alpha\left(1 - e^{-a\tau}\cos(b\tau)\right). \tag{46}$$

The same conclusion applies to the point $\mathbf{x}^*_{\text{eq}_3}$ due to the symmetry of the system. Finally, the heteroclinic orbit from $\mathbf{x}^*_{\text{eq}_1}$ to $\mathbf{x}^*_{\text{eq}_2}$ and the one from $\mathbf{x}^*_{\text{eq}_4}$ to $\mathbf{x}^*_{\text{eq}_3}$ are always present in the system as there are no more switching surfaces. □

To illustrate the effect of the parameters γ, α, a, and b on the existence of heteroclinic orbits of the system given by (1), (3), (5), (13), and (15), we use Proposition 3 to determine the open interval of real values for γ given by

$$\Gamma = \left(\alpha\left(1 - e^{-a\tau}\cos(b\tau)\right), \frac{\alpha\left(e^{-a\tau}\cos(b\tau) - 1\right)}{e^{-a\tau}\cos(b\tau)}\right), \tag{47}$$

with $\tau = (\arctan(b/a) + \pi/2)/b$. So, six initial conditions were calculated as in (10) and (11) with $k = 50$ for the parameters $a = 0.2$, $b = 5$, $c = -3$, and $\alpha = 1$. Four cases of different values of γ are analyzed. The first two correspond to $\gamma_{1,2} \in \Gamma$ and the last two correspond to $\gamma_{L,U} \notin \Gamma$:.

(1) For this case $\gamma_1 \in \Gamma$, with $\gamma_1 = \alpha(1 - e^{-a\tau}\cos(b\tau)) + 0.00001$, so there exist six heteroclinic orbits, as shown in Figure 3(a).

(2) For $\gamma_2 = ((\alpha(e^{-a\tau}\cos(b\tau) - 1)/e^{-a\tau}\cos(b\tau)) - 0.00001) \in \Gamma$, in this case, there exist also six heteroclinic orbits as shown in Figure 3(b).

(3) In this case $\gamma_L = \alpha(1 - e^{-a\tau}\cos(b\tau)) \notin \Gamma$, then there exist four heteroclinic orbits, as shown in Figure 3(c). The green orbit stating close to $\mathbf{x}^*_{\text{eq}_2}$ cannot reach $\mathbf{x}^*_{\text{eq}_1}$ and goes to P_3. In the same way, the yellow orbit starting close to $\mathbf{x}^*_{\text{eq}_3}$ cannot reach $\mathbf{x}^*_{\text{eq}_4}$ and goes to P_2. Then there is no heteroclinic orbits from $\mathbf{x}^*_{\text{eq}_2}$ to $\mathbf{x}^*_{\text{eq}_1}$ and from $\mathbf{x}^*_{\text{eq}_3}$ to $\mathbf{x}^*_{\text{eq}_4}$.

(4) For $\gamma_U = (\alpha(e^{-a\tau}\cos(b\tau) - 1)/e^{-a\tau}\cos(b\tau)) \notin \Gamma$, there also exist four heteroclinic orbits as shown in Figure 3(d). The red orbit stating close to $\mathbf{x}^*_{\text{eq}_2}$ cannot reach $\mathbf{x}^*_{\text{eq}_3}$ and goes to P_1. In the same way, the blue orbit starting close to $\mathbf{x}^*_{\text{eq}_3}$ cannot reach $\mathbf{x}^*_{\text{eq}_2}$ and goes to P_4. Then there is no heteroclinic orbit from $\mathbf{x}^*_{\text{eq}_2}$ to $\mathbf{x}^*_{\text{eq}_3}$, nor vice versa.

The open interval Γ is given as $\Gamma = (\gamma_L, \gamma_U)$, where

$$\gamma_L = \alpha\left(1 - e^{-a\tau}\cos(b\tau)\right) \approx 1.8826170015164836,$$
$$\gamma_U = \frac{\alpha\left(e^{-a\tau}\cos(b\tau) - 1\right)}{e^{-a\tau}\cos(b\tau)} \approx 2.1329942639693464. \tag{48}$$

The four cases mentioned generate three types of systems determined by γ and Γ. For instance, for $\gamma = 2 \in \Gamma$ and $\alpha = 1$

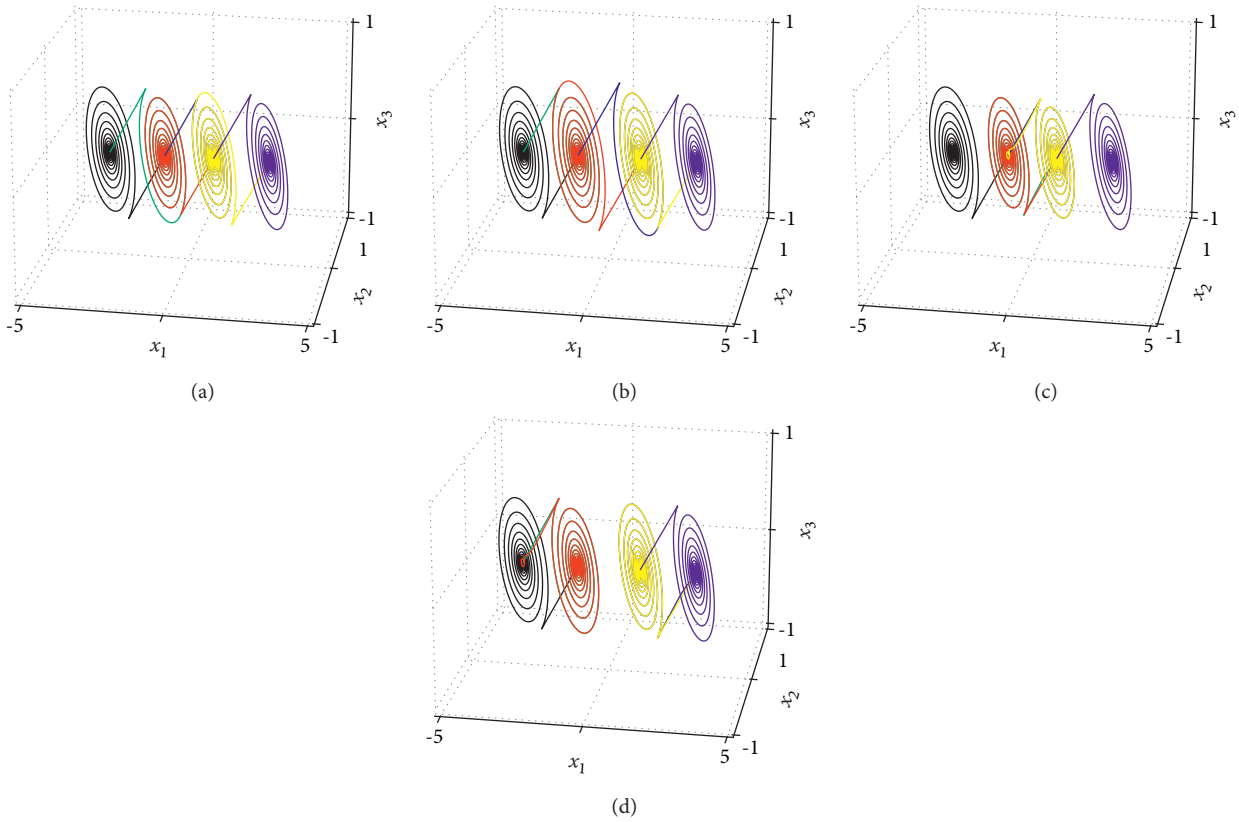

FIGURE 3: Heteroclinic orbits of the system given by (1), (3), (5), (13), and (15) for the parameters $a = 0.2$, $b = 5$, $c = -3$, $\alpha = 1$ and different values of γ. There are six heteroclinic orbits for: (a) $\gamma_1 = \alpha(1 - e^{-a\tau}\cos(b\tau)) + .00001$, and (b) $\gamma_2 = (\alpha(e^{-a\tau}\cos(b\tau) - 1)\ /e^{-a\tau}\cos(b\tau)) - .00001$. Four heteroclinic orbits for (c) $\gamma_L = \alpha(1 - e^{-a\tau}\cos(b\tau))$, and (d) $\gamma_U = (\alpha(e^{-a\tau}\cos(b\tau) - 1)/e^{-a\tau}\cos(b\tau))$.

corresponds to the above first and second cases. Then the system presents six heteroclinic orbits which comprise three heteroclinic loops between equilibria: $\mathbf{x}^*_{eq_1}$ and $\mathbf{x}^*_{eq_2}$; $\mathbf{x}^*_{eq_2}$ and $\mathbf{x}^*_{eq_3}$; $\mathbf{x}^*_{eq_3}$ and $\mathbf{x}^*_{eq_4}$. For $\gamma = 1.5 < \gamma_L$, then $\gamma \notin \Gamma$, and this case corresponds to the above third case. So there are four heteroclinic orbits, and two of them comprise a heteroclinic loop between equilibria $\mathbf{x}^*_{eq_2}$ and $\mathbf{x}^*_{eq_3}$. For $\gamma_U < \gamma = 3$, then $\gamma \notin \Gamma$, and this case corresponds to the above fourth case. So there are four heteroclinic orbits that comprise two heteroclinic loops, but now between equilibria: $\mathbf{x}^*_{eq_1}$ and $\mathbf{x}^*_{eq_2}$; $\mathbf{x}^*_{eq_3}$ and $\mathbf{x}^*_{eq_4}$. The above three cases generate self-excited attractors as shown below:.

(1) For $\gamma = 2 \in \Gamma$, the system presents a self-excited attractor with four scrolls which are shown in Figure 4(a), and its corresponding three heteroclinic loops are shown in Figure 4(d). According to [30], a scroll attractor can be considered a multiscroll attractor when it has at least three scrolls. Thus the attractor shown in Figure 4(a) is a multiscroll attractor. The scrolls are generated around each equilibrium point of the system $\mathbf{x}^*_{eq_i}$, with $i = 1, 2, 3, 4$.

(2) For $\gamma = 3$, $\gamma > \gamma_U$, then $\gamma \notin \Gamma$. The system presents bistability; the two double-scroll self-excited attractors are shown in Figure 4(b). In this case, two heteroclinic orbits are lost, the system exhibits four heteroclinic orbits, i.e., two heteroclinic loops, as shown in Figure 4(e). One double-scroll self-excited attractor oscillates around equilibria $\mathbf{x}^*_{eq_1}$ and $\mathbf{x}^*_{eq_2}$, while the other self-excited attractor oscillates around equilibria $\mathbf{x}^*_{eq_3}$ and $\mathbf{x}^*_{eq_4}$. The basin of attraction of each self-excited attractor has surrounded both attractors.

(3) For $\gamma = 1.5$, $\gamma < \gamma_L$, then $\gamma \notin \Gamma$. The system presents only one double-scroll self-excited attractor, shown in Figure 4(c). In this case, two heteroclinic orbits are also lost, but only a heteroclinic loop is exhibited. The heteroclinic orbits are shown in Figure 4(f). The double-scroll self-excited attractor oscillates around equilibria $\mathbf{x}^*_{eq_2}$ and $\mathbf{x}^*_{eq_3}$.

Based on the results reported in [24] about the relation between the location of the symmetric equilibria and the size of the basin of attraction, we could ponder the possible existence of a hidden attractor for the case $\gamma > \gamma_U$ because there are oscillations surrounding the two self-excited attractors as a hidden attractor exists. However, the simulations of these systems let us know that hidden attractors are not present. For example, if the γ value is increased, then also the distance between the two self-excited attractors increases. This provokes that some initial conditions in the basins of attraction of both attractors generate transitory oscillations resembling a double-scroll attractor. However,

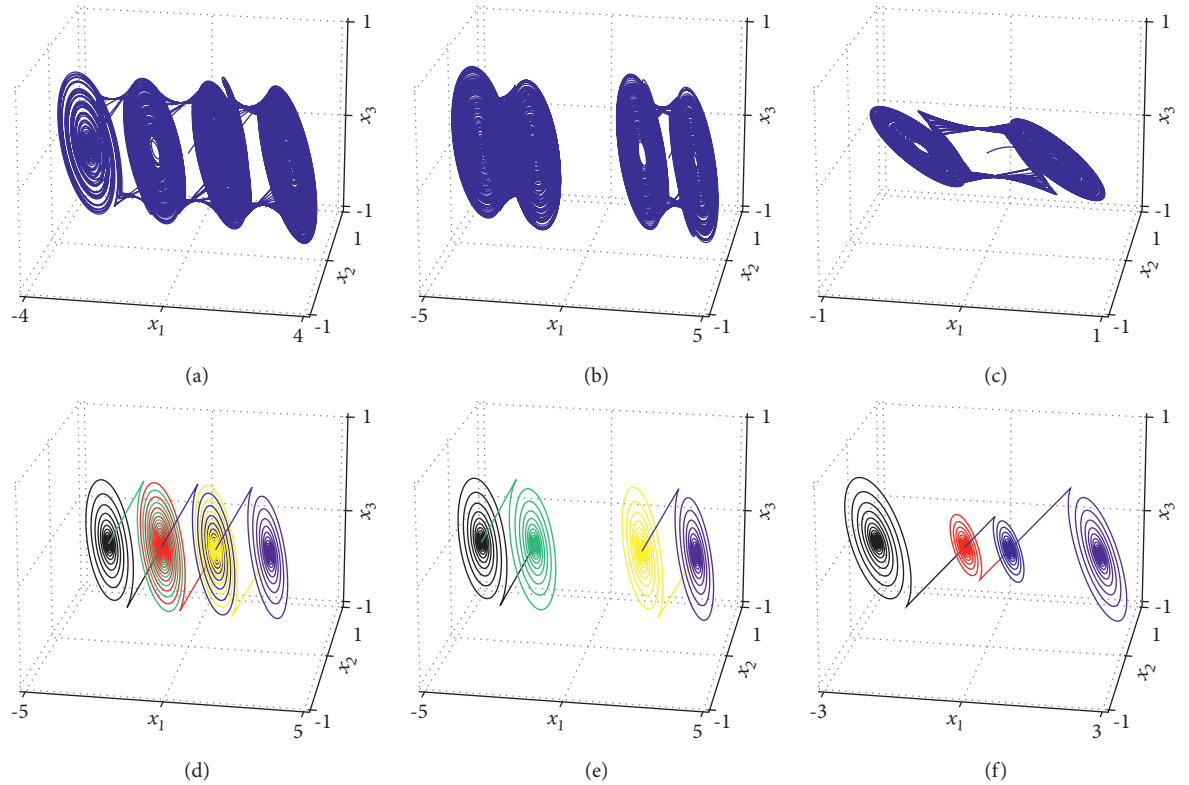

FIGURE 4: Attractors and heteroclinic orbits of the system are given by (1), (3), (5), (13), and (15) for $\alpha = 1$ and different values of γ. For $\gamma = 2$ the system is exhibited in (a) a quad-scroll attractor, and in (d) six heteroclinic orbits. For $\gamma = 3$ the system is exhibited in (b) two double-scroll attractors, and in (e) four heteroclinic orbits. For $\gamma = 1.5$ the system is exhibited in (c) a double-scroll attractor and in (f) four heteroclinic orbits.

after some time, these transitory oscillations converge to one of the double-scroll self-excited attractors.

We analyze the trajectory for the initial condition $\mathbf{x}_0 = (0,0,0)^T$ and different values of γ fulfilling $\gamma_U < \gamma$. The first case is $\gamma = 5$ and $t \in [0,40]$ in arbitrary units (a.u). The equilibria are at

$$\begin{aligned}
\mathbf{x}^*_{\text{eq}_1} &= \begin{bmatrix} -6 \\ 0 \\ 0 \end{bmatrix}, \\
\mathbf{x}^*_{\text{eq}_2} &= \begin{bmatrix} -4 \\ 0 \\ 0 \end{bmatrix}, \\
\mathbf{x}^*_{\text{eq}_3} &= \begin{bmatrix} 4 \\ 0 \\ 0 \end{bmatrix}, \\
\mathbf{x}^*_{\text{eq}_4} &= \begin{bmatrix} 6 \\ 0 \\ 0 \end{bmatrix}.
\end{aligned} \tag{49}$$

Figure 5(a) shows the trajectory which consists of the transitory behavior resembling a double-scroll attractor and after a short time reaches a double-scroll self-excited attractor around equilibria $\mathbf{x}^*_{\text{eq}_1}$ and $\mathbf{x}^*_{\text{eq}_2}$.

Increasing the value of γ to 15, the equilibria are located at

$$\begin{aligned}
\mathbf{x}^*_{\text{eq}_1} &= \begin{bmatrix} -16 \\ 0 \\ 0 \end{bmatrix}, \\
\mathbf{x}^*_{\text{eq}_2} &= \begin{bmatrix} -14 \\ 0 \\ 0 \end{bmatrix}, \\
\mathbf{x}^*_{\text{eq}_3} &= \begin{bmatrix} 14 \\ 0 \\ 0 \end{bmatrix}, \\
\mathbf{x}^*_{\text{eq}_4} &= \begin{bmatrix} 16 \\ 0 \\ 0 \end{bmatrix}.
\end{aligned} \tag{50}$$

And the transitory time to reaches the self-excited attractor is increased. In Figure 5(b), the trajectory is shown for $t \in [0,60]$a.u. Now, for $\gamma = 100$ the equilibria are located at

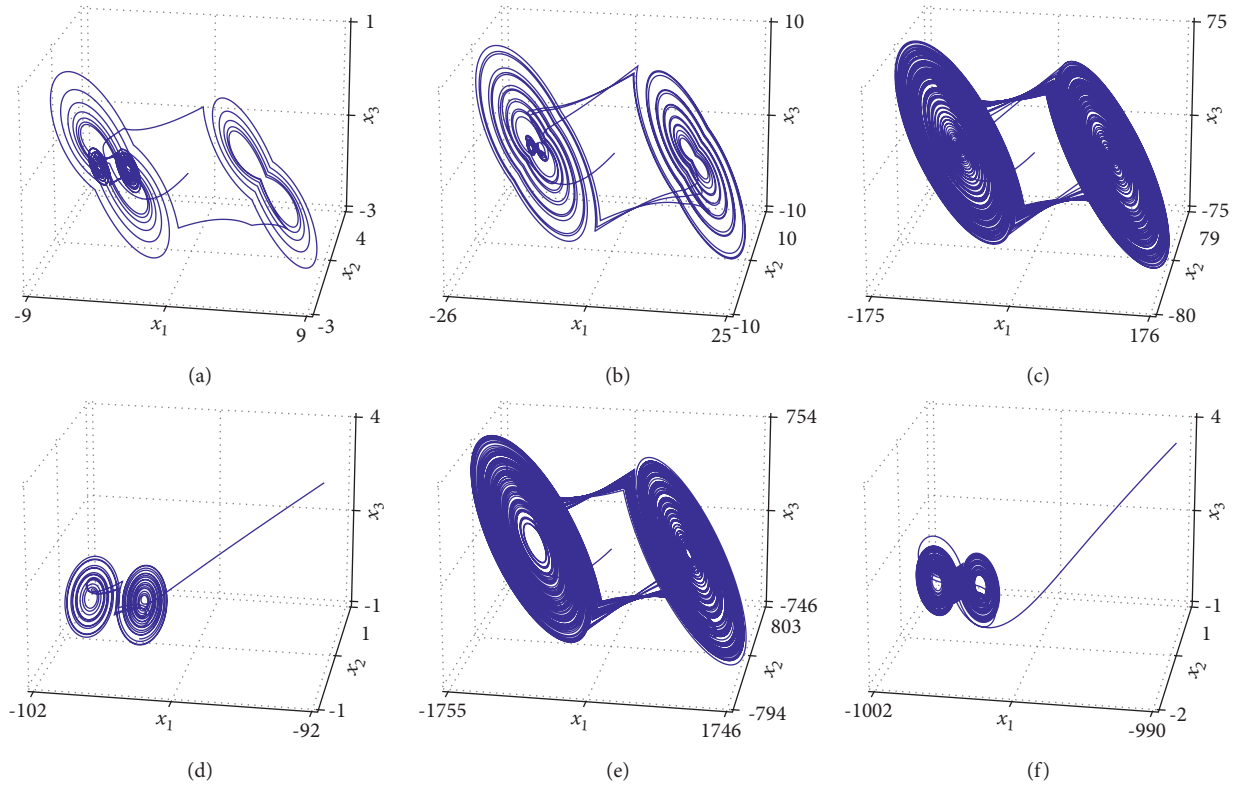

FIGURE 5: Trajectory of the system given by (1), (3), (5), (13), and (15) for the initial condition $x = (0, 0, 0)^T$, $a = 0.2$, $b = 5$, $c = -7$, $\alpha = 1$ and different values of γ: (a) $\gamma = 5$, the transitory oscillation of double-scroll exhibited and after some time converge to one of the double-scroll self-excited attractors, $t \in [0, 40]$a.u.; (b) $\gamma = 15$, the transitory oscillation of double-scroll exhibited and after some time converge to one of the double-scroll self-excited attractors, $t \in [0, 60]$a.u.; (c) $\gamma = 100$, the transitory oscillation of double-scroll exhibited for $t \in [0, 300]$a.u.; (d) $\gamma = 100$, double-scroll self-excited attractor for $t = [356.6, 400]$a.u.; (e) $\gamma = 1000$, the transitory oscillation of double-scroll exhibited for $t \in [0, 300]$a.u.; (f) $\gamma = 1000$, the double-scroll self-excited attractor for $t = [3091, 3200]$a.u.

$$\mathbf{x}^*_{eq_1} = \begin{bmatrix} -101 \\ 0 \\ 0 \end{bmatrix},$$
$$\mathbf{x}^*_{eq_2} = \begin{bmatrix} -99 \\ 0 \\ 0 \end{bmatrix},$$
$$\mathbf{x}^*_{eq_3} = \begin{bmatrix} 99 \\ 0 \\ 0 \end{bmatrix}, \tag{51}$$
$$\mathbf{x}^*_{eq_4} = \begin{bmatrix} 101 \\ 0 \\ 0 \end{bmatrix}.$$

$$\mathbf{x}^*_{eq_1} = \begin{bmatrix} -1001 \\ 0 \\ 0 \end{bmatrix},$$
$$\mathbf{x}^*_{eq_2} = \begin{bmatrix} -999 \\ 0 \\ 0 \end{bmatrix},$$
$$\mathbf{x}^*_{eq_3} = \begin{bmatrix} 999 \\ 0 \\ 0 \end{bmatrix}, \tag{52}$$
$$\mathbf{x}^*_{eq_4} = \begin{bmatrix} 1001 \\ 0 \\ 0 \end{bmatrix}.$$

The transitory time lasts longer for the same initial condition. Figure 5(c) shows the transitory oscillations of the trajectory for $t \in [0, 300]$a.u. After a long time, the trajectory reaches a double-scroll self-excited attractor around equilibria $\mathbf{x}^*_{eq_1}$ and $\mathbf{x}^*_{eq_2}$; see Figure 5(d) for $t \in [356.6, 400]$a.u. Continuing to increase the value to $\gamma = 1000$, then this sets the equilibria at

Figure 5(e) shows the transitory oscillation of the trajectory when $t \in [0, 300]$a.u., again, transitory time increases, and after this long time, the trajectory again reaches a double-scroll self-excited attractor around equilibria $\mathbf{x}^*_{eq_1}$ and $\mathbf{x}^*_{eq_2}$, see 5f for $t \in [3091, 3200]$a.u.

In brief, for $\gamma = 5$ it took the trajectory around 35 a.u. To converge to a self-excited attractor, for $\gamma = 15$ around 50 a.u.

To converge, for $\gamma = 100$ around 350 a.u. And for $\gamma = 1000$ around 3090 a.u. Thus, transitory time seems to increase for some initial conditions when γ increases. In all the cases, the trajectories reach a self-excited attractor. □

4. Route to a Self-Excited Attractor

In this section, the transitory behavior presented in the previous section is studied in order to visualize the route of the transitory double scroll to a self-excited attractor. The idea is to estimate two regions $R_1, R_2 \subset SW_{23}$, such that any trajectory $\varphi(x_0)$, with $x_0 \in R_1 \cup R_2$, will eventually go to the self-excited attractor A_{self1} or A_{self2}. These regions are symmetric with respect to the origin and are crossed by the trajectories of the transitory double scroll.

Consider the point pa and its symmetric point $pc = -pa$:

$$pa = \begin{pmatrix} -\dfrac{\gamma-\alpha}{3} \\ 0 \\ -\dfrac{2(\gamma-\alpha)}{3} \end{pmatrix}, \quad pc = \begin{pmatrix} \dfrac{\gamma-\alpha}{3} \\ 0 \\ \dfrac{2(\gamma-\alpha)}{3} \end{pmatrix}. \tag{53}$$

These points are the intersections of the local manifolds in SW_{23} and are shown in Figure 6.

The trajectories with initial conditions in the points $pa, pc \in SW_{23}$ converge to equilibria $\mathbf{x}_{eq_3}$ and $\mathbf{x}_{eq_2}$, respectively. So, the transient oscillation of the trajectory that resembles a double-scroll attractor interferes when the trajectory reaches neighborhoods $N(pa) \subset SW_{23}$ and $N(pc) \subset SW_{23}$ around pa or pc, respectively, because each trajectory with initial condition in $N(pa)$ or $N(pc)$ is led to one of the self-excited attractors A_{self1} or A_{self2}, respectively. So, the aim is to visualize the route to a self-excited attractor when $N(pa) \cap R_1 \neq \varnothing$ and $N(pc) \cap R_2 \neq \varnothing$.

Thus, the study in this section has the following structure: First, two regions R_1 and R_2 are estimated. The regions are then evaluated numerically to verify their validity. Finally, based on the geometry of the system and the observation of the simulations, conjecture about the necessary conditions for the existence of the hidden attractor.

To simplify the study, some assumptions are made to restrict the systems to a subset of the class.

Assumption 1. The parameter values fulfill the following relations: $(b/a) \geq 25$, $2 \geq |c/b| \geq (7/5)$ and $(\gamma/\alpha) \geq 10$.

To start the analysis, let us find the points in SW_{23} where the vector fields of P_2 and P_3 are tangent to the plane SW_{23}. These points will be called tangent points and can be found from the following equation:

$$(2,0,-1)\begin{pmatrix} \dfrac{a}{3}+\dfrac{2c}{3} & b & \dfrac{2c}{3}-\dfrac{2a}{3} \\ -\dfrac{b}{3} & a & \dfrac{2b}{3} \\ \dfrac{c}{3}-\dfrac{a}{3} & -b & \dfrac{2a}{3}+\dfrac{c}{3} \end{pmatrix}\begin{pmatrix} \dfrac{x_3}{2}-x_{1eq_i} \\ x_2 \\ x_3 \end{pmatrix} = -(a+c)x_{1eq_i} + \frac{3(c-a)}{2}x_3 + 3bx_2 = 0. \tag{54}$$

It follows that

$$x_2 = \frac{(a+c)}{3b}x_{1eq_i} - \frac{(c-a)}{2b}x_3, \quad \text{with } i = 1,2. \tag{55}$$

For the vector field of P_2, $x_{1eq_2} = -\gamma + \alpha$, then

$$x_2 = \frac{(a+c)}{3b}(-\gamma+\alpha) - \frac{(c-a)}{2b}x_3, \tag{56}$$

while for the vector field of P_3, $x_{1eq_3} = \gamma - \alpha$:

$$x_2 = \frac{(a+c)}{3b}(\gamma-\alpha) - \frac{(c-a)}{2b}x_3. \tag{57}$$

According to (16), if $x_3 > 0$ then SW_{23} belongs to P_2, and the tangent points to consider in SW_{23} for $x_3 > 0$ are given by (56). And if $x_3 \leq 0$, then SW_{23} belongs to P_3 and the tangent points are given by (57). An illustration of the tangent points in SW_{23} is shown in Figure 7, where the points for P_2 are indicated by a dotted line, while for P_3 are drawn as a continuous line.

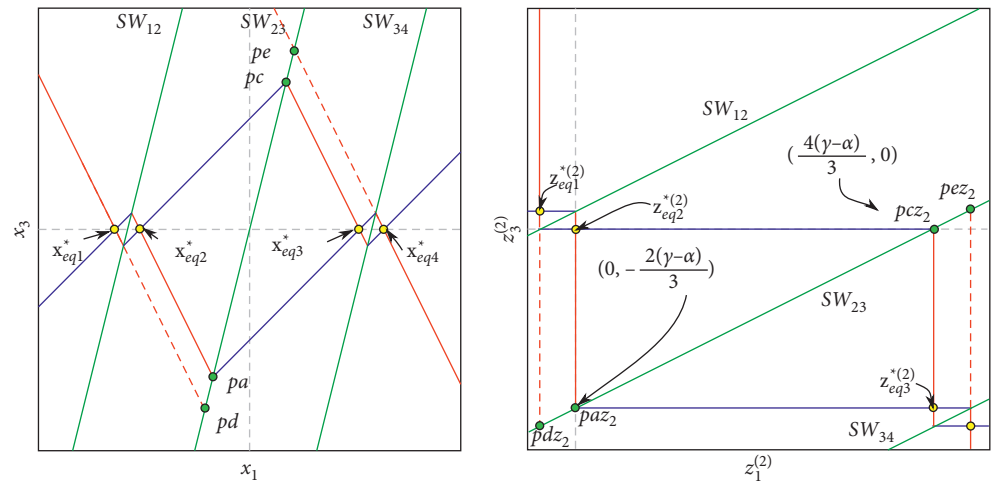

FIGURE 6: Projection of the manifolds on (a) $(x_1 - x_3)$ plane and (b) $(z_1^{(2)} - z_3^{(2)})$ plane. The stable and unstable manifolds are marked with blue and red solid lines, respectively, the switching surfaces with green lines.

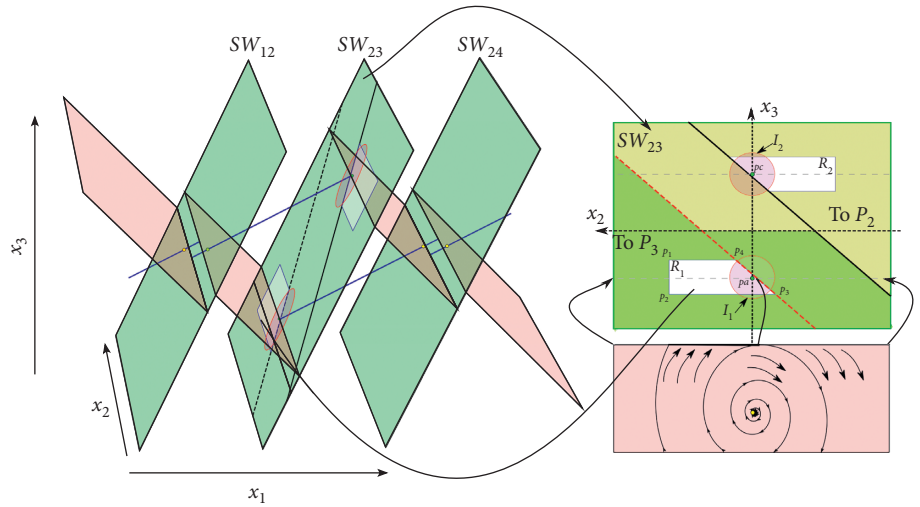

FIGURE 7: Illustration of the local manifold of the system. Stable manifolds are in blue, unstable manifold in red, and switching surfaces in green. The points where the vector field of P_2 is tangent to SW_{23} are in a red dotted line, while the points where the vector field of P_3 are tangent to SW_{23} are in a continuous black line. The symmetric regions R_1 and R_2 are in white.

As a starting point to propose the region R_1 defined by four points $p_1, \ldots, p_4$, consider the point in $\mathrm{cl}(W^u_{\mathbf{x}_{eq_2}}) \cap SW_{23}$ given by (19) that fulfills (56):

$$pt_1 = \begin{pmatrix} -\frac{\gamma-\alpha}{3} \\ -\frac{2a(\gamma-\alpha)}{3b} \\ -\frac{2(\gamma-\alpha)}{3} \end{pmatrix}, \tag{58}$$

and in $\mathbf{z}^{(2)}$ coordinates

$$pt_1 z_2 = \begin{pmatrix} 0 \\ \frac{2a(\gamma-\alpha)}{3b} \\ -\frac{2(\gamma-\alpha)}{3} \end{pmatrix}. \tag{59}$$

The points in $\mathbf{z}^{(2)}$ coordinate system are denoted with the suffix z_2. If we evaluate the trajectory with an initial condition in $x_0 = pt_1 z_2$, under the vector field of P_2 and ignoring the effect of the vector field of P_1 and P_3, reaches the point $pt_2 z_2 \in SW_{23}$. The flow φ could go from P_2 to P_3 through the segment $\overline{pt_1 z_2\, pt_2 z_2}$. Thus, trajectories with

initial condition are close to A_{self1} but not in the attractor cross SW_{23} close to the segment $\overline{pt_1z_2\ pt_2z_2}$ then R_1 should include this segment. However, when the vector field of all atoms is considered, trajectories with initial conditions close to pt_1z_2 could reach SW_{23} in points whose second component in $z^{(2)}$ coordinates are further from 0 than the second component in $z^{(2)}$ coordinates of pt_2z_2. Thus, let us propose the region R_1 based on a larger segment $\overline{pa_1z_2\ pa_2z_2}$ such that $\overline{pt_1z_2\ pt_2z_2} \subset \overline{pa_1z_2\ pa_2z_2}$. Consider the initial condition paz_2 given in $\mathbf{z}^{(2)}$ coordinates by

$$paz_2 = \begin{pmatrix} 0 \\ 0 \\ -\dfrac{2(\gamma-\alpha)}{3} \end{pmatrix}, \tag{60}$$

then, the radius with respect to $\mathbf{z}^*_{\text{eq}_2}$ would be $(2(\gamma-\alpha)/3)$. Remember that only the vector field of P_2 is considered and the trajectory rotates around the axis $z_1^{(2)}$. Let us think in an imaginary and impossible case when a trajectory with an initial condition in paz_2 rotates around the axis $z_1^{(2)}$ and reaches SW_{23}, but instead of the normal increment of radius, let us imagine that the increment in radius corresponds to an evolution time $t = 2\pi/b$ (360°). Thus, the $z_2^{(2)}$ component of this point is further from 0 than the $z_2^{(2)}$ component of pt_2z_2. Then, we could take $pa_2z_2 = pt_1z_2$ and find the $z_2^{(2)}$ component of pa_1z_2 from

$$\sqrt{\left(\frac{2(\gamma-\alpha)}{3}e^{a(2\pi/b)}\right)^2 - \left(\frac{2(\gamma-\alpha)}{3}\right)^2}. \tag{61}$$

By using Assumption 1,

$$\sqrt{\left(\frac{2(\gamma-\alpha)}{3}e^{a(2\pi/b)}\right)^2 - \left(\frac{2(\gamma-\alpha)}{3}\right)^2} \le \gamma\sqrt{\left(\frac{2}{3}e^{a(2\pi/b)}\right)^2 - \left(\frac{2}{3}\right)^2} \le 0.5388\gamma < \frac{3\gamma}{5}. \tag{62}$$

Remember that $z_2^{(2)} = -x_2$, then, the points pa_1 and pa_2 are given by

$$pa_1 = \begin{pmatrix} -\dfrac{\gamma-\alpha}{3} \\ \dfrac{3\gamma}{5} \\ -\dfrac{2(\gamma-\alpha)}{3} \end{pmatrix}, \quad pa_2 = \begin{pmatrix} -\dfrac{\gamma-\alpha}{3} \\ -\dfrac{2a(\gamma-\alpha)}{3b} \\ -\dfrac{2(\gamma-\alpha)}{3} \end{pmatrix}, \tag{63}$$

where $-(2a(\gamma-\alpha)/3b)$ is the tangent coordinate given by (56) for $x_3 = -(2(\gamma-\alpha)/3)$.

So, let us propose the region R_1 delimited by the following four points:

$$\begin{aligned} p_1 &= pa_1 + \left(\frac{\gamma}{10}, 0, \frac{\gamma}{5}\right)^T, \\ p_2 &= pa_1 - \left(\frac{\gamma}{10}, 0, \frac{\gamma}{5}\right)^T, \\ p_3 &= pa_2 + \left(-\frac{\gamma}{10}, -\frac{(c-a)(-\gamma/5)}{2b}, -\frac{\gamma}{5}\right)^T, \\ p_4 &= pa_2 + \left(\frac{\gamma}{10}, -\frac{(c-a)(\gamma/5)}{2b}, \frac{\gamma}{5}\right)^T. \end{aligned} \tag{64}$$

Because R_2 is symmetric to R_1 with respect to the origin, then the symmetric region R_2 is delimited by the points:

$$\begin{aligned} q_1 &= -p_1, \\ q_2 &= -p_2, \\ q_3 &= -p_3, \\ q_4 &= -p_4. \end{aligned} \tag{65}$$

These regions R_1 and R_2 have been proposed taking into consideration that points p_d and p_e shown in Figure 6(b) are part of the regions. In Figure 8, R_1 and R_2 are shown in $\mathbf{z}^{(2)}$ coordinates.

Now, let us analyze some scenarios on these regions to see if the proposed regions are good candidates, at least in an

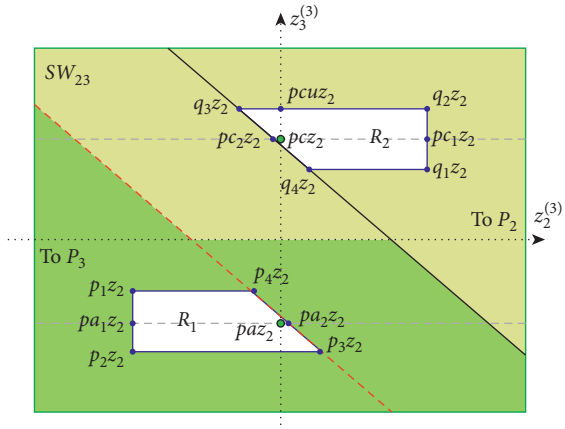

Figure 8: Regions R_1 and R_2 on the projection $z_2^{(2)} - z_3^{(2)}$.

estimated manner. In order to simplify the scenarios, in the following, it is considered that trajectories in $P_1 \cup P_2$ rotate only around the stable manifold of $\mathbf{x}_{eq_2}$, i.e., if only the vector field of P_2 is considered.

Let us define the set R_1b as follows:

$$R_1b = \left\{\mathbf{z}^{(2)} \in \mathbb{R}^3 \colon z_1^{(2)} \in \left[-\frac{\gamma}{5}, \frac{\gamma}{5}\right]\right\}. \tag{66}$$

First, let us verify that the points in R_2 go to R_1b.

The evaluation of the vector field in pc_1z_2 tells us that the spin is counterclockwise in $\mathbf{z}^{(2)}$ coordinates. From Figures 8 and 6(b), it is not hard to see that the points below the segment $\overline{pcz_2\ pc_1z_2}$ produce trajectories that can perform a turn of π around the $z_1^{(2)}$ axis without reaching SW_{23} again. The time that corresponds to a turn of 2π is $T = 2\pi/b$. The point pc_1z_2 is given by

$$pc_1z_2 = \begin{pmatrix} \frac{4(\gamma-\alpha)}{3} \\ \frac{3\gamma}{5} \\ 0 \end{pmatrix}. \tag{67}$$

Consider the trajectory with an initial condition in pc_1z_2, and an evolution time that corresponds to a turn of π around the $z_1^{(2)}$ axis. After this time, the first component of the state vector can be found from

$$z_1^{(2)} = \left(\frac{4(\gamma-\alpha)}{3}\right)e^{c(\pi/b)}. \tag{68}$$

If $z_1^{(2)} \le \gamma/5$ means that the trajectory with an initial condition in pc_1z_2 reaches R_1b. Consider Assumption 1 for a big value of $z_1^{(2)}$ (when γ is too big):

$$\left(\frac{4(\gamma-\alpha)}{3}\right)e^{c(\pi/b)} \le \frac{4\gamma}{3}e^{c(\pi/b)} \le 0.0164\gamma < \frac{\gamma}{5}. \tag{69}$$

Thus the set $\left\{\mathbf{z}^{(2)} \in R_2 \colon z_2^{(2)} \ge 0, z_3^{(2)} \le 0\right\}$ reaches the set R_1b.

Now consider the point q_2z_2 given by

$$q_2z_2 = \begin{pmatrix} \frac{23\gamma}{15} - \frac{4\alpha}{3} \\ \frac{3\gamma}{5} \\ \frac{\gamma}{10} \end{pmatrix}. \tag{70}$$

The angle produced by the radius from the point q_2z_2 to the $z_1^{(2)}$ axis and the plane $z_1^{(2)} - z_2^{(2)}$ is given by

$$\arctan\left(\frac{\gamma/10}{3\gamma/5}\right) = \arctan\left(\frac{1}{6}\right) = 0.1654. \tag{71}$$

Let us consider that the trajectory with the initial condition in q_2z_2 evolves for a duration time that corresponds to $\pi - 2(0.1654) = 2.8113$. The first component of the state vector after this duration is given by

$$z_1^{(2)} = \left(\frac{23\gamma}{15} - \frac{4\alpha}{3}\right)e^{c(2.8113/b)}. \tag{72}$$

As before, if $z_1^{(2)} \le \gamma/5$ means that the trajectory with an initial condition in q_2z_2 reaches R_1b. Consider again Assumption 1 for a big value of $z_1^{(2)}$:

$$\left(\frac{23\gamma}{15} - \frac{4\alpha}{3}\right)e^{c(2.8113/b)} \le \left(\frac{23\gamma}{15}\right)e^{c(2.8113/b)} \le 0.0299\gamma < \frac{\gamma}{5}. \tag{73}$$

Thus, q_2z_2 reaches the region R_1b. Moreover, since the points in the segment $\overline{q_2z_2\ pc_1z_2}$ produce a radius whose angle with the plane $z_1^{(2)} - z_2^{(2)}$ is between 0 and 2.8113, the trajectories starting in this segment also reach the set R_1b.

Now consider the point $pcuz_2$ given by

$$pcuz_2 = \begin{pmatrix} \frac{23\gamma}{15} - \frac{4\alpha}{3} \\ 0 \\ \frac{\gamma}{10} \end{pmatrix}. \tag{74}$$

The trajectories with the initial condition in the segment $\overline{pcz_2\ pcuz_2}$ can turn $\pi/2$ without reaching SW_{23}. Thus, let us consider that the trajectory with the initial condition in $pcuz_2$ evolves for a duration time that corresponds to $\pi/2$. The first component of the state vector after this duration is given by

$$z_1^{(2)} = \left(\frac{23\gamma}{15} - \frac{4\alpha}{3}\right)e^{c(\pi/2b)}. \tag{75}$$

If $z_1^{(2)} \le \gamma/5$ means that the trajectory with an initial condition in $pcuz_2$ reaches R_1b, consider Assumption 1 for a big value of $z_1^{(2)}$:

$$\left(\frac{23\gamma}{15} - \frac{4\alpha}{3}\right)e^{c(\pi/2b)} \le \left(\frac{23\gamma}{15}\right)e^{c(\pi/2b)} \le 0.17\gamma < \frac{\gamma}{5}. \tag{76}$$

Thus the trajectories with the initial condition in the set $\{\mathbf{z}^{(2)} \in R_2 \colon z_2^{(2)} \geq 0, z_3^{(2)} \geq 0\}$ converge to the set $R_1 b$.

Now consider the point $q_3 z_2$

$$q_3 z_2 = \begin{pmatrix} \dfrac{23\gamma}{15} - \dfrac{4\alpha}{3} \\ \dfrac{3c\gamma - 23a\gamma}{30b} + \dfrac{2a\alpha}{3b} \\ \dfrac{\gamma}{10} \end{pmatrix}. \tag{77}$$

To estimate if that the trajectory starting in $q_3 z_2$ is not going to reach SW_{23} when the radius form an angle of $3\pi/2$ with the plane $z_1^{(2)} - z_2^{(2)}$, let us consider the following exaggerated scenario: The radius size corresponds to a duration equivalent to $3\pi/2$, but the $z_1^{(2)}$ component corresponds to a duration equivalent to $\pi/2$ of oscillation, i.e., when the radius form an angle of $3\pi/2$ with the plane $z_1^{(2)} - z_2^{(2)}$, a smaller radius than the real one is considered; also, a larger value of $z_1^{(2)}$ than the real value is considered.

Then to obtain the radius:

$$r = e^{a(3\pi/2b)} \sqrt{\left(\frac{3c\gamma - 23a\gamma}{30b} + \frac{2a\alpha}{3b}\right)^2 + \left(\frac{\gamma}{10}\right)^2}. \tag{78}$$

Under Assumption 1 for the largest radius:

$$\begin{aligned} e^{a(3\pi/2b)} \sqrt{\left(\frac{3c\gamma - 23a\gamma}{30b} + \frac{2a\alpha}{3b}\right)^2 + \left(\frac{\gamma}{10}\right)^2} &\leq e^{a(3\pi/2b)} \sqrt{\left(\frac{3c\gamma - 23a\gamma}{30b}\right)^2 + \left(\frac{\gamma}{10}\right)^2}, \\ e^{a(3\pi/2b)} \sqrt{\left(\frac{3c\gamma}{30b} - \frac{23a\gamma}{30b}\right)^2 + \left(\frac{\gamma}{10}\right)^2} &\leq e^{a(3\pi/2b)} \sqrt{\left(-\frac{1\gamma}{5} - \frac{23\gamma}{750}\right)^2 + \left(\frac{\gamma}{10}\right)^2}, \\ e^{a(3\pi/2b)} \sqrt{\left(-\frac{1\gamma}{5} - \frac{23\gamma}{750}\right)^2 + \left(\frac{\gamma}{10}\right)^2} &= \gamma e^{a(3\pi/2b)} \sqrt{\left(-\frac{173}{750}\right)^2 + \left(\frac{1}{10}\right)^2}, \\ \gamma e^{a(3\pi/2b)} \sqrt{\left(-\frac{173}{750}\right)^2 + \left(\frac{1}{10}\right)^2} &\leq 0.3036\gamma. \end{aligned} \tag{79}$$

The value of $z_1^{(2)}$ after a duration equivalent to 90° is given by

$$z_1^{(2)} = \left(\frac{23\gamma}{15} - \frac{4\alpha}{3}\right) e^{c(\pi/2b)}. \tag{80}$$

Under Assumption 1 for the biggest $z_1^{(2)}$

$$\begin{aligned} \left(\frac{23\gamma}{15} - \frac{4\alpha}{3}\right) e^{c(\pi/2b)} &\leq \left(\frac{23\gamma}{15}\right) e^{c(\pi/2b)}, \\ \left(\frac{23\gamma}{15}\right) e^{c(\pi/2b)} &\leq 0.17\gamma < \frac{\gamma}{5}. \end{aligned} \tag{81}$$

In $\mathbf{z}^{(2)}$ coordinates, a specific value of $z_1^{(2)}$ SW_{23} fulfills $z_3^{(2)} = -(2(\gamma - \alpha)/3) + (z_1^{(2)}/2)$. At this angle of $3\pi/2$ the radius is $r = -z_3^{(2)}$. Then, if the values found for this scenario fulfill the following inequality, it can be concluded that the trajectory with an initial condition in $q_3 z_2$ does not reach SW_{23} after a duration that corresponds to an oscillation of $\pi/2$:

$$-0.3036\gamma > -\frac{2(\gamma - \alpha)}{3} + 0.085\gamma, \tag{82}$$

under Assumption 1 for the worst case

$$-0.3036\gamma > -\frac{18\gamma}{30} + 0.085\gamma = -0.515\gamma. \tag{83}$$

Then, the trajectory remains for the duration that corresponds to $\pi/2$. Also, the trajectory does not reach SW_{23} when the radius is at an angle of $3\pi/2$ with the plane $z_1^{(2)} - z_2^{(2)}$ even when the radius growth is exaggerated. It can be concluded that the trajectory with the initial condition in $q_3 z_2$ could reach SW_{23} until the second time it approaches SW_{23} and reaches $R_1 b$.

Since $q_3 z_2$ is the point in the set $\{\mathbf{z}^{(2)} \in R_2 \colon z_2^{(2)} \leq 0\}$ that produces the largest radius of that set, the trajectories with the initial condition in this set also reach $R_1 b$. Then the trajectories starting at R_2 reach $R_1 b$.

Now to estimate if the trajectories that start in R_2 reach $R_1 \subset R_1 b$ is enough to verify the trajectories starting in the segment $\overline{q_1 z_2 q_2 z_2}$ since these produce the largest radius in $R_1 b$.

Consider the points $q_1 z_2$ and $q_2 z_2$

$$q_1z_2 = \begin{pmatrix} \frac{17\gamma}{15} - \frac{4\alpha}{3} \\ \frac{3\gamma}{5} \\ -\frac{\gamma}{10} \end{pmatrix}, \quad q_2z_2 = \begin{pmatrix} \frac{23\gamma}{15} - \frac{4\alpha}{3} \\ \frac{3\gamma}{5} \\ \frac{\gamma}{10} \end{pmatrix}, \tag{84}$$

both points produce the same radius with a different angle. However, more oscillation time before reaching SW_{23} is expected from q_1z_2. Thus, consider the trajectory with the initial condition in q_1z_2 and the evolution time that corresponds to $3\pi/2 + 0.1651 = 4.8775$, which is an exaggerated angle since SW_{23} is reached before that.

$$r = e^{a(4.8775/b)}\sqrt{\left(\frac{3\gamma}{5}\right)^2 + \left(\frac{\gamma}{10}\right)^2} = \gamma e^{a(4.8775/b)}\sqrt{\frac{37}{100}}. \tag{85}$$

Under Assumption 1,

$$\gamma\sqrt{\frac{37}{100}}e^{a(4.8775/b)} \leq 0.7393\gamma. \tag{86}$$

Consider the points p_1z_2, pa_1z_2 and p_2z_2

$$p_1z_2 = \begin{pmatrix} \frac{\gamma}{5} \\ -\frac{3\gamma}{5} \\ \frac{2\alpha}{3} - \frac{17\gamma}{30} \end{pmatrix}, \quad pa_1z_2 = \begin{pmatrix} 0 \\ -\frac{3\gamma}{5} \\ -\frac{2(\gamma-\alpha)}{3} \end{pmatrix}, \quad p_2z_2 = \begin{pmatrix} -\frac{\gamma}{5} \\ -\frac{3\gamma}{5} \\ \frac{2\alpha}{3} - \frac{23\gamma}{30} \end{pmatrix}. \tag{87}$$

The minimum radius in the segment $\overline{pa_1z_2, pa_2z_2}$ is as follows:

$$r = \sqrt{\left(\frac{3\gamma}{5}\right)^2 + \left(\frac{2\alpha}{3} - \frac{17\gamma}{30}\right)^2}. \tag{88}$$

Under Assumption 1, the radius from the segment $\overline{pa_1z_2, pa_2z_2}$ is as follows:

$$\sqrt{\left(\frac{3\gamma}{5}\right)^2 + \left(\frac{2\alpha}{3} - \frac{17\gamma}{30}\right)^2} \geq \sqrt{\left(\frac{3\gamma}{5}\right)^2 + \left(-\frac{\gamma}{2}\right)^2}, \quad \gamma\sqrt{\left(\frac{3}{5}\right)^2 + \left(-\frac{1}{2}\right)^2} = 0.781\gamma. \tag{89}$$

Since $0.7393\gamma < 0.781\gamma$ even when the increment of radius was exaggerated, it is expected that the trajectories with an initial condition in R_2 reach R_1 or a self-excited attractor. In the same way, the trajectories with an initial condition in R_1 reach R_2 or go to a self-excited attractor.

To verify the region for the parameters $a = 0.2$, $b = 5$, $c = -7$ and $\alpha = 1$, seven trajectories have been simulated and are shown in Figure 9(a) for $\gamma = 10$ and $\gamma = 100$ in Figure 9(b).

Now consider two sets of initial conditions in SW_{23}, I_1 and I_2, such that subsets $N(pa)$ and $N(pc)$ of these sets produce trajectories that end in one of the self-excited attractors. These sets are drawn by circles in Figure 7.

It is easy to see that if γ increases, then the regions R_1 and R_2 grow, but the subsets of initial conditions in I_1 and I_2 that reach a self-excited attractor without reaching SW_{23} again are reduced.

Let us look at the system in $\mathbf{z}^{(2)}$ coordinates, as γ grows, SW_{23} and pcz_2 are further from the $\mathbf{z}^*_{eq2}$ and then it takes more time for the trajectories close to pcz_2 to travel along the $z_1^{(2)}$ direction to get close to $\mathbf{z}^*_{eq2}$; however, the expansion along $z_2^{(2)}$ and $z_3^{(2)}$ remains the same; then the subsets of initial conditions that reach the self-excited attractors without reaching SW_{23} again shrink in I_1 and I_2 but never disappear. As pc and pa belong to R_1 and R_2, respectively, then there will always be an intersection of these regions R_1 and R_2 with the subsets of initial conditions that reaches the self-excited attractors in the regions I_1 and I_2.

This explains why as γ is increased, it is easy to find initial conditions such that the transitory lasts long. Then we come to the conjecture that a necessary condition for the existence of a hidden attractor is that the intersection of regions R_1 and R_2 with those sets given by I_1 and I_2 must be empty, i.e., $N(pa) \cap R_1 = \emptyset$ and $N(pc) \cap R_2 = \emptyset$.

5. Emergence of Hidden Attractors

In this section, a modification is made to the previous class of systems to meet the conjecture requirement. A way to produce $N(pa) \cap R_1 = \emptyset$ and $N(pc) \cap R_2 = \emptyset$ and allow the existence of a hidden attractor is by modifying the commutation surface SW_{23} between the two self-excited attractors. Consider the following switching planes:

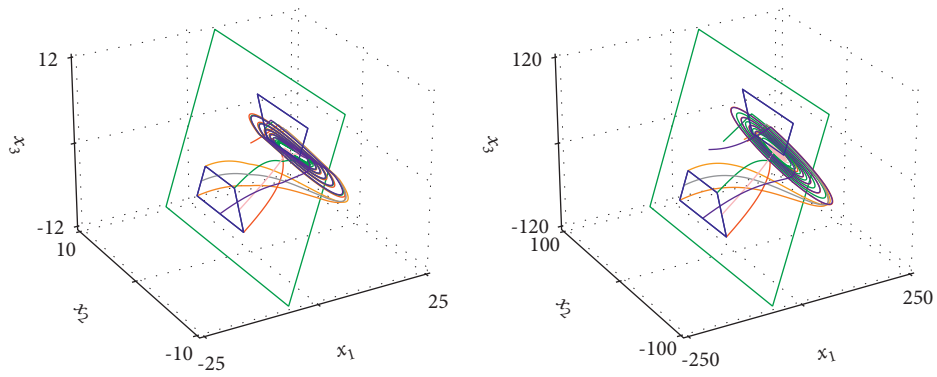

FIGURE 9: Seven trajectories of the system given by (1), (3), (5), (13), and (15) starting in R_1 with $a = 0.2$, $b = 5$, $c = -7$, $\alpha = 1$ and different values of γ: (a) $\gamma = 10$ and (b) $\gamma = 100$.

$$\begin{aligned}
SW_{12} &= \mathrm{cl}(P_1) \cup \mathrm{cl}(P_2) = \{\mathbf{x} \in \mathbb{R}^3 : 2x_1 - x_3 = -2\gamma, x_1 < 0\},\\
SW_{23} &= \mathrm{cl}(P_2) \cup \mathrm{cl}(P_3) = \{\mathbf{x} \in \mathbb{R}^3 : x_1 = 0\},\\
SW_{34} &= \mathrm{cl}(P_3) \cup \mathrm{cl}(P_4) = \{\mathbf{x} \in \mathbb{R}^3 : 2x_1 - x_3 = 2\gamma, x_1 > 0\}.
\end{aligned} \tag{90}$$

Note that the switching surface SW_{23} has a new location while the switching surfaces SW_{12} and SW_{34} keep their original locations. This new arrangement keeps the existence of the two heteroclinic loops and thus the two self-excited attractors. The new projections of the system in $\mathbf{x}$ and $\mathbf{z}^{(2)}$ coordinates are shown in Figure 10.

To study the emergence of a hidden attractor, the same procedure is followed as in the previous section.

Let us find the points in SW_{23} where the vector fields of P_2 and P_3 are tangent to the plane SW_{23}. These points can be found from the following equation:

$$(1,0,0)\begin{pmatrix} \frac{a}{3}+\frac{2c}{3} & b & \frac{2c}{3}-\frac{2a}{3} \\ -\frac{b}{3} & a & \frac{2b}{3} \\ \frac{c}{3}-\frac{a}{3} & -b & \frac{2a}{3}+\frac{c}{3} \end{pmatrix}\begin{pmatrix} -x_{\mathrm{eq}_i} \\ x_2 \\ x_3 \end{pmatrix} = -x_{\mathrm{eq}_i}\frac{(a+2c)}{3} + bx_2 + \frac{2c-2a}{3}x_3 = 0, \tag{91}$$

$$x_2 = x_{\mathrm{eq}_i}\frac{(a+2c)}{3b} - \frac{2c-2a}{3b}x_3, \quad \text{with } i = 1, 2.$$

Then for the vector field of P_2 we have the following expression:

$$x_2 = \frac{-(\gamma-\alpha)(a+2c)}{3b} - \frac{2c-2a}{3b}x_3. \tag{92}$$

For the vector field of P_3 the expression is as follows:

$$x_2 = \frac{(\gamma-\alpha)(a+2c)}{3b} - \frac{2c-2a}{3b}x_3. \tag{93}$$

Consider the point in $\mathrm{cl}(W^u_{\mathbf{x}_{\mathrm{eq}_2}} \cap SW_{23})$ that fulfills (92):

$$pt_1 = \begin{pmatrix} 0 \\ -\frac{a(\gamma-\alpha)}{b} \\ -(\gamma-\alpha) \end{pmatrix}, \tag{94}$$

and in $\mathbf{z}^{(2)}$ coordinates

$$pt_1 z_2 = \begin{pmatrix} 0 \\ \frac{a(\gamma-\alpha)}{b} \\ -(\gamma-\alpha) \end{pmatrix}. \tag{95}$$

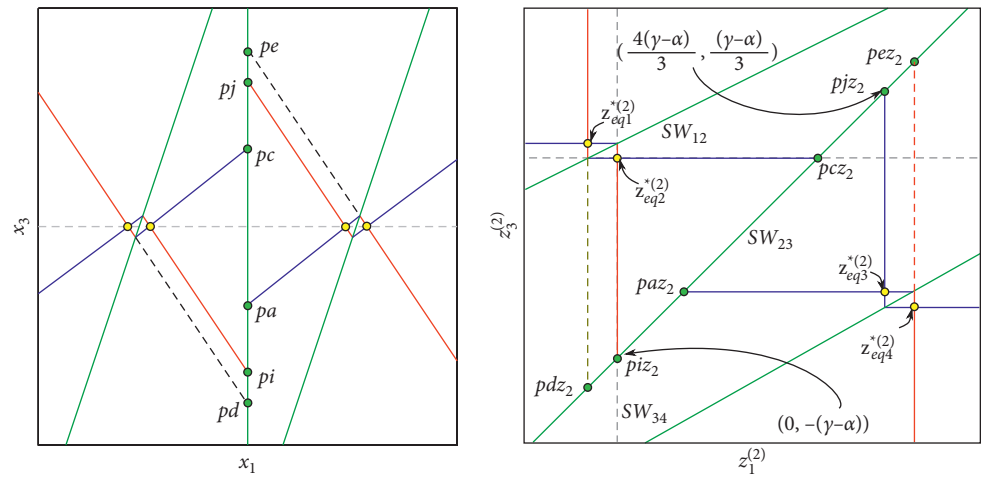

(a) (b)

FIGURE 10: Projection of the manifolds on (a) $x_1 - x_3$ and (b) $z_1^{(2)} - z_3^{(2)}$. The stable and unstable manifolds are marked with blue and red solid lines, respectively, the switching surfaces with green lines.

If we evaluate the trajectory with initial condition in $x_0 = pt_1z_2$, under the vector field of P_2 ignoring the effect of the vector field of P_1 and P_3, reaches the point $pt_2z_2 \in \mathrm{SW}_{23}$. The flow φ could go from P_2 to P_3 through the segment $\overline{pt_1z_2\, pt_2z_2}$. Thus, trajectories with initial condition close to A_{self1} but not in the attractor cross SW_{23} close to the segment $\overline{pt_1z_2\, pt_2z_2}$, then, R_1 should include this segment. However, when the vector field of all atoms is considered, trajectories with initial conditions close to pt_1z_2 could reach SW_{23} in points whose second component in $z^{(2)}$ coordinates is further from 0 than the second component in $z^{(2)}$ coordinates of pt_2z_2. This allows us to propose the region R_1 based on a larger segment $\overline{pi_1z_2\, pi_2z_2}$ such that $\overline{pt_1z_2\, pt_2z_2} \subset \overline{pi_1z_2\, pi_2z_2}$. Consider the initial condition piz_2 given in $\mathbf{z}^{(2)}$ coordinates by

$$piz_2 = \begin{pmatrix} 0 \\ 0 \\ -(\gamma - \alpha) \end{pmatrix}, \tag{96}$$

then, the radius with respect to $\mathbf{z}^*_{\mathrm{eq}_2}$ would be $(\gamma - \alpha)$. Remember that only the vector field of P_2 is considered and the trajectory rotates around the axis $z_1^{(2)}$. Let us think in an imaginary and impossible case when a trajectory with an initial condition in piz_2 rotates around the axis $z_1^{(2)}$ and reaches SW_{23}, but instead of the normal increment of radius, let us imagine that the increment in radius corresponds to an evolution time $t = 2\pi/b$ (360°). Thus, the $z_2^{(2)}$ component of this point is further from 0 than the $z_2^{(2)}$ component of pt_2z_2. Then, we could take $pi_2z_2 = pt_1z_2$ and find the $z_2^{(2)}$ component of pa_1z_2 from

$$\sqrt{\left(e^{a(2\pi/b)}(\gamma - \alpha)\right)^2 - (\gamma - \alpha)^2}. \tag{97}$$

Consider Assumption 1, then,

$$\sqrt{\left(e^{a(2\pi/b)}(\gamma - \alpha)\right)^2 - (\gamma - \alpha)^2} \le \gamma\sqrt{\left(e^{a(2\pi/b)}\right)^2 - 1} \le 0.80815\gamma \approx \frac{4\gamma}{5}. \tag{98}$$

Remember that $z_2^{(2)} = -x_2$, then, the points pi_1 and pi_2 are given by

$$pi_1 = \begin{pmatrix} 0 \\ \dfrac{4\gamma}{5} \\ -(\gamma - \alpha) \end{pmatrix}, \qquad pi_2 = \begin{pmatrix} 0 \\ -\dfrac{a(\gamma - \alpha)}{b} \\ -(\gamma - \alpha) \end{pmatrix}, \tag{99}$$

where $-(a(\gamma - \alpha)/b)$ is the tangent coordinate given by (92) for $x_3 = -(\gamma - \alpha)$.

Let us propose a region R_1 delimited by the following four points:

$$\begin{aligned} p_1 &= pi_1 + \left(0, 0, \frac{\gamma}{5}\right)^T, \\ p_2 &= pi_1 - \left(0, 0, \frac{\gamma}{5}\right)^T, \\ p_3 &= pi_2 + \left(0, -\left(\frac{2c - 2a}{3b}\right)\left(-\frac{\gamma}{5}\right), -\frac{\gamma}{5}\right)^T, \\ p_4 &= pi_2 + \left(0, -\left(\frac{2c - 2a}{3b}\right)\left(\frac{\gamma}{5}\right), \frac{\gamma}{5}\right)^T. \end{aligned} \tag{100}$$

Then, the symmetric region R_2 is delimited by the points:

$$\begin{aligned} q_1 &= -p_1, \\ q_2 &= -p_2, \\ q_3 &= -p_3, \\ q_4 &= -p_4. \end{aligned} \tag{101}$$

The regions R_1 and R_2 have been proposed taking into consideration that p d and pe are part of the regions and pa and pc are not. In Figure 11, R_1 and R_2 are shown in $\mathbf{z}^{(2)}$ coordinates.

Now, let us analyze some scenarios on these regions to see if the proposed regions are good candidates, at least in an estimated manner. In order to simplify the scenarios, in the following, it is considered that trajectories in $P_1 \cup P_2$ rotate only around the stable manifold of $\mathbf{x}_{eq_2}$, i.e., if only the vector field of P_2 is considered. Since $p_1z_2 - pi$ and $piz_2 - p_2z_2$ are given by

$$p_1z_2 - pi = \begin{pmatrix} \frac{2\gamma}{15} \\ -\frac{4\gamma}{5} \\ \frac{2\gamma}{15} \end{pmatrix}, \qquad pi - p_2z_2 = \begin{pmatrix} \frac{2\gamma}{15} \\ \frac{4\gamma}{5} \\ \frac{2\gamma}{15} \end{pmatrix}. \tag{102}$$

Let us define the set R_1b as follows:

$$R_1b = \left\{ \mathbf{z}^{(2)} \in \mathbb{R}^3 \colon z_1^{(2)} \in \left[-\frac{2\gamma}{15}, \frac{2\gamma}{15} \right] \right\}. \tag{103}$$

First, let us verify that the points in R_2 go to R_1b. The evaluation of the vector field in pj_1z_2 tells us that the spin is counterclockwise in $\mathbf{z}^{(2)}$ coordinates.

Consider the point q_2z_2 given by

$$q_2z_2 = \begin{pmatrix} \frac{22\gamma}{15} - \frac{4\alpha}{3} \\ \frac{4\gamma}{5} \\ \frac{7\gamma}{15} - \frac{\alpha}{3} \end{pmatrix}. \tag{104}$$

The angle produced by the radius from the point q_2z_2 to the $z_1(2)$ axis and the plane $z_1^{(2)} - z_2^{(2)}$ is given by

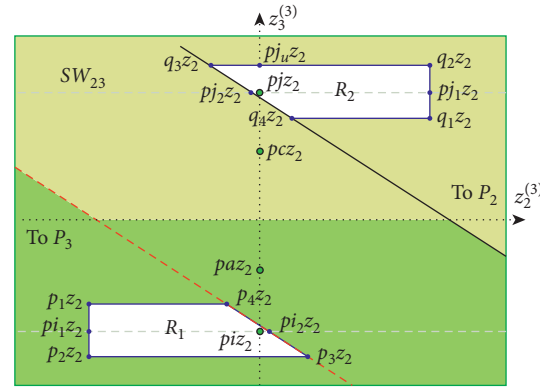

Figure 11: Regions R_1 and R_2 on the projection $z_2^{(2)} - z_3^{(2)}$.

$$\arctan\left(\frac{(7\gamma/15) - (\alpha/3)}{(4\gamma/5)} \right) = \arctan\left(\frac{7}{12} - \frac{5\alpha}{12\gamma} \right). \tag{105}$$

Under Assumption 1, the angle obeys the following inequality:

$$\arctan\left(\frac{7}{12} - \frac{5\alpha}{12\gamma} \right) \leq \arctan\left(\frac{7}{12} \right) \leq 0.5281. \tag{106}$$

Consider then that the trajectory with an initial condition in q_2z_2 evolves for a duration that corresponds to $\pi - 2(0.5281) = 2.0854$. If after this duration the first component of the state vector $z_1^{(2)} \leq 2\gamma/15$ means that the trajectory with initial condition in q_2z_2 reaches R_1b. After this duration, $z_1^{(2)}$ is given by

$$z_1^{(2)} = \left(\frac{22\gamma}{15} - \frac{4\alpha}{3} \right) e^{c(2.0854/b)}. \tag{107}$$

Under Assumption 1 for a big value of $z_1^{(2)}$:

$$\left(\frac{22\gamma}{15} - \frac{4\alpha}{3} \right) e^{c(2.0854/b)} \leq \left(\frac{22\gamma}{15} \right) e^{c(2.0854/b)} \leq 0.0791\gamma < \frac{2\gamma}{15}. \tag{108}$$

Thus, q_2z_2 reaches the region R_1b. Moreover, since the points in the segment $\overline{q_2z_2q_1z_2}$ produce a radius whose angle with the plane $z_1^{(2)} - z_2^{(2)}$ is between 0 and 0.5281, the trajectories with the initial condition in this segment also reach the set R_1b.

Now consider the point q_3z_2

$$q_3z_2 = \begin{pmatrix} \frac{22\gamma}{15} - \frac{4\alpha}{3} \\ \frac{2c\gamma - 17a\gamma}{15b} + \frac{a\alpha}{b} \\ \frac{7\gamma - 5\alpha}{15} \end{pmatrix}. \tag{109}$$

The angle of the radius at q_3z_2 with the plane $z_1^{(2)} - z_2^{(2)}$ is as follows:

$$-\arctan\left(\frac{((2c\gamma-17a\gamma)/15b)+a\alpha/b}{(7\gamma-5\alpha)/15}\right)=-\arctan\left(\frac{2c\gamma-17a\gamma+15a\alpha}{7b\gamma-5b\alpha}\right). \tag{110}$$

Under Assumption 1, the angle should be less than

$$\begin{aligned}-\arctan\left(\frac{2c\gamma-17a\gamma+15a\alpha}{7b\gamma-5b\alpha}\right)&\leq -\arctan\left(\frac{2c}{6.5b}-\frac{17a}{6.5b}+\frac{1.5a}{6.5b}\right),\\ -\arctan\left(\frac{2c}{6.5b}-\frac{17a}{6.5b}+\frac{1.5a}{6.5b}\right)&\leq -\arctan\left(-\frac{4}{6.5}-\frac{17}{6.5(25)}+\frac{1.5}{6.5(25)}\right)=0.6179.\end{aligned} \tag{111}$$

To verify that the trajectory starting in q_3z_2 is not going to reach SW_{23} when the radius form an angle of $3\pi/2$ with the plane $z_1^{(2)}-z_2^{(2)}$, let us consider the following exaggerated scenario: The radius size corresponds to a duration equivalent to $10\pi/9$, but the $z_1^{(2)}$ component corresponds to a duration equivalent to $2\pi/3$ of oscillation, i.e., when the radius forms an angle of $3\pi/2$ with the plane $z_1^{(2)}-z_2^{(2)}$ a smaller radius than the real one is considered; also, a larger value of $z_1^{(2)}$ than the real value is considered.

Then to obtain the radius,

$$r=e^{a(10\pi/9b)}\sqrt{\left(\frac{2c\gamma-17a\gamma}{15b}+\frac{a\alpha}{b}\right)^2+\left(\frac{7\gamma-5\alpha}{15}\right)^2}. \tag{112}$$

Under Assumption 1 for the largest radius,

$$\begin{aligned}e^{a(10\pi/9b)}\sqrt{\left(\frac{2c\gamma-17a\gamma}{15b}+\frac{a\alpha}{b}\right)^2+\left(\frac{7\gamma-5\alpha}{15}\right)^2}&\leq e^{a(10\pi/9b)}\sqrt{\left(\frac{2c\gamma-17a\gamma}{15b}\right)^2+\left(\frac{7\gamma}{15}\right)^2},\\ e^{a(10\pi/9b)}\gamma\sqrt{\left(\frac{2c-17a}{15b}\right)^2+\left(\frac{7}{15}\right)^2}&\leq 0.5984\gamma.\end{aligned} \tag{113}$$

The value of $z_1^{(2)}$ after the duration that corresponds to $2\pi/3$ is as follows:

$$\left(\frac{22\gamma}{15}-\frac{4\alpha}{3}\right)e^{c(2\pi/3b)}. \tag{114}$$

Under Assumption 1, for the biggest value of $z_1^{(2)}$

$$\begin{aligned}\left(\frac{22\gamma}{15}-\frac{4\alpha}{3}\right)e^{c(2\pi/3b)}&\leq\left(\frac{22\gamma}{15}\right)e^{c(2\pi/3b)},\\ \left(\frac{22\gamma}{15}\right)e^{c(2\pi/3b)}&\leq 0.07814\gamma<\frac{2\gamma}{15}.\end{aligned} \tag{115}$$

The points in SW_{23} fulfills the following equation:

$$z_3^{(2)}=-(\gamma-\alpha)+z_1^{(2)}. \tag{116}$$

At this angle of $3\pi/2$ the radius is $r=-z_3^{(2)}$. Then, if the found values for this scenario fulfill the following inequality, it can be concluded that the trajectory with an initial condition in q_3z_2 does not reach SW_{23} after a duration that corresponds to an oscillation of 120°:

$$-.5984\gamma>-(\gamma-\alpha)+0.07814\gamma. \tag{117}$$

Under Assumption 1 and the worst case,

$$-.5984\gamma>-\frac{9\gamma}{10}+0.07814\gamma=-0.82186\gamma. \tag{118}$$

Then, the trajectory remains for the duration that corresponds to $2\pi/3$. Furthermore, since $z_1^{(2)}<2\gamma/15$ the trajectory reaches R_1b. Since q_3z_2 is the point in the set $\left\{\mathbf{z}^{(2)}\in R_2\colon z_2^{(2)}\leq 0\right\}$ that produces the largest radius of that set, the same conclusion applies to the points in this set.

For the trajectories with the initial condition in the set $\left\{\mathbf{z}^{(2)}\in R_2\colon z_2^{(2)}>0\right\}$ the duration is equivalent to more than $2\pi/3$. Thus, the trajectories that start in R_2 reach the set R_1b.

Now to verify that the trajectories that start in R_2 reach $R_1\subset R_1b$ is enough to verify the trajectories starting in the

segment $\overline{q_1z_2q_2z_2}$, since these produce the largest radius in R_1b.

Consider the points q_1z_2 and q_2z_2

$$q_1z_2 = \begin{pmatrix} \frac{6\gamma}{5} - \frac{4\alpha}{3} \\ \frac{4\gamma}{5} \\ \frac{\gamma}{5} - \frac{\alpha}{3} \end{pmatrix}, \quad q_2z_2 = \begin{pmatrix} \frac{22\gamma}{15} - \frac{4\alpha}{3} \\ \frac{4\gamma}{5} \\ \frac{7\gamma}{15} - \frac{\alpha}{3} \end{pmatrix}. \tag{119}$$

The largest radius is at q_2z_2 while the smaller angle is at q_1z_2, then let us consider that radius of q_2z_2 with the angle of q_1z_2 and the end position at $3\pi/2$ with respect to the plane $z_1^{(2)} - z_2^{(2)}$, which is more than the possible rotation. The angle is given by

$$\arctan\left(\frac{(\gamma/5) - (\alpha/3)}{(4\gamma/5)}\right) = \arctan\left(\frac{1}{4} - \frac{5\alpha}{12\gamma}\right). \tag{120}$$

Under Assumption 1, the smallest angle is as follows:

$$\arctan\left(\frac{1}{4} - \frac{5\alpha}{12\gamma}\right) \geq \arctan\left(\frac{5}{24}\right) = 0.2054. \tag{121}$$

Thus for $3\pi/2 - 0.2054 = 4.507$

$$\sqrt{\left(\frac{4\gamma}{5}\right)^2 + \left(\frac{7\gamma}{15} - \frac{\alpha}{3}\right)^2}\, e^{a(4.507/b)}. \tag{122}$$

Under Assumption 1 for the biggest radius,

$$\sqrt{\left(\frac{4\gamma}{5}\right)^2 + \left(\frac{7\gamma}{15} - \frac{\alpha}{3}\right)^2}\, e^{a(4.507/b)} \leq \sqrt{\left(\frac{4\gamma}{5}\right)^2 + \left(\frac{7\gamma}{15}\right)^2}\, e^{a(4.507/b)},$$

$$\sqrt{\left(\frac{4\gamma}{5}\right)^2 + \left(\frac{7\gamma}{15}\right)^2}\, e^{a(4.507/b)} \leq \gamma\sqrt{\frac{193}{225}} e^{a(4.507/b)} \leq 1.1091\gamma. \tag{123}$$

Consider the points p_1z_2, pa_1z_2, and p_2z_2

$$p_1z_2 = \begin{pmatrix} \frac{2\gamma}{15} \\ -\frac{4\gamma}{5} \\ \alpha - \frac{13\gamma}{15} \end{pmatrix}, \quad pa_1z_2 = \begin{pmatrix} 0 \\ -\frac{4\gamma}{5} \\ \alpha - \gamma \end{pmatrix}, \quad p_2z_2 = \begin{pmatrix} -\frac{2\gamma}{15} \\ -\frac{4\gamma}{5} \\ \alpha - \frac{17\gamma}{15} \end{pmatrix}. \tag{124}$$

The minimum radius in the segment $\overline{pa_1z_2, pa_2z_2}$ is as follows:

$$\sqrt{\left(\frac{4\gamma}{5}\right)^2 + \left(\alpha - \frac{13\gamma}{15}\right)^2}. \tag{125}$$

Under Assumption 1 for the smallest radius,

$$\sqrt{\left(\frac{4\gamma}{5}\right)^2 + \left(\alpha - \frac{13\gamma}{15}\right)^2} \geq \sqrt{\left(\frac{4\gamma}{5}\right)^2 + \left(\frac{23\gamma}{30}\right)^2} = 1.1081\gamma. \tag{126}$$

$1.1092\gamma \approx 1.1081\gamma$, even when the angle of rotation was exaggerated, it is expected that the trajectories with an initial condition in R_1 reach R_2 or a self-excited attractor. In the same way, the trajectories with an initial condition in R_2 reach R_1 or go to a self-excited attractor.

Let us look at the system in $\mathbf{z}^{(2)}$ coordinates, as in the previous section with the previous switching surfaces, as γ grows, SW_{23} and pcz_2 is further from the $\mathbf{z}^*_{eq2}$ and then it take more time for the trajectories close to pcz_2 to travel along the $z_1^{(2)}$ direction to get close to $\mathbf{z}^*_{eq2}$. However, the expansion along $z_2^{(2)}$ and $z_3^{(2)}$ remains the same; then the subsets of initial conditions that reach the self-excited attractors without reaching SW_{23} again shrink in I_1 and I_2 but this time, as opposed to the previous case there exist a value of γ such that the intersection disappear.

Then for a sufficiently big value of γ we have a region R_1 such that any trajectory starting there remains crossing R_1 for $t > 0$. Then, we could expect that exists either a periodic orbit, a hidden limit cycle, a hidden chaotic attractor, or a combination of the previous, which should go through R_1 and R_2.

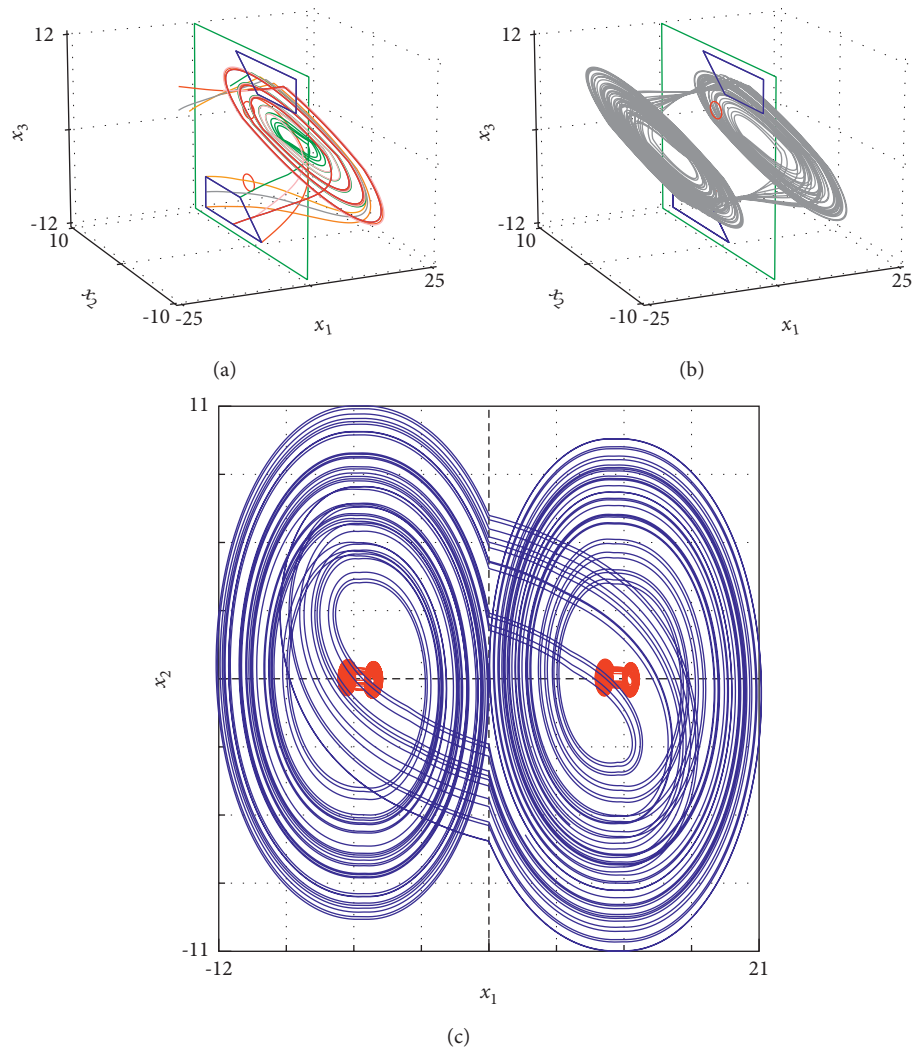

FIGURE 12: In (a), seven trajectories of the system given by (1), (3), (5), (13), and (90) starting in R_1 with $a = 0.2$, $b = 5$, $c = -7$, $\alpha = 1$ and $\gamma = 10$. In (b), hidden attractor for the same parameters and the initial condition $\mathbf{x}_0 = (0, 0, 0)^T$ for $t \in [50000, 50100]$. In (c), the projection of the self-excited attractors and the hidden attractor onto the plane $x_1 - x_2$.

Also, as small differences in the initial conditions in R_1 could eventually produce a big separation of trajectories in SW_{23}, sensitivity to initial conditions could also be expected. However, the formal proof is out of the scope of this work.

To verify the region for the parameters $a = 0.2$, $b = 5$, $c = -7$, $\alpha = 1$ and $\gamma = 10$ seven trajectories have been simulated and are shown in Figure 1(a).

The simulations of the two particular cases coincide with the conjecture. In Figure 12(b) it is shown the hidden attractor for the parameters $a = 0.2, b = 5, c = -7, \alpha = 1$ and $\gamma = 10$ and the initial condition $\mathbf{x}_0 = (0, 0, 0)^T$ for $t \in [50000, 50100]$. In Figure 1(c), it is shown the projection of the hidden attractor and the two self-excited attractors onto the plane $x_1 - x_2$ for the same parameters.

6. Conclusions

In this work, an approach for the generation of multiscroll attractors was studied based on heteroclinic orbits. Particularly, we presented a quad-scroll self-excited attractor, which is split into two double-scroll self-excited attractor, so the system bifurcates from monostability to biestability. The approach is based on the coexistence of double-scroll self-excited attractors surrounded the equilibria and presenting heteroclinic orbits. Increasing the distances between the double-scroll self-excited attractors generates a heteroclinic-like orbit between the equilibria of two different double-scroll self-excited attractors. It is possible to generate hidden attractors surrounding the self-excited attractors by

breaking the heteroclinic-like orbit. The study revealed a relationship between the existence of a hidden attractor and the trajectories that, when are seen on a larger scale resemble heteroclinic orbits which join the self-excited attractors. The findings suggest that new classes of multistable systems with a different number of self-excited and hidden attractors can be designed with a geometric approach.

Data Availability

The data used to support the findings of this study are included within the article.

Disclosure

A preprint of this study has previously been published (https://arxiv.org/abs/1908.03789).

Conflicts of Interest

There are no conflicts of interest regarding the publication of this paper.

Acknowledgments

R.J. Escalante-González is thankful to CONACYT for the scholarships granted. Eric Campos acknowledges CONACYT for the financial support through Project No. A1-S-30433.

References

[1] G. A. Leonov, N. V. Kuznetsov, and V. I. Vagaitsev, "Localization of hidden Chua's attractors," *Physics Letters A*, vol. 375, no. 23, pp. 2230–2233, 2011.

[2] D. Dudkowski, S. Jafari, T. Kapitaniak, N. V. Kuznetsov, G. A. Leonov, and A. Prasad, "Hidden attractors in dynamical systems," *Physics Reports*, vol. 637, pp. 1–50, 2016.

[3] A. Anzo-Hernández, H. E. Gilardi-Velázquez, and E. Campos-Cantón, "On multistability behavior of unstable dissipative systems," *Chaos: An Interdisciplinary Journal of Nonlinear Science*, vol. 28, no. 3, Article ID 033613, 2018.

[4] M. A. Kiseleva, N. V. Kuznetsov, and G. A. Leonov, "Hidden attractors in electromechanical systems with and without equilibria," *IFAC-PapersOnLine*, vol. 49, no. 14, pp. 51–55, 2016.

[5] J. C. Sprott, "Some simple chaotic flows," *Physical Review. E, Statistical Physics, Plasmas, Fluids, and Related Interdisciplinary Topics*, vol. 50, no. 2, pp. R647–R650, 1994.

[6] W. G. Hoover, "Remark on "Some simple chaotic flows"" *Physical Review A*, vol. 51, no. 1, pp. 759-760, 1995.

[7] Z. Wei, "Dynamical behaviors of a chaotic system with no equilibria," *Physics Letters A*, vol. 376, no. 2, pp. 102–108, 2011.

[8] X. Wang and G. Chen, "Constructing a chaotic system with any number of equilibria," *Nonlinear Dynamics*, vol. 71, no. 3, pp. 429–436, 2013.

[9] R. J. Escalante-González and E. Campos-Cantón, "Generation of chaotic attractors without equilibria via piecewise linear systems," *International Journal of Modern Physics C*, vol. 28, no. 01, Article ID 1750008, 2017.

[10] S. Jafari, J. C. Sprott, and S. M. R. Hashemi Golpayegani, "Elementary quadratic chaotic flows with no equilibria," *Physics Letters A*, vol. 377, no. 9, pp. 699–702, 2013.

[11] Z. Wang, S. Cang, E. O. Ochola, and Y. Sun, "A hyperchaotic system without equilibrium," *Nonlinear Dynamics*, vol. 69, no. 1-2, pp. 531–537, 2012.

[12] V.-T. Pham, "Sundarapandian vaidyanathan, christos volos, sajad jafari, and sifeu takougang kingni. A no-equilibrium hyperchaotic system with a cubic nonlinear term," *Optik*, vol. 127, no. 1, pp. 3259–3265, 2016.

[13] C. Li, J. C. Sprott, W. Thio, and H. Zhu, "A new piecewise linear hyperchaotic circuit," *IEEE Transactions on Circuits and Systems II: Express Briefs*, vol. 61, no. 12, pp. 977–981, 2014.

[14] F. R. Tahir, S. Jafari, V.-T. Pham, C. Volos, and X. Wang, "A novel no-equilibrium chaotic system with multiwing butterfly attractors," *International Journal of Bifurcation and Chaos*, vol. 25, no. 4, Article ID 1550056, 2015.

[15] J. A. K. Suykens, A. Huang, and L. O. Chua, "A family of n-scroll attractors from a generalized Chua's circuit," *Archiv fur Elektronik und Ubertragungstechnik*, vol. 51, no. 3, pp. 131–138, 1997.

[16] W. K. S. Tang, G. Q. Zhong, G. Chen, and K. F. Man, "Generation of N-Scroll attractors via sine function," *IEEE Transactions on Circuits and Systems I: Fundamental Theory and Applications*, vol. 48, no. 11, pp. 1369–1372, 2001.

[17] M. . E. Yalçin, J. A. K. Suykens, and J. Vandewalle, "Families of scroll grid attractors," *International Journal of Bifurcation and Chaos*, vol. 12, no. 1, pp. 23–41, 2002.

[18] B. Aguirre-Hernández, E. Campos-Cantón, J. A. López-Renteria, and E. C. Díaz González, "A polynomial approach for generating a monoparametric family of chaotic attractors via switched linear systems," *Chaos, Solitons & Fractals*, vol. 71, no. 1, pp. 100–106, 2015.

[19] E. Campos-Cantón, "Chaotic attractors based on unstable dissipative systems via third-order differential equation," *International Journal of Modern Physics C*, vol. 27, no. 1, Article ID 1650008, 2016.

[20] R. J. Escalante-González, E. Campos-Cantón, and M. Nicol, "Generation of multi-scroll attractors without equilibria via piecewise linear systems," *Chaos: An Interdisciplinary Journal of Nonlinear Science*, vol. 27, no. 5, Article ID 053109, 2017.

[21] X. Hu, C. Liu, L. Liu, J. Ni, and S. Li, "Multi-scroll hidden attractors in improved sprott a system," *Nonlinear Dynamics*, vol. 86, no. 3, pp. 1725–1734, 2016.

[22] S. Jafari, V.-T. Pham, and T. Kapitaniak, "Multiscroll chaotic sea obtained from a simple 3d system without equilibrium," *International Journal of Bifurcation and Chaos*, vol. 26, no. 02, Article ID 1650031, 2016.

[23] X. Hu, C. Liu, L. Liu, Y. Yao, and G. Zheng, "Multi-scroll hidden attractors and multi-wing hidden attractors in a 5-dimensional memristive system," *Chinese Physics B*, vol. 26, no. 11, Article ID 110502, 2017.

[24] L. J. Ontañón-García and E. Campos-Cantón, "Widening of the basins of attraction of a multistable switching dynamical system with the location of symmetric equilibria," *Nonlinear Analysis: Hybrid Systems*, vol. 26, pp. 38–47, 2017.

[25] S. Ergun and S. Ozoguz, "Truly random number generators based on a double-scroll attractor," in *Proceedings of the 2006 49th IEEE International Midwest Symposium on Circuits and Systems*, vol. 1, pp. 322–326, Puerto Rico, Mexico, August 2006.

[26] M. García-Martínez, L. J. Ontañón-García, E. Campos-Cantón, and S. Čelikovský, "Hyperchaotic encryption based

on multi-scroll piecewise linear systems," *Applied Mathematics and Computation*, vol. 270, pp. 413–424, 2015.

[27] X. Jin, X. Duan, H. Jin, and Y. Ma, "A novel hybrid secure image encryption based on the shuffle algorithm and the hidden attractor chaos system," *Entropy*, vol. 22, no. 6, 2020.

[28] R. J. Escalante-González and E. Campos, "Multistable systems with hidden and self-excited scroll attractors generated via piecewise linear systems," *Complexity*, vol. 2020, Article ID 7832489, 12 pages, 2020.

[29] R. J. Escalante-González and E. Campos-Cantón, "Coexistence of hidden attractors and self-excited attractors through breaking heteroclinic-like orbits of switched systems," arXiv, 2019, https://arxiv.org/abs/1908.03789.

[30] E. Campos-Cantón, J. G. Barajas-Ramirez, G. Solís-Perales, and R. Femat, "Multiscroll attractors by switching systems," *Chaos*, vol. 20, no. 1, Article ID 013116, 2010.

Hindawi
Complexity
Volume 2021, Article ID 9913114, 11 pages
https://doi.org/10.1155/2021/9913114

Research Article

Mamdani-Type Fuzzy-Based Adaptive Nonhomogeneous Synchronization

J. R. Pulido–Luna,[1] **J. A. López–Rentería**,[2] **and N. R. Cazarez–Castro**[1]

[1]*Departamento de Ingeniería Eléctrica y Electrónica, Tecnológico Nacional de México, Instituto Tecnológico de Tijuana, Calzada Tecnológico S/N, Fracc, Tomás Aquino, Tijuana, Baja California, CP 22414, Mexico*
[2]*CONACyT-Tecnológico Nacional de México, Instituto Tecnológico de Tijuana, Calzada Tecnológico S/N, Fracc, Tomás Aquino, Tijuana, Baja California, CP 22414, Mexico*

Correspondence should be addressed to J. A. López–Rentería; jorge.lopez@tectijuana.edu.mx and N. R. Cazarez–Castro; nohe@ieee.org

Received 26 March 2021; Accepted 28 July 2021; Published 24 August 2021

Academic Editor: Zakia Hammouch

The aim of this work is the design of an adaptive controller based on Mamdani-type fuzzy inference systems. The input control is constructed with saturation functions' fuzzy-equivalents, which works as the adaptive scheme of the controller. This control law is designed to stabilize the error system to synchronize a pair of chaotic nonhomogeneous piecewise systems. Finally, an illustrative example as numerical evidence is developed.

1. Introduction

The synchronization phenomena among dynamical systems are a widely studied topic in the last decades due to the vast amount of applications in science and engineering [1–3]. In the related literature, dynamical systems and synchronization applications in many fields can be found, from biology [4, 5], mechanical systems [6–9], chemistry [10], physics [11, 12], fuzzy modeling [13–16] to secure communications [17–19], among many others. In general, it is said that a set of dynamical systems achieve synchronization if trajectories in each system approach a common trajectory.

Among the systems studied in synchronization, the ones that stand out are the chaotic systems; chaotic systems exhibit more complex dynamics, and they must satisfy the next conditions according to Devaney's definition of chaos [20]: (i) sensitive dependence to initial conditions, (ii) dense periodic orbits, and (iii) must be transitive. Many works consider the problem of chaos synchronization; in [21], the authors synchronize chaotic systems by linking them with common signals. Chua et al. [22] explore the synchronization phenomena in Chua's circuit, proven to be the simplest electronic circuit to exhibit chaotic behaviour; on the contrary, Femat and Solís-Perales [23] discuss several phenomena involved with chaos synchronization, and a feedback controller is implemented to illustrate such synchronization. In [24], chaos synchronization between two coupled chaotic dynamical systems is presented. Conditions for global asymptotic synchronization are presented and a new method for the analysis of the stability of the synchronization is reported, but different techniques and applications are still developed for this type of system in the last years. In [25], the authors present the design of a rule-based controller for a class of master-slave chaos synchronization, and unlike traditional methods, the control law obtained from this method has less maximum magnitude of the control signal and reduces the actuator saturation phenomenon in mechanical systems. AL-Azzawi and Aziz [26] present the synchronization between two nonhomogeneous hyperchaotic systems. A nonlinear control is used to achieve synchronization and also report a stability analysis of the error dynamics system using Lyapunov's second method and Cardano's method. In [27], higher-order adaptive PID controllers as a new generation of PID controllers for chaos

synchronization is designed, and in [28], the authors study the collected dynamics of a n-coupled piecewise linear systems with different numbers of scrolls.

Along the synchronization schemes and controllers designed, the adaptive type has been proven useful depending on the application [29–32], and this kind of controller allows the optimization of the energy necessary to accomplish the synchronization between systems.

Wu et al. [29] study the synchronization of two chaotic systems which are not identical and use adaptive controllers to adjust the parameters of the systems such that the two systems will synchronize. In [25], the design of a rule-based fuzzy controller for a class of master-slave chaos synchronization is presented; however, the whole control action is substituted by the fuzzy controller, while Xi et al. propose an adaptive robust finite-time control method based on a global sliding surface for the synchronization of a class of chaotic systems in [32].

The main contribution of this work is the design of an adaptive synchronization scheme based on a Mamdani-type inference system, an equivalence with saturation functions is used, and the stability of the error system is proven using Lyapunov stability theory. Both, master and slave systems can be described in as many pieces as necessary. In order to provide evidence of energy optimization, a comparison between fixed gain and adaptive gain in the same synchronization scheme is reported in a satisfactory fashion.

The rest of this work is organized as follows. Section 2 presents the problem statement and the systems description. Section 3 introduces the basic concepts of synchronization and Mamdani fuzzy inference system (FIS). Section 4 presents the main results with an example as numeric evidence; finally, in Section 5, the conclusions are presented.

2. Problem Statement

Consider a classic master-slave synchronization scheme as

$$\text{Master: } \dot{x} = f(x), \tag{1}$$

$$\text{Slave: } \dot{y} = g(y) + u, \tag{2}$$

where both the master and slave system are piecewise switching systems [33–36] of the form

$$\dot{z} = \mathrm{A}z + B, \tag{3}$$

with

$$B = \begin{cases} B_1 & \text{if} \quad z \in \mathscr{D}_1 \\ B_2 & \text{if} \quad z \in \mathscr{D}_2 \\ \vdots & \vdots \quad \vdots \\ B_j & \text{if} \quad z \in \mathscr{D}_j \end{cases}, \tag{4}$$

that undergo chaotic behaviour, where $x, y \in \mathbb{R}^3$ are the state variables, $B_j = (b_{j1}, b_{j2}, b_{j3})^T$, which are the switching laws of the piecewise chaotic systems, and $u \in \mathbb{R}^3$ is the actuator in charge of achieve the synchronization of the slave over the master. Moreover, the domains $\mathscr{D}_j$ satisfy $\mathbb{R}^3 = \cup_{j=1}^{m} \mathscr{D}_j$ and $\cap_{j=1}^{m} \mathscr{D}_j = \varnothing$ for $m > 1$. The objective of this work is to design the controller u as an adaptive controller of the form

$$u = \begin{cases} u_1 & \text{if} \quad y \in \mathscr{E}_1 \\ u_2 & \text{if} \quad y \in \mathscr{E}_2 \\ \vdots & \vdots \quad \vdots \\ u_k & \text{if} \quad y \in \mathscr{E}_k \end{cases}, \tag{5}$$

for $k = 1, 2, \ldots, n$, using a Mamdani-based fuzzy inference system for each u_k to synchronize the master and slave systems, optimizing the energy usage for the control action. Consequently, there are three major objectives to develop in this work:

(1) The equivalence relation between the fuzzy-based controller and the saturation functions

(2) Achieve adaptive synchronization between systems

(3) Ensure asymptotic stability of the error system via Lyapunov's theory

3. Preliminaries

In this section, the basic concepts of synchronization and fuzzy inference system design will be presented; this concept will be convenient to understand how it is possible to achieve the principal objective of this work.

3.1. Synchronization Scheme. Consider the master-slave synchronization scheme defined in [37] as

$$\begin{aligned} \text{Master: } \dot{x} &= f(x), \\ \text{Slave: } \dot{y} &= g(y) + u, \end{aligned} \tag{6}$$

with $x, y \in \mathbb{R}^n$ as the system states and

$$u = -Pe + f(x) - g(y), \tag{7}$$

where $P = \mathrm{diag}\{p_1^2, p_2^2, p_3^2\}$. The synchronization is achieved when the master and slave system synchronize, i.e., when the synchronization objective,

$$\lim_{t \longrightarrow \infty} \| y(t) - x(t) \| = 0, \tag{8}$$

is reached.

Definition 1 (see [3]). A system of the form $\dot{x} = f(x)$ is called master system if its flow $x(t)$ is independent. A system of the form $\dot{y} = g(y) + u$ is called slave system of the master system if its flow $y(t)$ is constrained by the flow of the master system.

From the previous definition, a slave system is constrained by a master system via a specific condition, which means that a slave system will be controlled towards a master system under a specific control law. This phenomenon is called the synchronization of the slave and master systems under such a specific condition [3, 38].

3.2. Fuzzy Inference System Design. The design of the fuzzy inference systems considers an IF-THEN fuzzy rules based on the form [39]

$$R_i\text{: IF } e \text{ is } M_i, \quad \text{THEN } p \text{ is } H_i, \tag{9}$$

where e is the error between two states, and the input of the membership functions is

$$M_{-1}(e) = \begin{cases} 1, & \text{if } e < \Phi_{-1}, \\ \dfrac{1}{\Phi_{-1}} e, & \text{if } \Phi_{-1} \le e \le \Phi_0, \\ 0, & \text{if } e > \Phi_0, \end{cases}$$

$$M_0(e) = \begin{cases} -\dfrac{1}{\Phi_{-1}} e + 1, & \text{if } \Phi_{-1} \le e < \Phi_0, \\ -\dfrac{1}{\Phi_1} e + 1, & \text{if } \Phi_0 \le e \le \Phi_1, \\ 0, & \text{elsewhere}, \end{cases} \tag{10}$$

$$M_1(e) = \begin{cases} 0, & \text{if } e < \Phi_0, \\ \dfrac{1}{\Phi_1} e, & \text{if } \Phi_0 \le e \le \Phi_1, \\ 1, & \text{if } e > \Phi_1, \end{cases}$$

with $\Phi_{-1} = -\Phi_1$, while the output membership functions are singletons, defined as

$$H_{-1}(p) = \begin{cases} 1, & \text{if } p = \Omega_{-1}, \\ 0, & \text{elsewhere}, \end{cases}$$
$$H_0(p) = \begin{cases} 1, & \text{if } p = \Omega_0, \\ 0, & \text{elsewhere}, \end{cases} \tag{11}$$
$$H_1(p) = \begin{cases} 1, & \text{if } p = \Omega_1, \\ 0, & \text{elsewhere}. \end{cases}$$

The input and output membership functions are depicted in Figure 1. Now, consider the Mamdani-type fuzzy inference system, with product in the antecedent and center of average as the defuzzifier method. Then, the fuzzy inference system is written as

$$p(e) = \sum_{i=-1}^{1} \left\{ \frac{M_i(e)}{\sum_{j=-1}^{1} M_j(e)} \right\} \Omega_i = \sum_{i=-1}^{1} X_i(e) \Omega_i, \tag{12}$$

where Ω_i refers the crisp value of the output regarding of e. The function $X_i(e)$ must satisfy the following conditions [40, 41]:

(i) $X_i(e)$ is a locally Lipschitz continuous and bounded function

(ii) $X_i(0) = 0$

(iii) $X_i(e) = X_i(-e)$

The designed rule base matrix is given in Table 1.

Only two rules are fired at the same time [41, 42], for any value of e. Moreover, it satisfies

$$\sum_{i=-1}^{1} X_i(e) = 1, \tag{13}$$

which is a linear convex combination.

4. Main Results

Consider the synchronization error as $e = y - x$. The error dynamics are defined as

$$\dot{e} = g(y) - f(x) + u, \tag{14}$$

where the controller u is

$$u = -Pe + f(x) - g(y), \tag{15}$$

with $P = \text{diag}\{p_1^2, p_2^2, p_3^2\}$. In the following, given the sectorial functions provided from the FIS (15), it is necessary to consider the matrix of adapting $P = \text{diag}\{p_1^2(e_1), p_2^2(e_2), p_3^2(e_3)\}$. Then, we can establish the following result.

Lemma 1. *The controller $u = -Pe + f(x) - g(y)$ can be expressed as*

$$u = -\begin{pmatrix} \left(\Omega_1^1 \,\text{sat}\left(\dfrac{e_1}{\Phi_1^1}\right)\right)^2 e_1 \\ \left(\Omega_1^2 \,\text{sat}\left(\dfrac{e_2}{\Phi_1^2}\right)\right)^2 e_2 \\ \left(\Omega_1^3 \,\text{sat}\left(\dfrac{e_3}{\Phi_1^3}\right)\right)^2 e_3 \end{pmatrix} + f(x) - g(y). \tag{16}$$

Proof. For each $l = 1, 2, 3$, it is possible to rewrite (15) as

$$p_l(e_l) = \begin{cases} \dfrac{\Omega_1^l}{\Phi_1^l} e_l, & \text{if } |e_l| \le \Phi_1^l, \\ \Omega_1^l, & \text{if } |e_l| > \Phi_1^l. \end{cases} \tag{17}$$

Thus, each FIS can be written as a piecewise linear function as follows:

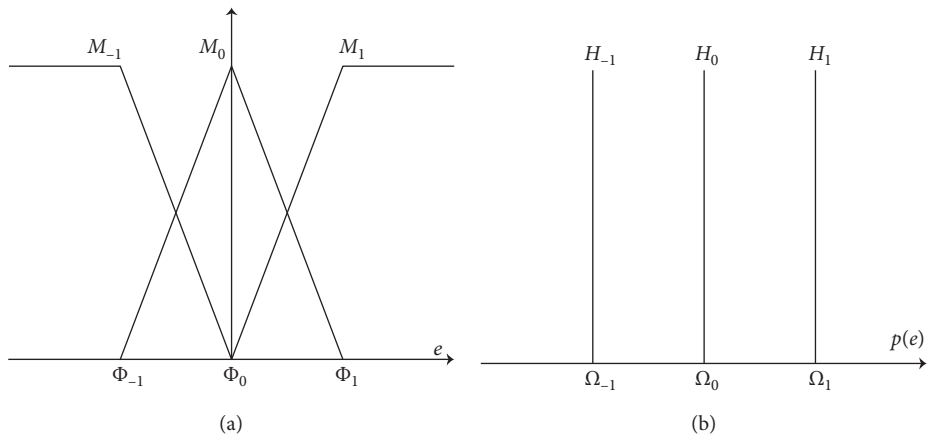

Figure 1: Membership functions: (a) input; (b) output.

Table 1: Fuzzy rule base.

Input (e)	Output ($p(e)$)
M_{-1}	H_{-1}
M_0	H_0
M_1	H_1

$$
\begin{aligned}
p_l(e_l) &= \Omega_1^l \begin{cases} \dfrac{e_l}{\Phi_1^l}, & if\ |e_l| \le \Phi_1^l, \\ 1, & if\ |e_l| > \Phi_1^l, \end{cases} \\
&= \Omega_1^l \begin{cases} \dfrac{e_l}{\Phi_1^l}, & \text{if } \dfrac{e_l}{\Phi_1^l} \le 1, \\ 1, & \text{if } \dfrac{e_l}{\Phi_1^l} > 1, \end{cases} \\
&= \Omega_1^l \operatorname{sat}\left(\frac{e_l}{\Phi_1^l}\right).
\end{aligned} \tag{18}
$$

Substituting (18) in each p_l of (15), it is possible to rewrite u as

$$
u = -\begin{pmatrix} \left(\Omega_1^1 \operatorname{sat}\left(\dfrac{e_1}{\Phi_1^1}\right)\right)^2 e_1 \\ \left(\Omega_1^2 \operatorname{sat}\left(\dfrac{e_2}{\Phi_1^2}\right)\right)^2 e_2 \\ \left(\Omega_1^3 \operatorname{sat}\left(\dfrac{e_3}{\Phi_1^3}\right)\right)^2 e_3 \end{pmatrix} + f(x) - g(y), \tag{19}
$$

as previously stated.

Once the piecewise controller is described, whose fuzzy component is the candidate to work as the adaptive scheme, in the following result, we formalize this assertion. □

Theorem 1. *The synchronization scheme formed by (1) and (2) achieves synchronization under the adaptive controller (16). Thus, the error system (14) is asymptotically stable.*

Proof. Consider the quadratic Lyapunov candidate function:

$$
V(e) = \frac{1}{2} e^T P e. \tag{20}
$$

From Lemma 1, it is known that

$$
Pe = \begin{pmatrix} \left(\Omega_1^1 \operatorname{sat}\left(\dfrac{e_1}{\Phi_1}\right)\right)^2 e_1 \\ \left(\Omega_1^2 \operatorname{sat}\left(\dfrac{e_2}{\Phi_1}\right)\right)^2 e_2 \\ \left(\Omega_1^3 \operatorname{sat}\left(\dfrac{e_3}{\Phi_1}\right)\right)^2 e_3 \end{pmatrix}. \tag{21}
$$

The time derivative of (20) is computed as

$$
\begin{aligned}
\dot{V}(e) &= \frac{1}{2}\left(\frac{\partial V}{\partial e_1} + \frac{\partial V}{\partial e_2} + \frac{\partial V}{\partial e_3}\right), \\
&= e^T \dot{e}, \\
&= e^T (g(y) - f(x) + u).
\end{aligned} \tag{22}
$$

Substituting the adaptive control law (16) in (22),

$$\dot{V}(e) = e^T \begin{pmatrix} g(y) - f(x) - \begin{pmatrix} \left(\Omega_1^1 \operatorname{sat}\left(\frac{e_1}{\Phi_1}\right)\right)^2 e_1 \\ \left(\Omega_1^2 \operatorname{sat}\left(\frac{e_2}{\Phi_1}\right)\right)^2 e_2 \\ \left(\Omega_1^3 \operatorname{sat}\left(\frac{e_3}{\Phi_1}\right)\right)^2 e_3 \end{pmatrix} + f(x) - g(y) \end{pmatrix},$$

$$= -e^T \begin{pmatrix} \left(\Omega_1^1 \operatorname{sat}\left(\frac{e_1}{\Phi_1}\right)\right)^2 e_1 \\ \left(\Omega_1^2 \operatorname{sat}\left(\frac{e_2}{\Phi_1}\right)\right)^2 e_2 \\ \left(\Omega_1^3 \operatorname{sat}\left(\frac{e_3}{\Phi_1}\right)\right)^2 e_3 \end{pmatrix},$$

$$= -e^T \begin{pmatrix} \left(\Omega_1^1 \operatorname{sat}\left(\frac{e_1}{\Phi_1^1}\right)\right)^2 & 0 & 0 \\ 0 & \left(\Omega_1^2 \operatorname{sat}\left(\frac{e_2}{\Phi_1^2}\right)\right)^2 & 0 \\ 0 & 0 & \left(\Omega_1^3 \operatorname{sat}\left(\frac{e_3}{\Phi_1^3}\right)\right)^2 \end{pmatrix} e,$$

$$= -e^T P e < 0, \tag{23}$$

which ensures the negativeness of (22) and consequently the asymptotic stability of the error system.

The following example illustrates the effectiveness and performance of the controller design, which comes to corroborate what we claim and prove. □

Example 1. According to [43], we synthesized the following master system:

$$\dot{x} = \begin{pmatrix} 0 & 1 & 0 \\ 0 & 0 & 1 \\ -a_1 & -a_2 & -a_3 \end{pmatrix} x + \begin{pmatrix} -\beta_1 \\ -\beta_2 \\ a_1\beta_3 + a_2\beta_1 + a_3\beta_2 \end{pmatrix}, \tag{24}$$

where $a_1 = 3/2$, $a_2 = 1$, $a_3 = 1$, and

$$\beta_1 = \begin{cases} 5 & \text{if } x_2 \geq 0, \\ -5 & \text{if } x_2 < 0, \end{cases}$$
$$\beta_2 = \begin{cases} 14 & \text{if } x_3 \geq 7, \\ 0 & \text{if } x_3 < 7, \end{cases} \tag{25}$$
$$\beta_3 = \begin{cases} 4 & \text{if } x_1 \geq 0, \\ -4 & \text{if } x_1 < 0. \end{cases}$$

In Figure 2, the 3D phase portrait plot of system (24) is depicted under initial conditions $x_0 = (0, 4, 10)^T$, and we can see that the master system presents a 8-scroll chaotic attractor in three different directions. The projections in the planes (x_1, x_2), (x_1, x_3), and (x_2, x_3) for the system are shown in Figure 3.

Now, following the same methodology used to design the master system, consider the slave system as

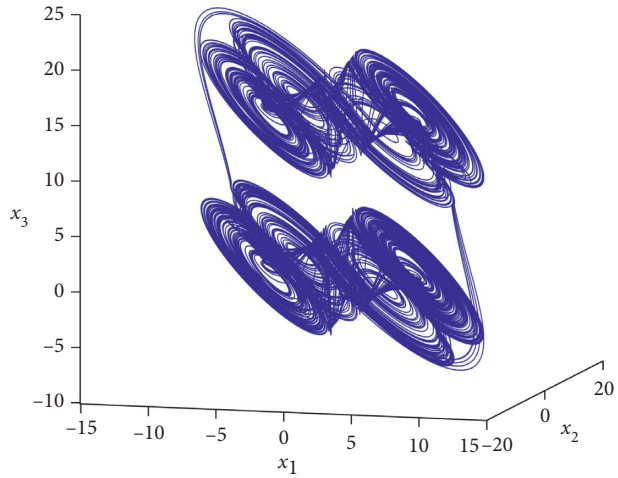

Figure 2: 3D phase portrait of the master chaotic system.

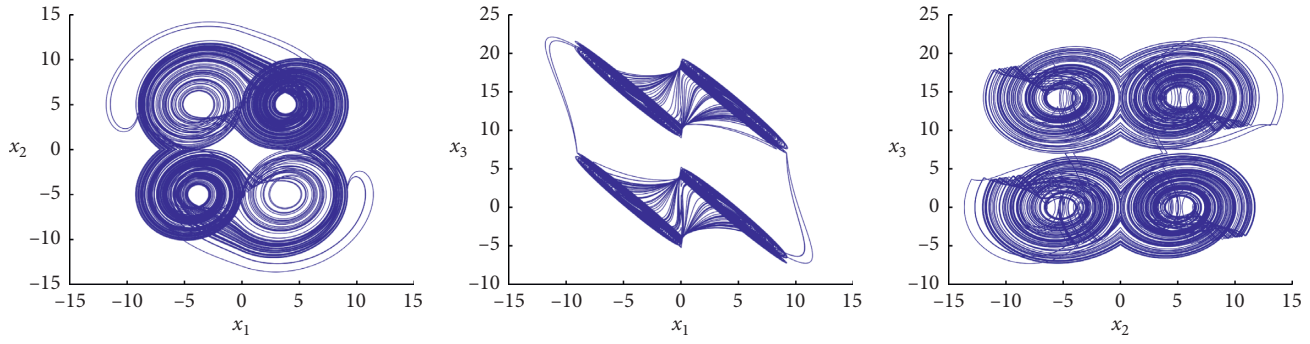

(a) (b) (c)

Figure 3: Plane projections for the master system: (a) (x_1, x_2); (b) (x_1, x_3); (c) (x_2, x_3).

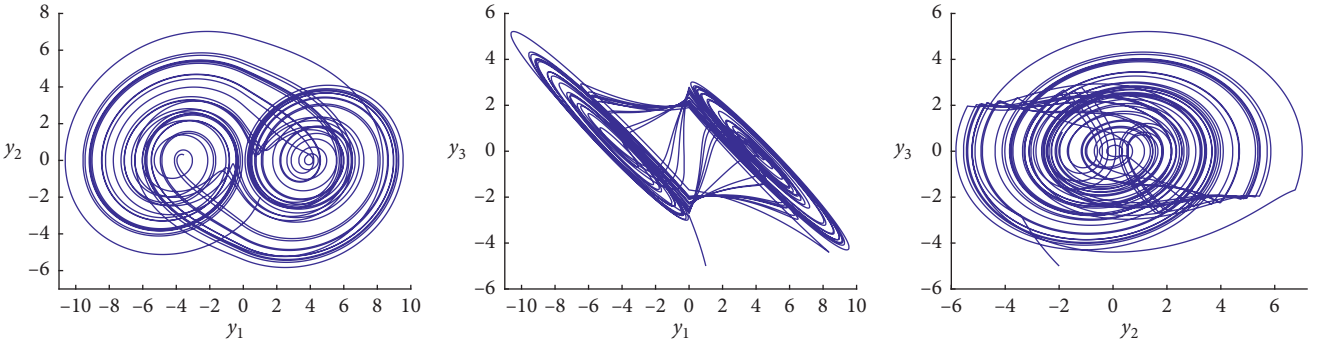

(a) (b) (c)

Figure 4: Slave system plane projections: (a) (y_1, y_2); (b) (y_1, y_3); (c) (y_2, y_3).

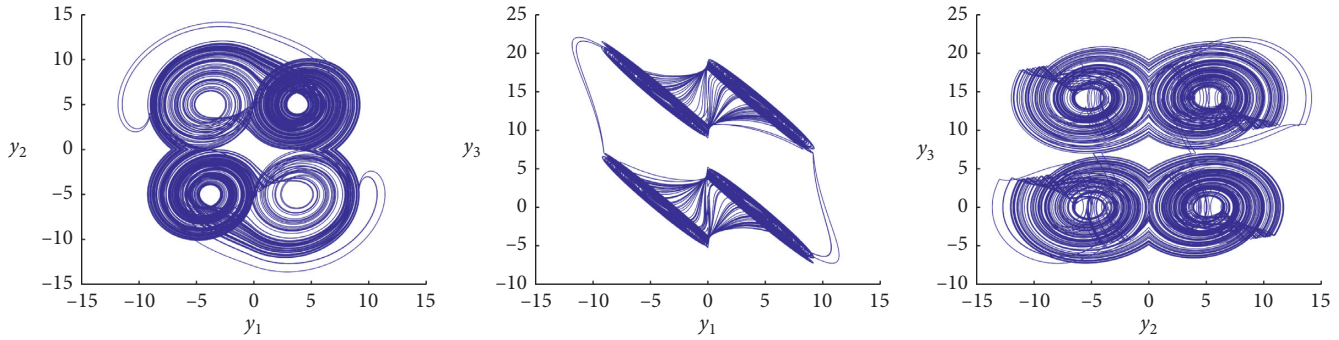

FIGURE 5: Synchronized slave system plane projections: (a) (y_1, y_2); (b) (y_1, y_3); (c) (y_2, y_3).

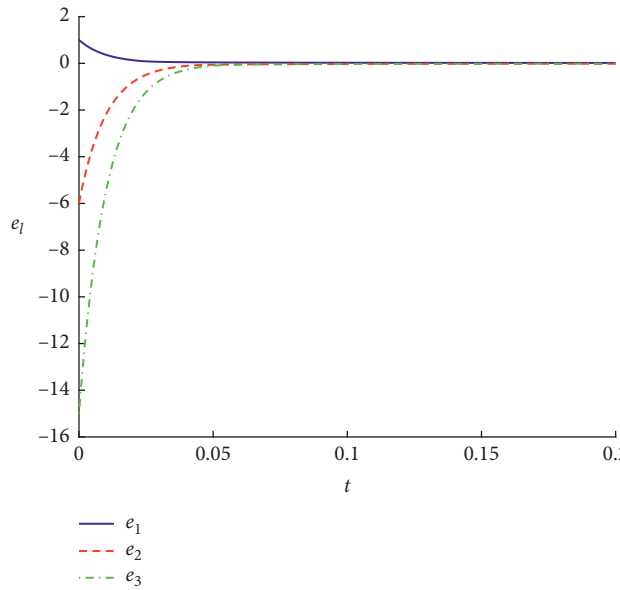

FIGURE 6: Error dynamics.

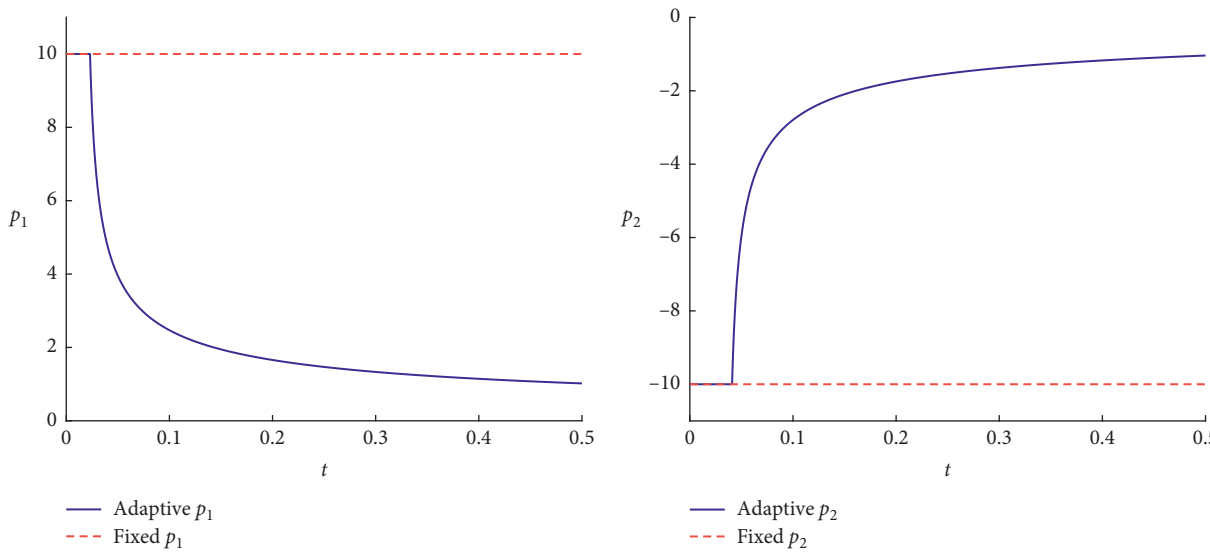

FIGURE 7: Continued.

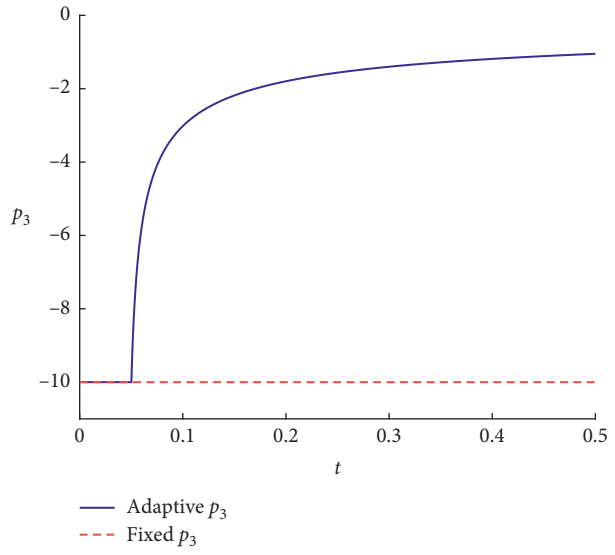

(c)

FIGURE 7: Evolution of $p_l(e_l)$ trough time: (a) $p_1(e_1)$; (b) $p_2(e_2)$; (c) $p_3(e_3)$.

$$\dot{y} = \begin{pmatrix} 0 & 1 & 0 \\ 0 & 0 & 1 \\ -\tilde{a}_1 & -\tilde{a}_2 & -\tilde{a}_3 \end{pmatrix} y + \begin{pmatrix} 0 \\ 0 \\ \tilde{a}_1\tilde{\beta}_3 \end{pmatrix} + u, \tag{26}$$

with $\tilde{a}_i = 3/5$, for $i = 1, 2, 3$, and

$$\tilde{\beta}_3 = \begin{cases} 4 & \text{if } y_1 \geq 0, \\ -4 & \text{if } y_1 < 0. \end{cases} \tag{27}$$

Unlike the master system, the slave system only presents a double scroll chaotic attractor by taking the initial condition point $y_0 = (1, -2, -5)^T$, whose projections in the planes (y_1, y_2), (y_1, y_3), and (y_2, y_3) for the slave system, when $u = (0, 0, 0)^T$, are shown in Figure 4.

The control law u is designed according to Lemma 1, and its explicit expression is given by

$$\begin{aligned} u &= -Pe + f(x) - g(y), \\ &= -\begin{pmatrix} \left(\Omega_1^1 \operatorname{sat}\left(\frac{e_1}{\Phi_1^1}\right)\right)^2 e_1 \\ \left(\Omega_1^2 \operatorname{sat}\left(\frac{e_2}{\Phi_1^2}\right)\right)^2 e_2 \\ \left(\Omega_1^3 \operatorname{sat}\left(\frac{e_3}{\Phi_1^3}\right)\right)^2 e_3 \end{pmatrix} + \begin{pmatrix} 0 & 1 & 0 \\ 0 & 0 & 1 \\ -a_1 & -a_2 & -a_3 \end{pmatrix} x, \\ &\quad + \begin{pmatrix} -\beta_1 \\ -\beta_2 \\ a_1\beta_3 + a_2\beta_1 + a_3\beta_2 \end{pmatrix} - \begin{pmatrix} 0 & 1 & 0 \\ 0 & 0 & 1 \\ -\tilde{a}_1 & -\tilde{a}_2 & -\tilde{a}_3 \end{pmatrix} y - \begin{pmatrix} 0 \\ 0 \\ \tilde{a}_1\tilde{\beta}_3 \end{pmatrix}, \end{aligned} \tag{28}$$

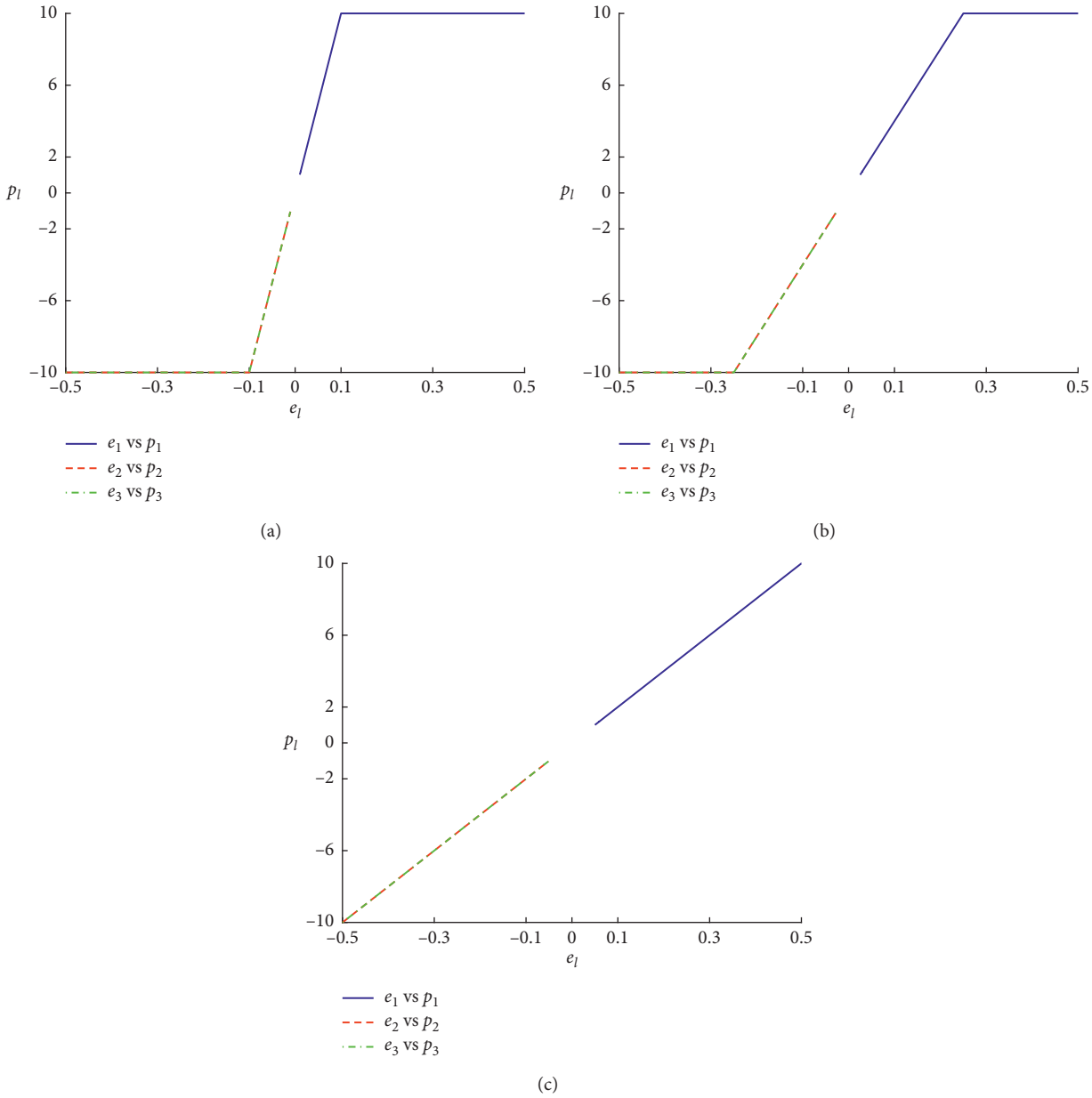

Figure 8: Comparative between the adaptation domains for (a) $\Phi_1^l = 0.1$; (b) $\Phi_1^l = 0.25$; (c) $\Phi_1^l = 0.5$.

where $\Omega_1^l = 10$ and $\Phi_1^l = 1/10$, for $l = 1, 2, 3$. The projections in the planes (y_1, y_2), (y_1, y_3), and (y_2, y_3) for the synchronized slave system are shown in Figure 5. It is clear that the slave system now exhibits the trajectories of the master system and went from a double scroll chaotic attractor to a 8-scroll chaotic attractor.

The errors between the master and slave systems are depicted in Figure 6, and these errors tend asymptotically to the origin as intended.

4.1. Energy Optimization. One of the advantages of using the adaptive synchronization proposed in this work is the optimization of the energy used to induce the dynamics of the master system in the slave system. Comparing the magnitude of $p_l(e_l)$, $l = 1, 2, 3$, against the magnitude of a fixed value shows clearly that the energy consumption is vastly improved.

At first, high values of $p_l(e_l)$ are injected in the fuzzy actuator in order that the error e_l reaches its following adaptive domain interval $\mathscr{A}_l = (-\Phi_1^l, \Phi_1^l)$, and then, the value of $p_l(e_l)$ decays until the error reaches the next interval of adaptation. Hence, the power stills decaying whilst the error system tends to zero.

Figure 7(a) shows the behaviour of the adaptive $p_1(e_1)$ (blue line) and the behaviour of a fixed not adaptive value of p_1 (dotted red line). This behaviour is also presented among the adaptives $p_2(e_2)$ and $p_3(e_3)$ (blue lines) and their respective fixed no adaptive values p_2 and p_3 (in red dots), depicted in Figures 7(b) and 7(c), respectively.

The energy optimization can be modified according the application where it is planned to be used by modifying the adapting interval $\mathscr{A}_l$ of each $p_l(e_l)$. This can be better appreciated in Figures 8(a)–8(c).

5. Conclusions

An adaptive synchronization scheme was provided using as adaptation law a Mamdani-type fuzzy inference system. An equivalence is given to express the fuzzy inference system as saturation functions and evidence is provided to ensure the stability of the error system between the master and the slave systems.

Data Availability

All underlying data that support results can be found in Tecnológico Nacional de México, Instituto Tecnológico de Tijuana, Calzada Tecnológico S/N, Tijuan, Baja California, México.

Conflicts of Interest

The authors declare that they have no conflicts of interest.

Acknowledgments

This research was supported by CONACyT with project no. A1-S-32341 and Tecnológico Nacional de México with project nos. 5564.19-P, 8085.20-P, and 11122.21-P. J. R. Pulido–Luna wants to thank CONACyT for the DSc scholarship.

References

[1] A. Pikovsky, M. Rosenblum, and J. K. Synchronization, "A universal concept in nonlinear sciences," in *The Edinburgh Building*, Cambridge University Press, Cambridge, UK, 1st edition, 2001.

[2] S. Boccaletti, "The synchronized dynamics of complex systems," *Monograph Series on Nonlinear Science and Complexity*, vol. 6, 2008.

[3] A. C. J. Luo, "A theory for synchronization of dynamical systems," *Communications in Nonlinear Science and Numerical Simulation*, vol. 14, no. 5, pp. 1901–1951, 2009.

[4] Z. Qu, "Chaos in the genesis and maintenance of cardiac arrhythmias," *Progress in Biophysics and Molecular Biology*, vol. 105, no. 3, pp. 247–257, 2011.

[5] L. J. Ontañón-García and E. Campos-Cantón, "Discrete coupling and synchronization in the insulin release in the mathematical model of the β Cells," *Discrete Dynamics in Nature and Society*, vol. 2013, Article ID 427050, 7 pages, 2013.

[6] P. J. Prieto, N. R. Cazarez-Castro, L. T. Aguilar, and S. L. Cardenas-Maciel, "Chattering existence and attenuation in fuzzy-based sliding mode control," *Engineering Applications of Artificial Intelligence*, vol. 61, pp. 152–160, 2017.

[7] P. J. Prieto-Entenza, L. T. Aguilar, S. L. Cardenas-Maciel, J. A. Lopez-Renteria, and N. R. Cazarezcastro, "Stability analysis for mamdani-type integral fuzzy-based sliding mode control of systems under persistent disturbances," *IEEE Transactions on Fuzzy Systems*, p. 1. In press, 2021.

[8] L. Herrera-Garcia, N. R. Cazarez-Castro, S. L. Cardenas-Maciel, J. A. Lopez-Renteria, and L. T. Aguilar, "Self-excited periodic motion in underactuated mechanical systems using two-fuzzy inference system," *Fuzzy Sets and Systems*, 2021, In press.

[9] J. A. Lopez-Renteria, L. Herrera-Garcia, S. L. Cardenas-Maciel, L. T. Aguilar, and N. R. Cazarezcastro, "Self-sustaining oscillations with an internal two-fuzzy inference system based on the poincar-bendixson method," *IEEE Transactions on Fuzzy Systems*, p. 1. In press, 2021.

[10] S. Vaidyanathan, "Adaptive synchronization of chemical chaotic reactors," *International Journal of ChemTech Research*, vol. 8, no. 2, pp. 612–621, 2015.

[11] B. A. Idowu and U. E. Vincent, "Synchronization and stabilization of chaotic dynamics in a quasi-1D bose-einstein condensate," *Journal of Chaos*, vol. 2013, Article ID 723581, 8 pages, 2013.

[12] G. Yuan, X. Zhang, and Z. Wang, "Generation and synchronization of feedbackinduced chaos in semiconductor ring lasers by injectionlocking," *Optik*, vol. 125.8, Article ID 19501953, 2014.

[13] N. R. Cazarez-Castro, S. L. Cardenas-Maciel, M. Odreman-Vera, G. Valencia-Palomo, and C. Leal-Ramrez, "Modeling PD closed-loop control problems with fuzzy differential equations," *Automatika*, vol. 57, no. 4, pp. 960–967, 2016.

[14] N. R. Cazarez-Castro, M. Odreman-Vera, S. L. Cardenas-Maciel, H. Echavarria-Heras, and C. Leal-Ramirez, "Fuzzy differential equations as a tool for teaching uncertainty in engineering and science," *Computación y Sistemas*, vol. 22, no. 2, pp. 439–449, 2018.

[15] M. Arfan, K. Shah, T. Abdeljawad, and Z. Hammouch, "An efficient tool for solving two-dimensional fuzzy fractional-ordered heat equation," *Numerical Methods for Partial Differential Equations*, vol. 37, no. 2, pp. 1407–1418, 2020.

[16] A. Ullah, Z. Ullah, T. Abdeljawad, Z. Hammouch, and K. Shah, "A hybrid method for solving fuzzy Volterra integral equations of separable type kernels," *Journal of King Saud University—Science*, vol. 33, no. 1, Article ID 101246, 2021.

[17] M. C. Soriano, I. Fischer, C. R. Mirasso, R. M. Nguimdo, and G. Van der Sande, "Encryption key distribution via chaos synchronization," *Scientific Reports*, vol. 7, no. 1, Article ID 43428, 2017.

[18] O. Guillén-Fernández, J. de Jesus Rangel-Magdaleno, A. Melendez-Cano, J. C. Nuñez-Perez, and L. G. de la Fraga, "FPGA implementation of chaotic oscillators, their synchronization, and application to secure communications," in *Recent Advances in Chaotic Systems and Synchronization*, pp. 301–328, Academic Press, Cambridge, MA, USA, 2019.

[19] S. Moon, J.-J. Baik, and J. M. Seo, "Chaos synchronization in generalized Lorenz systems and an application to image encryption," *Communications in Nonlinear Science and Numerical Simulation*, vol. 96, Article ID 105708, 2021.

[20] R. L. Devaney, *An Introduction to Chaotic Dynamical Systems*, Westview Press, Boulder, CO, USA, 2nd edition, 2003.

[21] L. M. Pecora and T. L. Carroll, "Synchronization in chaotic systems," *Physical Review Letters*, vol. 64, no. 8, Article ID 821824, 1990.

[22] L. O. Chua, L. Kocarev, K. Eckert, and M. Itoh, "Experimental chaos synchronization in chua's circuit," *International Journal of Bifurcation and Chaos*, vol. 2, no. 3, pp. 705–708, 1992.

[23] R. Femat and G. Solís-Perales, "On the chaos synchronization phenomena," *Physics Letters A*, vol. 262, no. 1, Article ID 5060, 1999.

[24] J. Lü, T. Zhou, and S. Zhang, "Chaos synchronization between linearly coupled chaotic systems," *Chaos, Solitons Fractals*, vol. 14, no. 4, Article ID 529541, 2002.

[25] H.-T. Yau and C.-S. Shieh, "Chaos synchronization using fuzzy logic controller," *Nonlinear Analysis: Real World Applications*, vol. 9, no. 4, pp. 1800–1810, 2008.

[26] S. F. AL-Azzawi and M. M. Aziz, "Chaos synchronization of nonlinear dynamical systems via a novel analytical approach," *Alexandria Engineering Journal*, vol. 57, no. 4, pp. 3493–3500, 2018.

[27] M. M. Zirkohi and S. Khorashadizadeh, "Chaos synchronization using higher-order adaptive PID controller," *AEU—International Journal of Electronics and Communications*, vol. 94, pp. 157–167, 2018.

[28] A. Anzo-Hernández, E. Campos-Cantón, and M. Nicol, "Itinerary synchronization between PWL systems coupled with unidirectional links," *Communications in Nonlinear Science and Numerical Simulation*, vol. 70, pp. 102–124, 2019.

[29] C. W. Wu, T. Yang, and L. O. Chua, "On adaptive synchronization and control of nonlinear dynamical systems," *International Journal of Bifurcation and Chaos*, vol. 6, no. 3, pp. 455–471, 1996.

[30] T.-L. Liao and S.-H. Tsai, "Adaptive synchronization of chaotic systems and its application to secure communications," *Chaos, Solitons & Fractals*, vol. 11, no. 9, pp. 1387–1396, 2000.

[31] H. Zhang, W. Huang, Z. Wang, and T. Chai, "Adaptive synchronization between two different chaotic systems with unknown parameters," *Physics Letters A*, vol. 350, no. 5-6, pp. 363–366, 2006.

[32] X. Xi, S. Mobayen, H. Ren, and S. Jafari, "Robust finite-time synchronization of a class of chaotic systems via adaptive global sliding mode control," *Journal of Vibration and Control*, vol. 24, no. 17, pp. 3842–3854, 2017.

[33] E. Campos-Cantón, R. Femat, and G. Chen, "Attractors generated from switching unstable dissipative systems," *Chaos: An Interdisciplinary Journal of Nonlinear Science*, vol. 22, no. 3, Article ID 033121, 2012.

[34] E.-C. Aguirre-Hernández, J. A. López-Rentería, E. Campos-Cantón, and C. A. Loredo-Villalobos, "Stability and multiscroll attractors of control systems via the abscissa," *Mathematical Problems in Engineering*, vol. 2017, Article ID 6743734, 9 pages, 2017.

[35] J. A. López-Rentería, E. Campos-Cantón, B. Aguirre-Hernández, and G. Fernández-Anaya, "A monoparametric family of piecewise linear systems to generate scroll attractors via path-connected set of polynomials," *International Journal of Bifurcation and Chaos*, vol. 31, no. 3, Article ID 2150034, 2021.

[36] J. R. Pulido-Luna, J. A. López-Rentería, N. R. Cazarez-Castro, and E. Campos, "A two-directional grid multiscroll hidden attractor based on piecewise linear system and its application in pseudo-random bit generator," *Integration*, vol. 81, pp. 34–42, 2021.

[37] J. R. Pulido-Luna, J. A. López-Rentería, and N. R. Cazarez-Castro, "Design of a nonhomogeneous nonlinear synchronizer and its implementation in reconfigurable hardware," *Mathematical and Computational Applications*, vol. 25, no. 3, p. 51, 2020.

[38] J. S. González-Salas, E. Campos-Cantón, F. C. Ordaz-Salazar, and E. Jiménez-López, "Nonlinear filtering preserves chaotic synchronization via master-slave system," *Abstract and Applied Analysis*, vol. 2013, Article ID 398293, 13 pages, 2013.

[39] G. Chen and T. T. Pham, "Introduction to fuzzy systems," in *Applied Mathematics and Nonlinear Science*, Chapman Hall/CRC, Boca Raton, FL, USA, 1st edition, 2005.

[40] V. Santibanez, R. Kelly, and M. A. Llama, "Global asymptotic stability of a tracking sectorial fuzzy controller for robot manipulators," *IEEE Transactions on Systems, Man and Cybernetics, Part B (Cybernetics)*, vol. 34, no. 1, pp. 710–718, 2004.

[41] P. J. Prieto-Entenza, N. R. Cazarez-Castro, L. T. Aguilar, S. L. Cardenas-Maciel, and J. A. López-Rentería, "A Lyapunov analysis for Mamdani type fuzzy-based sliding mode control," *IEEE Transactions on Fuzzy Systems*, vol. 28, no. 8, pp. 1887–1895, 2020.

[42] E. Euntai Kim, H. Heejin Lee, and M. Mignon Park, "Limit-cycle prediction of a fuzzy control system based on describing function method," *IEEE Transactions on Fuzzy Systems*, vol. 8, no. 1, pp. 11–22, 2000.

[43] E. Campos-Cantón, "Chaotic attractors based on unstable dissipative systems via third-order differential equation," *International Journal of Modern Physics C*, vol. 27, no. 1, Article ID 1650008, 2016.

Hindawi
Complexity
Volume 2021, Article ID 9037271, 11 pages
https://doi.org/10.1155/2021/9037271

WILEY | Hindawi

Research Article

Proposing and Dynamical Analysis of a Hyperjerk Piecewise Linear Chaotic System with Offset Boostable Variable and Hidden Attractors

M. D. Vijayakumar,[1] Sajjad Shaukat Jamal,[2] Ahmed M. Ali Ali,[3] Karthikeyan Rajagopal,[4] Sajad Jafari,[5,6] and Iqtadar Hussain[7]

[1]*Center for Materials Research, Chennai Institute of Technology, Chennai, India*
[2]*Department of Mathematics, College of Science, King Khalid University, Abha, Saudi Arabia*
[3]*Department of Power Mechanics, Babylon Technical Institute, Al-Furat Al-Awsat Technical University, Babylon 51001, Iraq*
[4]*Centre for Nonlinear Systems, Chennai Institute of Technology, Chennai, Tamilnadu 600069, India*
[5]*Health Technology Research Institute, Amirkabir University of Technology, 424 Hafez Ave., Tehran 15875-4413, Iran*
[6]*Department of Biomedical Engineering, Amirkabir University of Technology, 424 Hafez Ave., Tehran 15875-4413, Iran*
[7]*Department of Mathematics, Statistics and Physics, Qatar University, Doha 2713, Qatar*

Correspondence should be addressed to Karthikeyan Rajagopal; rkarthiekeyan@gmail.com

Received 14 May 2021; Revised 10 July 2021; Accepted 2 August 2021; Published 9 August 2021

Academic Editor: Eric Campos

Designing chaotic systems with different properties helps to increase our knowledge about real-world chaotic systems. In this article, a piecewise linear (PWL) term is employed to modify a simple chaotic system and obtain a new chaotic model. The proposed model does not have any equilibrium for different values of the control parameters. Therefore, its attractor is hidden. It is shown that the PWL term causes an offset boostable variable. This feature provides more flexibility and controllability in the designed system. Numerical analyses show that periodic and chaotic attractors coexist in some fixed values of the parameters, indicating multistability. Also, the feasibility of the system is approved by designing field programmable gate arrays (FPGA).

1. Introduction

Chaotic systems are characterized by sensitivity to initial conditions, known as the butterfly effect, and unpredictability. Recently, the analyzing, designing, and applications of chaotic systems have been progressed in different fields. The existence of chaotic behaviors in real-world systems [1, 2] encourages proposing physical [3], biological [4, 5], economic [6], and engineering [7, 8] chaotic models. Previous studies suggested that chaotic systems have different numbers and geometric forms of equilibria, e.g., chaotic systems with no [9–11], a line [12], a circle [13], a curve [14], and a surface [15] of equilibria. Chaotic oscillators can be applied in functional subsystems of digital and radio-wave communication systems such as compression, filter, encryption, and modulation [16].

Most classical and well-known attractors, such as Lorenz, Rössler, Chua, and Chen, are excited from unstable equilibria. So, there is at least one unstable equilibrium in these attractors' basins of attraction. Hence, they are called self-excited attractors [17]. However, about ten years ago, Leonov et al. showed that the Chua's circuit has another kind of attractor for which its basin of attraction does not collide with unstable manifolds [18]. Such attractors are called hidden attractors. Strange attractors in systems with no equilibria are placed in this category [19, 20]. Exploring the basin of attraction [21] and parameter switching [22] algorithms can detect the hidden attractors of the system.

The existence of different stable attractors divides the phase space into different regions demonstrating as the basin of attractions [23–26]. Sometimes attractors coexist with each other and are characterized by the initial conditions. Systems with these separated attractors (and their corresponding basins of attraction) are called multistable [27–29]. Altering a multistable system to a monostable one [30] or synchronization of some multistable systems to luck on a particular attractor [31] are two different controlling approaches related to multistable systems. As there is no analytical way to investigate the detect coexisting attractors, numerical approaches are used in most researches [32]. Also, varying initial conditions, as a bifurcation parameter, may help in finding coexisting attractors, especially in systems with extreme multistability [28, 33].

Piecewise linear (PWL) systems are in the category of switching systems with different affine or nonlinear functions in diverse regions of the state variables [34]. Chua's system is one of the most popular PWL systems, which shows chaotic behavior [35]. Different PWL systems have been proposed with multiscroll chaotic attractors and different numbers of equilibria [36, 37]. Primarily, polynomial approaches have been used to generate such chaotic attractors [38, 39]. As PWL functions can generate various chaotic attractors [40], they can be used in controlling [41] and dynamics editing [42]. Also, error state feedback controllers are proposed, which synchronize master-slave PWL chaotic system [43, 44].

Controlling the amplitude of the chaotic attractors is divided into partial and total control schemes [45]. Moreover, researches showed that these approaches might help to find the multistability in systems [46]. Boosting a state variable through adding a DC offset to the variable (offset boosting) is a property that exists in some chaotic systems [47]. The offset boostable variables of a system can even change from unipolar signal to bipolar one and vice versa [48]. Also, researches have shown that conditional symmetry could be preserved for the asymmetric systems using the offset boosting variables which provides polarity balance in these systems [49].

The remainder of this paper is organized as follows: the proposed chaotic system is introduced and statistically analyzed in Section 2. In Section 3, the system's dynamical properties are analyzed using the bifurcation diagram and Lyapunov exponents diagram. The offset boosting property is studied in Section 4. Section 5 includes the FPGA realization of this system. Finally, the discussion and conclusion of this study are presented in Section 6.

2. Hidden Chaotic Hyperjerk System with PWL Term

To study the effect of a PWL term on the dynamical properties of chaotic systems, a simple 4D chaotic hyperjerk system is considered as [50]

$$\begin{aligned}\dot{x} &= y,\\ \dot{y} &= z,\\ \dot{z} &= w,\\ \dot{w} &= -1.02w + 1.64x^2 - 1.36y^2\\ &\quad + 0.28xy + 2.42xz + 1.45,\end{aligned} \tag{1}$$

where x, y, z, and w are the state variables of this ordinary differential equation. Analyzing the steady state, $(\dot{x}, \dot{y}, \dot{z}, \dot{w}) = (0, 0, 0, 0)$, shows that this system does not have any equilibria, and its chaotic responses are in the group of hidden attractors. In this work, this system is modified with one PWL term as

$$\begin{aligned}\dot{x} &= y,\\ \dot{y} &= z,\\ \dot{z} &= w,\\ \dot{w} &= -1.02w + 1.64x^2 - 1.36y^2\\ &\quad + 0.28xy + 2.42xz + 1.45 + a|y - x - b|.\end{aligned} \tag{2}$$

The system has two control parameters (a and b) and five nonlinearities (one of them is an absolute function of x and y, $g(x, y) = a|y - x - b|$). For $a > 0$, this system does not have any equilibria. Therefore, its chaotic attractor is hidden. Equation (3) determines the volume contraction rate of system (2):

$$\nabla V = \frac{\partial \dot{x}}{\partial x} + \frac{\partial \dot{y}}{\partial y} + \frac{\partial \dot{z}}{\partial z} + \frac{\partial \dot{w}}{\partial w} = -1.02. \tag{3}$$

As $\nabla V < 0$, the proposed model is dissipative and has the condition of exhibiting bounded attractors. The state spaces of system (2), Figure 1, show that it has chaotic attractor when $a = 3.5$, $b = 1$, and $(x_0, y_0, z_0, w_0) = [-2.77, -0.53, 2.7, -0.34]$. Also, both the piecewise linear functions $g(x, y)$ and the attractor are plotted in the 3D phase space of the system shown in Figure 2.

It should be noted that the fourth-order Runge–Kutta (RK4) [51] method with time-step $h = 0.001$ was used to do the numerical simulations.

3. Dynamical Analysis

To analyze the effect of parameters of PWL term in the system dynamics, the bifurcation diagram of system (2) is plotted as the bifurcation parameter changes from −1 to 4.5 in Figure 3(a). The parameter b is 1, and the initial conditions are $(-2.77, 0.53, 2.7, -0.34)$. The bifurcation diagram shows that the system exhibits both period-doubling and period-halving routes to chaos in different parameter values. Also, Lyapunov exponents (LEs) of the system are computed for the same conditions and a runtime of $t = 40000$ s in Figure 3(b). To calculate the LEs of the system, the Wolf method [52] is used. The largest Lyapunov exponent (LLE, shown in green) is positive when the bifurcation diagram displays chaotic behavior.

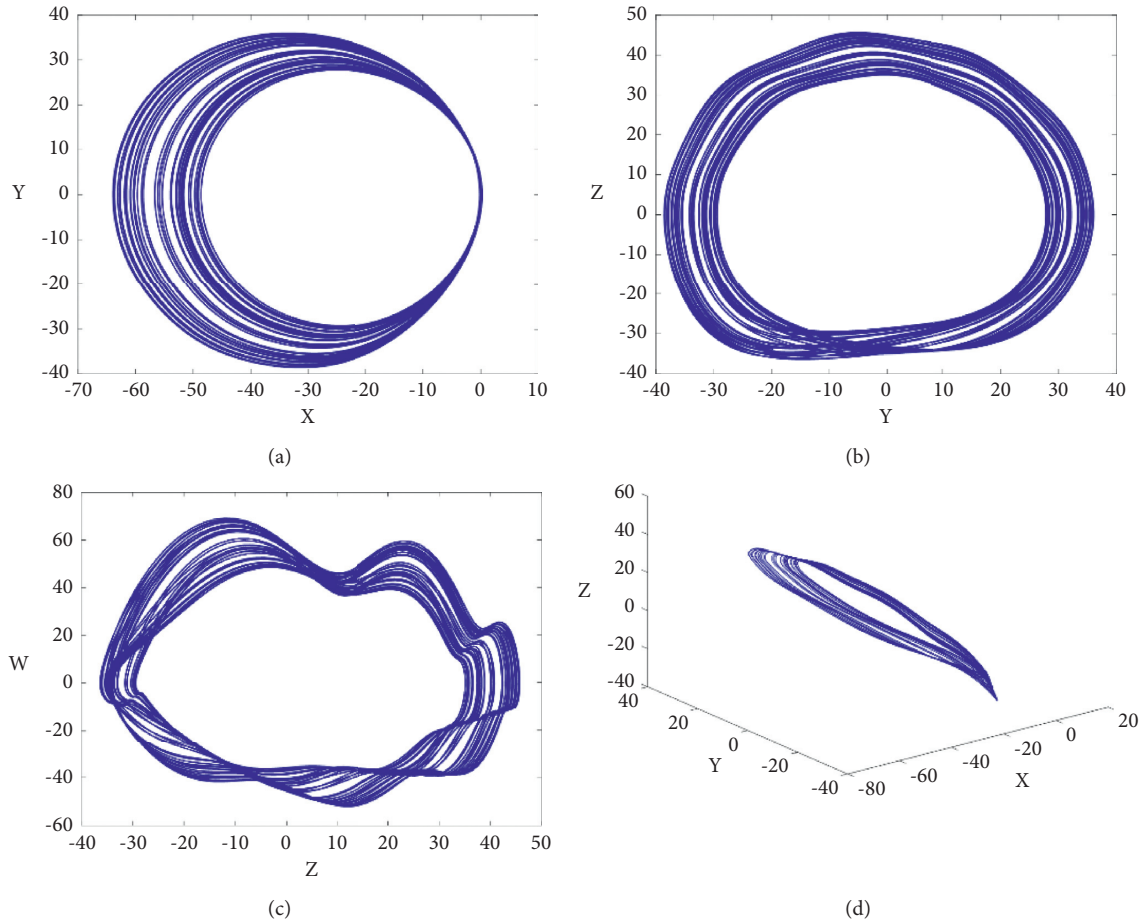

Figure 1: Attractor of system (2) and its projections in (a) xy, (b) yz, and (c) zw planes and (d) xyz space with $a = 3.5$ and $b = 1$ and the initial conditions are $(x_0, y_0, z_0, w_0) = (-2.77, 0.53, 2.7, -0.34)$.

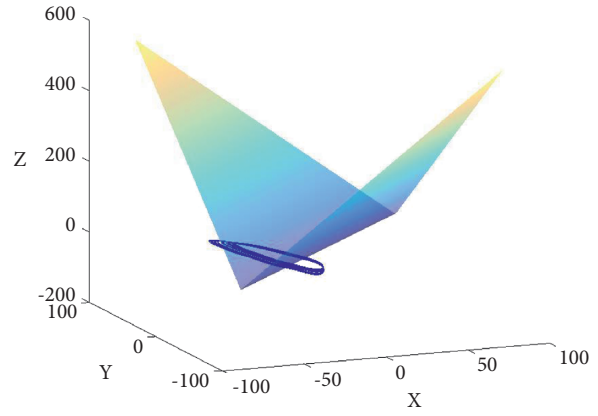

Figure 2: The piecewise linear function of the proposed system when $a = 3.5$ and $b = 1$ in xyz view. Also, the attractor of the system is plotted in dark blue.

Also, changing the control parameter b results in different dynamical behaviors in this system. To investigate, the bifurcation diagram of the system is plotted in Figure 4(a), in which b changes from -0.2 to 2.8. Figure 4(a) shows that different values of this parameter result in period-doubling and period-halving routes to chaos. Figure 4(b) shows the corresponding LEs. Both panels of Figure 4 are plotted when $a = 3.5$ and $(x_0, y_0, z_0, w_0) = (-2.77, 0.53, 2.7, -0.34)$.

Different initial conditions are checked for constant values of the parameters. This system has two coexisting attractors, a chaotic one and a limit cycle one, when $a = 3.9$ and $b = 1$. Figure 5 displays these attractors in red and blue

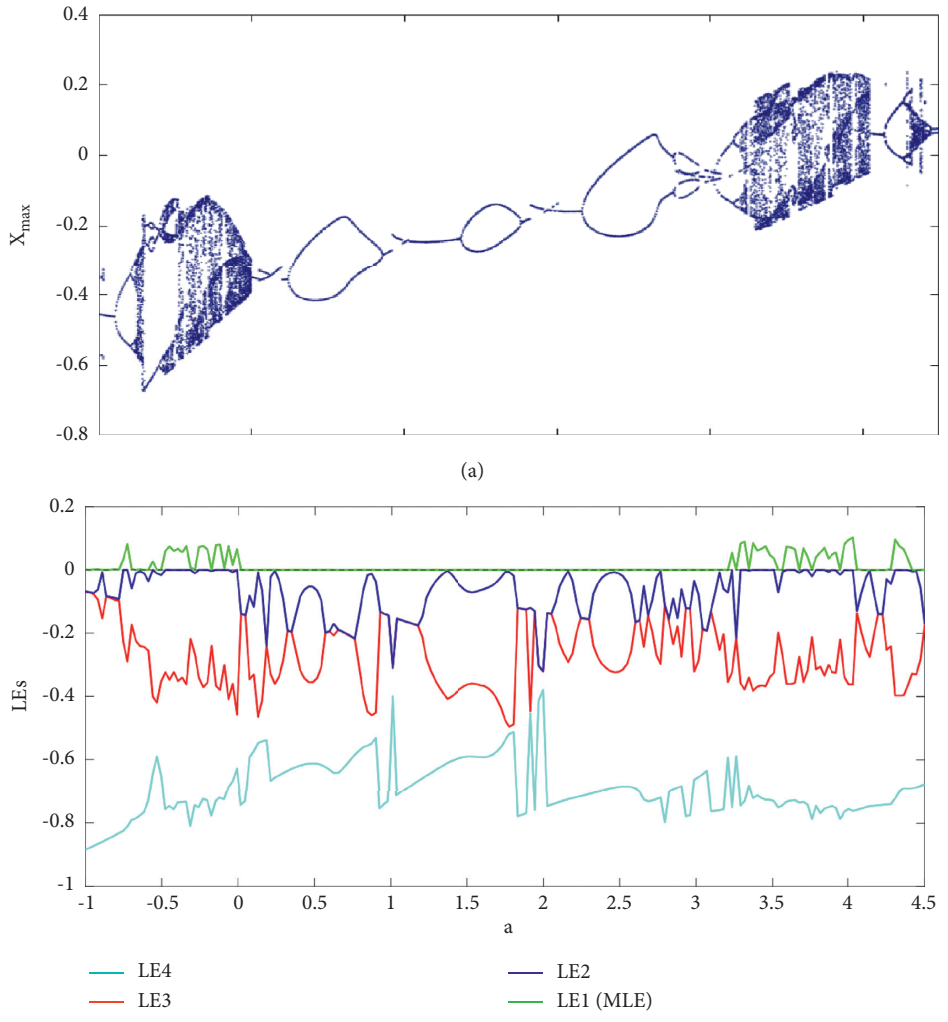

Figure 3: (a) Bifurcation diagram and (b) Lyapunov exponents of system (2) when parameter a changes and $b = 1$. The initial conditions are $(-2.77, 0.53, 2.7, -0.34)$.

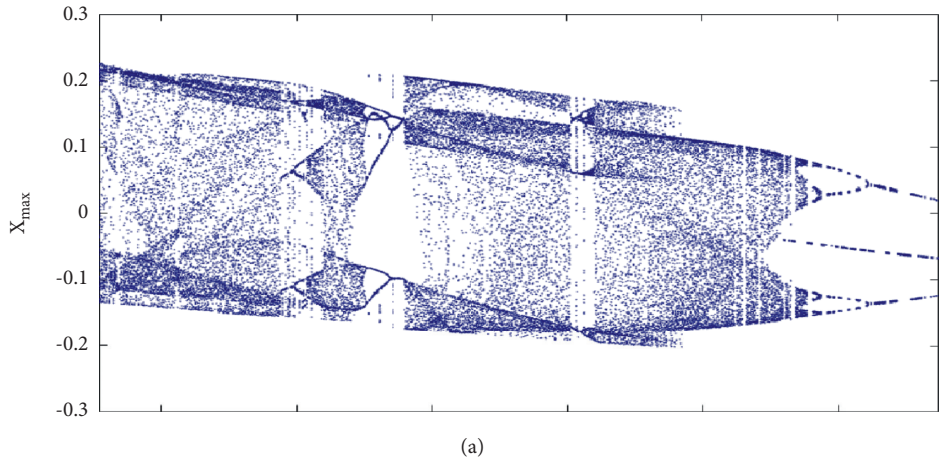

Figure 4: Continued.

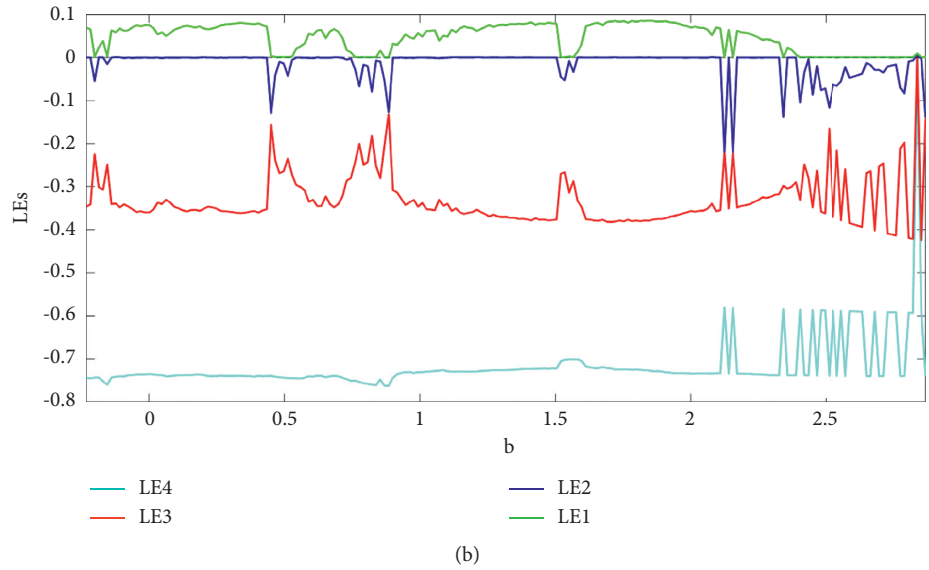

(b)

Figure 4: (a) Bifurcation diagram and (b) Lyapunov exponents of system (2) when parameter b changes and $a = 3.5$. The initial conditions are $(-2.77, 0.53, 2.7, -0.34)$.

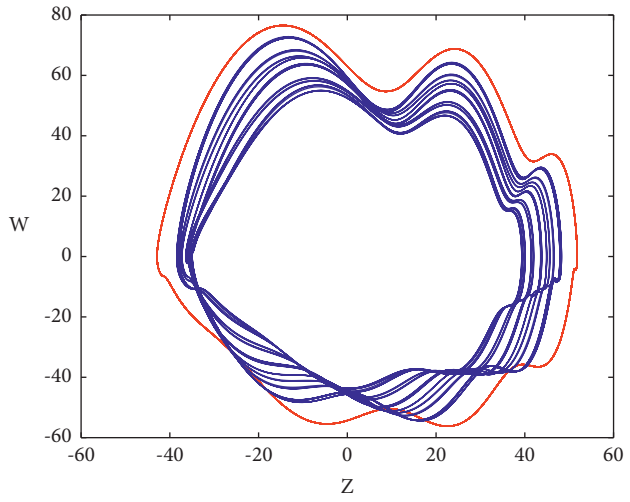

Figure 5: The system is multistable when $a = 3.9$ and $b = 1$. Initial conditions for red and blue colors are $(-2.77, -0.4021, 6.2522, -0.0634)$ and $(-2.77, -0.4140, -1.5095, -0.3374)$, respectively.

colors for the initial conditions equal to $(-2.77, -0.4021, 6.2522, -0.0634)$ and $(-2.77, -0.4140, -1.5095, -0.3374)$, respectively.

4. Offset Boosting of the Attractors

One or more state variables are offset boostable in some chaotic systems if adding a DC offset to this variable can boost the attractor in its dimension line. In this system, variable z is offset boostable, and by the transformation $z \longrightarrow z + k$ where k is a constant, the system's attractor moves forward and backward in the z dimension. So, equation (2) changes to

$$\begin{aligned}
\dot{x} &= y,\\
\dot{y} &= z + k,\\
\dot{z} &= w,\\
\dot{w} &= -1.02w + 1.64x^2 + \left(-1.36y^2\right)\\
&\quad + 0.28xy + 2.42x(z + k) + 1.45 + a|y - x - b|.
\end{aligned} \tag{4}$$

Considering this transformation in system (1), without the PWL term, shows that variable z is not offset boostable in the original system. In this case (Figure 6(a)), the attractor of the system changes from limit cycle to chaotic one as k varies from -3 to 3, with the step size equal to 0.5. However, in system (2), changing the parameter k from -30 to 30 boosts the attractor, as shown in Figure 6(b). It should be noted that increasing the parameter k alters the state variable z from a bipolar signal to a unipolar one.

To better represent the effect of the offset boosting parameter, the average of the state variables should be analyzed. The average of offset boostable variables should increase linearly as the parameter k increases, while other state variables' averages should remain constant. Figure 7(b) shows that these conditions are satisfied in system (2) while the original system does not have this feature. In system (1), X_{mean} does not remain constant, and Z_{mean} has some fluctuations.

5. FPGA Implementation of 4D PWL Hyperjerk System

Digital implementations of a chaotic system have incredible importance in capturing the main characteristics of nonlinear systems. Recent literature has shown an increasing interest in hardware implementation of nonlinear models

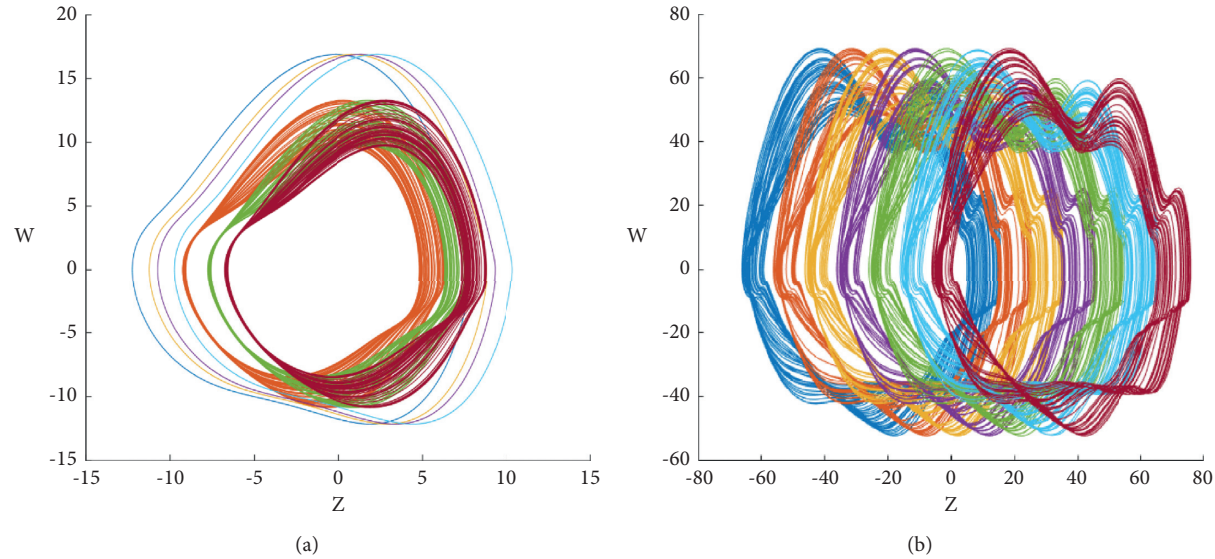

FIGURE 6: Projection of systems (1) and (2) in the zw plane. Varying the control parameter k, (a) from −3 to 3 in system (1), shows that this system is not offset boostable. However, in (b), when k changes from −30 to 30 in system (2), the system shows offset boostable property. In both panels, $a = 3.5$, $b = 1$, and $(x_0, y_0, z_0, w_0) = (-2.77 - 0.53\ 2.7 - 0.34)$.

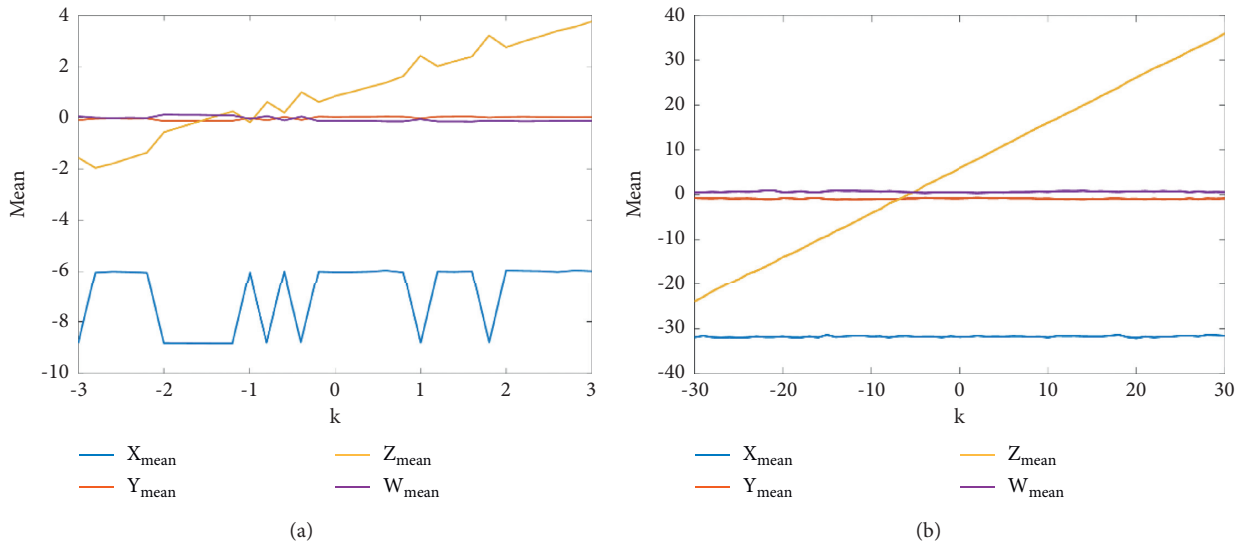

FIGURE 7: (a) and (b) the state variables' average in systems (1) and (2). (a) The average of variable z does not precisely increase linearly when the control parameter k increases. Also, X_{mean} does not remain constant. However, in system (2), the linear increase of Z_{mean} is seen.

[53–57]. Field programmable gate arrays (FPGA) became a vital tool in characterizing the applications of different implementations of chaotic systems. Many references have shown the practical implementation of nonlinear systems using FPGA [58–62]. The main attraction of FPGA is its lower power consumption compared to other hardware platforms [63–67].

The proposed 4D PWL hyperjerk system is implemented in the FPGA platform, which has high throughput and utilizes fewer resources. The system's schematic and power analysis chart show the number of resources used for the implementation and its utilization percentage of power. The phase space diagram of the system is obtained using Xilinx System Generator tool [64, 66, 67]. This tool is integrated with MATLAB software, and a Simulink diagram is designed using Xilinx blocks which are readily available in the system generator tool kit. Xilinx block sets used in the Simulink design are configured according to the IEEE 754 standard with 32/16 (input/output) bits floating-point and latency equal zero. A forward Euler (FE) numerical method is used to design an integrator of each state equation of system (2). The general form of the FE numerical method and its discretized state equation of system (2) are shown in equations (5) and (6), respectively, as

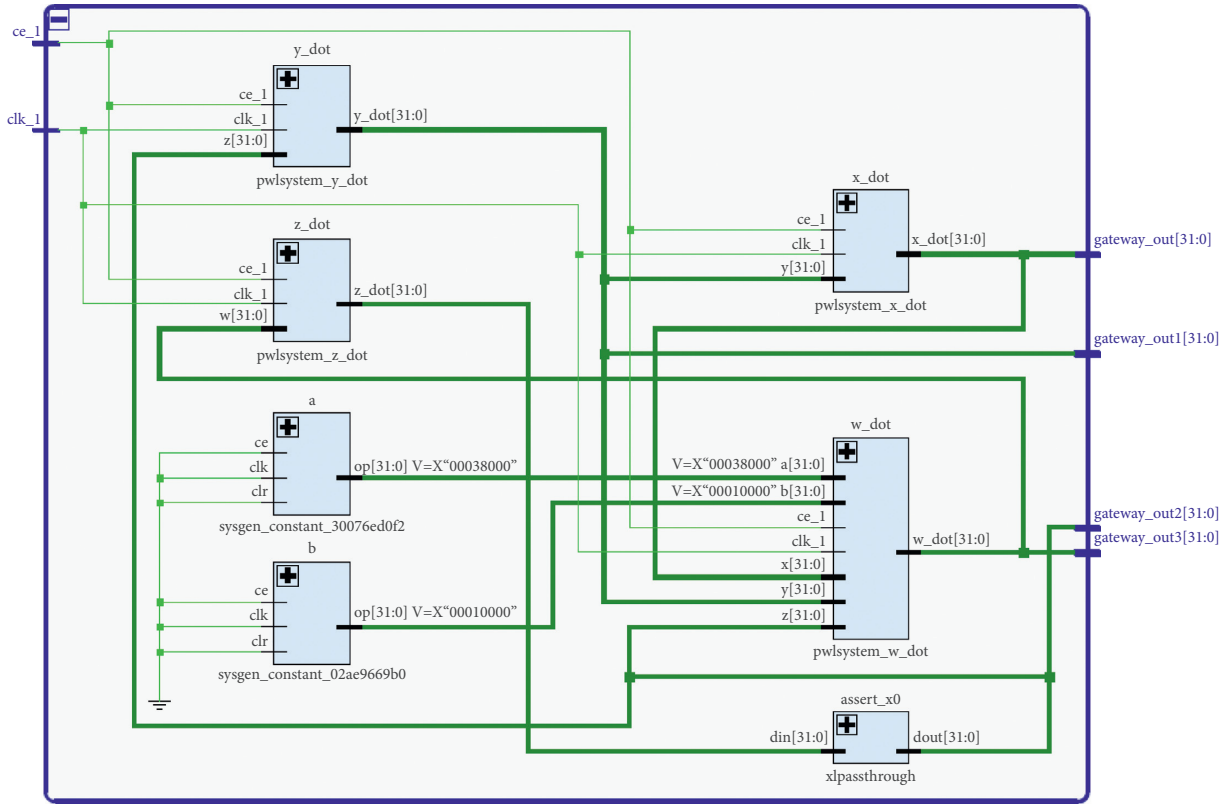

Figure 8: Register transfer level schematic of 4D PWL hyperjerk system implemented in Kintex 7 KC705.

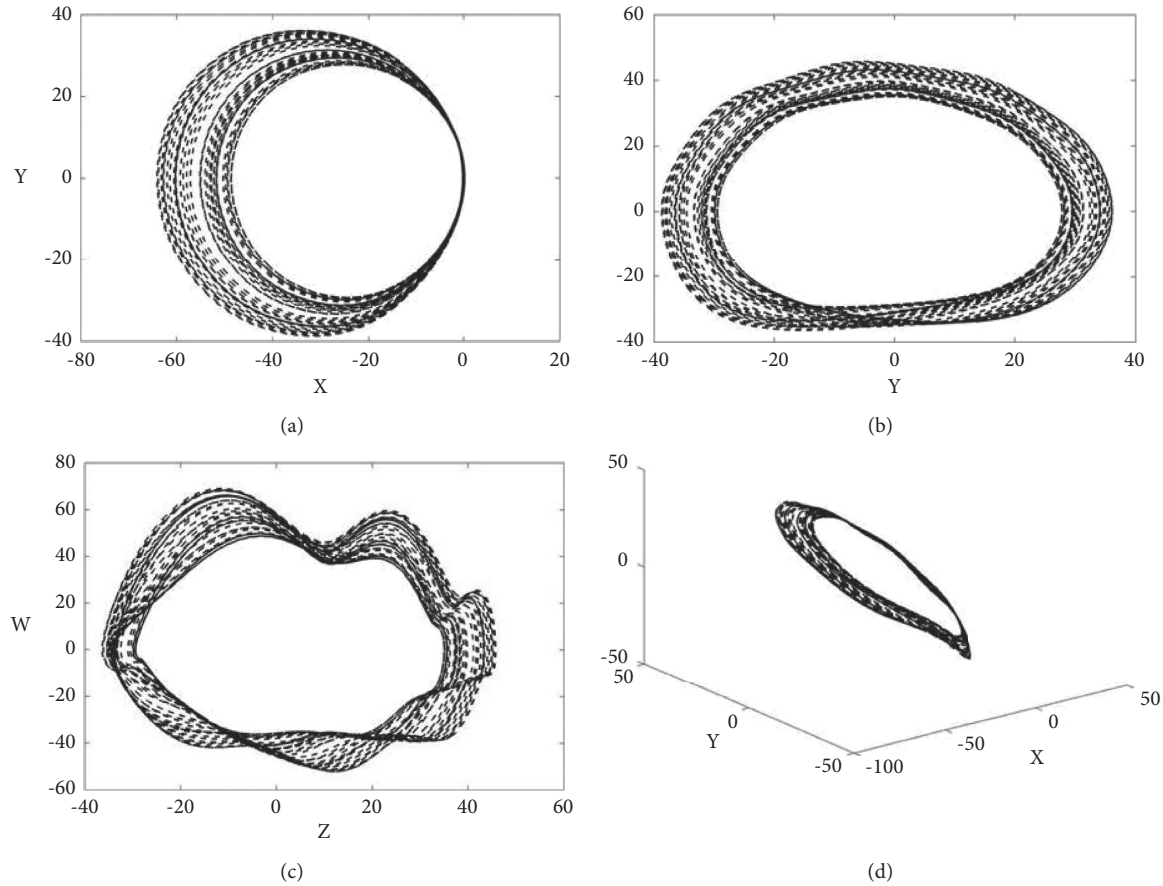

Figure 9: State space in (a) xy, (b) yz, (c) zw, and (d) xyz of system (2) when $a = 3.5$ and $b = 1$ with initial conditions $(x_0, y_0, z_0, w_0) = (-2.77, -0.53, 2.7, -0.34)$.

Table 1: Resource utilization table for the 4D PWL hyperjerk system implemented in FPGA.

S. no.	Name of resources	Utilization of resources	Total available resources	Percentage of utilization
1	FF	256	202800	0.13
2	LUT	753	101400	0.74
3	I/O	129	285	45.26
5	DSP48	40	600	6.67
6	BUFG	1	32	3.13

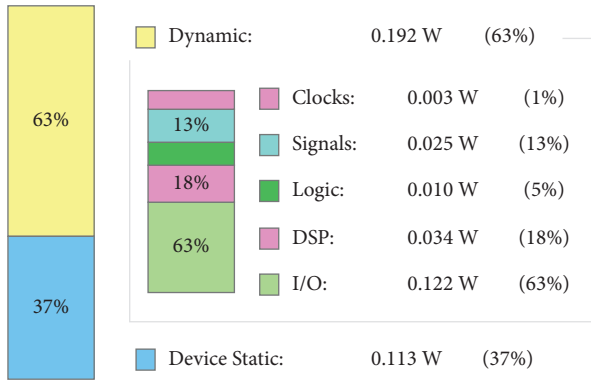

Figure 10: Power utilization of the FPGA implemented 4D PWL hyperjerk system.

$$u_{n+1} = u_n + hf(u_{n-1}), \tag{5}$$

$$\begin{aligned} x_{n+1} &= x_n + h(y_{n-1}),\\ y_{n+1} &= y_n + h(z_{n-1}),\\ z_{n+1} &= z_n + h(w_{n-1}),\\ w_{n+1} &= w_n + h(-1.02w_{n-1}\\ &\quad + 1.64x_{n-1}^2 - 1.36y_{n-1}^2\\ &\quad + 0.28x_{n-1}y_{n-1}\\ &\quad + 2.42x_{n-1}z_{n-1} + 1.45\\ &\quad + a|y_{n-1} - x_{n-1} - b|). \end{aligned} \tag{6}$$

The step size h is set to 0.001. Also, the parameter values $a = 3.5$ and $b = 1$ are generated using Xilinx constant block. The state phase diagram is produced and shown in Figure 8 when $(x_0, y_0, z_0, w_0) = (-2.77, -0.53, 2.7, -0.34)$. Following the Simulink design [56, 57], the system is then synthesized and implemented through Vivado design tool, and its VHDL or VERILOG description is automatically generated. An elaborated design of system (2) using the Kintex 7 xc7k160t-1fbg484 chip is presented in Figure 9. Hardware-software cosimulation is performed with Kintex 7 KC705 kit to prove that the proposed system is implemented using hardware [66, 67]. The utilization of resources and power is presented in Table 1 and Figure 10, respectively.

6. Discussion and Conclusion

About ten years ago, Leonov et al. discovered a kind of attractor in which the basin of attraction did not intersect with neighborhoods of equilibria [68]. Such attractors are different from the previously known ones, which can be excited from unstable equilibria. Investigating hidden attractors in real-world systems has received much interest as they may cause undesired dynamics and stability issues. Systems with no equilibria are an important subgroup of hidden attractors. Therefore, we were motivated to design a system with no equilibria which employed the absolute function as the nonlinear term.

Numerical results showed that taking the polarity information from one term of the proposed system makes it have offset boosting property. Due to this rare feature, the proposed system's attractor is moved through the z-axis when the control parameter k is changed as $z \longrightarrow z + k$ in equation (2), while the other state variables' average remained constant. Comparing the proposed system with the original system indicated that this property was inserted through the absolute function. The offset boostable variable z allowed adjusting the location of the attractor in its direction, which provides controllability in this system.

Using the absolute function made the proposed system a piecewise linear (PWL) one. PWL systems mostly consist of two or more affine functions. These affine functions provide the situation in which adding more equilibria and switching surfaces provide multiscroll attractors [34, 37]. Although, in the proposed system, a general case was considered with nonlinear terms that empower the attractors' complexity, this claim can be confirmed by comparing the bifurcation diagrams derived from both these subgroups of PWL systems.

Chaotic systems have been frequently used in encryption block of secure communication systems according to their robustness against noise and attack [69]. Previous studies suggested that the chaos-encrypted images, both grayscale and RGB, have no correlation with the original image [70].

Also, the quality of the image does not decrease during the decryption process. Chaotic systems also have been used to generate random numbers in cryptography [71]. To improve the application of chaotic systems, optimization methods can be used [72]. These single and multiobjective optimization methods have used different numerical approaches to increase (or decrease) the Lyapunov exponents [73], Kaplan–Yorke dimension [74], and complexity indexes [75]. Future works can focus on optimizing the indexes of the proposed system to provide its application in image encryption and random number generator.

Data Availability

All the numerical simulation parameters are mentioned in the respective text part, and there are no additional data requirements for the simulation results.

Conflicts of Interest

The authors declare no conflicts of interest.

Acknowledgments

The authors extend their gratitude to the Deanship of Scientific Research at King Khalid University for funding this work through research groups program under grant number R.G.P.1/72/42.

References

[1] H. D. Abarbanel, R. Brown, J. J. Sidorowich, and L. S. Tsimring, "The analysis of observed chaotic data in physical systems," *Reviews of Modern Physics*, vol. 65, p. 1331, 1993.

[2] H. Korn and P. Faure, "Is there chaos in the brain? II. experimental evidence and related models," *Comptes Rendus Biologies*, vol. 326, pp. 787–840, 2003.

[3] R. Rollins and E. Hunt, "Exactly solvable model of a physical system exhibiting universal chaotic behavior," *Physical Review Letters*, vol. 49, p. 1295, 1982.

[4] K. Aihara, T. Takabe, and M. Toyoda, "Chaotic neural networks," *Physics Letters A*, vol. 144, pp. 333–340, 1990.

[5] Q. Xu, X. Tan, D. Zhu, H. Bao, Y. Hu, and B. Bao, "Bifurcations to bursting and spiking in the chay neuron and their validation in a digital circuit," *Chaos, Solitons & Fractals*, vol. 141, Article ID 110353, 2020.

[6] M. Frank and T. Stengos, "Chaotic dynamics in economic time-series," *Journal of Economic Surveys*, vol. 2, pp. 103–133, 1988.

[7] B. Bao, N. Wang, Q. Xu, H. Wu, and Y. Hu, "A simple third-order memristive band pass filter chaotic circuit," *IEEE Transactions on Circuits and Systems II: Express Briefs*, vol. 64, pp. 977–981, 2016.

[8] J. Kengne, G. D. Leutcho, and A. N. K. Telem, "Reversals of period doubling, coexisting multiple attractors, and offset boosting in a novel memristive diode bridge-based hyperjerk circuit," *Analog Integrated Circuits and Signal Processing*, vol. 101, pp. 379–399, 2019.

[9] S. Jafari, J. Sprott, and S. M. R. H. Golpayegani, "Elementary quadratic chaotic flows with no equilibria," *Physics Letters A*, vol. 377, pp. 699–702, 2013.

[10] R. D. J. Escalante-González and E. Campos-Cantón, "Generation of chaotic attractors without equilibria via piecewise linear systems," *International Journal of Modern Physics C*, vol. 28, Article ID 1750008, 2017.

[11] R. D. J. Escalante-González and E. Campos-Cantón, "A class of piecewise linear systems without equilibria with 3-D grid multiscroll chaotic attractors," *IEEE Transactions on Circuits and Systems II: Express Briefs*, vol. 66, pp. 1456–1460, 2018.

[12] J. P. Singh and B. Roy, "The simplest 4-D chaotic system with line of equilibria, chaotic 2-torus and 3-torus behaviour," *Nonlinear Dynamics*, vol. 89, pp. 1845–1862, 2017.

[13] T. Gotthans, J. C. Sprott, and J. Petrzela, "Simple chaotic flow with circle and square equilibrium," *International Journal of Bifurcation and Chaos*, vol. 26, Article ID 1650137, 2016.

[14] K. Barati, S. Jafari, J. C. Sprott, and V. T. Pham, "Simple chaotic flows with a curve of equilibria," *International Journal of Bifurcation and Chaos*, vol. 26, Article ID 1630034, 2016.

[15] S. Jafari, J. Sprott, V. T. Pham, C. Volos, and C. Li, "Simple chaotic 3D flows with surfaces of equilibria," *Nonlinear Dynamics*, vol. 86, pp. 1349–1358, 2016.

[16] L. Kocarev, "Chaos-based cryptography: a brief overview," *IEEE Circuits and Systems Magazine*, vol. 1, pp. 6–21, 2001.

[17] D. Dudkowski, S. Jafari, T. Kapitaniak, N. V. Kuznetsov, G. A. Leonov, and A. Prasad, "Hidden attractors in dynamical systems," *Physics Reports*, vol. 637, pp. 1–50, 2016.

[18] M. F. Danca, N. Kuznetsov, and G. Chen, "Unusual dynamics and hidden attractors of the rabinovich–fabrikant system," *Nonlinear Dynamics*, vol. 88, pp. 791–805, 2017.

[19] P. Li, T. Zheng, C. Li, X. Wang, and W. Hu, "A unique jerk system with hidden chaotic oscillation," *Nonlinear Dynamics*, vol. 86, pp. 197–203, 2016.

[20] C. Li and J. C. Sprott, "Coexisting hidden attractors in a 4-D simplified lorenz system," *International Journal of Bifurcation and Chaos*, vol. 24, Article ID 1450034, 2014.

[21] M. F. Danca, P. Bourke, and N. Kuznetsov, "Graphical structure of attraction basins of hidden chaotic attractors: the rabinovich–fabrikant system," *International Journal of Bifurcation and Chaos*, vol. 29, Article ID 1930001, 2019.

[22] M. F. Danca, N. V. Kuznetsov, and G. Chen, "Approximating hidden chaotic attractors via parameter switching," *Chaos: An Interdisciplinary Journal of Nonlinear Science*, vol. 28, Article ID 013127, 2018.

[23] X. Wang and G. Chen, "A chaotic system with only one stable equilibrium," *Communications in Nonlinear Science and Numerical Simulation*, vol. 17, pp. 1264–1272, 2012.

[24] Q. Li, H. Zeng, and J. Li, "Hyperchaos in a 4D memristive circuit with infinitely many stable equilibria," *Nonlinear Dynamics*, vol. 79, pp. 2295–2308, 2015.

[25] Q. Xu, Y. Lin, B. Bao, and M. Chen, "Multiple attractors in a non-ideal active voltage-controlled memristor based chua's circuit," *Chaos, Solitons & Fractals*, vol. 83, pp. 186–200, 2016.

[26] T. Kapitaniak and G. A. Leonov, *Multistability: Uncovering Hidden Attractors*, Springer, Berlin, Germany, 2015.

[27] P. Sharma, M. Shrimali, A. Prasad, N. Kuznetsov, and G. Leonov, "Control of multistability in hidden attractors," *The European Physical Journal-Special Topics*, vol. 224, pp. 1485–1491, 2015.

[28] M. Chen, Y. Feng, H. Bao, B. Bao, H. Wu, and Q. Xu, "Hybrid state variable incremental integral for reconstructing extreme multistability in memristive jerk system with cubic nonlinearity," *Complexity*, vol. 2019, Article ID 8549472, 16 pages, 2019.

[29] B. Bao, Y. Zhu, C. Li, H. Bao, and Q. Xu, "Global multistability and analog circuit implementation of an adapting synapse-

based neuron model," *Nonlinear Dynamics*, vol. 101, pp. 1105–1118, 2020.

[30] R. Sevilla-Escoboza, G. Huerta-Cuéllar, R. Jaimes-Reátegui et al., "Error-feedback control of multistability," *Journal of the Franklin Institute*, vol. 354, pp. 7346–7358, 2017.

[31] R. Sevilla-Escoboza, J. Buldú, A. Pisarchik, S. Boccaletti, and R. Gutiérrez, "Synchronization of intermittent behavior in ensembles of multistable dynamical systems," *Physical Review E*, vol. 91, Article ID 32902, 2015.

[32] N. Kuznetsov and G. Leonov, "Hidden attractors in dynamical systems: systems with no equilibria, multistability and coexisting attractors," *IFAC Proceedings Volumes*, vol. 47, pp. 5445–5454, 2014.

[33] A. Pisarchik, R. Jaimes-Reátegui, C. Rodríguez-Flores, J. García-López, G. Huerta-Cuellar, and F. Martín-Pasquín, "Secure chaotic communication based on extreme multistability," *Journal of the Franklin Institute*, vol. 358, pp. 2561–2575, 2021.

[34] R. D. J. Escalante-González, E. Campos-Cantón, and M. Nicol, "Generation of multi-scroll attractors without equilibria via piecewise linear systems," *Chaos: An Interdisciplinary Journal of Nonlinear Science*, vol. 27, Article ID 53109, 2017.

[35] E. Campos, "Derivation of a continuous time dynamic planar system with two unstable foci from a three-dimensional chaotic piecewise linear system," *Chaos: An Interdisciplinary Journal of Nonlinear Science*, vol. 30, Article ID 53114, 2020.

[36] C. Li, J. C. Sprott, W. Thio, and H. Zhu, "A new piecewise linear hyperchaotic circuit," *IEEE Transactions on Circuits and Systems II: Express Briefs*, vol. 61, pp. 977–981, 2014.

[37] F. Delgado-Aranda, I. Campos-Cantón, E. Tristán-Hernández, and P. Salas-Castro, "Hidden attractors from the switching linear systems," *Revista Mexicana de Física*, vol. 66, pp. 683–691, 2020.

[38] J. López-Rentería, E. Campos-Cantón, B. Aguirre-Hernández, and G. Fernández-Anaya, "A monoparametric family of piecewise linear systems to generate scroll attractors via path-connected set of polynomials," *International Journal of Bifurcation and Chaos*, vol. 31, Article ID 2150034, 2021.

[39] B. Aguirre-Hernández, E. Campos-Cantón, J. A. López-Renteria, and E. D. González, "A polynomial approach for generating a monoparametric family of chaotic attractors via switched linear systems," *Chaos, Solitons & Fractals*, vol. 71, pp. 100–106, 2015.

[40] Z. Njitacke, T. Fozin, L. K. Kengne, G. Leutcho, E. M. Kengne, and J. Kengne, "Multistability and its annihilation in the chua's oscillator with piecewise-linear nonlinearity," *Chaos Theory and Applications*, vol. 2, pp. 77–89, 2020.

[41] J. Lü, T. Zhou, G. Chen, and X. Yang, "Generating chaos with a switching piecewise-linear controller," *Chaos: An Interdisciplinary Journal of Nonlinear Science*, vol. 12, pp. 344–349, 2002.

[42] C. Li, T. Lei, X. Wang, and G. Chen, "Dynamics editing based on offset boosting," *Chaos: An Interdisciplinary Journal of Nonlinear Science*.vol. 30, Article ID 63124, 2020.

[43] J. R. Pulido–Luna, J. A. López–Renterıa, and N. R. Cazarez–Castro, "Chaos synchronization by an observer–based active control," 2004.

[44] J. R. Pulido-Luna, J. A. López-Rentería, and N. R. Cazarez-Castro, "Design of a nonhomogeneous nonlinear synchronizer and its implementation in reconfigurable hardware," *Mathematical and Computational Applications*, vol. 25, p. 51, 2020.

[45] C. Li, J. C. Sprott, Z. Yuan, and H. Li, "Constructing chaotic systems with total amplitude control," *International Journal of Bifurcation and Chaos*, vol. 25, Article ID 1530025, 2015.

[46] C. Li, W. Hu, J. C. Sprott, and X. Wang, "Multistability in symmetric chaotic systems," *The European Physical Journal - Special Topics*, vol. 224, pp. 1493–1506, 2015.

[47] C. Li, X. Wang, and G. Chen, "Diagnosing multistability by offset boosting," *Nonlinear Dynamics*, vol. 90, pp. 1335–1341, 2017.

[48] C. Li and J. C. Sprott, "Variable-boostable chaotic flows," *Optik*, vol. 127, pp. 10389–10398, 2016.

[49] C. Li, J. C. Sprott, Y. Liu, Z. Gu, and J. Zhang, "Offset boosting for breeding conditional symmetry," *International Journal of Bifurcation and Chaos*, vol. 28, Article ID 1850163, 2018.

[50] S. Panahi, V. T. Pham, K. Rajagopal, O. Boubaker, and S. Jafari, "A new four-dimensional chaotic system with no equilibrium point," *Recent Advances in Chaotic Systems and Synchronization*, Elsevier, Amsterdam, The Netherlands, pp. 63–76, 2019.

[51] O. Guillén-Fernández, M. F. Moreno-López, and E. Tlelo-Cuautle, "Issues on applying one-and multi-step numerical methods to chaotic oscillators for FPGA implementation," *Mathematics*, vol. 9, p. 151, 2021.

[52] A. Wolf, J. B. Swift, H. L. Swinney, and J. A. Vastano, "Determining lyapunov exponents from a time series," *Physica D: Nonlinear Phenomena*, vol. 16, pp. 285–317, 1985.

[53] M. F. Tolba, A. H. Elsafty, M. Armanyos, L. A. Said, A. H. Madian, and A. G. Radwan, "Synchronization and fpga realization of fractional-order izhikevich neuron model," *Microelectronics Journal*, vol. 89, pp. 56–69, 2019.

[54] M. Tuna, M. Alçın, I. Koyuncu, C. B. Fidan, and I. Pehlivan, "High speed FPGA-based chaotic oscillator design," *Microprocessors and Microsystems*, vol. 66, pp. 72–80, 2019.

[55] M. Tuna and C. B. Fidan, "Electronic circuit design, implementation and FPGA-based realization of a new 3D chaotic system with single equilibrium point," *Optik*, vol. 127, pp. 11786–11799, 2016.

[56] K. Rajagopal, L. Guessas, A. Karthikeyan, A. Srinivasan, and G. Adam, "Fractional order memristor no equilibrium chaotic system with its adaptive sliding mode synchronization and genetically optimized fractional order PID synchronization," *Complexity*, vol. 2017, Article ID 1892618, 19 pages, 2017.

[57] K. Rajagopal, F. Nazarimehr, A. Karthikeyan, A. Srinivasan, and S. Jafari, "CAMO: self-excited and hidden chaotic flows," *International Journal of Bifurcation and Chaos*, vol. 29, Article ID 1950143, 2019.

[58] S. Sadoudi, M. S. Azzaz, M. Djeddou, and M. Benssalah, "An FPGA real-time implementation of the chen's chaotic system for securing chaotic communications," *International Journal of Nonlinear Science*, vol. 7, pp. 467–474, 2009.

[59] L. Ávalos-Ruiz, C. Zúñiga-Aguilar, J. Gómez-Aguilar, R. Escobar-Jiménez, and H. Romero-Ugalde, "FPGA implementation and control of chaotic systems involving the variable-order fractional operator with mittag–leffler law," *Chaos, Solitons & Fractals*, vol. 115, pp. 177–189, 2018.

[60] I. Koyuncu, A. T. Ozcerit, and I. Pehlivan, "Implementation of FPGA-based real time novel chaotic oscillator," *Nonlinear Dynamics*, vol. 77, pp. 49–59, 2014.

[61] E. Tlelo-Cuautle, V. Carbajal-Gomez, P. Obeso-Rodelo, J. Rangel-Magdaleno, and J. C. Nunez-Perez, "FPGA realization of a chaotic communication system applied to image processing," *Nonlinear Dynamics*, vol. 82, pp. 1879–1892, 2015.

[62] H. Chen, S. He, A. D. P. Azucena et al., "A multistable chaotic jerk system with coexisting and hidden attractors: dynamical and complexity analysis, FPGA-based realization, and chaos stabilization using a robust controller," *Symmetry*, vol. 12, p. 569, 2020.

[63] B. Karakaya, A. Gülten, and M. Frasca, "A true random bit generator based on a memristive chaotic circuit: analysis, design and FPGA implementation," *Chaos, Solitons & Fractals*, vol. 119, pp. 143–149, 2019.

[64] A. Karthikeyan and K. Rajagopal, "FPGA implementation of fractional-order discrete memristor chaotic system and its commensurate and incommensurate synchronisations," *Pramana*, vol. 90, p. 14, 2018.

[65] Q. Ding, J. Pang, J. Fang, and X. Peng, "Designing of chaotic system output sequence circuit based on FPGA and its applications in network encryption card," *International Journal of Innovative Computing, Information and Control*, vol. 3, pp. 449–456, 2007.

[66] K. Rajagopal, L. Guessas, S. Vaidyanathan, A. Karthikeyan, and A. Srinivasan, "Dynamical analysis and FPGA implementation of a novel hyperchaotic system and its synchronization using adaptive sliding mode control and genetically optimized PID control," *Mathematical Problems in Engineering*, vol. 2017, Article ID 7307452, 14 pages, 2017.

[67] K. Rajagopal, A. Karthikeyan, and A. K. Srinivasan, "FPGA implementation of novel fractional-order chaotic systems with two equilibriums and no equilibrium and its adaptive sliding mode synchronization," *Nonlinear Dynamics*, vol. 87, pp. 2281–2304, 2017.

[68] G. Leonov, N. Kuznetsov, and V. Vagaitsev, "Localization of hidden chua's attractors," *Physics Letters A*, vol. 375, pp. 2230–2233, 2011.

[69] E. García-Guerrero, E. Inzunza-González, O. López-Bonilla, J. Cárdenas-Valdez, and E. Tlelo-Cuautle, "Randomness improvement of chaotic maps for image encryption in a wireless communication scheme using PIC-microcontroller via zigbee channels," *Chaos, Solitons & Fractals*, vol. 133, Article ID 109646, 2020.

[70] A. Sambas, S. Vaidyanathan, E. Tlelo-Cuautle et al., "A 3-D multistable system with a peanut-shaped equilibrium curve: circuit design, FPGA realization, and an application to image encryption," *IEEE Access*, vol. 8, pp. 137116–137132, 2020.

[71] S. Vaidyanathan, A. Sambas, B. Abd-El-Atty et al., "A 5-D multistable hyperchaotic two-disk dynamo system with no equilibrium point: circuit design, FPGA realization and applications to TRNGs and image encryption," *IEEE Access*, vol. 9, 2021.

[72] E. Tlelo-Cuautle, L. G. De La Fraga, O. Guillén-Fernández, and A. Silva-Juárez, *Optimization of Integer/Fractional Order Chaotic Systems by Metaheuristics and Their Electronic Realization*, CRC Press, Boca Raton, FL, USA, 2021.

[73] A. Silva-Juárez, C. J. Morales-Pérez, L. G. de la Fraga, E. Tlelo-Cuautle, and J. de Jesús Rangel-Magdaleno, "On maximizing the positive lyapunov exponent of chaotic oscillators applying DE and PSO," *International Journal of Dynamics and Control*, vol. 7, pp. 1157–1172, 2019.

[74] A. Silva-Juárez, E. Tlelo-Cuautle, L. G. de la Fraga, and R. Li, "Optimization of the kaplan-yorke dimension in fractional-order chaotic oscillators by metaheuristics," *Applied Mathematics and Computation*, vol. 394, Article ID 125831, 2021.

[75] M. Sadeghpour, H. Salarieh, and A. Alasty, "Minimum entropy control of chaos via online particle swarm optimization method," *Applied Mathematical Modelling*, vol. 36, pp. 3931–3940, 2012.

Hindawi
Complexity
Volume 2021, Article ID 5499538, 19 pages
https://doi.org/10.1155/2021/5499538

Research Article

Analytic Study of a Novel Color Image Encryption Method Based on the Chaos System and Color Codes

Shamsa Kanwal,[1] **Saba Inam**,[1] **Omar Cheikhrouhou**,[2] **Kinza Mahnoor**,[1] **Atef Zaguia**,[3] **and Habib Hamam**[4,5]

[1]*Deparment of Mathematical Sciences, Faculty of Science and Technology, Fatima Jinnah Women University, The Mall, Rawalpindi, Pakistan*
[2]*CES Laboratory, ENIS, University of Sfax, Sfax 3038, Tunisia*
[3]*College of Computers and Information Technology, Taif University, P.O. Box 11099, Taif 21944, Saudi Arabia*
[4]*Faculty of Engineering, Uni de Moncton, Moncton, Canada*
[5]*International Institute of Technology (IIT), Sfax, Tunisia*

Correspondence should be addressed to Omar Cheikhrouhou; omar.cheikhrouhou@isetsf.rnu.tn

Received 6 April 2021; Revised 2 May 2021; Accepted 25 May 2021; Published 3 June 2021

Academic Editor: Jorge-Antonio Lopez-Renteria

Due to the growing of the use of Internet and communication media, image encryption is rapidly increased. Image sharing through unsafe open channels is vulnerable for attacking and stealing. For protecting the images from attacks, encryption techniques are required. Recently, new and efficient chaos-based techniques have been suggested to develop secure image encryption. This study presents a novel image encryption framework based on integrating the chaotic maps and color codes. Three phases are involved in the proposed image encryption technique. Piecewise chaotic linear map (PWLCM) is used in the first phase for permuting the digital image. In the second phase, substitution is done using Hill cipher which is the mixing of color codes with the permuted image. The third phase is implemented by XORing, a sequence generated by the chaotic logistic map (CLM). The proposed approach enhances the diffusion ability of the image encryption making the encrypted images resistant to the statistical differential attacks. The results of several analyses such as information entropy, histogram correlation of adjacent pixels, unified average changing intensity (UACI), number of pixel change rate (NPCR), and peak signal-to-noise ratio (PSNR) guarantee the security and robustness of the proposed algorithm. The measurements show that the proposed algorithm is a noble overall solution for image encryption. Thorough comparison with other image encryption algorithms is also carried out.

1. Introduction

Images are a substantial source of information not limited to the daily routine of a common person, but having diverse applications in various fields of military, medical, and industry. For example, we may enumerate military image records, trusted video conferencing, satellite imagery, planetary motion images, and keeping a person's medical record [1]. The requirements of consistent, fast, and robust techniques to store and transmit digital images have led to the development of novel encryption techniques. The information conveyed through images is very complex as compared to simple text. Data sent through open channels such as Internet can be illegally accessed and restored. Therefore, the progress in the field of image encryption creates diverse opportunities and applications in upcoming future. Several assessment criteria including the information entropy, correlation between adjacent pixels, peak signal-to-noise ratio (PSNR), the number of pixels change rate (NPCR), and unified average changing intensity (UACI) related to the image encryption are essential for performance evaluation of the encryption algorithms. The algorithm for which the values of these criteria fulfill the standard expectation level can resist the statistical and differential

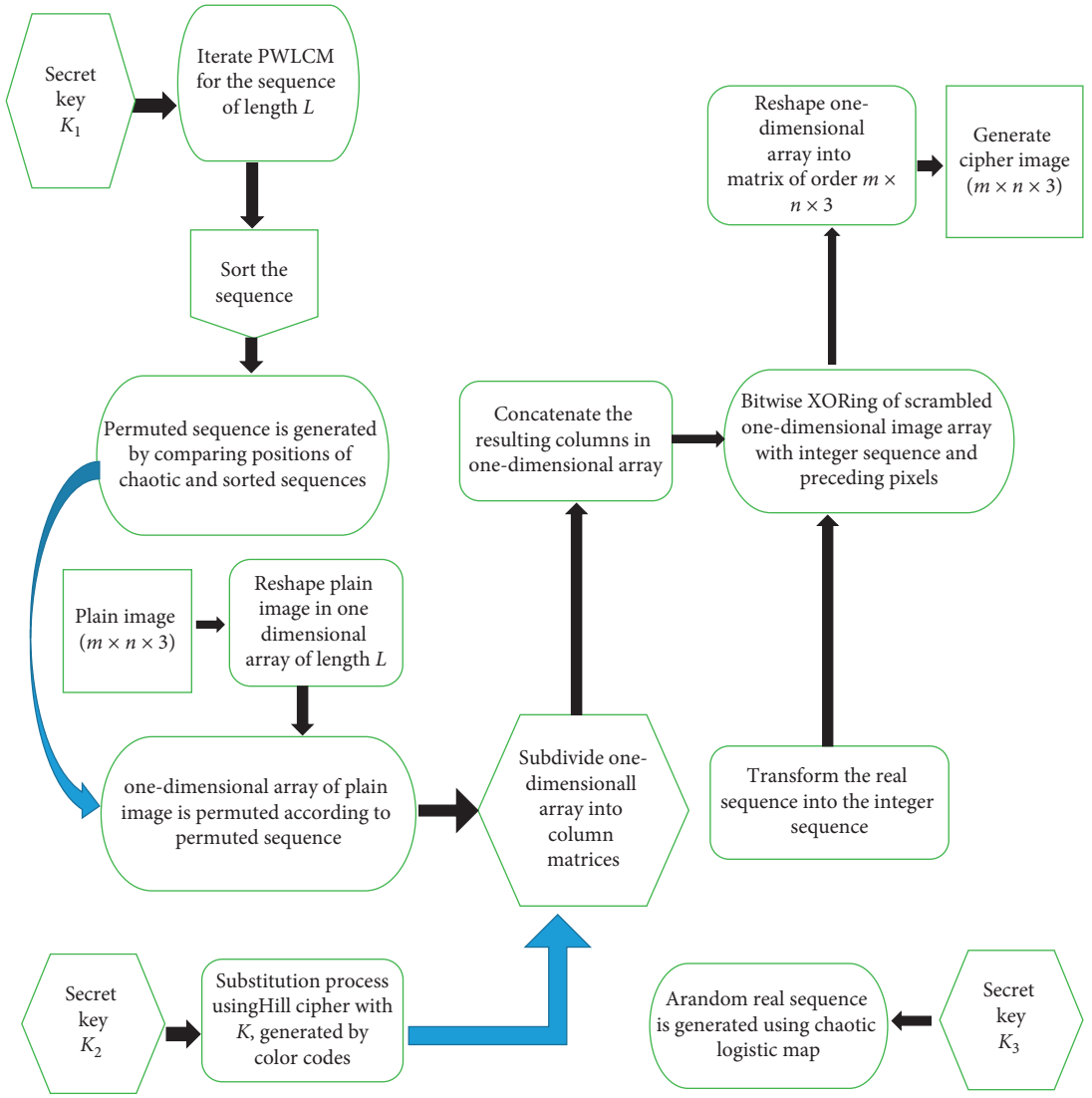

Figure 1: Flowchart of the proposed image encryption algorithm.

Input. Color image I, secret key $K_1 = (\xi_0, \eta)$, PWLCM (1)
Output. Image array PM with scrambled pixels
Step 1. One-dimensional array$P$ of size $L = m \times n \times 3$ is created by reshaping the original image matrix I to one-dimensional array, where m, n are the number of rows and columns, respectively, of the original image matrix I
Step 2. Using PWLCM (1) with the keyK_1, generate the chaotic sequence $X = \{x_1, x_2, ..., x_L\}$ and sort the resulting sequence $\overline{X} = \{\overline{x}_1, \overline{x}_2, ..., \overline{x}_L\}$ in ascending order
Step 3. Compute the position vector of X in $\overline{X}$ and note down the transformed positions TRAN $= \{p_1, p_2, ..., p_L\}$
Step 4. The array P is permuted using TRAN to get PM

Algorithm 1: (Pixel permutation).

attacks [2]. Moreover, for resisting the brute-force attacks, an algorithm with large key space and sensitive to initial conditions is recommended.

Imaging technology meets chaos and propagation requirements compared with traditional encryption systems; chaotic systems [3] have powerful features, such as nonperiodicity, nonlinearity, unpredictability, and extreme sensitivity to initial conditions [4]. Matthews [5] introduced the concept of chaotic function in cryptography. He suggested that a random sequence can be generated by iterating a nonlinear function with certain conditions. In 1998, [6] Friedrich first applied the chaotic system to image encryption. Since then, image encryption based on chaotic systems has gradually become the main field of cryptography

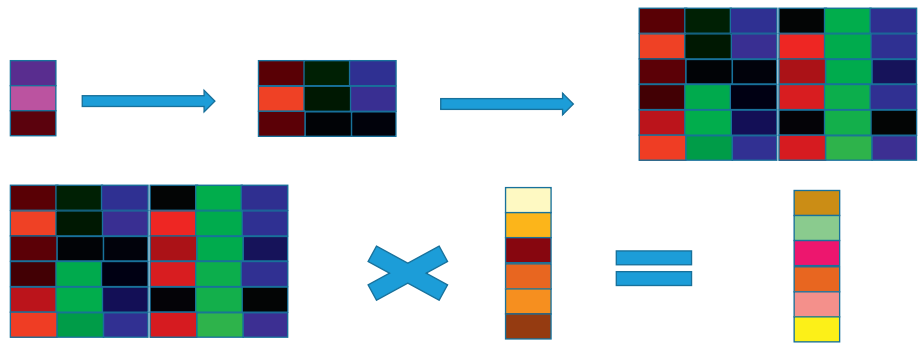

Figure 2: Schematic representation of key mixing with color codes.

Input. Permuted array PM, $K_2 = (\text{color } 1, \text{color } 2, \text{color } 3)$, where color $1 = (R_1, G_1, B_1)$,color $2 = (R_2, G_2, B_2)$, and color $3 = (R_3, G_3, B_3)$ are any three random secret colors in (R, G, B) format and k is any random integer, such that $\gcd(k, 256) = 1$.
Output. An array Q of order L
Step 1. Computing self-invertible matrix
(a) Make a matrix K_{11} (mod256) of order 3×3 as $K_{11} = \begin{bmatrix} R_1 & G_1 & B_1 \\ R_2 & G_2 & B_2 \\ R_3 & G_3 & B_3 \end{bmatrix}$
(b) Take a random integer $k \in (1, 256)$, such that $\gcd(k, 256) = 1$
(c) Calculate $K_{12} = k(I_3 - K_{11}) \text{mod} 256$, $K_{21} = k^{-1}(I_3 + K_{11}) \text{mod} 256$, and $K_{22} = -K_{11} \text{mod} 256$, where I_3 is the identity matrix.
(d) Form a 6×6 self-invertible matrix K_p as $K_p = \begin{bmatrix} K_{11} & K_{12} \\ K_{21} & K_{22} \end{bmatrix}$
Step 2. Making submatrices M_i
(a) Convert one-dimensional array PM into submatrices of order6×1. The i^{th} matrix is M_i, where $i = 1, 2, \ldots, (L/6)$.
(b) Key mixing is performed using the subsequent formula of Hill cipher $C_i = K_p \times M_i \, (\text{mod} 256)$.
(c) Concatenate all the C_i's in the form of one-dimensional array again as $Q = \{C_1 \| C_2 \| \ldots \| C_{(L/6)}\}$.

Algorithm 2: (Key mixing with color codes).

Input. An arrayQ, secret key $K_3 = (\phi_0, \beta)$, CLM (2).
Output. Encrypted image CI
Step 1. With key K_3 and CLM (2), generate a sequence $R = \{r_1, r_2, \ldots, r_L\}$
Step 2. The sequence R is transformed into a sequence of integers using the following formula: $\text{DF} = \text{floor}(\text{mod}(R_i \times 10^{14}, 256))$.
Step 3. Bitwise XOR each element of Q with element of DF at the corresponding positions and preceding ciphered pixel as $C_i = \text{DF}_i \oplus Q_i \oplus C_{i-1}$, $i = 1, 2, \ldots, L$.
Step 4. Reshape array C in the form of a matrix CI of order $L = m \times n \times 3$
Step 5. Convert resulting matrix in step (4) to get the cipher image

Algorithm 3: (Pixel diffusion).

[7]. Chen and Mao used chaotic 3D cat maps [8] and Baker maps [9] to create permuted image in their proposals. Guan used a chaotic 2D cat map [10] to swap pixels in 2005. Patidar et al. [11] presented image encryption scheme based on substitution-diffusion using chaotic standard map and chaotic logistic maps.

In 2014, [12] Zhang and Wang proposed a new multi-image encryption algorithm based on mixed pixels and piecewise linear chaotic mapping. It is the fastest way to solve the problem. Many researchers have designed image encryption techniques by using various combinations of chaotic maps such as logistic map and Baker map [13], tent and logistic map [14], and the logistic-sine-coupling map [15]. The security and efficiency of algorithms is improved by these suggestions. Liao et al. [16] recently implemented a shorthand strategy based on the enlarged channel model's probability. He also used critical functions and pixel correlation functions [17] for stenographic purpose.

Chaos system plays a vital role in the different fields of mathematics. Many complicated systems can be investigating through chaos systems. Chaotic maps have very interesting features such as sensitivity to the initial value: a completely different sequence is generated with the small change in the initial value. Other features may include nonperiodicity, the map which is used to generate the chaotic sequence is nonperiodic, and randomness behavior, the chaotic sequences which are generated by the chaotic map are mostly pseudorandom sequences with complex

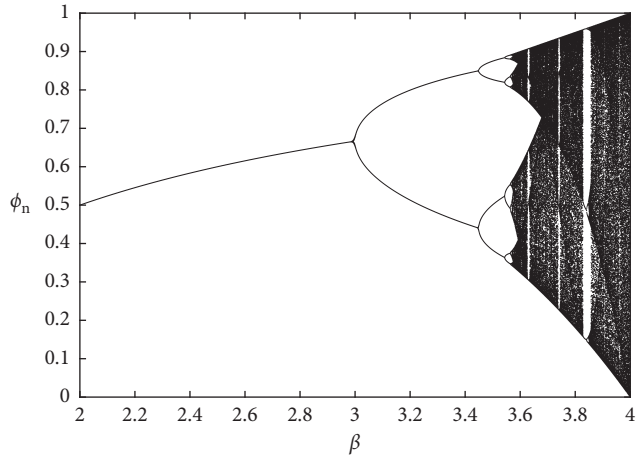

Figure 3: Bifurcation diagram of CLM.

Input. Encrypted imageCI, secret keys K_1, K_2, K_3, PWLCM (1), CLM (2).
Output. Plain color image I
Step 1. The encrypted image matrix CI is placed in an array of size $L = m \times n \times 3$
Step 2. As in step 1 and step 2 in Algorithm 3, the receiver generates a sequence R of size L by secret key K_3 and CLM (2)
Step 3. Each element of CI in step 2 is passing through the following formula:
$D_j = \mathrm{CI}_j \oplus \mathrm{DF}_j \oplus D_{j-1}$, $j = 1, 2, \ldots, L$.
Step 4. By using key K_2, receiver generates matrix K_p as in Algorithm 2, which is self-invertible matrix
Step 5.Convert one-dimensional array D into submatrices $\mathrm{DM}_j$of order 6×1
Step 6. Key mixing is reversed by using the formula
$B_j = K_p \times \mathrm{DM}_j \,(\mathrm{mod}256)$, $j = 1, 2, \ldots, L$.
Step 7. Rewrite all B_j's in the form of one-dimensional array DQ
Step 8. By iterating the PWLCM and using the shared secret key K_1, get a sequence X and get $\overline{X}$ by sorting X in ascending order
Step 9. The permutation array is computed by inverse transform position $(\mathrm{TRAN})^{-1}$
Step 10. Use $(\mathrm{TRAN})^{-1}$ on DQ to get P
Step 11. Reshape P in a matrix form of order $L = m \times n \times 3$ and converted to image I

Algorithm 4: (Image decryption).

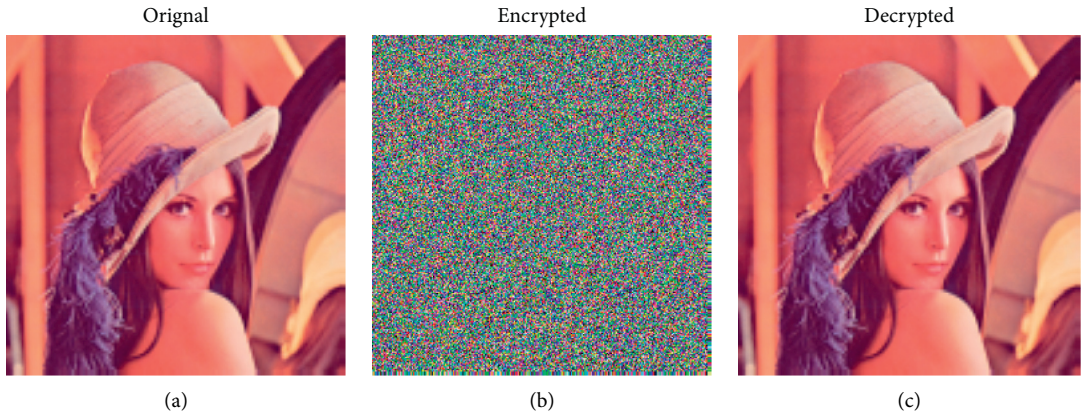

Figure 4: Sample Lena (colored 256×256 pixels). (a) Original image. (b) Encrypted image. (c) Decrypted image.

structures. Due to these features, security of image encryption can be improved because without knowing the correct values of control parameters and initial conditions, an attacker cannot predict the chaos map. These features of chaotic maps enable them to be highly recommended for creating the confusion and diffusion in image encryption. For instance, see references [18–23].

The present study is inspired by the above cited investigations and their applications to different areas. The core goal of this work is to make advanced venture in the regime

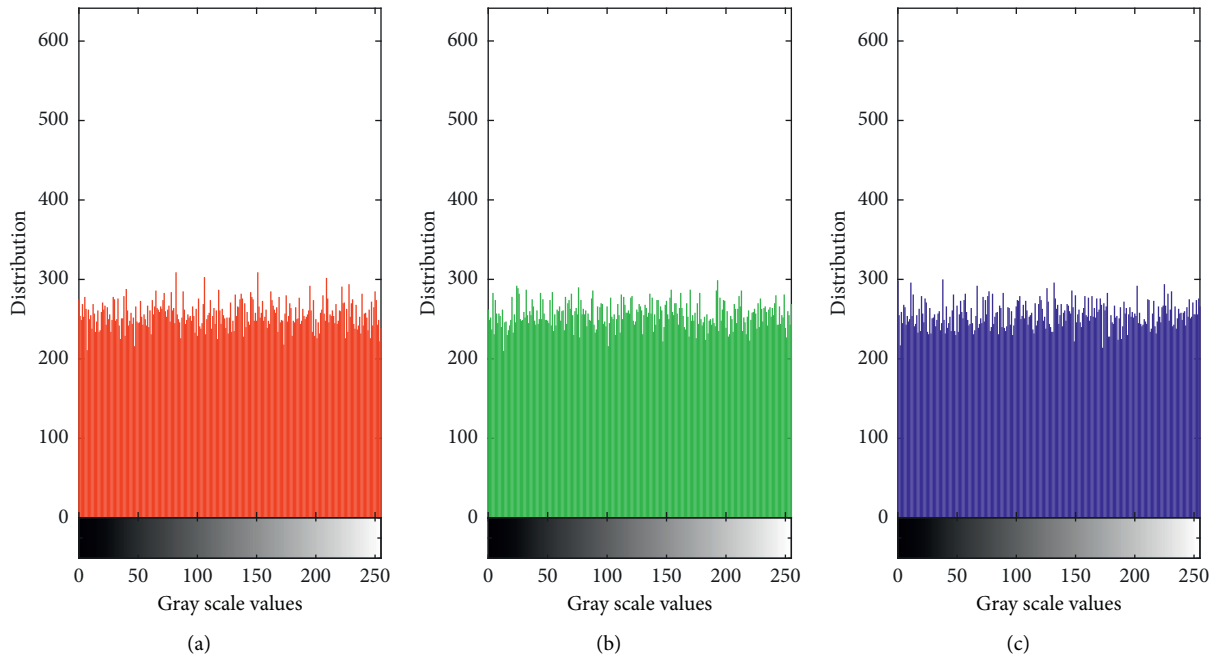

Figure 5: Histogram analysis of encrypted image of Lena (colored 256×256 pixels). (a) Red component. (b) Green component. (c) Blue component.

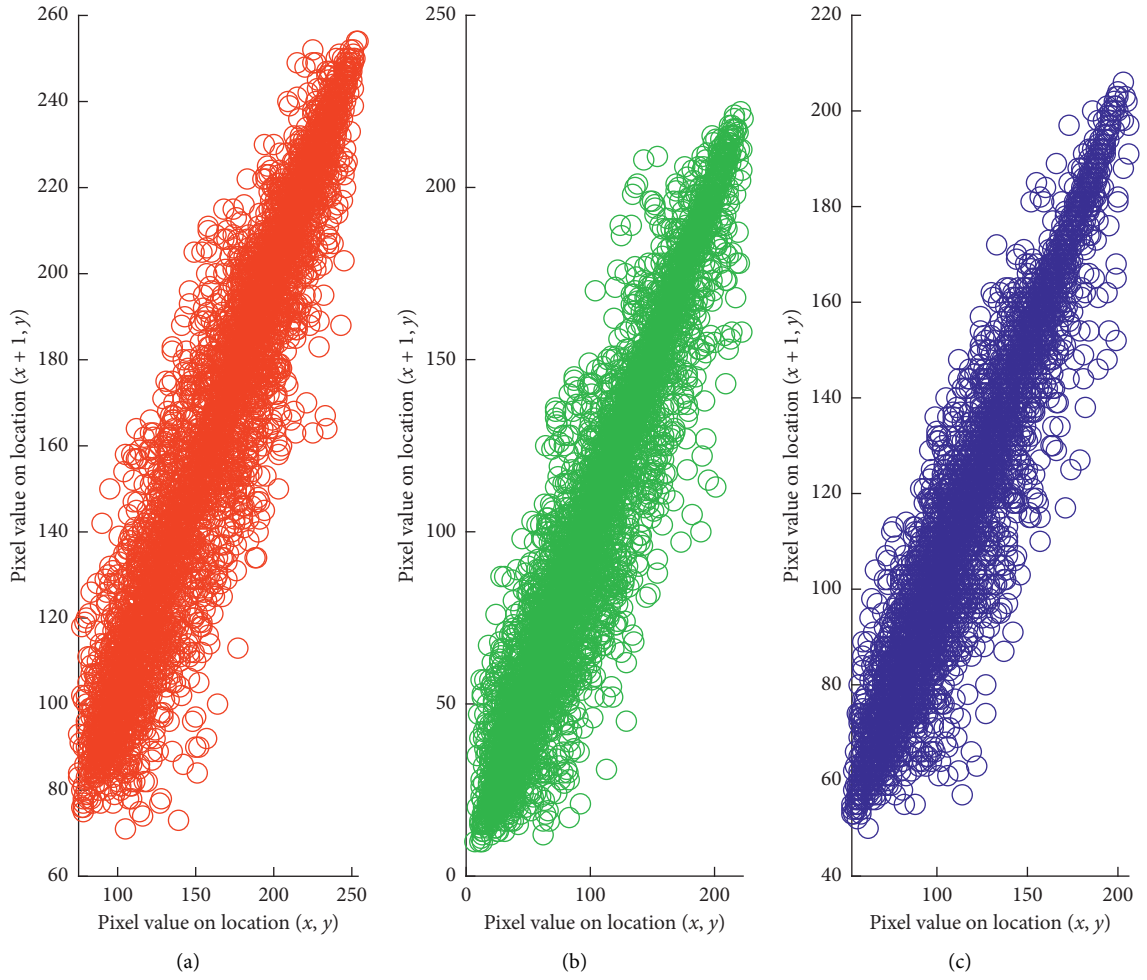

Figure 6: Correlation (row wise) of original image of Lena. (a) Red component. (b) Green component. (c) Blue component.

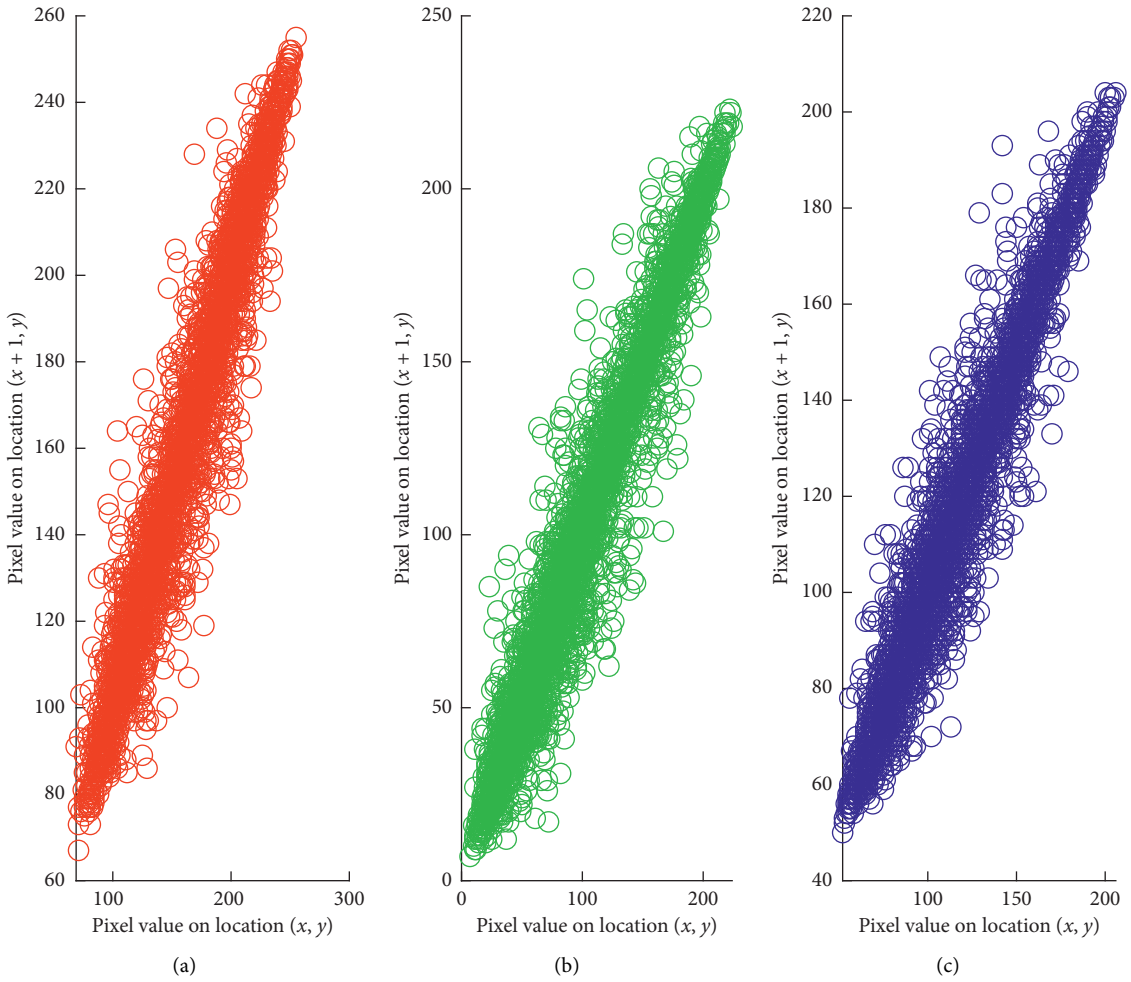

Figure 7: Correlation (column wise) of original image of Lena. (a) Red component. (b) Green component. (c) Blue component.

of image encryption using chaotic maps. More accurately, this manuscript deals with developing and analyzing a novel image encryption that comprises three phases: pixel permutation process, substitution process, and pixel diffusion process. The permutation sequence for the first phase is generated by PWLCM, and the pixels of the plain image are then permuted according to the permutation sequence. Instead of using S-boxes for substitution phase, the substitution of pixels in the permuted image is determined by Hill cipher whose key is generated by color codes. The same key is used in the decryption process because it is self-invertible. At the end, the diffusion process is completed by CLM to ensure the secrecy of the entire image encryption technique. The effectiveness of the proposal is shown by several experimental results. By using information entropy analysis along with other indicative parameters such as entropy, PSNR, UACI, NPCR, and correlation factors, the proposed image encryption technique is compared with some existing techniques.

The remaining study is outlined as follows. The proposed image encryption algorithm is given in Section 2. In Section 3, we present the decryption process. Section 4 is based on the details of implementation results generated by executing the encryption and decryption algorithm to some test images. Section 5 consists of assessments of the algorithm in different aspects. Section 6 concludes the presented work.

2. The Proposed Image Encryption Algorithm

To develop an algorithm, following three aspects should be considered:

(1) The evaluation and implementation of the algorithm must be simple and easy

(2) The design of the encryption algorithm must resist the known attacks

(3) For the algorithms, the concepts and basic ideas must be well established and reliable

Keeping in mind all the three aspects, an efficient and secure technique for image encryption is proposed here, using the chaotic logistic map and color codes.

For the image selection, the size of $m \times n \times 3$ pixels image is recommended for its encryption. The original image is processed into one-dimensional array for encryption, but the encrypted image is again of the size $m \times n \times 3$.

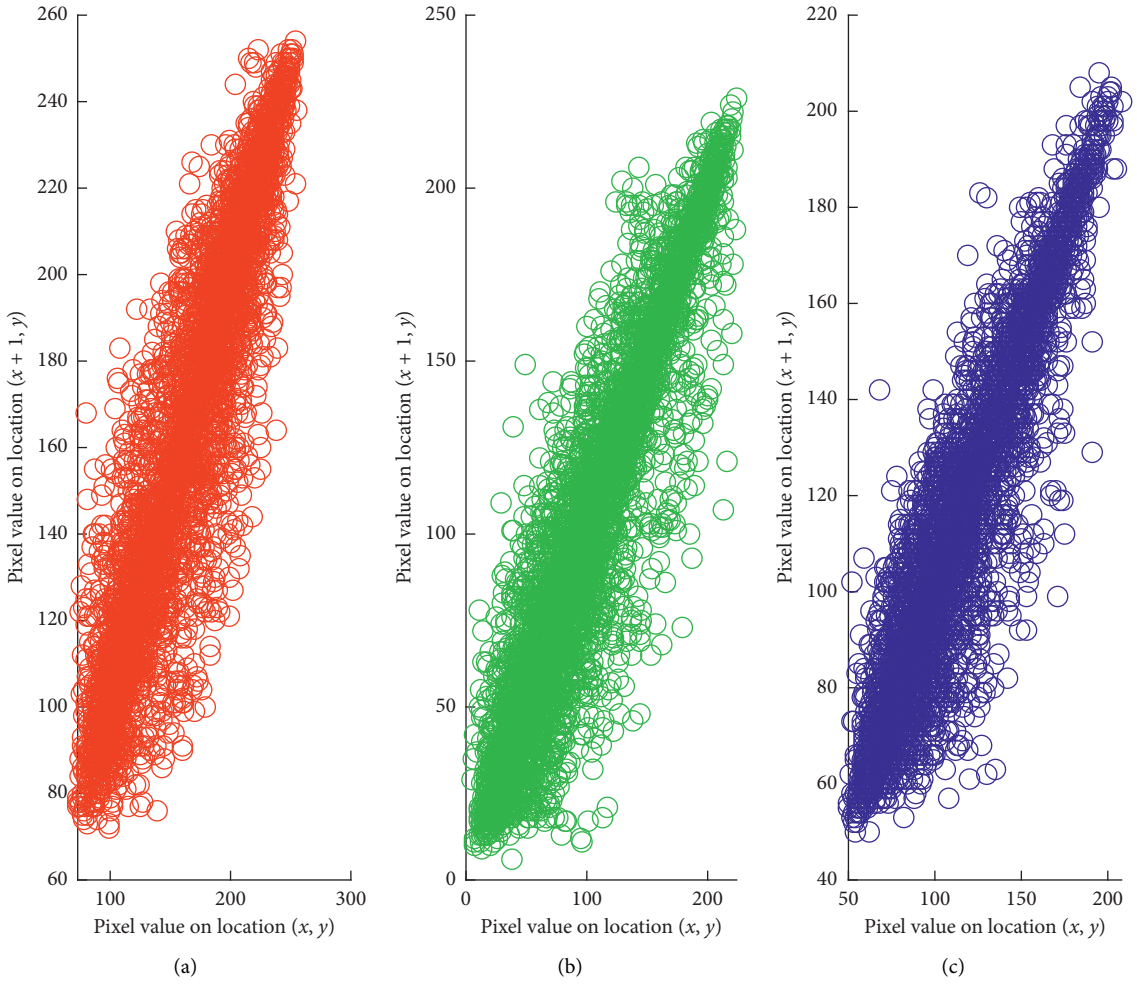

Figure 8: Correlation (diagonal wise wise) of original image of Lena. (a) Red component. (b) Green component. (c) Blue component.

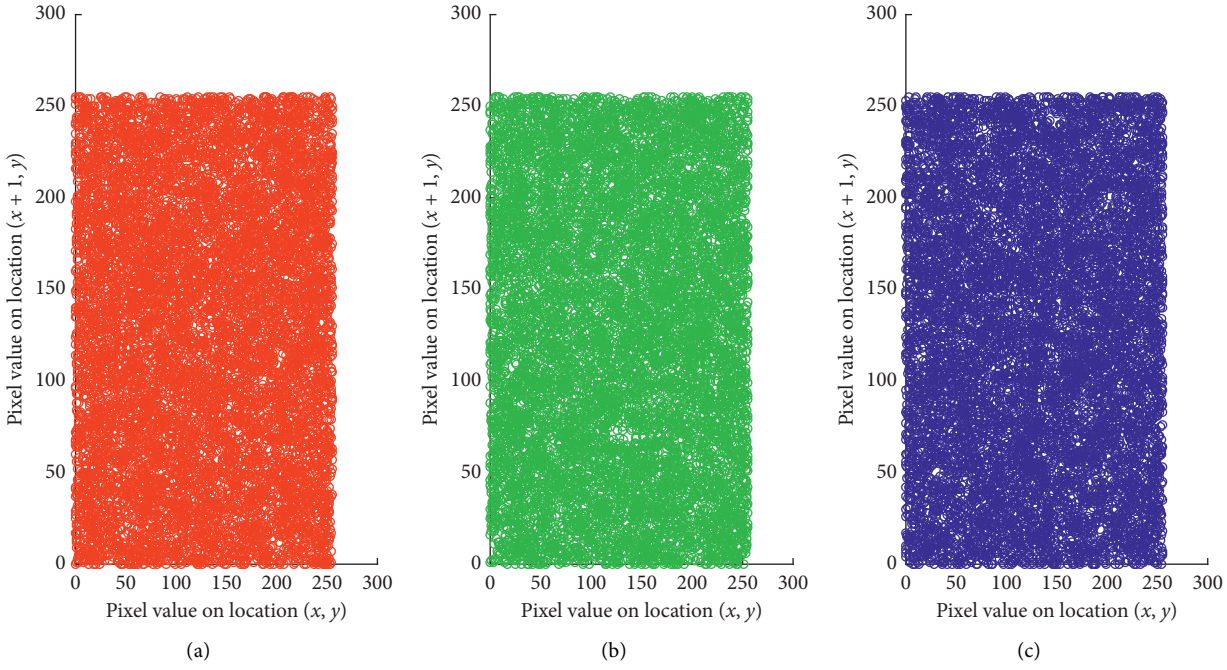

Figure 9: Correlation (row wise) of encrypted image of Lena. (a) Red component. (b) Green component. (c) Blue component.

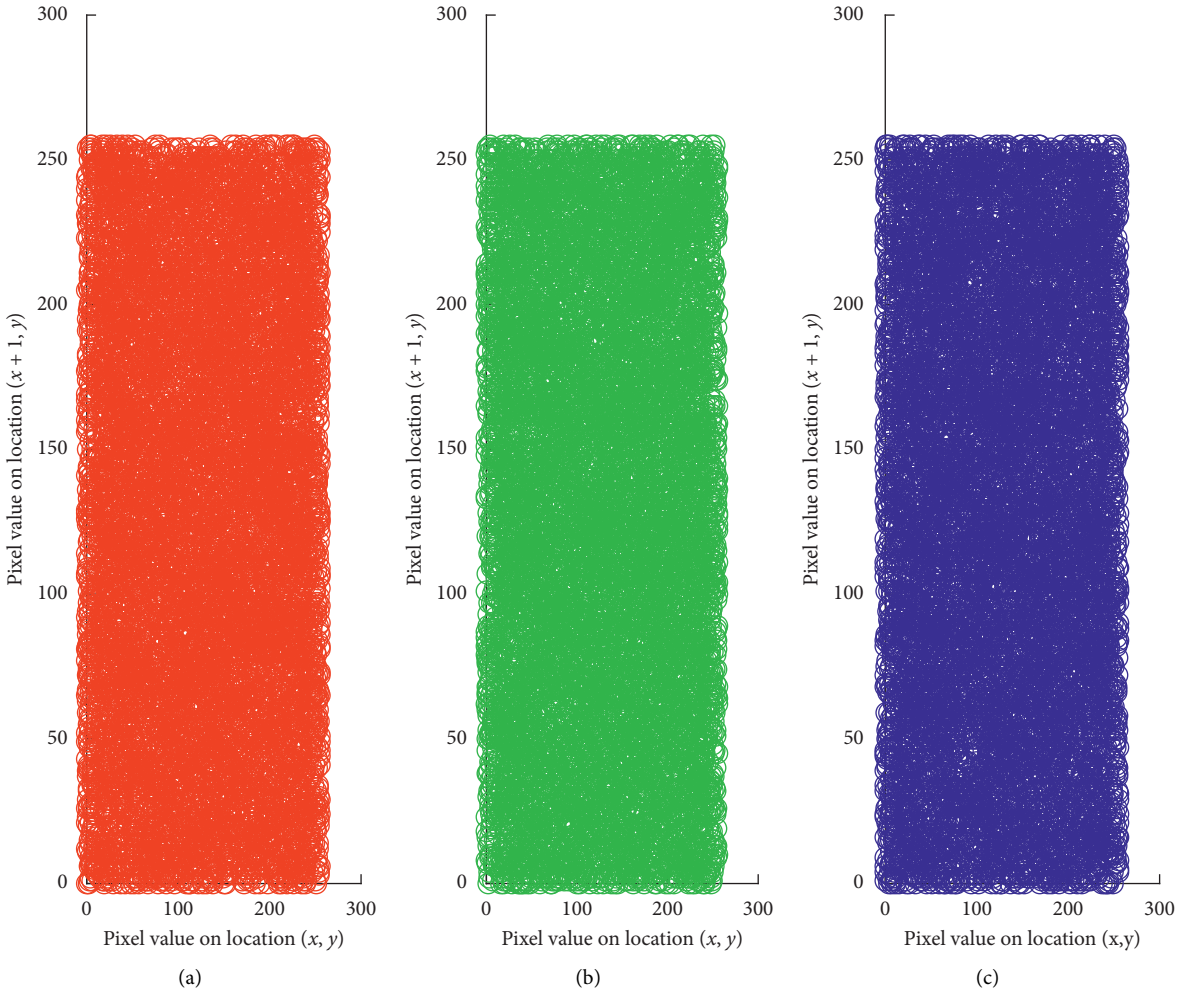

Figure 10: Correlation (column wise) of encrypted image of Lena. (a) Red component. (b) Green component. (c) Blue component.

There are three phases involved in encryption; pixel permutation, substitution process using Hill cipher with color codes, and pixel diffusion. In the first phase, the piecewise linear chaotic map is used for permuting the pixels, so that the statistical structure of the plain image is dissipated into long-range statistics of the cipher image. The permuted image is then mixed with a self-invertible key matrix generated by secret color codes, in the second phase. Finally, confusion is achieved by XORing with another chaotic map to make the relationship between the statistics of the cipher image and the value of the key as complex as possible to thwart attempts of cryptanalyst. The designed flowchart shown in Figure 1 summarizes our proposed encryption algorithm.

2.1. Permutation Process. Three keys K_1, K_2, and K_3 are used in three phases, respectively, of our proposed encryption algorithm. The first phase changes the position of pixels of the original image I. The piecewise chaotic linear map is used to permute the pixels. Using K_1, iterate the piecewise chaotic linear map (PWLCM) to get a chaotic sequence and sort the obtained chaotic sequence in ascending order. By comparing the positions of the chaotic sequence and sorted sequence, obtain the permutation sequence. This permutation sequence is used to permute the one-dimensional array of the plain image.

2.1.1. Piecewise Linear Chaotic Map (PWLCM). There are many different ways to generate the chaotic sequences or the piecewise chaotic maps for the encryption. The authors of [24] proposed hyperchaotic encryption based on multiscroll piecewise linear systems. The manuscript [25] describes maximal unstable dissipative interval to preserve multiscroll attractors via multisaturated functions.

The piecewise linear chaotic map is defined [26] as

$$\xi_{n+1} = f(\xi_n, \eta) = \begin{cases} \dfrac{\xi_n}{\eta}, & \text{if } 0 \le \xi_n \le \eta, \\ \dfrac{(\xi_n - \eta)}{(0.5 - \eta)}, & \text{if } \eta < \xi_n \le 0.5, \\ 1 - \xi_n, & \text{if } 0.5 < \xi_n < 1, \end{cases} \tag{1}$$

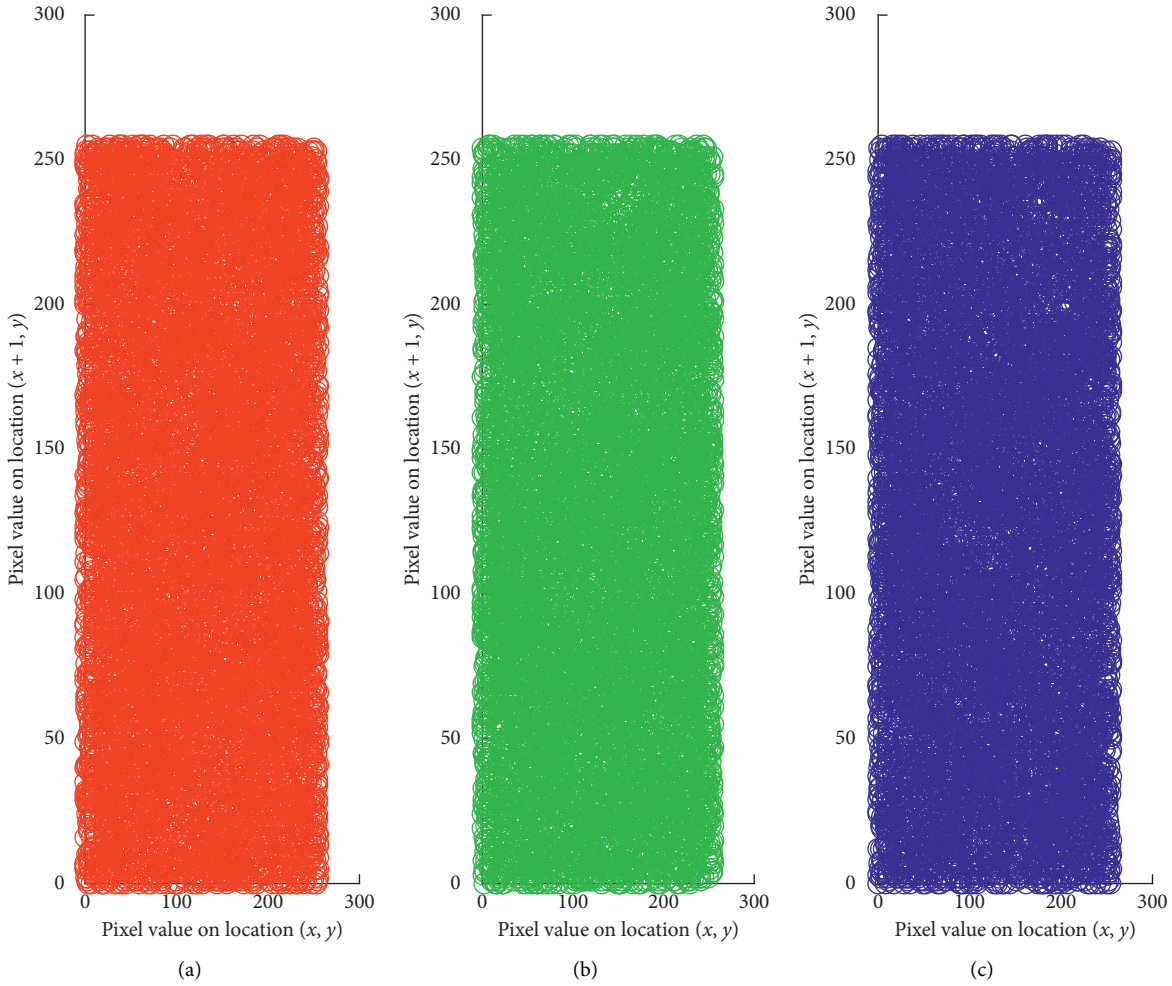

Figure 11: Correlation (diagonal wise) of encrypted image of Lena. (a) Red component. (b) Green component. (c) Blue component.

Table 1: Lena (colored 256 × 256 pixels) image correlation coefficient values.

Direction	Red		Green		Blue	
	Original	Cipher	Original	Cipher	Original	Cipher
Horizontal	0.9910	0.0046	0.9889	0.0005	0.9846	0.0084
Vertical	0.9781	0.0009	0.9741	0.0028	0.9709	−0.0032
Diagonal	0.9648	−0.0012	0.9613	0.0030	0.9563	−0.0022

Table 2: The comparison of values of information entropy.

Image encryption algorithm	Entropy values
Reference [30]	7.9967
Reference [31]	7.9970
Proposed algorithm	7.9990

Table 3: Comparison of NCPR and UACI values.

Image encryption algorithm	NPCR	UACI
Reference [30]	99.61	33.46
Reference [31]	99.22	33.40
Reference [32]	99.61	33.41
Proposed algorithm	99.61	33.46

Table 4: Estimate of critical values of NPCR and UACI.

Image encryption algorithm	Obtained value	NPCR test results		
		0.05 level	0.01 level	0.001 level
			Theoretical NPCR values	
		99.5693%	99.5527%	99.5341%
	99.61%	Pass	Pass	Pass
			UACI test results	
Proposed algorithm		0.05 level	0.01 level	0.001 level
			Theoretical UACI values	
		33.2824–33.6447%	33.2255–33.7016%	33.1594–33.7677%
Proposed algorithm	33.46%	Pass	Pass	Pass

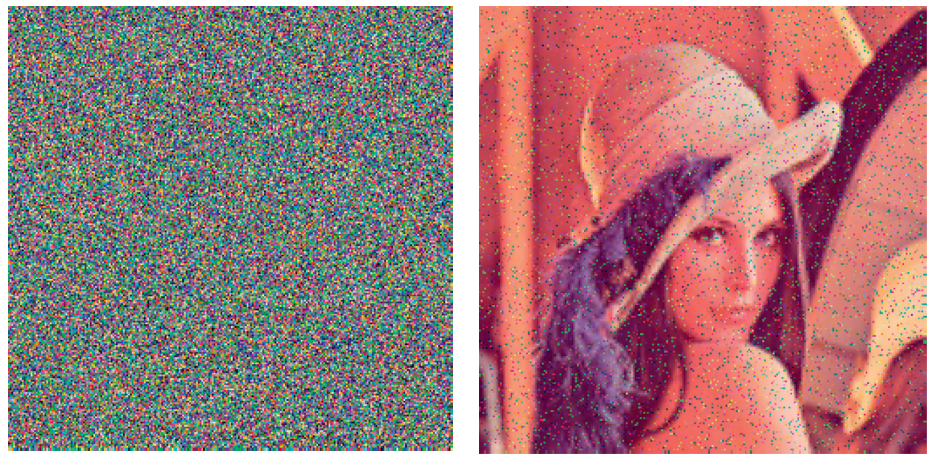

(a) (b)

Figure 12: Experimental results for the performance evaluation of data loss attacks. (a), (b) Cipher images and decryption result of corresponding images using our algorithm with 1% salt and pepper noise.

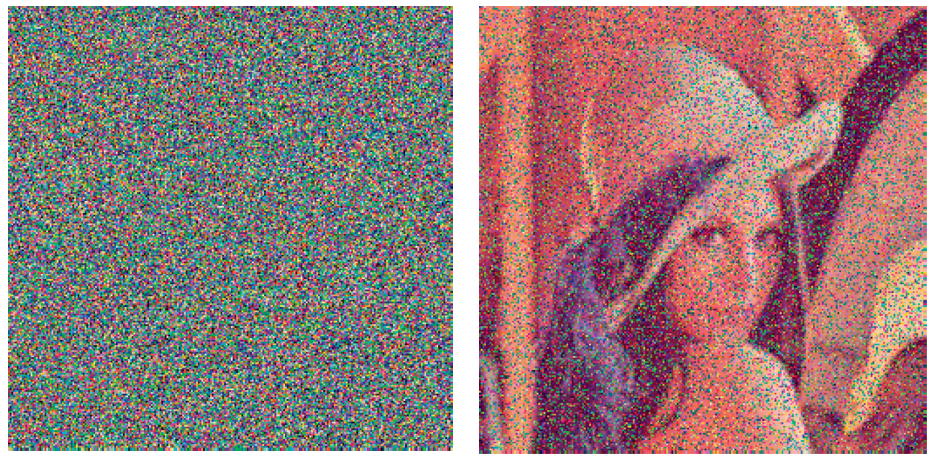

(a) (b)

Figure 13: Experimental results for the performance evaluation of data loss attacks. (a), (b) Cipher images and decryption result of corresponding images using our algorithm with 5% salt and pepper noise.

has many dynamic properties, for example, Lyapunov exponent, random-like behavior, and uniform unvarying density function. For these attributes, PWLCM is highly recommended for cryptographic purposes. The conditions and parameters of PWLCM are as follows:

(1) $\xi_0 \in [0, 1)$, where ξ_0 is the initial value

(2) $\eta \in (0, 0.5)$, where η is the control parameter

(3) $K_1 = (\xi_0, \eta)$, where K_1 is the secret key of the permutation process

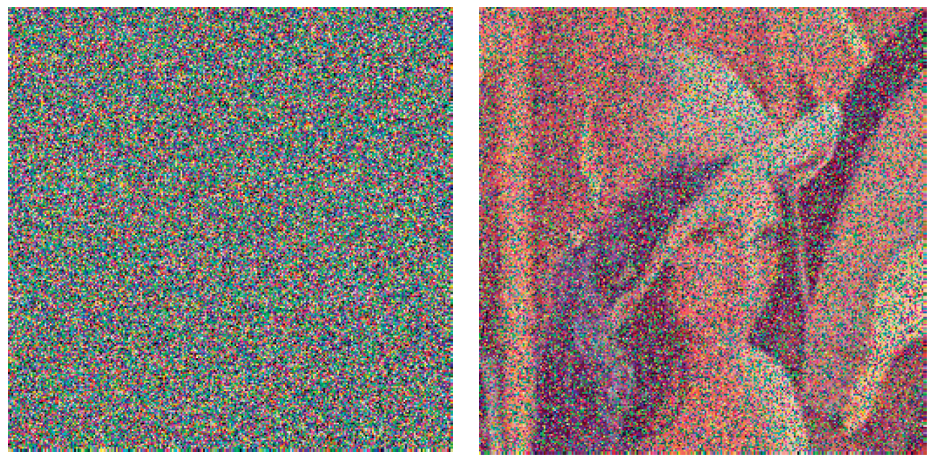

(a) (b)

Figure 14: Experimental results for the performance evaluation of data loss attacks. (a), (b) Cipher images and decryption result of corresponding images using our algorithm with 10% salt and pepper noise.

Table 5: Performance of MSE and PSNR.

Salt and pepper noise (%)	MSE	PSNR
1	8716.6	8.7273
5	8815.9	8.8263
10	8926.2	9.6253

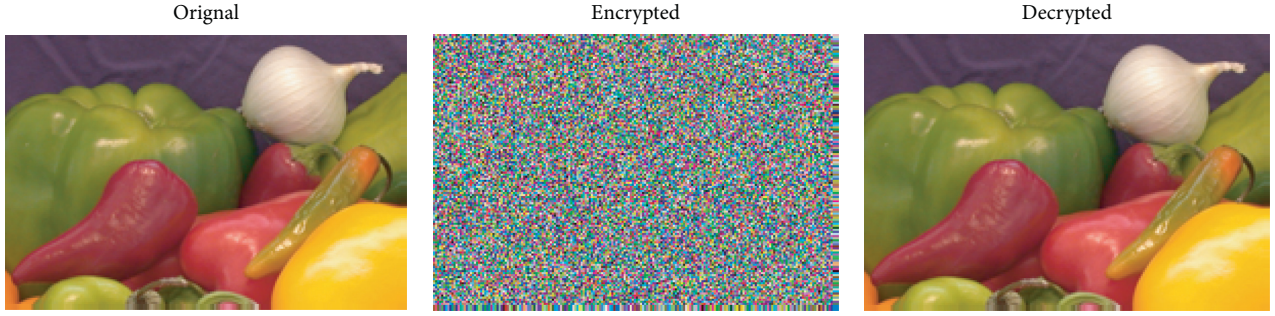

(a) (b) (c)

Figure 15: Sample onion (colored 198 × 135 pixels). (a) Original image. (b) Encrypted image. (c) Decrypted image.

The following Algorithm 1 describes the permutation process.

2.2. Substitution Process Using Hill Cipher and Color Codes. The Hill cipher [27, 28] is a polygraphic block cipher invented by Lester S. Hill in 1929. It serves a significant role in cryptography because of its simplicity, high speed, high throughput, and resistance against frequency analysis attack.

The Hill cipher method requires an invertible key matrix, so that the decryption can be allowed. To overcome the difficulty of having an invertible key matrix, self-invertible matrix is introduced by Acharya et al. [29]. The substitution process is carried out by employing Hill cipher which uses the self-invertible key matrix based on color codes, making the substitution phase simple and efficient.

RGB color format is a model that adds red, blue, and green colors in different quantities and produces new colors. Total bits that each color uses are 8, and hence, they can have any integer value from 0 to 255. There are $256 \times 256 \times 256 = 16777216$ possibilities of generating different colors. Any three colors, color1, color2, and color3, from these possible colors can be selected as our second secret keyK_2. Now, $K_2$is used to generate a self-invertible matrix of order 6×6. The permuted image array PM is divided into $(L/6)$ submatrices of order 6×1. These submatrices are multiplied one by one withK_2. The resulting matrices are combined once again to make a one-dimensional array Q. Figure 2 shows the schematic representation of key mixing

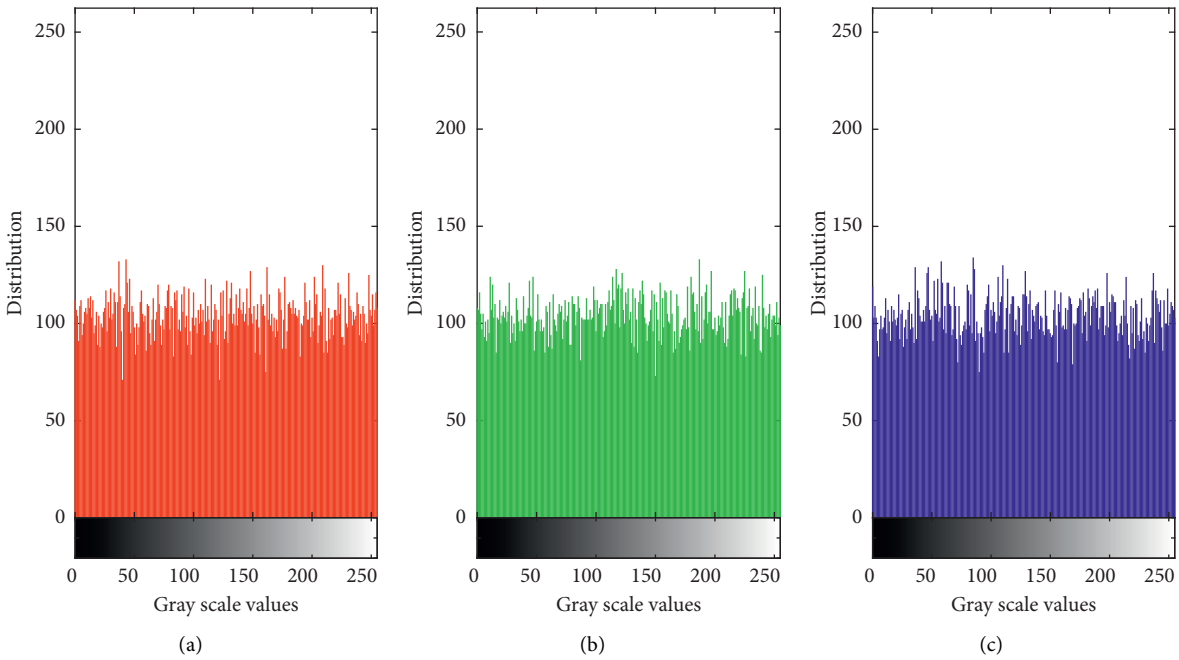

Figure 16: Histogram of cipher image of onion (colored 198 × 135 pixels). (a) Red component. (b) Green component. (c) Blue component.

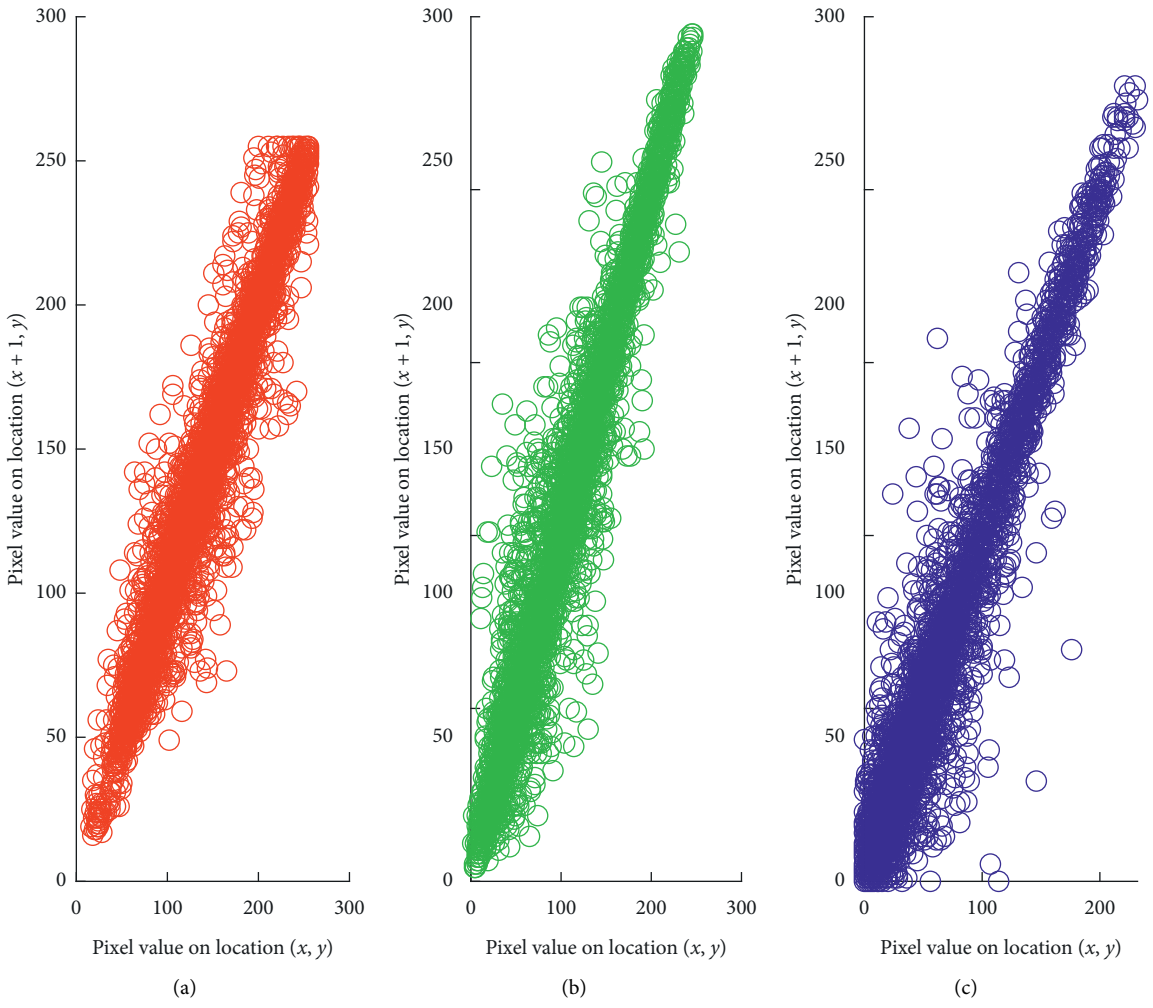

Figure 17: Correlation (row wise) plot of plain onion image. (a) Red component. (b) Green component. (c) Blue component.

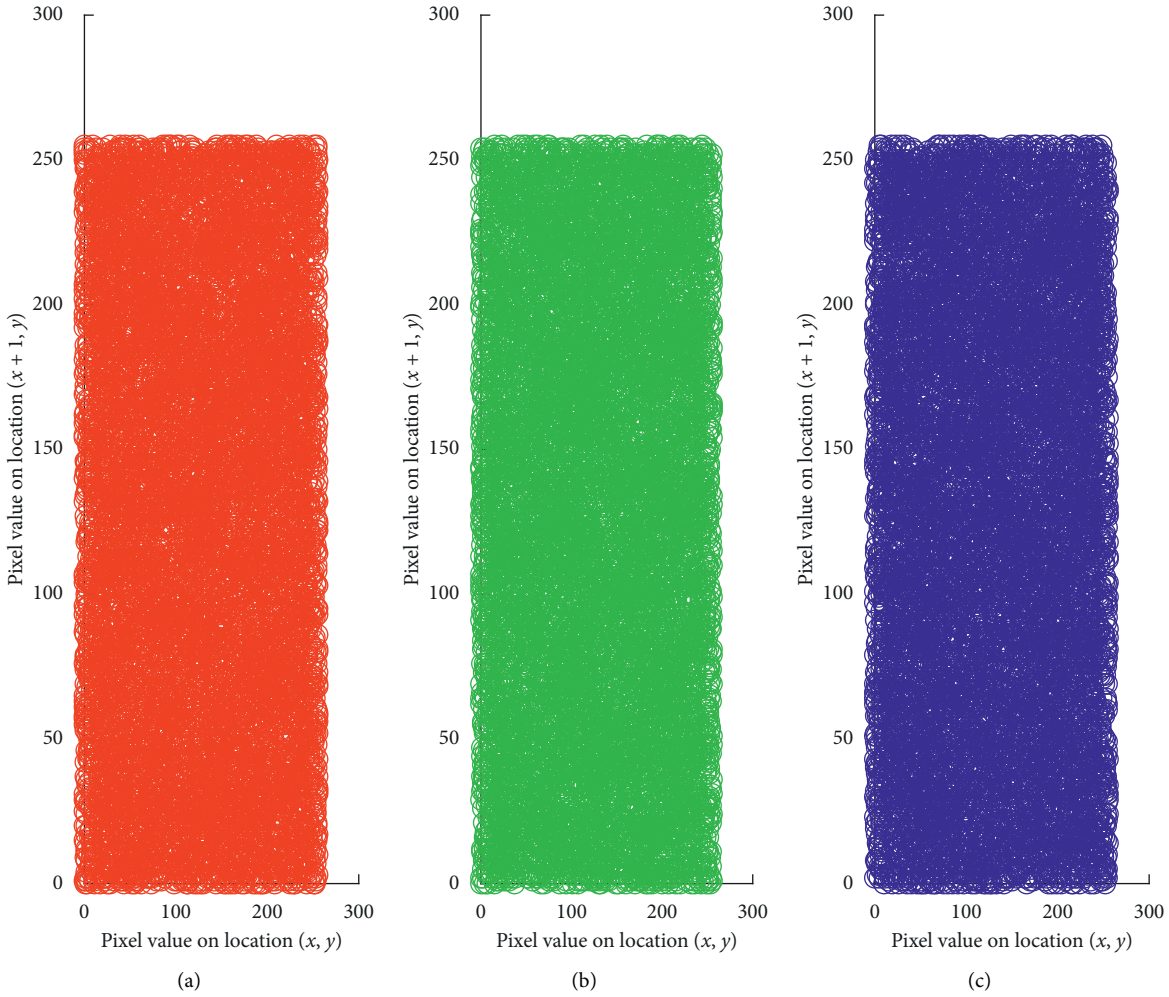

FIGURE 18: Correlation (row wise) plot of color components of onion cipher image. (a) Red component. (b) Green component. (c) Blue component.

with color codes. The Algorithm 2 describes the substitution process.

2.3. Pixel Diffusion Process. In the final phase, using key K_3, a sequence of real numbers, is generated by iterating CLM (2) and converted into integer's sequence using Algorithm 3. To create diffusion, one-dimensional array Q is bitwise XORed with the integer sequence. The resulting one-dimensional array is reshaped as a matrix of order $m \times n \times 3$ again, and cipher image is generated by this matrix.

2.3.1. Chaotic Logistic Map (CLM). The final phase is a combination of a chaotic logistic map and XOR operation to apply the diffusion of pixels. Due to this change of pixel value, the pixels of the cipher image drastically change with even small one bit change in the plain image. For this process, we generate a random sequence using CLM which is defined as follows:

$$\phi_{n+1} = g(\phi_n) = \beta\phi_n(1 - \phi_n). \quad (2)$$

The conditions and parameters of CLM are defined as

(1) $\phi_0 \in (0, 1)$, where ϕ_0 is the initial state of the system

(2) $\beta \in (0, 4)$, where β is the bifurcation control parameter

The chaotic behavior of the CLM with infinite period is shown in Figure 3.

The following Algorithm 3 describes the diffusion process.

3. Image Decryption Process

The following image decryption algorithm is used to revert back to the encryption algorithm for getting the original image. The decryption process also comprises three stages. In the first stage, the XOR operation is eradicated with the sequence generated with key K_3. The effect of color mixing is wiped out by multiplying with the self-invertible key matrix generated by key K_2. Finally, a random sequence and ultimately the inverse of permutation is constructed using key K_1. To reverse the

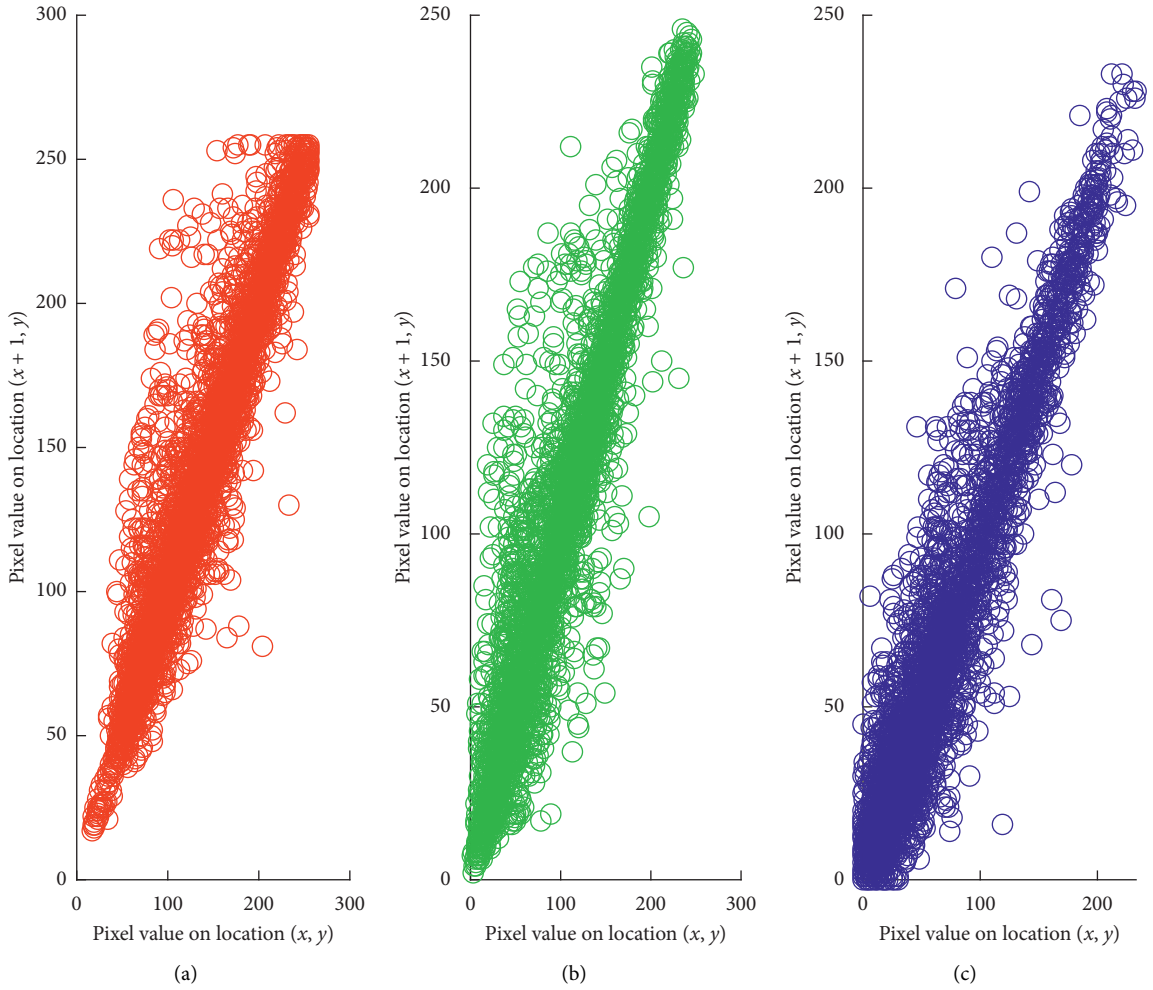

Figure 19: Correlation (column wise) of original image of onion. (a) Red component. (b) Green component. (c) Blue component.

permutation, the inverse permutation is used. The original image is obtained by transforming the subsequent array into image form.

The following Algorithm 4 describes the decryption process.

4. Implementation of Proposed Algorithms

For the evaluation of the proposed scheme, we used Matlab 2018a. The algorithms of pixel permutation, key mixing using Hill cipher with color codes, and pixel diffusion are executed to get the encrypted image and decryption algorithm to again get the plain image back. The standard colored images of Lena with (256×256) pixels are taken for the testing of our proposal. We perform the encryption using $K_1 = (0.766, 0.3432)$, $K_2 =$ (purple haze, bright neon pink, fire brick, 123), and $K_3 = (0.7666, 3.999)$. For comparison purpose, we take image of Lena to compare our results with many other schemes present in the literature. The sample input and output of Lena image by proposed algorithms is shown in Figure 4. The proposed algorithm takes 12.41 seconds to encrypt the Lena image.

5. Results, Analysis, and Performance Evaluation

In this section, proposed algorithm is evaluated by analyzing the statistical and differential parameters. We have developed the guidelines, both generally and specifically to compare the algorithm with different techniques. For performing correct encryption and decryption, these guidelines should be followed when choosing certain parameters involved in the algorithms.

5.1. Statistical Histogram Analysis. Figure 5 shows the histogram of red, green, and blue channels of the cipher image. It is clearly observed that the histogram of the cipher image is fairly uniform. It is evident that no information is leaked from the cipher image of the dispersal of pixels in the original image.

5.2. Correlation Analysis of Adjacent Pixels. The confusion and diffusion can be tested by using correlation analysis between neighboring pixels in the original image and the

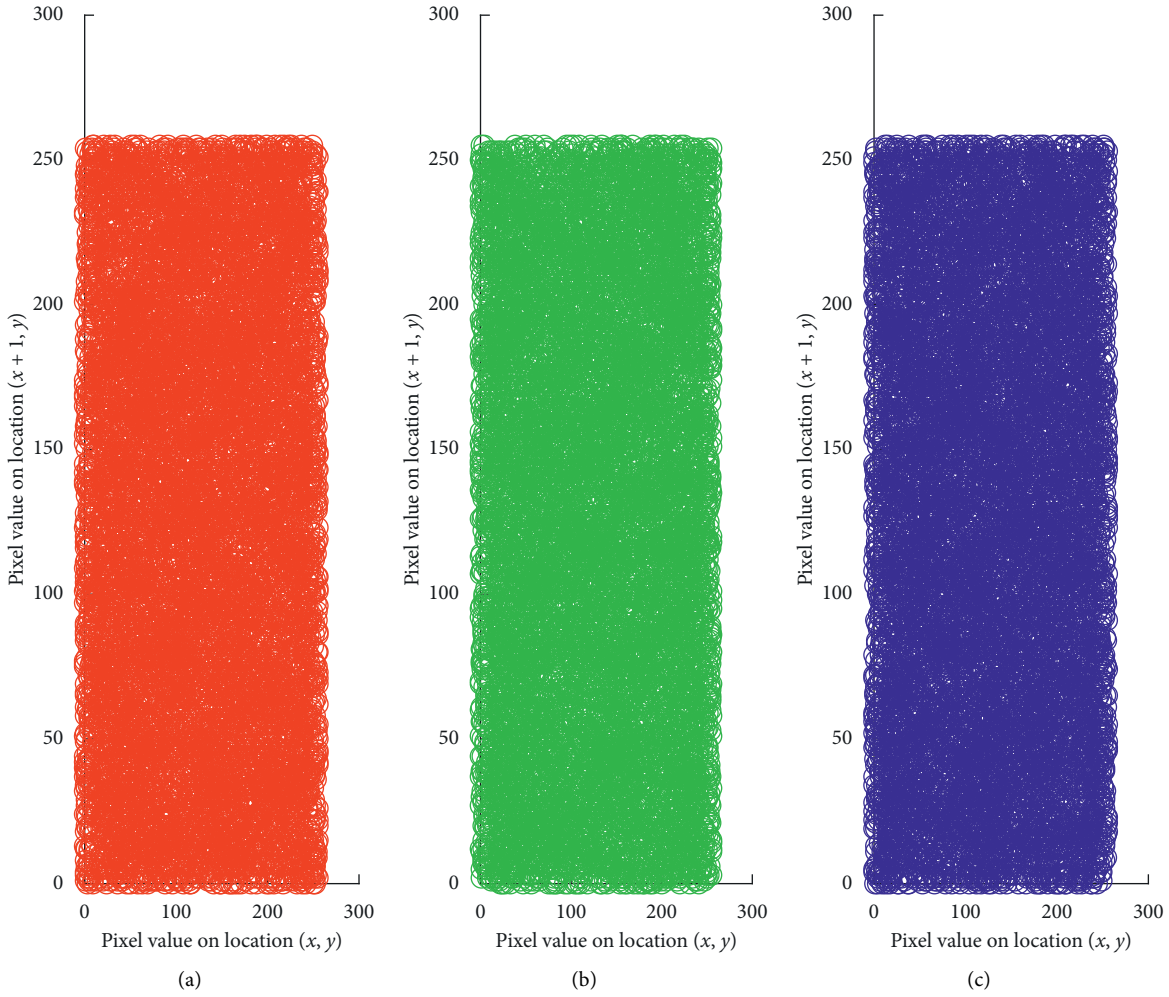

Figure 20: Correlation (column wise) of encrypted image of onion. (a) Red component. (b) Green component. (c) Blue component.

corresponding encrypted image. The correlation is calculated by using the following formula:

$$C_r = \frac{n\left(\sum_{t=1}^{n} x_t y_t - \sum_{t=1}^{n} x_t \sum_{t=1}^{n} y_t\right)}{\left(n\sum_{t=1}^{n}(x_t)^2 - \left(\sum_{t=1}^{n} x_t\right)^2\right)\left(n\sum_{t=1}^{n}(y_t)^2 - \left(\sum_{t=1}^{n} y_t\right)^2\right)}, \tag{3}$$

where x_t and y_t are the values of two neighboring pixels and n is the total number of pixels taken for calculating correlation. The highest value of correlation coefficient equals 1 and shows that the adjacent pixels are having high correlation. So, our encryption algorithm must encrypt the image with correlation coefficients very small and near to zero, so that the cryptanalyst cannot get any valuable information. Figures 6–8 display the correlation of the original image pixels in row, column, and diagonal directions, respectively. Figures 9–11 show the correlation of the cipher image pixels in row, column, and diagonal directions, respectively. Table 1 gives the values of correlation of scattering pixels in the horizontal, vertical, and diagonal directions for the plain and cipher image. The value obtained from equation (3) for cipher image is close to zero which shows that adjacent pixels in cipher image are almost uncorrelated.

5.3. Information Entropy Analysis. Entropy is a measurement of unpredictability of the pixel concentrations in the encrypted image. For an 8 bit image, the encryption algorithm with a value of the entropy close to 8 is considered as a good algorithm. It is calculated by the following equation:

$$H(C) = \sum_{i=0}^{2^N-1} P(C_i)\log_2\frac{1}{P(C_i)}, \tag{4}$$

where C be a ciphered image and $P(C_i)$ is the probability of character C_i in encrypted image. For the security of the image encryption algorithm, it should be least possible to predict the original image from the encrypted image. With the entropy value 8, there are less chances of predicting plain image from cipher image. Using Matlab R2018a, the entropy value of encrypted image obtained from the proposed encryption turns out to be 7.9990. Table 2 gives a brief comparison of obtained information entropy value with various image encryption algorithms. The resulting value depicts that entropy of the proposed encryption is close enough to the ideal value 8. It guarantees that there is no loss of information.

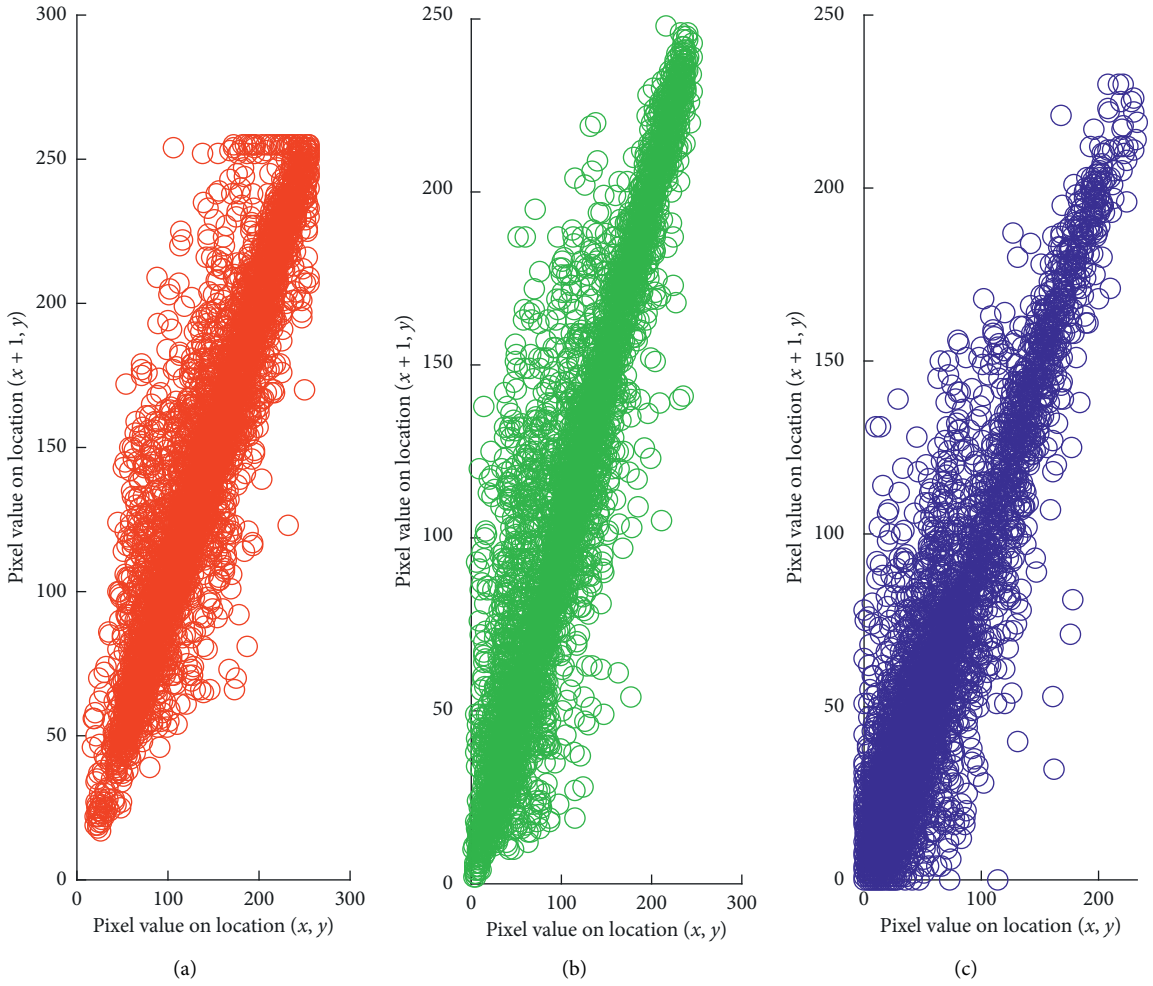

Figure 21: Correlation (diagonal wise) of original image of onion. (a) Red component. (b) Green component. (c) Blue component.

5.4. Sensitivity Analysis of the Proposed Algorithm. The net pixel change rate (NPCR) and unified average changing intensity (UACI) are two measuring criteria used for investigating the effect of altering one pixel of the plain image on the cipher image. Both indicators are defined by the following formulas, respectively:

$$\text{NPCR} = \frac{\sum_{i,j} K(i,j)}{w \times h} \times 100, \tag{5}$$

$$\text{UACI} = \frac{1}{w \times h}\left[\sum_{i,j} \frac{\left|X(i,j) - X'(i,j)\right|}{255}\right] \times 100, \tag{6}$$

where w and h show the width and height of ciphered image, respectively. X represents cipher image corresponding to plain image, while X' represents the cipher image corresponding to plain image with change of one pixel, respectively. If $X(i,j) \neq X'(i,j)$, then $K(i,j) = 1$; else, $K(i,j) = 0$.

The NPCR and UACI measures indicate the resistance of the algorithm against differential attacks, such as a ciphertext-only attack, a plaintext attack, or a known plaintext attack. The higher values of NPCR and UACI give the best security measures. The comparison of the NPCR and UACI values of encrypted Lena image is given in Table 3. The estimate of critical values of NPCR and UACI of proposed scheme is given in Table 4.

5.5. Mean Square Error Analysis. In the cipher image of test image Lena, we add 1%, 5%, and 10% salt and pepper noise as shown in Figures 12(a), 13(a), and 14(a) , respectively. The corresponding decrypted images of noised cipher images are shown in Figures 12(b), 13(b), and 14(b), respectively. From these figures, it is evident that when the cipher image bear salt and pepper noise or data loss attacks, the decrypted image preserves huge majority of original image information having only a small portion of uniformly distributed noise.

The mean square error (MSE) is the measurement of difference between the original and cipher images. The high value of MSE is related to a high difference between original image and cipher image. It can be calculated by the following equation:

$$\text{MSE} = \frac{1}{m \times n \times 3} \sum_{i=0}^{m-1} \sum_{i=0}^{n-1} \left(I_P(i,j) - I_D(i,j)\right)^2, \tag{7}$$

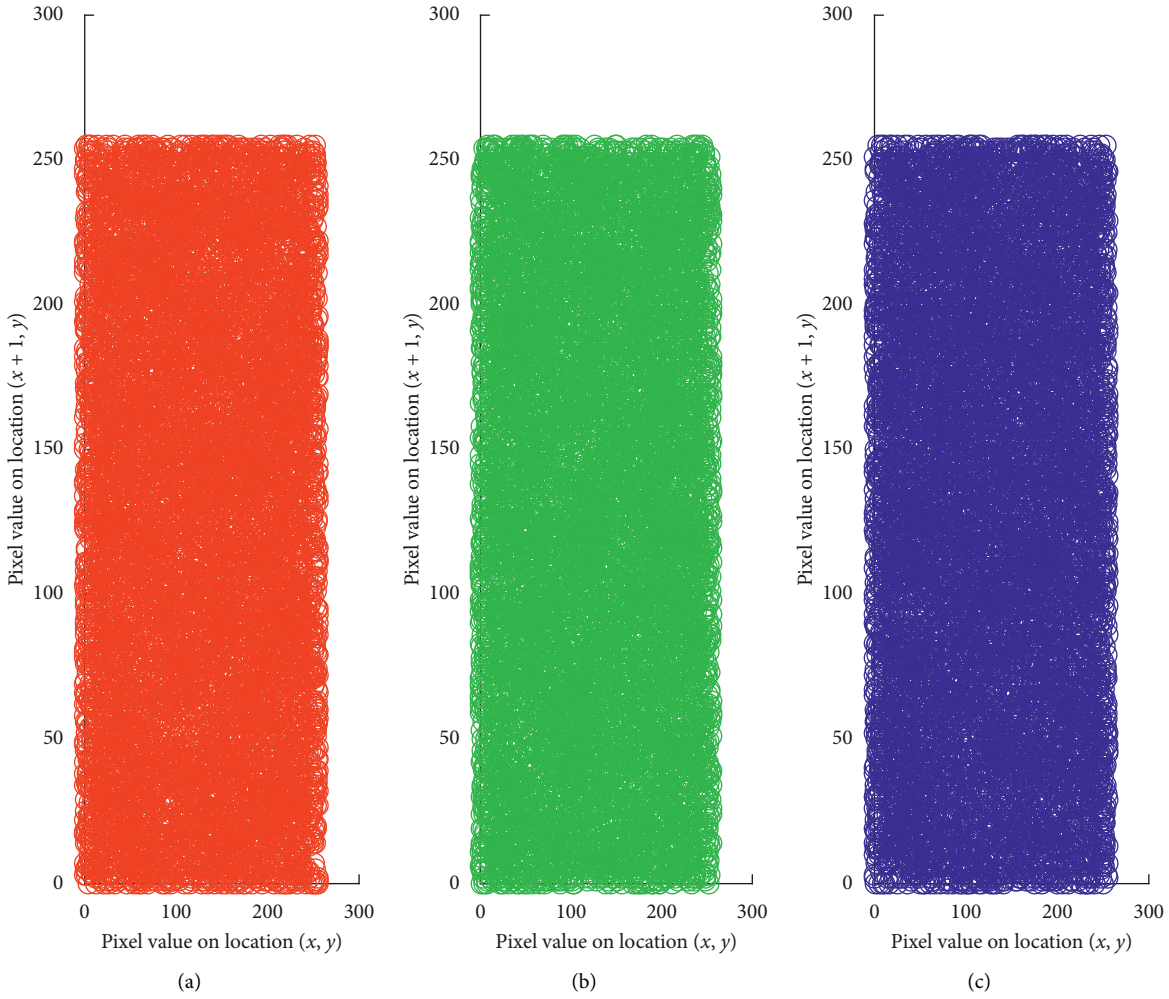

Figure 22: Correlation (diagonal wise) of encrypted image of onion. (a) Red component. (b) Green component. (c) Blue component.

Table 6: Correlation coefficient values of two adjacent pixels of onion (198 × 135 pixels) ciphered image.

Direction	Red		Green		Blue	
	Original image	Cipher image	Original image	Cipher image	Original image	Cipher image
Horizontal	0.9826	−0.0007	0.9786	−0.0068	0.9648	0.0003
Vertical	0.9900	−0.0034	0.9880	0.0046	0.9751	−0.0018
Diagonal	0.9721	−0.0054	0.9675	−0.0083	0.9427	−0.0021

where m, n represent the number of rows and columns, respectively. I_P and $I_D$represent the plain image and cipher image, respectively. For the difference between the plain image and cipher image, MSE ≥ 30 db. The MSE of proposed image algorithm is given in Table 5.

5.6. Peak Signal-to-Noise Ratio Analysis. The peak signal-to-noise ratio (PSNR) measures the conformity between the plain and cipher images. It can be calculated using the following formula:

$$\text{PSN} = 10.\ \log\frac{255^2}{\text{MSE}}\ (\text{db}). \tag{8}$$

Table 7: Comparison of size of key space.

Image encryption algorithms	Size of key space
Reference [30]	2^{193}
Reference [31]	2^{233}
Reference [32]	2^{138}
Reference [34]	2^{194}
Proposed algorithm	2^{282}

The value of PSNR should be as low as possible between the plain and cipher images for good encryption algorithms. The value of PSNR of the proposed algorithm is given in Table 5.

Table 8: Summary of properties comparison of different algorithms.

Algorithms	NPCR	UACI	Correlation coefficients			Entropy
			Horizontal	Vertical	Diagonal	
Reference [31]	99.22	33.40	0.0042	0.0033	0.0024	7.9967
Reference [32]	99.61	33.41	−0.0026	−0.0038	0.0017	7.9970
Reference [35]	99.61	33.47	−0.0075	−0.0011	−0.0012	7.9998
Reference [36]	99.62	30.91	−0.0049	0.0067	0.0010	7.9960
Proposed algorithm	99.61	33.46	0.0045	0.00016	−0.0013	7.9990

The proposed algorithms are also applied to another sample colored image of onion (198×135 pixels). The entropy value of onion image is 7.9975. The resulting encrypted and decrypted images are shown in Figure 15. The histogram of cipher image and correlation of neighboring pixels of plain and cipher images are shown in Figures 16–22 , respectively. Table 6 illustrates the values of correlation of neighboring pixels of cipher image of onion.

5.7. Key Space Analysis. The key space is all the possibilities of keys that can be utilized in the encryption algorithm. The size of key space is treated as a significant aspect of the algorithm. It should be huge enough to avoid brute-force attacks. With today's computing abilities, an algorithm can resist exhaustive attacks [33] if the size of key space is larger than 2^{128}. There are three keys involved in our proposed image encryption algorithm. The secret keys $K_1$and K_3contain parameters of associated chaotic maps which are ξ_0, η, ϕ_0, and β.By considering the precision of these parameters to be 2^{52}, the total number of possibilities of choosing these two keys will be $(2^{52})^2 \times (2^{52})^2 = 2^{208}$. The key $K_2 = (\text{color}\,1, \text{color}\,2, \text{color}\,3, k)$ is a combination of three random colors and a random number k. The number of possibilities for choosing three colors are ${}^{16777216}P_3 = 4.722365638 \times 10^{21} = 2^{72}$. The integers that satisfy the condition $\gcd(k, 256) = 1$ are $128 = 2^7$. So the total possibilities of choosing K_2 are $2^{72} \times 2^2 = 2^{74}$. The total size of key space is $2^{208} \times 2^{74} = 2^{282} > 2^{128}$. Therefore, our proposed algorithm is resistant against the brute-force attacks because the size of the key space is large enough. Table 7 lists the key space size of several schemes.

The computational complexity is analyzed as follows.

Assume that a fastest computer can calculate 2^{80} computations in one second. So, in one year, the number of computations performed by the computer is $2^{80} \times 365\,(\text{days}) \times 24\,(\text{hr}) \times 60\,(\text{min}) \times 60\,(\text{sec})$. Hence, the total of $(2^{282}/2^{80} \times 365 \times 24 \times 60 \times 60) = 10^{53}$ years is required. To resist the brute-force attack against this encryption algorithm, this computational load is large enough.

5.8. Key Sensitivity Analysis. An image encryption algorithm should be highly sensitive to its secret key, that is, a variation of single bit in secret key should yield a totally different cipher result. A highly sensitive key may contribute towards the security of the image encryption algorithm. The output of our decryption algorithm is totally changed with a slight modification in any part of the key $K = (K_1, K_2, K_3)$. Making even a slight variation in value of one part of encryption key ξ_0 as 0.7660000000000001, the image will be produced but not same as plain image. So, it is observed that the cipher image does not contain any clue or gesture about the original image. The proposed algorithm is highly sensitive to secret keys.

6. Conclusion

This study presents a novel color image scheme based on chaotic maps. In contrast to the traditional chaos-based cryptosystems, the suggested cryptosystem is proposed using Hill cipher and color codes. The confusion phase is done by the piecewise chaotic linear map. The Hill cipher with color codes is employed for the substitution phase. The diffusion process is performed by a chaotic logistic map and bitwise XOR. The key space size of the encryption algorithm is adequately high to combat brute-force attacks. Also, the algorithm is highly sensitive to keys. Several experimental tests have been carried out with detailed numerical analysis which exhibits the robustness of the suggested algorithm against numerous attacks such as statistical and differential attacks. The proposed image encryption algorithm is highly secure which is demonstrated by performing different assessment tests. The results of these experiments and performance tests are compared with different algorithms and summarized in Table 8.

Data Availability

The data used to support the findings of this study are included within the article.

Conflicts of Interest

The authors declare that they have no conflicts of interest.

Acknowledgments

The authors thank Taif University, Taif, Saudi Arabia, for its support under the project Taif University Researchers Supporting Project number (TURSP-2020/114).

References

[1] B. Park, A. Korbach, and R. Brünken, "Does thinking-aloud affect learning, visual information processing and cognitive load when learning with seductive details as expected from self-regulation perspective?" *Computers in Human Behavior*, vol. 111, Article ID 106411, 2020.

[2] B. Norouzi, S. Mirzakuchaki, S. M. Seyedzadeh, and M. R. Mosavi, "A simple, sensitive and secure image

encryption algorithm based on hyper-chaotic system with only one round diffusion process," *Multimedia Tools and Applications*, vol. 71, no. 3, pp. 1469–1497, 2014.

[3] E. N. Lorenz, "Atmospheric predictability as revealed by naturally occurring analogues," *Journal of the Atmospheric Sciences*, vol. 26, no. 4, pp. 636–646, 1969.

[4] S. Dhall, S. K. Pal, and K. Sharma, "Cryptanalysis of image encryption scheme based on a new 1D chaotic system," *Signal Processing*, vol. 146, pp. 22–32, 2018.

[5] R. Mathews, "On the derivation of a chaotic encryption algorithm," *Cryptolgia*, vol. 13, no. 1, pp. 29–42, 1989.

[6] J. Fridrich, "Symmetric ciphers based on two-dimensional chaotic maps," *International Journal of Bifurcation and Chaos*, vol. 8, no. 6, pp. 1259–1284, 1998.

[7] E. Emad, "Watermarking 3D models using spectral mesh compression," *Signal Image and Video Processing*, vol. 3, p. 375, 2009.

[8] G. Chen, Y. Mao, and C. K. Chui, "A symmetric image encryption scheme based on 3D chaotic cat maps," *Chaos, Solitons & Fractals*, vol. 21, no. 3, pp. 749–761, 2004.

[9] Y. Mao, G. Chen, and S. Lian, "A novel fast image encryption scheme based on 3D chaotic Baker maps," *International Journal of Bifurcation and Chaos*, vol. 14, no. 10, pp. 3613–3624, 2004.

[10] Z. H. Guan, F. Huang, and W. Guan, "Chaos based image encryption algorithm," *Physics Letters A*, vol. 346, no. 1-3, pp. 153–157, 2005.

[11] V. Patidar, N. K. Pareek, G. Purohit, and K. K. Sud, "Modified substitution-diffusion image cipher using chaotic standard and logistic maps," *Communications in Nonlinear Science and Numerical Simulation*, vol. 15, no. 10, pp. 2755–2765, 2010.

[12] X. Zhang and X. Wang, "Multiple image encryption algorithm based on mixed image element and chaos," *Computers and Electrical Engineering*, vol. 92, no. 6, 16 pages, 2017.

[13] Y. Luo, J. Yu, W. Lai, and L. Liu, "A novel chaotic image encryption algorithm based on improved baker map and logistic map," *Multimedia Tools and Applications*, vol. 78, no. 15, pp. 22023–22043, 2019.

[14] P. Ramasamy, V. Ranganathan, S. Kadry, R. Damaševičius, and T. Blažauskas, "An image encryption scheme based on block scrambling, modified zigzag transformation and key generation using enhanced logistic-tent map," *Entropy*, vol. 21, no. 7, p. 656, 2019.

[15] Z. Hua, F. Jin, B. Xu, and H. Huang, "2D logistic-sine-coupling map for image encryption," *Signal Processing*, vol. 149, pp. 148–161, 2018.

[16] X. Liao, Y. Yu, B. Li, Z. Li, and Z. Qin, "A new payload partition strategy in color image steganography," *IEEE Transactions on Circuits and Systems for Video Technology*, vol. 30, no. 3, pp. 685–696, 2019.

[17] X. Liao, Z. Qin, and L. Ding, "Data embedding in digital images using critical functions," *Signal Process Image Commun*, vol. 58, pp. 146–156, 2017.

[18] K. A. Kumar Patro and B. Acharya, "An efficient colour image encryption scheme based on 1-D chaotic maps," *Journal of Information Security and Applications*, vol. 46, pp. 23–41, 2019.

[19] K. A. Kumar Patro, A. Soni, P. Kumar Netam, and B. Acharya, "Multiple grayscale image encryption using cross-coupled chaotic maps," *Journal of Information Security and Applications*, vol. 52, 2020.

[20] Z. Li, C. Peng, W. Tan, and L. Li, "An effective chaos-based image encryption scheme using imitating jigsaw method," *Complexity*, vol. 2021, Article ID 8824915, 18 pages, 2021.

[21] S. Xiao, Z. J. Yu, and YaS. Deng, "Design and analysis of a novel chaos-based image encryption algorithm via switch control mechanism," *Security and Communication Networks*, vol. 2020, Article ID 7913061, 12 pages, 2020.

[22] M. Gafsi, N. Abbassi, M. Ali Hajjaji, J. Malek, and A. Mtibaa, "Improved chaos-based cryptosystem for medical image encryption and decryption," *Scientific Programming*, vol. 2020, Article ID 6612390, 22 pages, 2020.

[23] K. A. K. Patro and B. Acharya, "An efficient dual-layer cross-coupled chaotic map security-based multi-image encryption system," *Nonlinear Dynamics*, vol. 10, 2021.

[24] M. García-Martínez, L. J. Ontañón-García, E. Campos-Cantón, and S. Čelikovský, "Hyperchaotic encryption based on multi-scroll piecewise linear systems," *Applied Mathematics and Computation*, vol. 270, pp. 413–424, 2015.

[25] E. C. Díaz-González, J.-A. López-Rentería, E. Campos-Cantón, and B. Aguirre-Hernández, "Maximal unstable dissipative interval to preserve multi-scroll attractors via multi-saturated functions," *Journal of Nonlinear Science*, vol. 26, no. 6, pp. 1833–1850, 2016.

[26] S. Li, G. Chen, and X. Mou, "On the dynamical degradation of digital piecewise linear chaotic maps," *International Journal of Bifurcation and Chaos*, vol. 15, no. 10, pp. 3119–3151, 2005.

[27] L. S. Hill, "Cryptography in an algebraic alphabet," *The American Mathematical Monthly*, vol. 36, no. 6, pp. 306–312, 1929.

[28] L. S. Hill, "Concerning certain linear transformation apparatus of cryptography," *The American Mathematical Monthly*, vol. 38, no. 3, pp. 135–154, 1931.

[29] B. Acharya, G. S. Rath, S. K. Patra, and S. K. Panigrahy, "Novel methods of generating self-invertible matrix for hill cipher algorithm," *International Journal of Security*, vol. 1, no. 1, p. 14, 2007.

[30] S. M. Seyedzadeh, S. M. S. Moosavi, and S. Mirzakuchaki, "Using self-adaptive coupled piecewise nonlinear chaotic map for color image encryption scheme," in *Proceedings of the 2011 19th Iranian Conference on Electrical Engineering*, p. 1, Tehran, Iran, May 2011.

[31] X. Wei, L. Guo, Q. Zhang, J. Zhang, and S. Lian, "A novel color image encryption algorithm based on DNA sequence operation and hyper-chaotic system," *Journal of Systems and Software*, vol. 85, no. 2, pp. 290–299, 2012.

[32] C. Pak and L. Huang, "A new color image encryption using combination of the 1D chaotic map," *Signal Processing*, vol. 138, pp. 129–137, 2017.

[33] N. Chidambaram, P. Raj, K. Thenmozhi, and R. Amirtharajan, "Advanced framework for highly secure and cloud-based storage of colour images," *IET Image Processing*, vol. 14, no. 13, pp. 3143–3153, 2020.

[34] G. Alvarez and S. Li, "Some basic cryptographic requirements for chaos-based cryptosystems," *International Journal of Bifurcation and Chaos*, vol. 16, no. 08, pp. 2129–2151, 2006.

[35] K. A. K. Patro, B. Acharya, and V. Nath, "Various dimensional colour image encryption based on non-overlapping block-level diffusion operation," *Microsystem Technologies*, vol. 26, no. 5, pp. 1437–1448, 2020.

[36] R. Sivaraman, S. Rajagopalan, J. B. B. Rayappan, R. Amirtharajan, and R. Amirtharajan, "Ring oscillator as confusion - diffusion agent: a complete TRNG drove image security," *IET Image Processing*, vol. 14, no. 13, pp. 2987–2997, 2020.

Hindawi
Complexity
Volume 2021, Article ID 5529282, 15 pages
https://doi.org/10.1155/2021/5529282

Research Article

A New 4*D* Piecewise Linear Multiscroll Chaotic System with Multistability and Its FPGA-Based Implementation

Faqiang Wang, Hongbo Cao, and Dingding Zhai

State Key Laboratory of Electrical Insulation and Power Equipment, School of Electrical Engineering, Xi'an Jiaotong University, Xi'an 710049, China

Correspondence should be addressed to Faqiang Wang; faqwang@xjtu.edu.cn

Received 12 February 2021; Revised 20 March 2021; Accepted 19 April 2021; Published 7 May 2021

Academic Editor: Eric Campos

Due to the complex behavior of a multiscroll chaotic system, it is a good candidate for the secure communications. In this paper, by adding an additional variable to the modified Lorenz-type system, a new chaotic system that includes only linear and piecewise items but can generate $4n+4$ scroll chaotic attractors via choosing the various values of natural number n is proposed. Its dynamics including bifurcation, multistability, and symmetric coexisting attractors, as well as various chaotic and periodic behaviors, are analyzed by means of attraction basin, bifurcation diagram, dynamic map, phase portrait, Lyapunov exponent spectrum, and C_0 complexity in detail. The mechanism of the occurrence for generating multiscroll chaotic attractors is presented. Finally, this multiscroll chaotic system is implemented by using the Altera Cyclone IV EP4CE10F17C8 FPGA. It is found that this FPGA-based design has an advantage of requiring less resources for 0% of the embedded multipliers and 0% of the PLLs of this FPGA are occupied.

1. Introduction

As indicated in many open literatures, the chaotic system that can generate multishape chaotic attractors has complex dynamical behaviors so that it is difficult to decode its information when it is used in the field of secure communications. Hence, exploring the multishape chaotic system and analyzing its complex dynamical behaviors through theoretical analysis, numerical simulations, implementations, and applications is a hot topic all the time, and many researchers exert much effort to investigate this research area. To date, many kinds of multiscroll chaotic systems have been presented [1–7]. For example, according to Chua's circuit and using the sine function, a multiscroll chaotic system was introduced and implemented by an electronic circuit, which consists of the commercial trigonometric function chip AD639 and the corresponding auxiliary chips and basic circuit elements [1]. Based on the cellular neural networks and using the trigonometric function, a multiscroll chaotic system was given and analyzed in [2]. By using the hyperbolic tangent function series as the unique nonlinear function, a multiscroll chaotic system was presented and confirmed by an electronic circuit which is constructed by a unity gain voltage buffer, a single current-feedback operational amplifier, and a transconductor in [3]. In [4], the theories, methods, and applications of generating multiscroll chaotic attractors were summarized. Based on the saturated function series, a multiscroll chaotic system that can generate 1*D* *n*-scroll, 2*D* *n*×*m*-grid scroll, and 3*D* *n*×*m*×*l*-grid scroll chaotic attractors was presented and implemented by using an electronic circuit in [8]. By using the Chen chaotic system and the sine function, a multiscroll chaotic and hyperchaotic system was given in [9]. An improved high-order Chua's circuit that can generate multiscroll chaotic attractor by introducing the signum function series was presented and analyzed in [10]. Also, multiwing chaotic systems that can generate multiwing chaotic attractors have also been concerned intensively and many good topologies were presented, such as multiwing Lorenz chaotic system [11], grid multiwing chaotic system [12], 3*D* grid multiwing chaotic system [13], 2*N*-butterfly wing chaotic system [14], and fractional-order multiwing chaotic system [15]. All these

achievements enrich the chaos theory and the nonlinear circuit and precede their potential application in practical engineering.

In addition, because of the applications of chaotic system in digital secure communication, the realization of chaotic system via digital signal processing circuit attracts people's attention. For example, the multiscroll chaotic systems were implemented in DSP [16], FPGA [17, 18], ARM [19, 20], and Arduino [21, 22]. Generally speaking, as indicated in [23], the implementation based on FPGA has more merits including more flexibility and lower cost. Therefore, in this paper, based on the modified Lorenz-type chaotic system that includes only linear and piecewise items, a new 4*D* piecewise linear chaotic system that can generate $4n+4$ scroll chaotic attractors is proposed and analyzed. By employing attraction basin, bifurcation diagram, dynamic map, phase portrait, Lyapunov exponent spectrum, and C_0 complexity, its dynamical behaviors including multistability, bifurcation, and chaotic and period behaviors are investigated. Also, the mechanism of generating multiscroll chaotic attractors is described theoretically. It is found that symmetrical coexisting attractors will appear in the system with respect to different initial conditions. In addition, the multiscroll chaotic signal generator is implemented by using the digital chip FPGA. Notably, since 0% of the embedded multipliers and 0% of the PLLs of the Altera Cyclone IV EP4CE10F17C8 FPGA are occupied in the realization of the proposed chaotic generator, the new multiscroll chaotic system has the advantage of low FPGA resource required.

The paper is organized as follows. In Section 2, the mathematical model of 4*D* linear piecewise chaotic system is presented. In Section 3, the dynamical behaviors of the proposed chaotic system are analyzed. In Section 4, the mechanism of generating multiscroll chaotic attractors is presented and some numerical simulations are provided. The FPGA implementation of the proposed multiscroll chaotic system is shown in Section 5. Finally, some concluding remarks are presented in Section 6.

2. A New 4*D* Piecewise Linear Chaotic System

In [24], based on the traditional Lorenz system, the modified 3*D* Lorenz-type chaotic system that includes only linear and piecewise items was introduced. Its differential equations are

$$\begin{cases} \dot{x} = a(y - x), \\ \dot{y}_{\mp} = \mp \mathrm{sgn}(x) z, \\ \dot{z}_{\pm} = \pm |x| \mp b, \end{cases} \tag{1}$$

where a and b are positive constant parameters and x, y, and z are variables. Here, by adding an additional variable w into equation (1), the following new 4*D* system that includes only linear and piecewise items can be obtained.

$$\begin{cases} \dot{x} = a(y - x), \\ \dot{y}_{\mp} = \mp 16 \mathrm{sgn}(4x) z \pm 16 \mathrm{sgn}(4y) w, \\ \dot{z}_{\pm} = \pm 16 |x| \mp b, \\ \dot{w} = -cw + f(z), \end{cases} \tag{2}$$

where

$$f(z) = \sum_{k=-n}^{n} \mathrm{sgn}(4z + 0.5k), \tag{3}$$

where sgn () is the signum function, a, b, and c are positive constant parameters, x, y, and z and w are variables, and n is a natural number.

Taking $n = 0$, obviously, there are two modes in system (2). One mode is $\dot{\mathbf{y}} = \dot{\mathbf{y}}_-$ and $\dot{z} = \dot{z}_+$ which is denoted by M (−, +), and the other mode is $\dot{\mathbf{y}} = \dot{\mathbf{y}}_+$ and $\dot{z} = \dot{z}_-$ which is denoted by M(+, −). For $f(z) = \mathrm{sgn}(4z)$, its value depends on the sign of z. If $z > 0$, $f(z)$=1. If $z < 0$, $f(z)$=−1. However, if $z = 0$, $f(z) = 0$. It is the same for sgn $(4x)$ and sgn $(4y)$.

Thus, from system (2), one can obtain that this chaotic system has the six following equilibrium points:

$$[X, Y, Z, W] = \begin{cases} S_{+1,+2} = ((\pm b/16), (\pm b/16), (1/c), (1/c)), & with\ z > 0, \\ S_{+0,-0} = ((\pm b/16), (\pm b/16), 0, 0), & with\ z = 0, \\ S_{-1,-2} = ((\pm b/16), (\pm b/16), (-1/c), (-1/c)) & with\ z < 0, \end{cases} \tag{4}$$

where X, Y, Z, and W are denoted by the equilibrium points of system (2). The Jacobian matrix of system (2) at the equilibrium points is

$$J = \begin{bmatrix} -a & a & 0 & 0 \\ \mp 128\delta(4X)Z & \pm 128\delta(4Y)W & \mp 16\mathrm{sgn}(4X) & \pm 16\mathrm{sgn}(4Y) \\ \pm 16\mathrm{sgn}(X) & 0 & 0 & 0 \\ 0 & 0 & 8\delta(4Z) & -c \end{bmatrix}. \tag{5}$$

where $\delta()$ is the delta function and it is the differential of sgn (). For δ $(4Z)$, its value equals zero for all Z, except $Z = 0$ where it is infinite. When $Z = 0$, the related equilibrium points are $S_{+0,-0}$. Because the value of δ (0) equals infinity, the corresponding eigenvalues of equation (5) cannot be calculated. However, we can obtain the characteristic equation of the Jacobian matrix (5) at $S_{+0,-0}$. For example, choosing $a = 32$, $b = 2.4$, and $c = 16$, the characteristic equation of equation (5) at $S_{+0,-0}$ is

$$\lambda^4 + 48\lambda^3 + 512\lambda^2 + 8192\lambda - \mathrm{inf} = 0, \tag{6}$$

where "inf" is positive infinite. Then, the Routh array can be derived to know the roots' characteristics of equation (6) for

judging the stability of system (2) under the above parameters. Its Routh array is

$$\begin{array}{c|ccc} s^4 & 1 & 512 & -\text{inf} \\ s^3 & 48 & 8192 & \\ s^2 & 341.3 & -\text{inf} & \\ s^1 & 8192 + 0.14 \times \text{inf} & & \\ s^0 & -\text{inf} & & \end{array} . \quad (7)$$

Therefore, based on the Routh-Hurwitz criterion, for the characteristic equation of the Jacobian matrix (5) at $S_{+0,-0}$, it has three roots with negative real part and one root with positive real number, since the number of changes in sign of the first column of the Routh array is one. Hence, these two equilibrium points ($S_{+0,-0}$) are unstable point so that the system's trajectory will be departed rapidly at $S_{+0,-0}$.

However, for $S_{+1,+2}$ and $S_{-1,-2}$, even if the Jacobian matrices of system (2) under two modes are different from each other, the characteristic equation of the Jacobian matrix (5) in both two modes is identical and given by

$$(\lambda + c)\left(\lambda^3 + a\lambda^2 + 256a\right) = 0. \quad (8)$$

Thus, under these four equilibrium points ($S_{+1,+2}$ and $S_{-1,-2}$), the sets of eigenvalues are the same. Based on the above parameters, the eigenvalues of the Jacobian matrix (5) of the system under two modes is (−37.7489, 2.8744 + 14.4482i, 2.8744–14.4482i, −16) which means that all these four equilibrium points are index-2 saddle foci. Thus, the system's trajectory will be in a spiral movement at these four equilibrium points which result in four-scroll attractors. For example, under the initial condition (x_0, y_0, z_0, w_0)=(0.01, 0.01, 0.01, 0.01), the time-domain waveforms, the phase portraits, and the Poincaré maps from the numerical simulations by using the Matlab software for system (2) under two modes which are shown in Figures 1 and 2, respectively, can be obtained.

Figures 1(a) and 1(b) show the phase portrait of system (2) under M (-, +) and Figures 2(a) and 2(b) show its phase portrait under M (+, -). Figures 1(c) and 2(c) show the respective time series and Figures 1(d) and 2(d) show the corresponding Poincaré maps. Moreover, based on the Wolf method [25, 26], by using the ode45 algorithm and choosing the simulation time $T = 1000$s with time step being 0.002s in Matlab software, the calculated Lyapunov exponents of system (2) under M (-, +) are $LE_1 = 2.88$, $LE_2 = 0$, $LE_3 = -12.15$, and $LE_4 = -38.43$, and the calculated results under M (+, -) are $LE_1 = 2.95$, $LE_2 = 0$, $LE_3 = -12.22$, and $LE_4 = -38.44$. From phase portraits, time series, Poincaré maps in Figures 1 and 2, and the Lyapunov exponents, one can determine that system (2) in both two modes under the above given parameters and initial conditions is in chaotic operation and it has four-scroll chaotic attractors. Note that, because M (+, −) is similar to M (−, +), only M (−, +) is investigated in the following sections.

3. Dynamical Behaviors of the New Chaotic System

3.1. Chaotic Attractors for Various Parameters. Suppose that the parameters $b = 2.4$, $c = 16$, $n = 0$, and (x_0, y_0, z_0, w_0)=(0.01, 0.01, 0.01, 0.01) are fixed and parameter a is changed from 11.2 to 171.2. The Lyapunov exponent spectrum and their enlargement are shown in Figures 3(a) and 3(b), respectively. One can see that system (2) is always in chaotic operation when a is within (11.2, 171.2), since LE_1 is bigger than zero. Figure 4(a) shows the bifurcation diagram about parameter a versus y under the initial condition (x_0, y_0, z_0, w_0)=(0.01, 0.01, 0.01, 0.01) (blue case) and (x_0, y_0, z_0, w_0)=(0.01, −0.01, −0.01, 0.01) (red case). From Figure 4, some typical phase portraits can be obtained.

Case 1. The red color and the blue color in Figure 4(a) are mixed in both positive and negative of y. That is to say, the four-scroll chaotic attractors under two types of initial conditions will appear. For example, let $a = 19.2$; the four chaotic attractors are shown in Figure 4(b).

Case 2. In Figure 4(a), the red color is only filled in the positive of y, while the blue color is only filled in the negative of y. Hence, under the initial condition (x_0, y_0, z_0, w_0)=(0.01, −0.01, −0.01, 0.01), it has two-scroll chaotic attractors in the positive of y. However, under the initial condition (x_0, y_0, z_0, w_0)=(0.01, 0.01, 0.01, 0.01), only two-scroll chaotic attractors will appear in the negative of y. For example, choose $a = 40$; the numerical simulations are shown in Figure 4(c).

Case 3. Both red and blue colors in Figure 4(a) are filled in the negative of y. Hence, under the initial condition (x_0, y_0, z_0, w_0)=(0.01, -0.01, −0.01, 0.01) and (x_0, y_0, z_0, w_0)=(0.01, 0.01, 0.01, 0.01), only two-scroll chaotic attractors in the negative of y will appear. For example, take $a = 48$; the two-scroll chaotic attractors are shown in Figure 4(d).

Case 4. Both the red color and the blue color in Figure 4(a) are filled in the positive of y. Hence, under the initial condition (x_0, y_0, z_0, w_0)=(0.01, −0.01, −0.01, 0.01) and (x_0, y_0, z_0, w_0)=(0.01, 0.01, 0.01, 0.01), only two-scroll chaotic attractors in the positive of y will appear. For example, choose $a = 60.8$; the two-scroll chaotic attractors are shown in Figure 4(e).

Case 5. In Figure 4(a), the red color is only filled in the negative of y, while the blue color is only in the positive of y. Hence, under the initial condition (x_0, y_0, z_0, w_0)=(0.01, −0.01, −0.01, 0.01), it has two-scroll chaotic attractors in the negative of y. But, under the initial condition (x_0, y_0, z_0, w_0)=(0.01, 0.01, 0.01, 0.01), it has two-scroll chaotic attractors in the positive of y. For example, choose $a = 112$; the numerical simulations are shown in Figure 4(f).

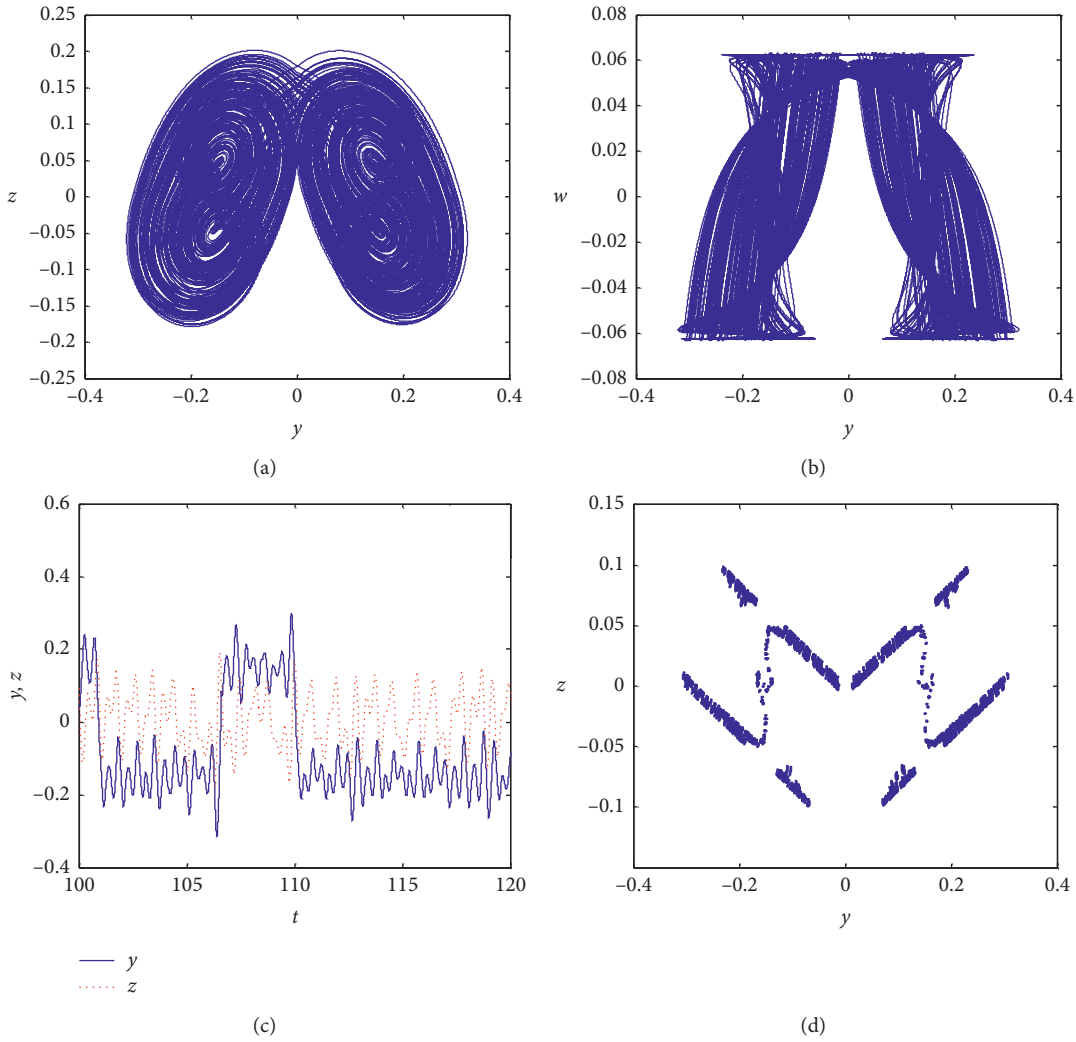

Figure 1: Numerical simulations for the proposed multiscroll chaotic system under mode 1: M (−, +). (a) y versus z, (b) y versus w, (c) t versus y and t versus z, and (d) Poincaré map in y versus z under $x = y$.

Note that the influence of parameters b and c on the dynamical behaviors can also be analyzed by using the above technique. Here, under the initial condition (x_0, y_0, z_0, w_0)=(0.01, 0.01, 0.01, 0.01) (blue case) and (x_0, y_0, z_0, w_0)=(0.01, −0.01, −0.01, 0.01) (red case), only the bifurcation diagram about the variation of parameters b and c is presented and shown in Figure 5.

3.2. C_0 Complexity Analysis on System Parameters. As indicated in [27], C_0 complexity is defined as the proportion of irregular components in the sequence, and C_0 algorithm based on fast Fourier transform removes the regular part of the signal transformation domain and leaves the irregular part. The larger the proportion of the irregular part in the sequence is, the closer the corresponding time series is to the random, and the greater the complexity is. Hence, C_0 algorithm can be used to calculate the randomness of chaotic time series; that is to say, it can be adopted to describe the complexity of chaotic time series [28].

When the length of chaotic time series of the new system is selected as $N = 8000$ and the complex parameter is selected as $r = 10$, also C_0 algorithm is used to calculate the complexity of x sequence with respect to varying parameter a, as shown in Figure 6(a). From Figures 6(a) and 3(a), one can obtain that a large C_0 complexity value corresponds to a positive Lyapunov exponent, indicating that the complexity of x sequence is high. Comparing Figure 6(a) with Figure 4(a), the C_0 complexity curve has good consistency with its bifurcation diagram. Similarly, the C_0 complexity of z sequence with respect to varying parameter b is shown in Figure 6(b), and the C_0 complexity of w sequence with respect to varying parameter c is shown in Figure 6(c). By combining Figures 6(b) and 5(a), as well as Figures 6(c) and 5(b), one can see that the C_0 complexity of the proposed system in the chaotic state is greater than that of the proposed system in its other states.

Hence, from C_0 complexity, it can effectively distinguish the dynamic characteristics of continuous chaotic time series

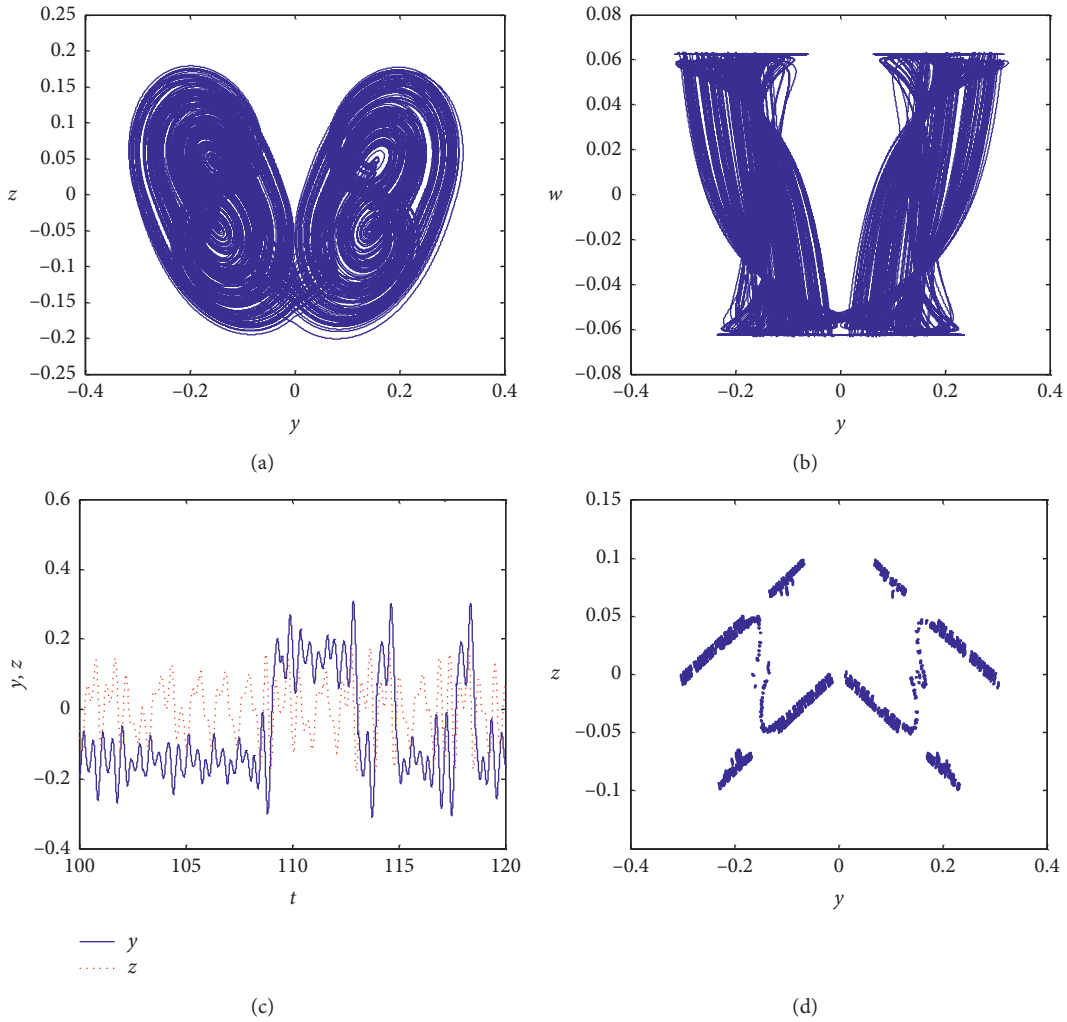

FIGURE 2: Numerical simulations for the proposed multiscroll chaotic system under mode 2: M (−, +). (a) y versus z, (b) y versus w, (c) t versus y and t versus z, and (d) Poincaré map in y versus z under $x = y$.

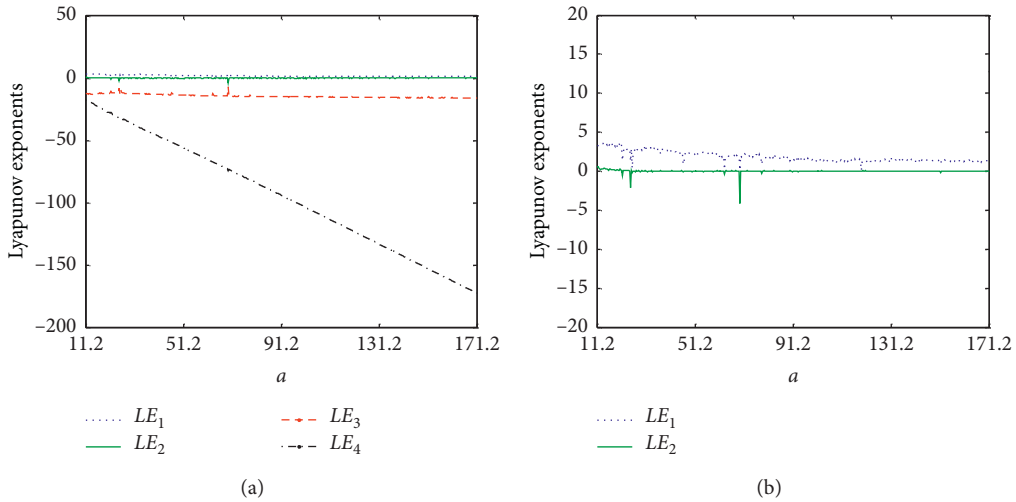

FIGURE 3: Lyapunov exponents for the proposed multiscroll chaotic system under M (-, +) with variation of α. (a) LE_1, LE_2, LE_3, and LE_4. (b) Closed-up view of LE_1 and LE_2.

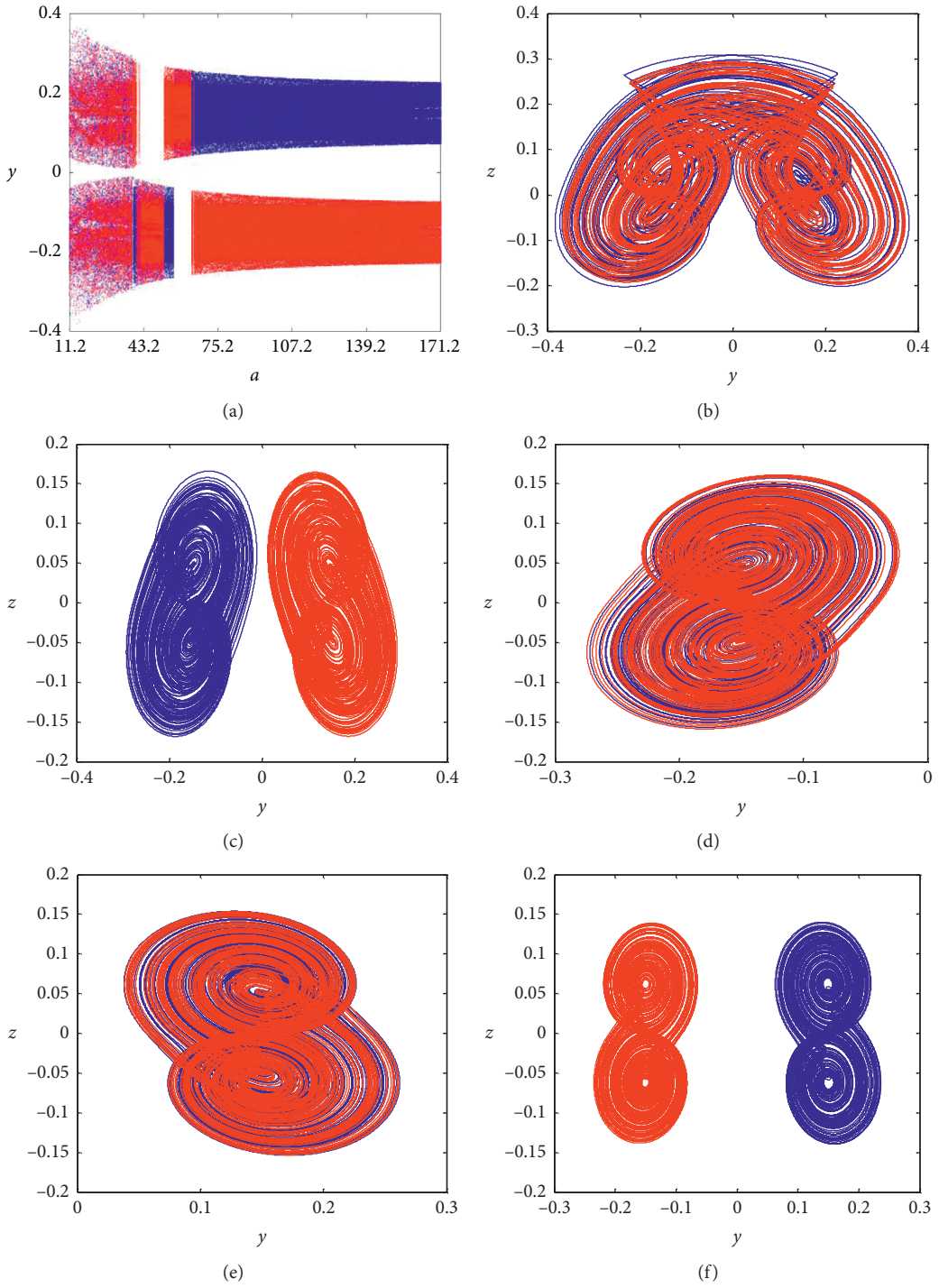

FIGURE 4: Numerical simulations for the proposed multiscroll chaotic system under mode 1: M (−, +) with variation of a under the initial condition (x_0, y_0, z_0, w_0)=(0.01, 0.01, 0.01, 0.01) (blue case) and (x_0, y_0, z_0, w_0) = (0.01, −0.01, −0.01, 0.01) (red case). (a) Bifurcation diagram, (b) $a = 19.2$, (c) $a = 40$, (d) $a = 48$, (e) $a = 60.8$, and (f) $a = 112$.

and can well describe the complexity of the proposed chaotic time seriescin.

3.3. Dynamic Map of the New Chaotic System. Under $a = 112$ and initial condition being (x_0, y_0, z_0, w_0)=(0.01, 0.01, 0.01, 0.01), dynamic map that is used to describe the dynamics of the proposed chaotic system with respect to the common influence of the varying parameters b and c is described in Figure 8. Obviously, there are three different color regions suggesting three different dynamic behaviors in Figure 8. The cyan area marked with L indicates that when the values of parameters b and c are within this region, the proposed chaotic system will be in a chaotic state, and the maximum

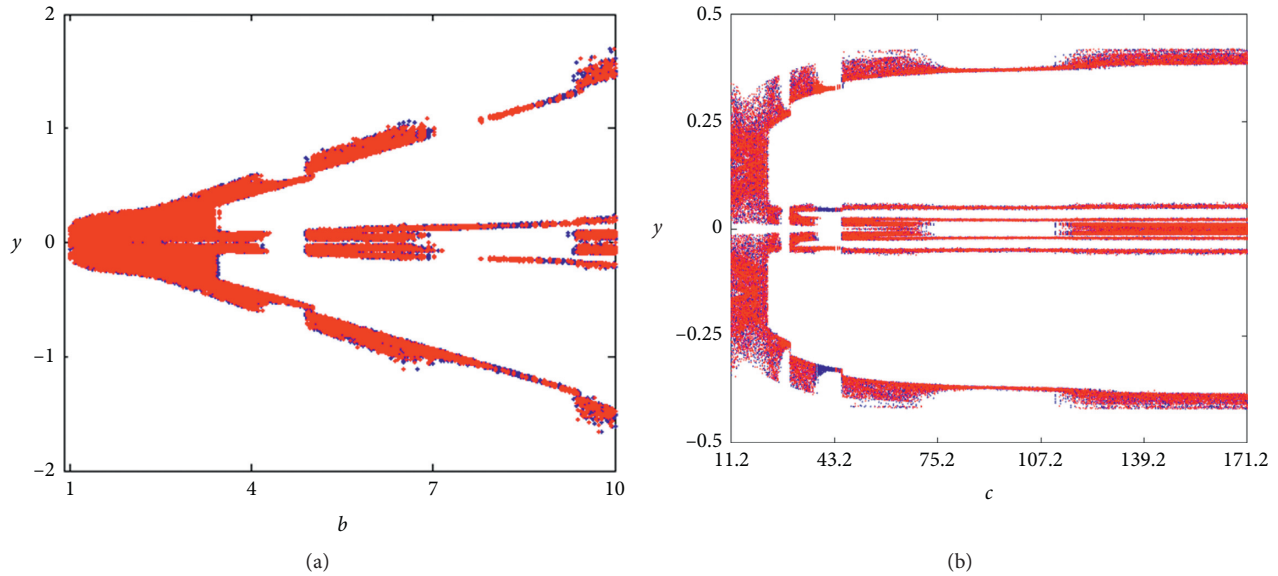

FIGURE 5: Bifurcation diagram of the proposed multiscroll chaotic system under mode 1: M (−, +) with the initial condition (x_0, y_0, z_0, w_0) = (0.01, 0.01, 0.01, 0.01) (blue case) and (x_0, y_0, z_0, w_0) = (0.01, −0.01, −0.01, 0.01) (red case). (a) Variation of b under $a = 32$ and $c = 16$; (b) variation of c under $b = 2.4$ and $c = 16$.

Lyapunov exponent corresponding to this area is positive. The blue area marked with H indicates that when the values of parameters b and c are within this region, the proposed chaotic system will be in a quasi-periodic state, and there are two maximum Lyapunov values, both of which are zero corresponding to the blue area. The green area marked with G indicates that the proposed chaotic system will be in a periodic state under these parameters values, while there is only one maximum Lyapunov exponent whose value is zero in the green region. Hence, the dynamics of the proposed chaotic system for various parameters b and c can be vividly described in the dynamics map.

Then different parameters b and c are selected in three regions of the dynamic map of the proposed chaotic system, and the maximum Lyapunov exponents for different parameters are calculated. The calculated results are summarized in Table 1, where the first point $b = 2.4$ and $c = 16$ is chosen in the L region, the second point $b = 1.5$ and $c = 33$ is chosen in the H region, and the third point $b = 3$ and $c = 55$ is chosen in the G region. According to the calculated results, one can judge that the proposed chaotic system moves in chaotic state, quasi-periodic state, or periodic state when the different parameters are chosen. In order to verify the maximum Lyapunov exponents of the proposed chaotic system under different parameters, we have given the time-domain diagrams and phase diagrams of this system in three different dynamical regions, as shown in Figure 7. Hence, based on the relationship [29] between the dynamical characteristics of the nonlinear system and the values of the Lyapunov exponents, one can see that the dynamic behaviors of the proposed chaotic system are consistent with the results judged by the calculated Lyapunov exponents. Besides, the analysis method described above can also be employed to investigate the dynamics of the proposed chaotic system with respect to other different parameters.

3.4. Attraction Basin and Multistability. The attraction domain is an important tool to analyze coexisting attractors with respect to different initial states of the dynamical system. Here, under $a = 112$, $b = 2.4$, $c = 16$, $x_0 = 0.01$, and $w_0 = 0.01$, the attraction basin of the proposed chaotic system is described in Figure 9. One can see that the basin of attraction contains two different color regions, indicating the coexisting characteristic of different state attractors; that is, the proposed chaotic system is of multistability. Among them, the pink region marked with E suggests that if the initial state starts from this region, the proposed chaotic system will be in one chaotic state. However, the yellow region marked with F indicates that if the initial state starts from this region, the proposed chaotic system will be in another chaotic state, which is symmetric to chaotic state in region E. That is to say, the initial trajectories of the proposed chaotic system from the pink region or the yellow region will enter two the symmetric chaotic motion states eventually and respectively.

As shown in Case 5 of Section 3.1, where the initial condition y_0=0.01 and z_0=0.01 is chosen in region F, the initial condition y_0=−0.01 and z_0=−0.01 is chosen in region E, respectively; they finally display two symmetric coexisting chaotic attractors in Figure 4(f). Hence, there is multistability in the proposed chaotic system whose motion trajectories starting from different initial states in chaotic region (pink and yellow regions) always enter one of the symmetric chaotic states.

4. Multiscroll Chaotic Attractors Generation

In this section, the system parameters are designed to generate multiscroll chaotic attractors. From the theoretical analysis of four-scroll chaotic attractors generation in system (2) under $n = 0$, one can see that system (2) has 6 equilibrium points

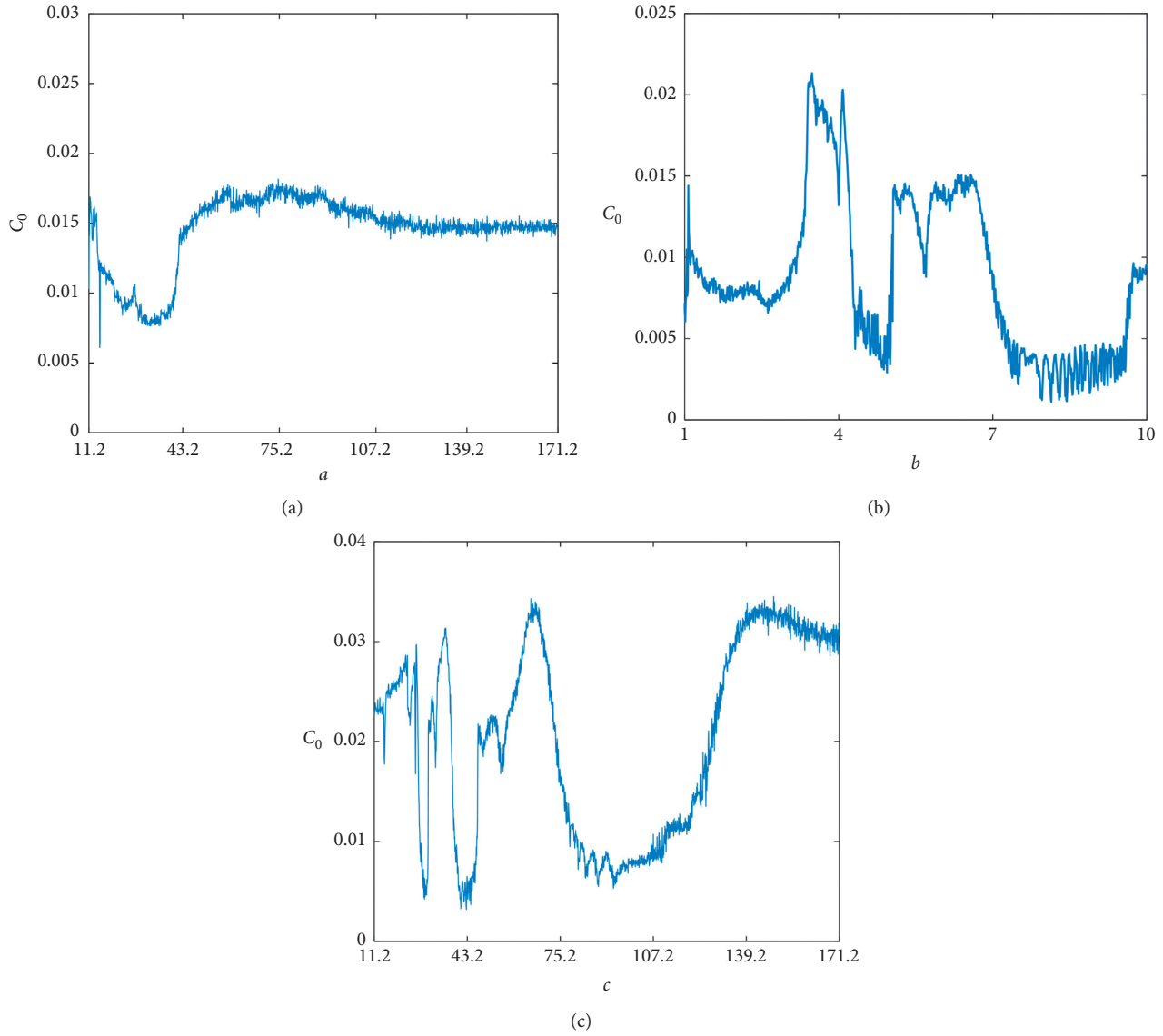

FIGURE 6: C_0 complexity analysis of the proposed chaotic system under mode 1: $M(-,+)$ for the initial condition being $(x_0, y_0, z_0, w_0) = (0.01, 0.01, 0.01, 0.01)$. (a) Related to parameter a when $b = 2.4$ and $c = 16$. (b) Related to parameter b when $a = 32$ and $c = 16$. (c) Related to parameter c when $a = 32$ and $b = 2.4$.

TABLE 1: Lyapunov exponents of the proposed chaotic system with varying parameters under $a = 112$.

Parameter values	Lyapunov exponents				Dynamics	Curves
	LE_1	LE_2	LE_3	LE_4		
$b = 2.4,\ c = 16$	1.33	0	−15.06	−114.07	Chaos	Figures 7(a) and 7(b)
$b = 1.5,\ c = 33$	0	0	−30.49	−114.16	Quasi-period	Figures 7(c) and 7(d)
$b = 3,\ c = 55$	0	−1.71	−54.66	−108.59	Period	Figures 7(e) and 7(f)

where two of them are unstable saddle point and the remaining four are index-2 saddle foci. For the unstable point, it cannot form the scroll attractors, since the trajectory of the system will be away from it quickly. So, the four index-2 saddle foci are essential to generate the four-scroll chaotic attractors. Thus, in order to obtain the multiscroll chaotic attractors, it is necessary

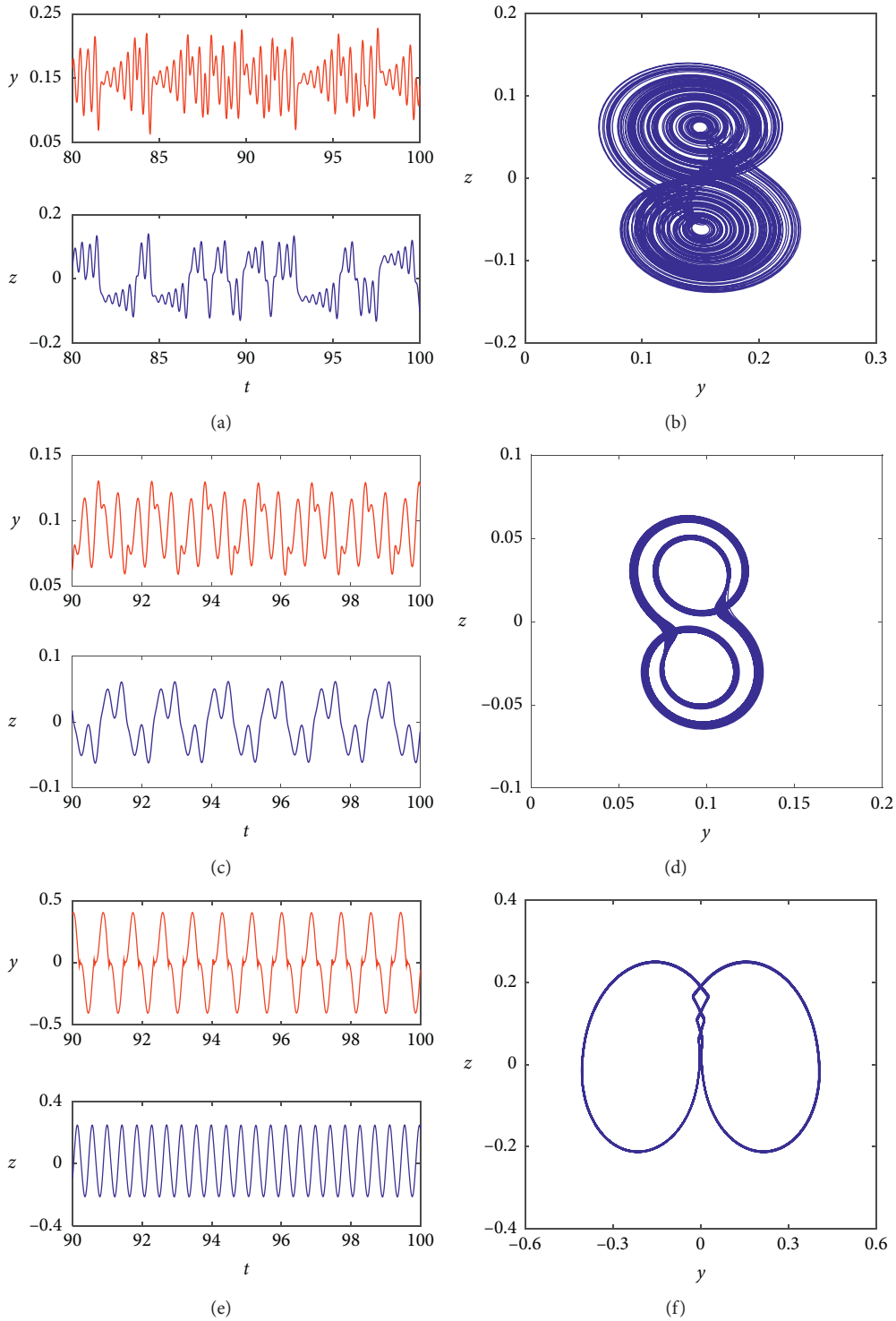

FIGURE 7: Different dynamics of the proposed chaotic system with respect to the initial condition being $(x_0, y_0, z_0, w_0) = (0.01, 0.01, 0.01, 0.01)$ and $a = 112$. For $b = 2.4$ and $c = 16$, (a) time-domain waveforms and (b) chaotic attractor. For $b = 1.5$ and $c = 33$, (c) time-domain waveforms and (d) quasi-periodic attractor. For $b = 3$ and $c = 55$, (e) time-domain waveforms and (f) periodic attractor.

to add the index-2 saddle foci to the system. Here, let $a = 32$, $b = 2.4$, and $c = 16$, and changing the values of n, the $4n + 4$ scroll chaotic attractors can be generated. For example, let $n = 1$; the equilibrium points of system (2) are

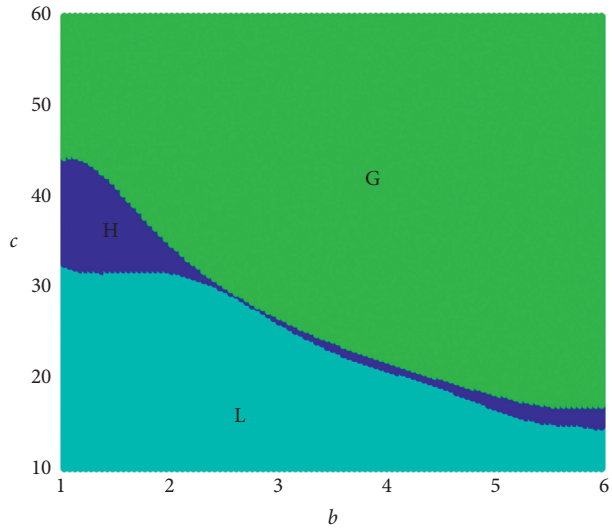

Figure 8: Dynamic map of the proposed chaotic system under mode 1: M (−, +) under $a = 112$.

$$[X, Y, Z, W] = \begin{cases} S_{+3,+4} = ((\pm b/16), (\pm b/16), (3/c), (3/c)), & \text{with } z > 0.125, \\ S_{+01,+02} = ((\pm b/16), (\pm b/16), (2/c), (2/c)), & \text{with } z = 0.125, \\ S_{+1,+2} = ((\pm b/16), (\pm b/16), (1/c), (1/c)), & \text{with } 0 < z < 0.125, \\ S_{+0,-0} = ((\pm b/16), (\pm b/16), 0, 0), & \text{with } z = 0, \\ S_{-1,-2} = ((\pm b/16), (\pm b/16), (-1/c), (-1/c)), & \text{with } -0.125 < z < 0, \\ S_{-01,-02} = ((\pm b/16), (\pm b/16), (-2/c), (-2/c)), & \text{with } z = -0.125, \\ S_{-3,-4} = ((\pm b/16), (\pm b/16), (-3/c), (-3/c)), & \text{with } z < -0.125. \end{cases} \tag{9}$$

The Jacobian matrix of system (2) at the equilibrium points is

$$J = \begin{bmatrix} -a & a & 0 & 0 & \\ \mp 128\delta(4X)Z & \pm 128\delta(4Y)W & \mp 16\text{sgn}(4X) & \pm 16\text{sgn}(4Y) & \\ \pm 16\text{sgn}(X) & 0 & 0 & 0 & \delta(4Z + 0.5k) - c \\ 0 & 0 & 8\sum_{k=-1}^{1} & & \end{bmatrix}. \tag{10}$$

From equation (10) and the definition of δ (), one can see that it has δ (4Z-0.5) whose value will be infinite under Z=0.125, δ (4Z) whose value will be infinite under $Z = 0$, and δ (4Z + 0.5) whose value will be infinite under Z=−0.125. Thus, under these three cases, the corresponding eigenvalues of equation (10) can also not be calculated.

Of course, the same technique in Section 2 can be used and the same results can be obtained; that is, $S_{+01,+02}$, $S_{+0,-0}$, and $S_{-01,-02}$ are unstable point. Hence, the system's trajectory will be departed rapidly at these six equilibrium points. However, for $S_{+3,+4}$, $S_{+1,+2}$, $S_{-1,-2}$, and $S_{-3,-4}$, the corresponding eigenvalues of equation (10) can be obtained and the results are the same as those in Section 2. Therefore, all these eight equilibrium points are index-2 saddle foci, which are necessary to form eight-scroll chaotic attractors. For example, based on $a = 32$, $b = 2.4$, $c = 16$, and $n = 1$ and under the initial condition (x_0, y_0, z_0, w_0)=(0.01, 0.01, 0.01, 0.01), the numerical simulations by using the ode45 algorithm with variable step size and the simulation time T = 1000s with time step being 0.002s in Matlab software are shown in Figure 10. One can see that the proposed multiscroll chaotic system has eight-scroll chaotic attractors. In addition, for the same conditions of simulation algorithm and simulation time, the calculated Lyapunov exponents of the proposed multiscroll chaotic system under this case are $LE_1 = 2.76$, $LE_2 = 0$, $LE_3 = -11.37$, and $LE_4 = -39.35$.

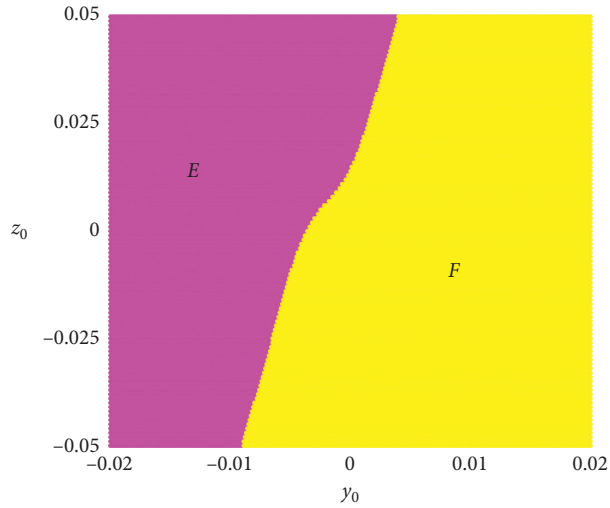

Figure 9: The basin of attraction of the proposed chaotic system under mode 1: M (−, +) under $a = 112$, $b = 2.4$, $c = 16$, $x_0 = 0.01$, and $w_0 = 0.01$.

5. FPGA Implementation

In this section, the proposed multiscroll chaotic system is implemented by using FPGA. Here, the second-order Runge–Kutta method and the fixed-point data format 32Q26, where 1 bit is the sign part, 5 bits is the integer part, and 26 bits is the decimal part, are applied to calculate the multiscroll chaotic system.

5.1. Two-Stage Iteration. Based on the second-order Runge–Kutta method, the discretization about system (2) under M (−, +) can be derived for implementing it in FPGA and its results are

$$\begin{cases} x_{k+1} = x_k + \Delta t \times (a(y_k - x_k)), \\ y_{k+1} = y_k + \Delta t \times (-16 z_k \operatorname{sgn}(4x_k) + 16 w_k \operatorname{sgn}(4y_k)), \\ z_{k+1} = z_k + \Delta t \times (16|x_k| - b), \\ w_{k+1} = w_k + \Delta t \times \left(-c w_k + \sum_{k=-n}^{n} \operatorname{sgn}(4z_k + 0.5k) \right), \end{cases} \tag{11}$$

where Δt is the discrete time step. Defining $V_k = (x_k, y_k, z_k, w_k)^T$, the proposed multiscroll chaotic system can be expressed as follows:

$$V_{k+1} = V_k + \Delta t \times G(V_k). \tag{12}$$

Based on the second-order Runge–Kutta method [30], there are two stage iteration routines. In stage 1, the state vector is updated as follows:

$$V_{k+(1/2)} = V_k + \frac{h}{2} \times G(V_k), \tag{13}$$

where h is the discrete time gap and $h = 1/128$ is taken for the implementation in experimental results. $V_{k+1/2}$ indicates the intermediate results in a half step, that is, $\Delta t = h/2$.

In stage 2, V_{k+1} is updated based on $V_{k+1/2}$ from stage 1, and its formula is as follows:

$$V_{k+1} = V_k + h \times G\left(V_{k+(1/2)}\right). \tag{14}$$

5.2. Verilog HDL Implementation. Here, Verilog HDL language [31, 32] is used to realize the digital chaotic system in FPGA. Notably, in programming, after initial state is defined, state machine method is applied to split the whole digital chaotic generator into several subprocesses, which includes nine states (S_0, S_1, S_2, S_3, S_4, S_5, S_6, S_7, and S_8) and the corresponding state machine flowchart is shown in Figure 11. We have the following:

(i) S_0: calculation about $4x$, $4y$, and $4z$ by using shift operation.

(ii) S_1: implementation of sgn $(4x)$, sgn $(4y)$, $|x|$, and sgn $(4z + 0.5k)$ operations where $k = -n{:}n$.

(iii) S_2: add up all sgn $(4z + 0.5k)$, parallel implementation of ax and ay operations, and parallel implementations to get the results of 16sgn $(4x)z$ and 16sgn $(4y)w$.

(iv) S_3: parallel implementations to get the results of $-cw$ and $f(z)$.

(v) S_4: parallel implementations to get the results of $\dot{x}$, $\dot{y}$, $\dot{z}$, and $\dot{w}$.

(vi) S_5: select 32 bits to present $\dot{x}$, $\dot{y}$, $\dot{z}$, and $\dot{w}$.

(vii) S_6: according to the second-order Runge–Kutta method expressed in equations (13) and (14), the variables $\dot{x}$, $\dot{y}$, $\dot{z}$, and $\dot{w}$ are iterated. Obviously, there are two iterative stages. When the iteration is in stage 1, implement the operation in equation (13) and then direct to state S_0. When the iteration is in stage 2, implement the operation in equation (14) and then direct to state S_7.

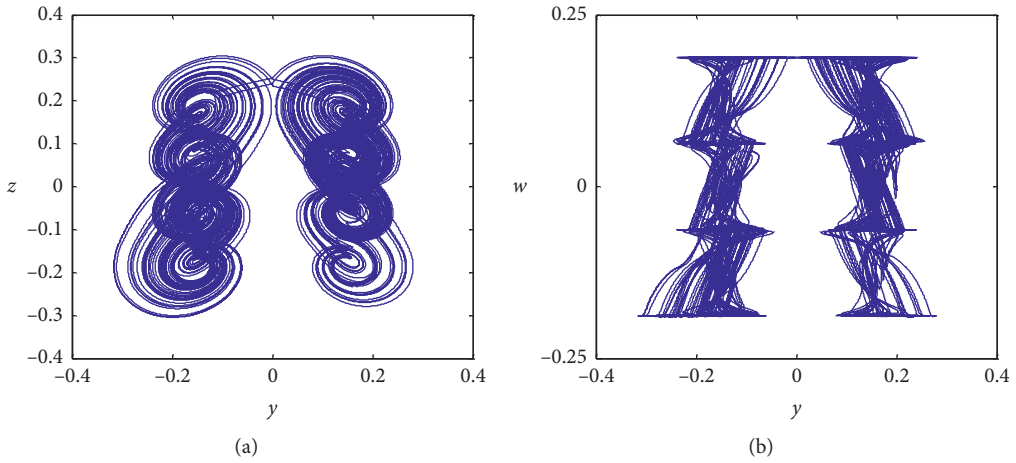

Figure 10: Numerical simulations for the chaotic system $n = 1$. (a) y versus z; (b) y versus w.

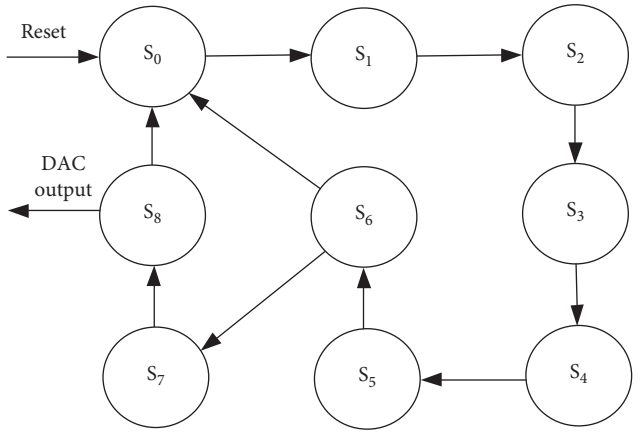

Figure 11: State machine flowchart.

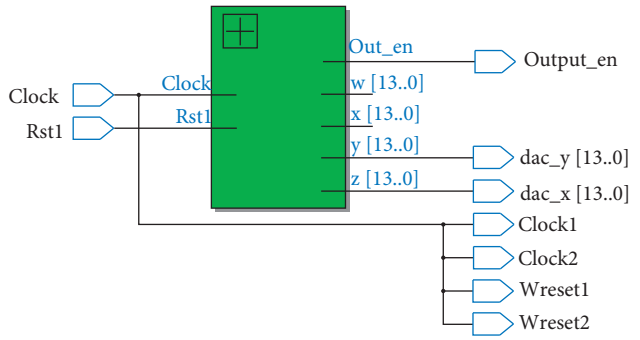

Figure 12: Top-layer RTL of the proposed chaotic system.

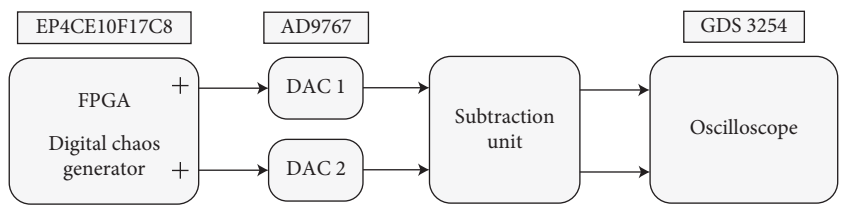

Figure 13: The architecture of experimental hardware platform for the proposed chaotic system.

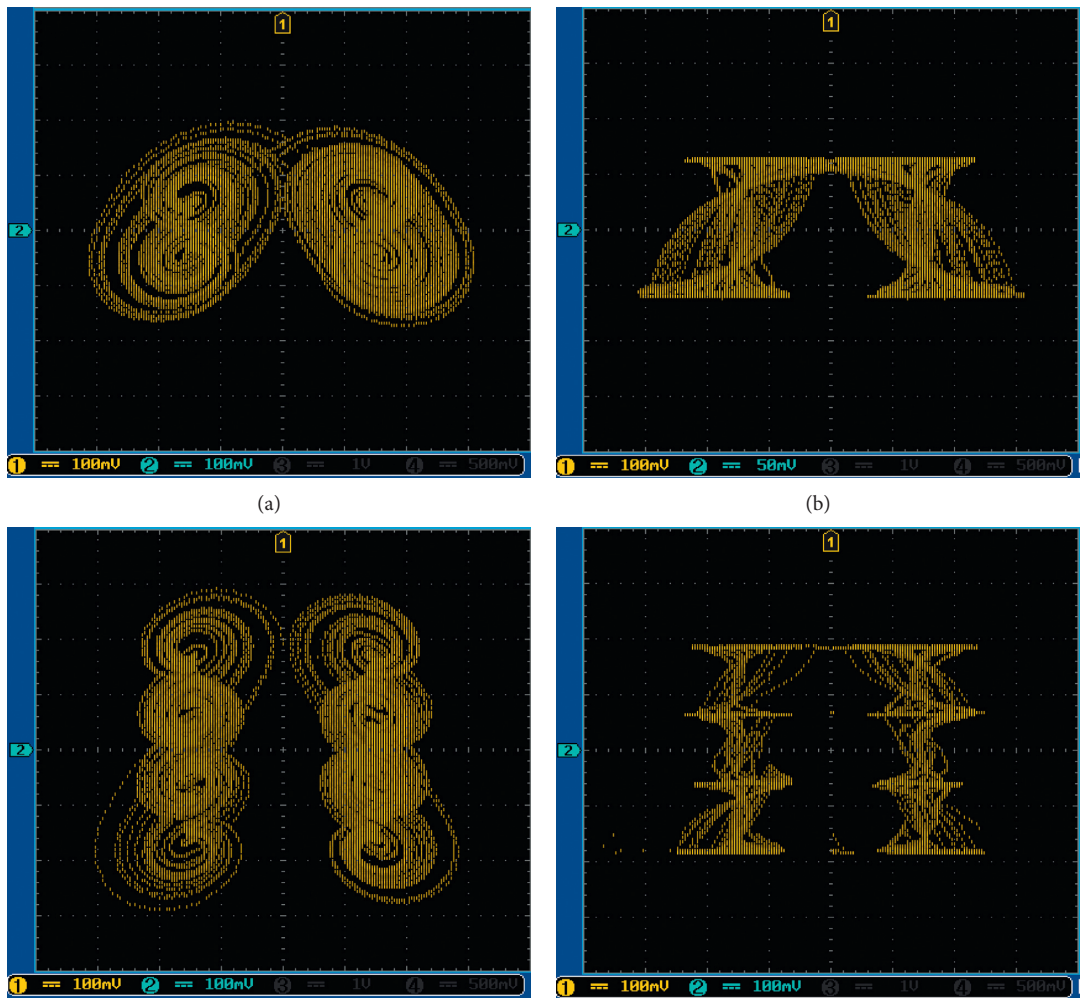

Figure 14: Phase portraits of chaotic system with $n = 0$ and $n = 1$ from the experimental results: (a) y versus z with $n = 0$, (b) y versus w with $n = 0$, (c) y versus z with $n = 1$, and (d) y versus w with $n = 1$.

(viii) S_7: add a positive offset to the results obtained in state S_6 to avoid negative outputs.

(ix) S_8: output the digital chaotic signal to the external digital-to-analog converter (DAC) chip and direct to state S_0.

The top-layer RTL viewer of the realization is shown in Figure 12, where we have the following: "clock" (the clock for FPGA, the input clock is set as 50 MHz in our experiments), "rst1" (the reset for FPGA), "clock1" and "clock2" (the clock for external DAC chip), "wreset1" and "wreset2" (the reset for external DAC chip), "ouput_en" (the output is valid under the high level signal), "x[13..0]" (the digital output of x in each step), "y[13..0]" (the digital output of y in each step), "z[13..0]" (the digital output of z in each step), "w[13..0]" (the digital output of w in each step), "dac_y[13..0]" (the output of y[13..0] to the external DAC chip), and "dac_x[13..0]" (the output of z[13..0] to the external DAC chip).

5.3. Experimental Results. After writing the Verilog HDL program for the multiscroll chaotic system successfully, this program can be downloaded into FPGA via USB Blaster so that it is converted to a hardware list and then be configured into FPGA to form the corresponding digital circuits. The Altera Cyclone IV EP4CE10F17C8 FPGA, which has available internal resources including 10320 logic elements, 423936 RAMs implement bits, 2 PLLs, and 46 hardware multipliers, is adopted. Also the external DAC chip AD9767 (14 bits) with two output channels is applied in the hardware platform.

The architecture of experimental hardware platform for the proposed chaotic system is shown in Figure 13. Notably, the proposed chaotic system can generate chaotic attractors containing negative signals; however, the digital chip AD9767 whose conversion rate up to 125 Msps can only process positive signals, so that a positive number should be added for each output of FPGA (+ in Figure 13). In order to keep consistency with the simulation results, the DAC output signal needs to be subtracted by the same positive number; that is, a subtraction unit before being captured by the digital oscilloscope GDS 3254 should be needed. The experimental results based on FPGA technology are shown

Table 2: Hardware resources required to implement the proposed multiscroll chaotic system.

Terms	Resource consumptions
Logic elements	2303/10320 (22%)
Registers	1816/10320 (18%)
RAMs implement bits	100352/423936 (24%)
Multipliers elements	0/46 (0%)
PLLs	0/2 (0%)
Throughput (Mbits/s)	100
Clock cycles by iteration	16
Latency (ns)	320

Table 3: Summary of the required resources to implement different chaotic systems by using FPGA.

Ref.	Iterative approach	Logic elements	Registers	Multiplier elements	Max. freq. (MHz)
[33]	Runge–Kutta 4	4422	1891	24	69.50
[34]	Runge–Kutta 4	4708	2662	208	84.77
This work	Runge–Kutta 2	2303	1816	0	75.59

in Figure 14. By comparing Figures 14(a), 14(b), 14(c), and 14(d) with Figures 1(a), 1(b), 10(a), and 10(b), respectively, one can see that the results from these two sides are in good agreement with each other.

In our experiments, the input clock is set as 50 MHz and the total thermal power dissipation is obtained as 77.01 mW by employing the PowerPlay Power Analyzer Tool in the software Quartus II. The other hardware resources required to implement the new multiscroll chaotic system based on FPGA chip are listed in Table 2. In this FPGA implementation, 22% of the logic elements, 18% of the logic registers, 24% of the RAMs, 0% of the embedded multipliers, and 0% of the PLLs of the Altera Cyclone IV EP4CE10F17C8 FPGA are occupied, where the resource utilization rates are determined by the ratio of the required number of resources to the total number of resources in the Altera Cyclone IV EP4CE10F17C8 FPGA board. Besides, the throughput of this digital implementation is given as 100Mbits/s, the last two lines provide that there are 16 clock cycles required to evaluate a single iteration, and the delay time is given as 320 nanoseconds when using a 50 MHz clock signal. In addition, the comparisons on FPGA implementations between some existent chaotic systems given in [33, 34] and the proposed chaotic system are shown in Table 3. In summary, one can see that the calculation accuracy of the second-order Runge–Kutta method is sufficient to meet the requirements of the proposed chaotic system, and it requires fewer FPGA's resources. Hence, in this paper, the FPGA realization is feasible, the resource consumption is reasonable, the operation is stable and the output speed is fast.

6. Conclusion

Based on the modified Lorenz-type system and adding an additional variable, a novel chaotic system that can generate multiscroll chaotic attractors is proposed. Attraction basin, bifurcation diagram, dynamic map, phase portrait, Lyapunov exponent spectrum, and C_0 complexity are carried out for this proposed chaotic system to analyze its dynamical behaviors. Research results show that there are some typical dynamics including multistability, bifurcation, chaotic attractors, quasi-periodic attractor, and periodic attractor in this proposed chaotic system. For the different initial conditions, symmetric coexisting attractors will occur in this system. Moreover, theoretical analysis, numerical simulations, and FPGA implementations together demonstrate that the $4n + 4$ scroll chaotic attractors can be obtained by selecting the value of the natural number n. Compared with other existent FPGA implementations of the chaotic generators, the proposed multiscroll chaotic system has an advantage of requiring less resources, especially only requiring 0% of the embedded multipliers and 0% of the PLLs of the FPGA chip. Hence, this work will benefit chaotic secure communications, which will be our future work.

Data Availability

The data used to support the findings of this study are available from the corresponding author upon request.

Conflicts of Interest

The authors declare that they have no conflicts of interest.

Acknowledgments

This work was supported in part by the New Star of Youth Science and Technology of Shaanxi Province under Grant 2016KJXX-40.

References

[1] W. K. S. Tang, G. Q. Zhong, G. Chen, and K. F. Man, "Generation of N-scroll attractors via sine function," *IEEE Transactions on Circuits and Systems I: Fundamental Theory and Applications*, vol. 48, no. 11, pp. 1369–1372, 2001.

[2] E. Günay and R. Kiliç, "A new way of generating *N*-scroll attractors via trigonometric function," *International Journal of Bifurcation and Chaos*, vol. 21, no. 03, pp. 897–901, 2011.

[3] S. Özoğuz, A. S. Elwakil, and K. N. Salama, "*N*-scroll chaos generator using nonlinear transconductor," *Electronics Letters*, vol. 38, no. 14, pp. 685-686, 2002.

[4] J. Lü and G. Chen, "Generating multiscroll chaotic attractors: theories, methods and applications," *International Journal of Bifurcation and Chaos*, vol. 16, no. 04, pp. 775–858, 2006.

[5] Y. Huang, Y. Chen, K. Li et al., "Multi scrolls chaotic encryption for physical layer security in OFDM-PON," *Optics Communications*, vol. 471, p. 126009, 2020.

[6] A. Atangana, G. Bouallegue, and K. Bouallegue, "New multi-scroll attractors obtained via Julia set mapping," *Chaos, Solitons & Fractals*, vol. 134, Article ID 109722, 2020.

[7] D. Mathale, E. F. Doungmo Goufo, and M. Khumalo, "Co-existence of multi-scroll chaotic attractors for fractional systems with exponential law and non-singular kernel," *Chaos, Solitons & Fractals*, vol. 139, Article ID 110021, 2020.

[8] J. H. Lü, S. M. Yu, H. Leung, and G. R. Chen, "Experimental verification of multidirectional multiscroll chaotic attractors," *IEEE Transactions on Circuits and Systems I: Fundamental Theory and Applications*, vol. 53, no. 1, pp. 149–165, 2006.

[9] X. Liu, X. S. Shen, and H. Zhang, "Multi-scroll chaotic and hyperchaotic attractors generated from Chen system," *International Journal of Bifurcation and Chaos*, vol. 22, no. 02, Article ID 1250033, 2012.

[10] C. H. Wang, H. Xu, and F. Yu, "A novel approach for constructing high-order chua's circuit with multi-directional multi-scroll chaotic attractors," *International Journal of Bifurcation and Chaos*, vol. 23, no. 3, Article ID 1350022, 2013.

[11] Q. Lai, Z.-H. Guan, Y. Wu, F. Liu, and D.-X. Zhang, "Generation of multi-wing chaotic attractors from a Lorenz-like system," *International Journal of Bifurcation and Chaos*, vol. 23, no. 09, Article ID 1350152, 2013.

[12] X. Luo, C. Wang, and Z. Wan, "Grid multi-wing butterfly chaotic attractors generated from a new 3-D quadratic autonomous system," *Nonlinear Analysis: Modelling and Control*, vol. 19, no. 2, pp. 272–285, 2014.

[13] N. Yu, Y.-W. Wang, X.-K. Liu, and J.-W. Xiao, "3D grid multi-wing chaotic attractors," *International Journal of Bifurcation and Chaos*, vol. 28, no. 04, Article ID 1850045, 2018.

[14] F. R. Tahir, R. S. Ali, V.-T. Pham, A. Buscarino, M. Frasca, and L. Fortuna, "A novel 4D autonomous 2 $$\varvec{n}$$ n -butterfly wing chaotic attractor," *Nonlinear Dynamics*, vol. 85, no. 4, pp. 2665–2671, 2016.

[15] C. Zhang and S. Yu, "Generation of multi-wing chaotic attractor in fractional order system," *Chaos, Solitons & Fractals*, vol. 44, no. 10, pp. 845–850, 2011.

[16] S. M. Yu, J. H. Lü, W. K. S. Tang, and G. R. Chen, "A general multiscroll Lorenz system family and its realization via digital signal processors," *Chaos*, vol. 16, no. 3, Article ID 033126, 2006.

[17] H. Cao and F. Wang, "Transient and steady coexisting attractors in a new memristor-based 4-D chaotic circuit," *AEU-International Journal of Electronics and Communications*, vol. 108, pp. 262–274, 2019.

[18] D. K. Shah, R. B. Chaurasiya, V. A. Vyawahare, K. Pichhode, and M. D. Patil, "FPGA implementation of fractional-order chaotic systems," *AEU - International Journal of Electronics and Communications*, vol. 78, pp. 245–257, 2017.

[19] P. Chen, S. Yu, X. Zhang et al., "ARM-embedded implementation of a video chaotic secure communication via WAN remote transmission with desirable security and frame rate," *Nonlinear Dynamics*, vol. 86, no. 2, pp. 725–740, 2016.

[20] Z. S. Lin, S. M. Yu, J. H. Lü, S. T. Cai, and G. R. Chen, "Design and ARM-embedded implementation of a chaotic map-based real-time secure video communication system," *IEEE Transactions on Circuit and Systems for Video Technology Circuits*, vol. 25, no. 7, pp. 1203–1216, 2015.

[21] Z. D. L. H. Mauricio, A. Leonardo, and V. Yolanda, "An experimental realization of a chaos-based secure communication using Arduino microcontrollers," *The Scientific World Journal*, vol. 2015, Article ID 123080, 10 pages, 2015.

[22] A. D. Pano-Azucena, J. de Jesus Rangel-Magdaleno, E. Tlelo-Cuautle, and A. de Jesus Quintas-Valles, "Arduino-based chaotic secure communication system using multi-directional multi-scroll chaotic oscillators," *Nonlinear Dynamics*, vol. 87, no. 4, pp. 2203–2217, 2017.

[23] M. Alçin, İ. Pehlivan, and İ. Koyuncu, "Hardware design and implementation of a novel ANN-based chaoticgenerator in FPGA," *Optik*, vol. 127, no. 13, pp. 5500–5505, 2016.

[24] A. S. Elwakil, S. Ozoguz, and M. P. Kennedy, "Creation of a complex butterfly attractor using a novel Lorenz-type system," *IEEE Transactions on Circuits and Systems I: Fundamental Theory and Applications*, vol. 49, no. 4, pp. 527–530, 2002.

[25] A. Wolf, J. B. Swift, H. L. Swinney, and J. A. Vastano, "Determining Lyapunov exponents from a time series," *Physica D: Nonlinear Phenomena*, vol. 16, no. 3, pp. 285–317, 1985.

[26] M. F. Danca, "Lyapunov exponents of a class of piecewise continuous systems of fractional order," *Nonlinear Dynamics*, vol. 81, no. 1-2, pp. 227–237, 2015.

[27] E. H. Shen, Z. J. Cai, and F. J. Gu, "Mathematical foundation of a new complexity measure," *Applied Mathemtics and Mechanics-English Edition*, vol. 26, no. 9, pp. 1188–1196, 2005.

[28] K. H. Sun, S. B. He, C. X. Zhu, and Y. He, "Analysis of chaotic complexity characteristics based on C_0 algorithm," *Acta Physica Sinica*, vol. 41, no. 9, pp. 0372–2112, 2013.

[29] J. P. Singh and B. K. Roy, "The nature of Lyapunov exponents is (+, +, −, −). Is it a hyperchaotic system?" *Chaos, Solitons & Fractals*, vol. 92, pp. 73–85, 2016.

[30] R. M. Wang, M. H. Liu, Y. Sheng, and J. C. Feng, "Implementation of a chaotic system based on runge-kutta algorithm and programmable gate array technology," *Journal of Southwest China Normal University (Natural Science Edition)*, vol. 37, no. 1, pp. 41–46, 2012.

[31] E. Tlelo-Cuautle, A. D. Quintas-Valles, L. G. de la Fraga, and J. D. Rangel-Magdaleno, "VHDL descriptions for the FPGA implementation of PWL-function-based multi-scroll chaotic oscillators," *Plos One*, vol. 11, no. 12, Article ID e0168300, 2016.

[32] E. Tlelo-Cuautle, J. J. Rangel-Magdaleno, and L. G. de la Fraga, *Engineering Applications of FPGAs*, Springer, Berlin, Germany, 2016.

[33] E. Tlelo-Cuautle, J. J. Rangel-Magdaleno, A. D. Pano-Azucena, P. J. Obeso-Rodelo, and J. C. Nunez-Perez, "FPGA realization of multi-scroll chaotic oscillators," *Communication in Nonlinear Science and Numerical Simulation*, vol. 27, no. 1–3, pp. 66–80, 2015.

[34] O. Guillén-Fernández, M. F. Moreno-López, and E. Tlelo-Cuautle, "Issues on applying one- and multi-step numerical methods to chaotic oscillators for FPGA implementation," *Mathematics*, vol. 9, no. 2, p. 151, 2021.

Hindawi
Complexity
Volume 2021, Article ID 5518633, 12 pages
https://doi.org/10.1155/2021/5518633

Research Article

A New Megastable Chaotic Oscillator with Blinking Oscillation terms

Dhinakaran Veeman,[1] Hayder Natiq,[2] Nadia M. G. Al-Saidi,[3] Karthikeyan Rajagopal,[4] Sajad Jafari,[5,6] and Iqtadar Hussain[7]

[1]*Centre for Applied Research, Chennai Institute of Technology, Chennai, India*
[2]*Information Technology Collage, Imam Ja'afar Al-Sadiq University, Baghdad 10001, Iraq*
[3]*Department of Applied Sciences, University of Technology, Baghdad, Iraq*
[4]*Centre for Nonlinear Systems, Chennai Institute of Technology, Chennai, India*
[5]*Health Technology Research Institute, Amirkabir University of Technology, 424 Hafez Ave., Tehran 15875-4413, Iran*
[6]*Department of Biomedical Engineering, Amirkabir University of Technology, 424 Hafez Ave., Tehran 15875-4413, Iran*
[7]*Department of Mathematics, Statistics and Physics, Qatar University, Doha 2713, Qatar*

Correspondence should be addressed to Karthikeyan Rajagopal; rkarthiekeyan@gmail.com

Received 25 February 2021; Revised 1 April 2021; Accepted 22 April 2021; Published 30 April 2021

Academic Editor: Jorge-Antonio Lopez-Renteria

Recently, megastable systems have grabbed many researchers' interests in the area of nonlinear dynamics and chaotic systems. In this paper, the oscillatory terms' coefficients of the simplest megastable oscillator are forced to blink in time. The forced system can generate an infinitive number of hidden attractors without changing parameters. The behavior of these hidden attractors can be chaotic, tori, and limit cycle. The attractors' topology of the system seems unique and looks like *picture frames*. Besides, the existence of different coexisting attractors with different kinds of behaviors reflects the system's high sensitivity. Using the sample entropy algorithm, the system's complexity for different initial values is assessed. In addition, the circuit of the introduced forced system is designed, and the possibility of implicating the system with analog elements is investigated.

1. Introduction

Simple and elegant oscillators are interesting for researchers in the fields of nonlinear dynamics [1]. Faghani et al. have introduced many of these simple oscillators, generating chaotic time series [2]. An equilibrium point in the basin of attraction is considered an important feature for chaotic attractors [3]. Therefore, attractors can be classified into two main groups based on this feature: self-excited attractors and hidden attractors [4]. For self-excited attractors, at least one fixed point can be found in their basin of attraction [5]. On the other hand, no-equilibrium exists in the basin of attraction of a hidden attractor [6]. Different kinds of oscillators with hidden attractors have been introduced yet. Instances for oscillators with hidden attractors can be chaotic dynamics which have one stable equilibrium [7], a line of equilibriums [8], or a surface of equilibriums [9] in their basin. Hidden attractors' existence in real-world systems also has been demonstrated [10]. Besides the classification among attractors based on their equilibrium(s), an important category of chaotic systems is the forced dynamics (time-variant systems) [11]. As one of the oldest examples, Van der Pol forced oscillator can be mentioned [12]. Forcing nonlinear systems is a method to generate strange attractors when the original versions of nonlinear systems are unable to generate chaotic behaviors [11].

Besides properties such as the existence and topology of fixed points and dynamics' time variability, some other features have grabbed researchers' attention. Oscillators with time delays in their equations [13], fractional equations [14], fuzzy differential equations [15], those with hyperchaos [16], and others with synchronization among a group of them [17]

can be examples of chaotic systems with specific features. Multistability is another of these features [18]. A system can be named multistable when it has more than one attractor without any change in its parameters [19]. In these systems, initial conditions determine trajectories which finally are attracted to which one of the attractors [20]. Multistability is sometimes considered a nonproper phenomenon that may make unexpected situations when it can also be used as a control strategy to switch among different attractors [21]. Multistable systems with uncountable infinitive attractors are called extreme multistable [22] when the ones with countable infinitive attractors are referred megastable [23]. The attractors of multistable systems can have chaotic or hyperchaotic behaviors [24], as well as some other features such as having a number of scrolls [25]. Multistable systems can have some applications such as secure communication [26]. Multistability is also investigated in natural phenomena such as the brain [27].

Besides the mentioned features, topology and the shape of strange attractors are considered as other important features that an oscillator may have [28]. Some chaotic dynamics with different types of symmetries have been introduced [29]. Among features related to the topology of attractors, ones which have multiscrolls are interesting for researchers [30]. Assessing the stability of multiscrolls attractors [31] and finding methods to preserve multiscrolls [32] are topics that grab much attention. Besides, some methods have been introduced to use multiscroll attractors such as switches in systems [33]. In addition, chaotic systems with some modifications sometimes have been used to generate Brownian motions [34]. These Brownian motions are also generated with fractional systems [35]. Besides all of these features, if an oscillator has simple algebraic equations, it can be its advantage [36].

Complexity is another feature that has been investigated among chaotic systems [37]. Richman et al. [38] have derived sample entropy (SamEn) from approximate entropy that is used for assessing the complexity of chaotic systems [39]. With this method, the complexity of the time series generated by the introduced system is investigated in this work.

The feasibility of chaotic dynamics has been a matter of interest since Lorenz discovered the first chaotic system [40]. To assess chaotic oscillators' feasibility, they have been simulated (with software such as Pspice [41]) and implemented (with analog circuits [42]). For instance, some fractional chaotic systems have been implicated with analog circuits [43] and/or digital circuits (such as field-programmable gate array (FPGA) [44]), and their feasibility has been shown [45]. The possibility of the implication of a chaotic system that has a multiscroll attractor has been demonstrated [46]. Besides, multistable systems are also implicated with both digital and analog circuits. For instance, the FPGA realization of a jerk multistable system has been investigated [47]. In another work, multistable systems with circles [48] or other strange curves of equilibrium points [49] have been realized using FPGA. Assessing the realization of the synchronization among chaotic systems is another matter of interest for researchers [50]. Such circuits can have different applications. Predicting the time series of chaotic systems [51], image encryption [52], secure communication [53], and random number generation [54] is an example of their application. In this paper, the introduced forced system's analog circuit is designed and simulated with Pspice to show its feasibility.

In this paper, the equations of a chaotic system are presented which are megastable. In this system, oscillator terms are forced to blink during the time. The dynamical system is introduced in Section 2. This system, which is inspired by the simplest megastable equations, has uncountable attractors. Coexisting limit cycles, torus, and chaotic attractors are investigated in this model in Section 2. In Section 3, the complexity of the system is assessed. Finally, the results are concluded in Section 5.

2. The Proposed System

The proposed model is inspired by the simplest megastable model, which was introduced by Jafari et al. [55]:

$$\dot{x} = -y, \dot{y} = 0.1x + \sin(y). \tag{1}$$

When (−y) and (0.1x) on the right side of equations have the responsibility of making oscillations. Some examples of transient trajectories and attractors of equation (1) are plotted in Figure 1. The system's only equilibrium point is (0, 0) in the center of the smallest limit cycle. Consequently, because other attractors have no equilibrium in their basin, they can be considered hidden attractors.

These equations are used as a platform to introduce the new method of forcing, which is referred to as forcing oscillation terms to blink. To make the oscillation terms blink, their coefficients should change during time. For this aim, time-varying functions are multiplied by the coefficient of the oscillatory terms. These time-variant functions should oscillate between zero (to turn off oscillatory terms for moments) and a positive threshold. In other words, these time-variant oscillatory functions should not have negative values. Note that if the coefficient of oscillation terms oscillates between a positive and a negative value, the trajectory's rotation direction changes repetitively. These repetitive changes in the direction of the oscillator can disturb its stability. Therefore, inspired from equation (1), the oscillator is designed based on the following equations:

$$\dot{x} = -\cos^2(wt)y, \dot{y} = 0.1\sin^2(wt)x + A\sin(y). \tag{2}$$

When $\cos^2(wt)$ and $\sin^2(wt)$ are coefficients of the linear oscillatory terms, the power two for sin and cos functions cause the coefficients to not have negative values. Consequently, this coefficients' oscillation between 0 and 1 caused the blinking of the equations' oscillatory terms. This system's fixed point is only $(0, 0)$. The system's Jacobean is

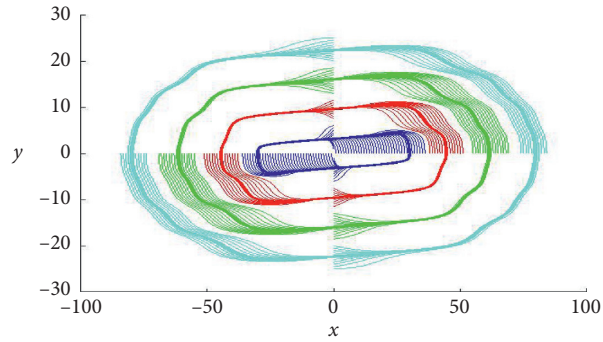

Figure 1: Attractor and some transient responses for equation (1). Attractors are plotted with thicker lines when transient responses are shown with thinner lines.

$$J = \begin{bmatrix} 0 & -\cos^2(wt) \\ 0.1\sin^2(wt) & A\cos(y) \end{bmatrix} \xrightarrow{(x,y)=(0,0)} \begin{bmatrix} 0 & -\cos^2(wt) \\ 0.1\sin^2(wt) & A \end{bmatrix}. \tag{3}$$

Therefore, the eigenvalues are

$$|\lambda I - J| = 0 \longrightarrow \begin{bmatrix} \lambda & +\cos^2(wt) \\ -0.1\sin^2(wt) & \lambda - A \end{bmatrix} \xrightarrow{(x,y)=(0,0)} \lambda^2 - A\lambda + 0.1\cos^2(wt)\sin^2(wt) = 0,$$
$$\lambda = \frac{A \pm \sqrt{1 - 0.4\cos^2(wt)\sin^2(wt)}}{2}. \tag{4}$$

In this paper, always $A > 1$ is considered. Paying attention that $0 < \cos^2(wt)\sin^2(wt) < 1$, the eigenvalues of the equilibrium are always positive. Therefore, the forced system always has an unstable equilibrium.

3. Bifurcations and Lyapunov Exponents' Diagrams

This work aims mainly to find possible chaotic behaviors in the proposed blinking system. Different compositions of A and w as the two bifurcation parameters may lead the system to chaotic behaviors. The ranges of these parameters are considered so that the system does not have unbounded solutions. Besides, ranges for the parameters have been presented in a way that system has different dynamical behaviors such as chaos, torus, and limit cycle. Therefore, firstly, $w = 0.8$ is set, and the system's bifurcation is plotted for a range of A. Next, in the same way, $A = 1$ is set, and a range for w is investigated. Finally, by fixing $A = 1$ and $w = 0.8$ and using the initial value $(x_0, 0)$ as the bifurcation parameter, different coexisting attractors behaviors are investigated.

The Lyapunov exponents (LEs) and bifurcation diagrams are used as two powerful tools for investigating the system's behaviors for different parameters and initial conditions in this section. For all LEs diagrams, the smallest, which have the largest absolute value, is removed in the related pictures. It is done for better visualization of the other two.

Now, paying attention to Figure 2, the LE diagram shows chaotic behaviors for large ranges of A values (one positive, one zero, and one negative (does not drown) [56]). Interestingly, by increasing the values of A, ranges that the system has a chaotic behavior become thinner; however, the values of the largest LEs increase.

Figure 2 shows LEs and bifurcation diagrams for a range of w. The LEs diagram in Figure 2 demonstrates chaotic solutions for different large ranges of w values. Increasing the values of w, the length of ranges that the system has a chaotic behavior increases (Figure 3).

LEs and bifurcation diagrams (Figure 4) are plotted as a function of the initial condition $(x_0, 0)$. It can be seen that, for inner cycles, chaos can be detected. Besides, for the larger values of x_0, the system can present limit cycles (when one LE is zero and the two other is negative [56]) and torus (when the two largest LEs are zero and the other is negative [56]).

The system's detractors for different sets of parameters and different initial conditions are plotted in Figures 5 and 6. These attractors look like *"picture frames."*

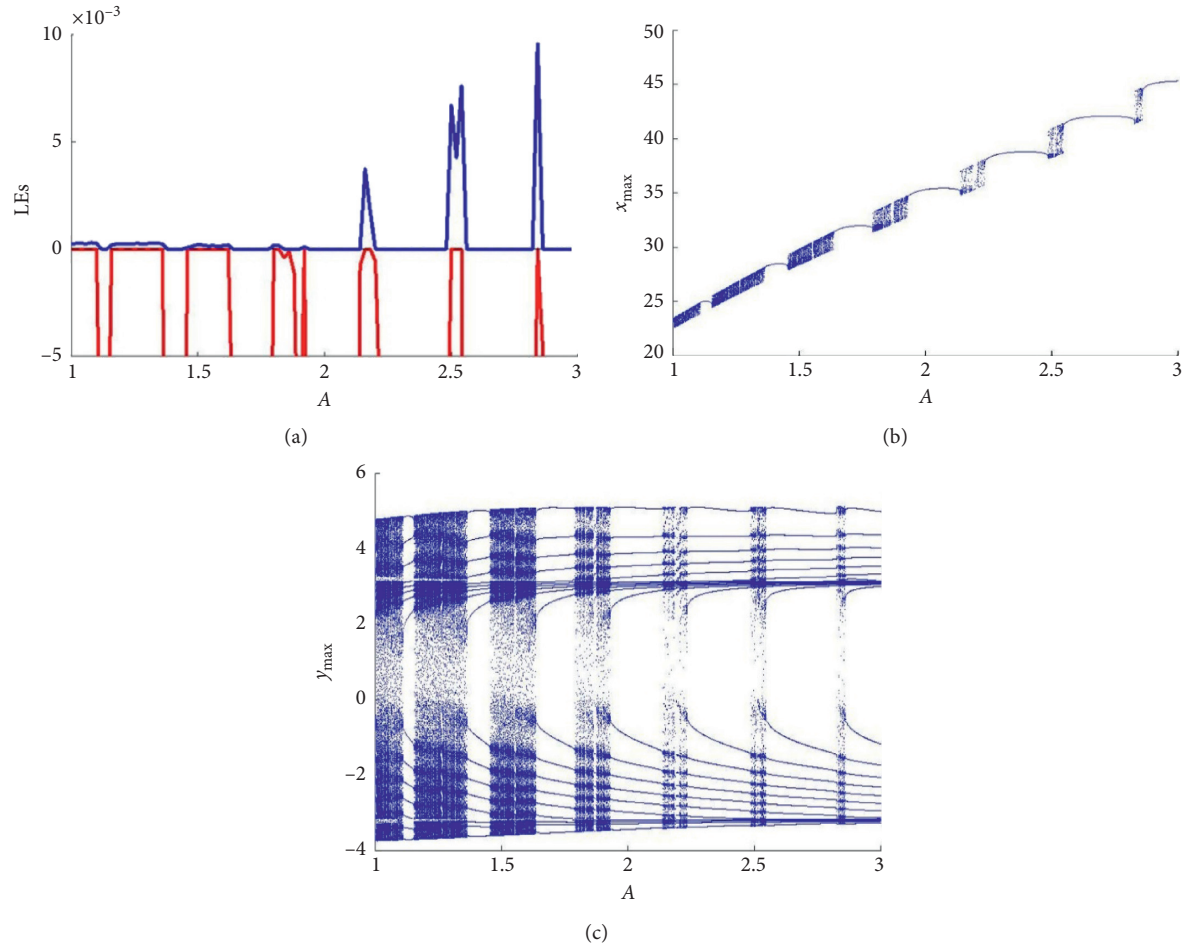

FIGURE 2: Lyapunov exponents and bifurcation diagrams are related to parameter A for $w = 0.8$ when the initial conditions are set $(0.01, 0)$. (a) The two largest Lyapunov exponents are plotted and zoomed. Therefore, the third, which is negative (and has the largest absolute value), and also parts of the second cannot be seen for better visualization. (b) The local maximums of the x variable time series. (c) The local maximums of the y variable time series.

4. Complexity-Based Sample Entropy Algorithm

The sample entropy (SamEn) is a mathematical algorithm introduced to estimate the predictability of time series. It is usually used for evaluating how much information needs to predict the $(t + 1)$th output of a trajectory of systems using its previous (t) outputs. Higher SamEn values indicate a dynamical system exhibits lower levels of regularity.

In this way, for a given time series $\{x(i)\}$, when $(i = 0, 1, \ldots, N - 1)$, SamEn algorithm is given by the following [38].

(1) Reconstruct the time series to be as follows:

$$X_i = \left\{x_i, x_{i+\tau}, \ldots, x_{i+(m-1)\tau}\right\}, \tag{5}$$

where $X_i \in R^m$, m is the embedding dimension, and τ is the time delay.

(2) Compute the vector pairs for a given tolerance parameter r by calculating the distance between X_i and X_j as follows:

$$d\left[X_i, X_j\right] \le r, d\left[X_i, X_j\right] = \max\left\{\left|x(i+k) - x(j+k)\right|: 0 \le k \le m-1\right\}. \tag{6}$$

(3) Calculate $C_i^m(r)$, which represents the probability that any vector X_j has a lower distance (r) than X_i, as follows:

$$C_i^m(r) = \frac{B_i}{N - (m-1)\tau}, \tag{7}$$

where B_i is the number of vectors X_j that have a lower distance (r) than X_i.

(4) Obtain $\theta^m(r)$, which is the average of the natural logarithm of the function $C_i^m(r)$, as follows:

$$\theta^m(r) = \frac{\sum_{i=1}^{N-(m-1)\tau} \ln C_i^m(r)}{[N - (m-1)\tau]}. \tag{8}$$

(5) Repeat the above steps to obtain $\theta^{m+1}(r)$, and then, calculate the SamEn as follows:

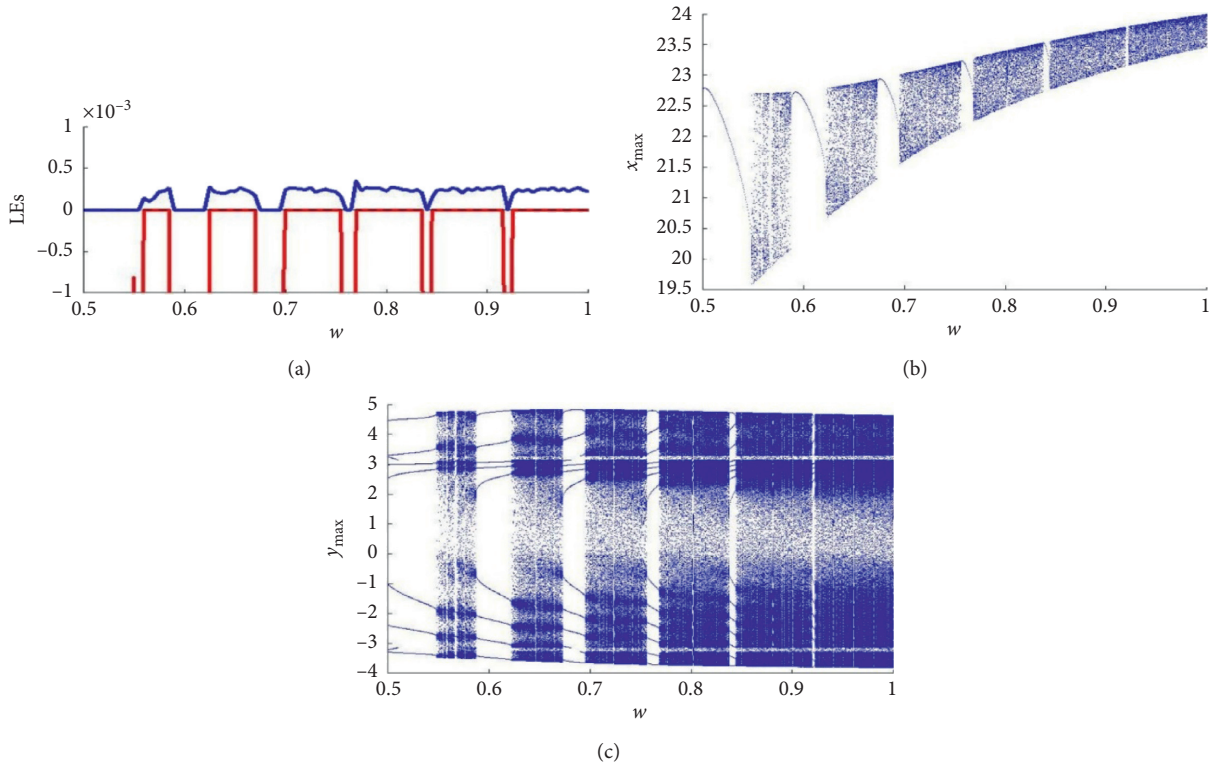

Figure 3: Lyapunov exponents and bifurcation diagrams when w changes as the bifurcation parameter. A and initial conditions are set 1 and $(0.01, 0)$, respectively. (a) The two largest Lyapunov exponents are shown and zoomed. Therefore, parts of the third, which is negative, and its absolute value is larger than the two others, are not plotted. Also, parts of the second Lyapunov exponent cannot be seen because of the zoom for better visualization. (b) Peaks of the x variable time series. (c) Peaks of the y variable time series.

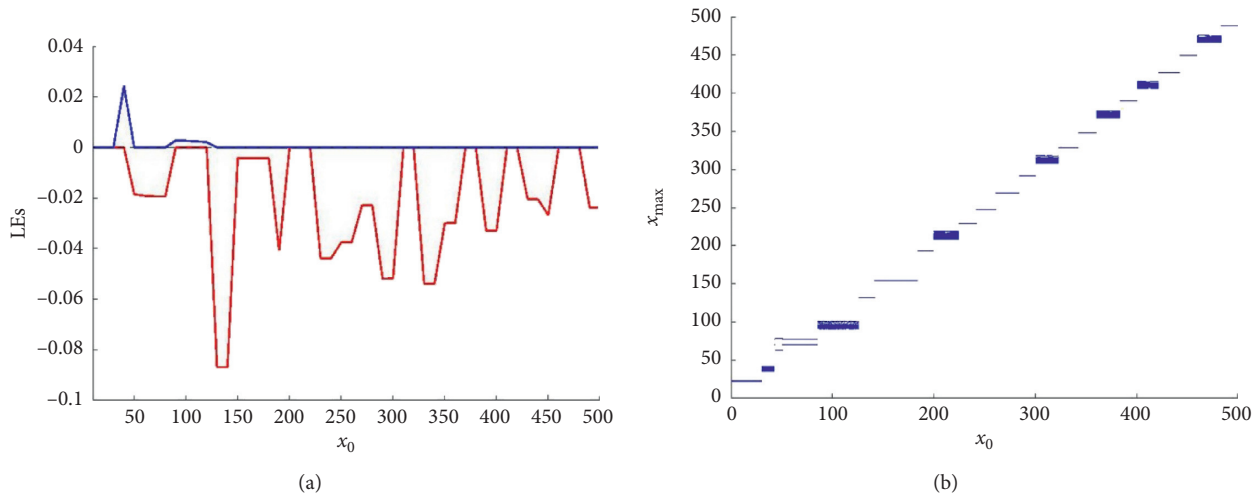

Figure 4: Continued.

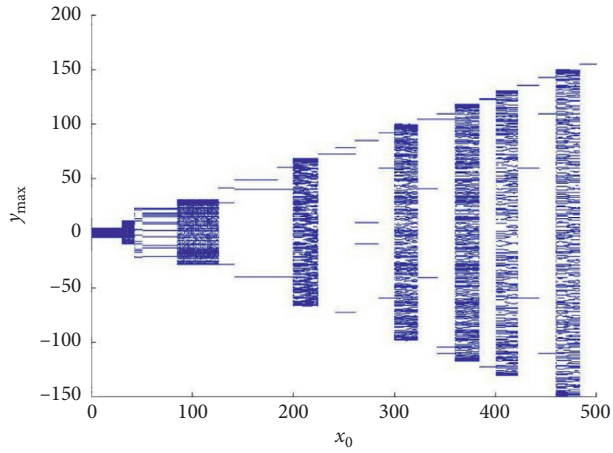

(c)

Figure 4: Lyapunov exponents and bifurcation diagrams for $A = 1$ and $w = 0.8$ when the initial conditions are set $(x_0, 0)$. (a) The two largest Lyapunov exponents are demonstrated. Therefore, the third, which is the most negative, is not shown. (b) x time-series local maximums. (c) y time-series local maximums.

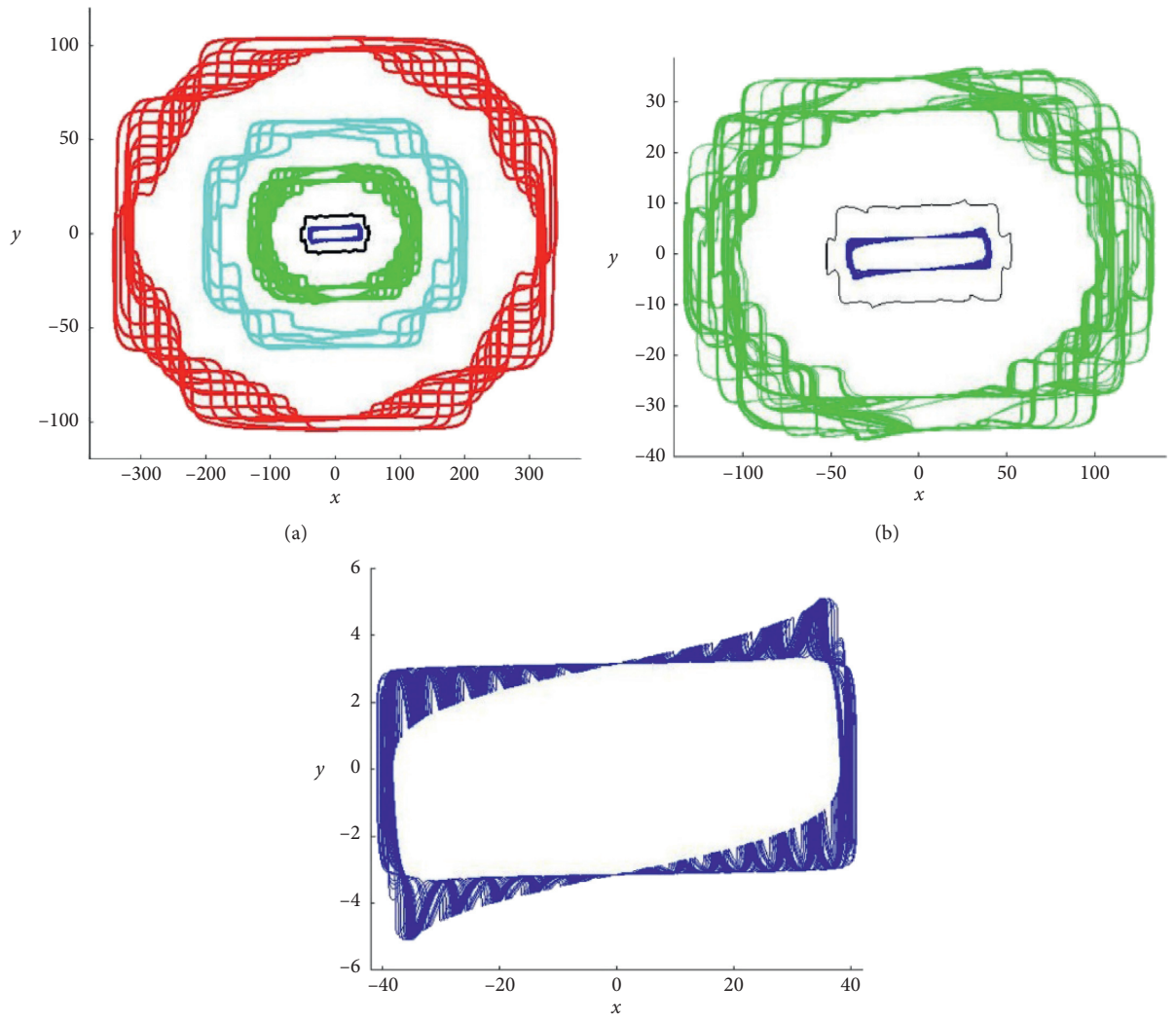

(a)

(b)

(c)

Figure 5: Trajectories when A and w are 2 and 0.5, respectively. (a) The set initial values are $(0, 2)$, $(0, 8)$, $(0, 30)$, $(0, 80)$, and $(0, 100)$. (b and c) are zoomed versions of (a) for a better visualization.

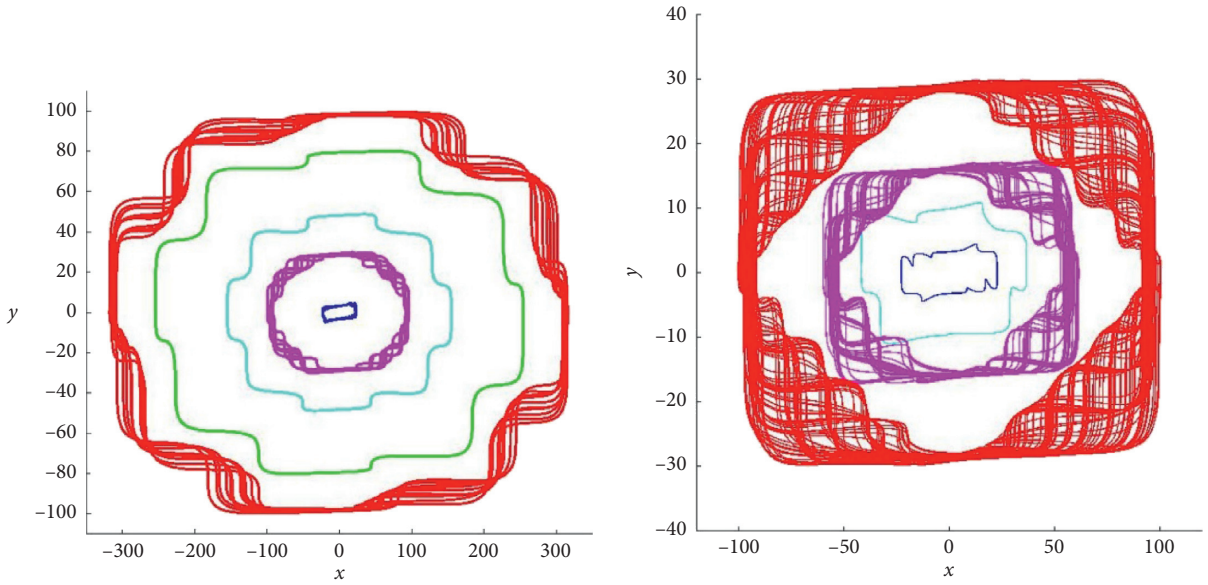

FIGURE 6: Trajectories for different sets of parameters and different initial values. (a) $A = 2, w = 0.5$, and the initial values are set $(0, 2)$, $(0, 30)$, $(0, 45)$, $(0, 80)$, and $(0, 150)$. (b) $A = 1, w = 0.5$, and the initial values are set $(0, 2)$, $(0, 9)$, $(0, 15)$, and $(0, 27)$.

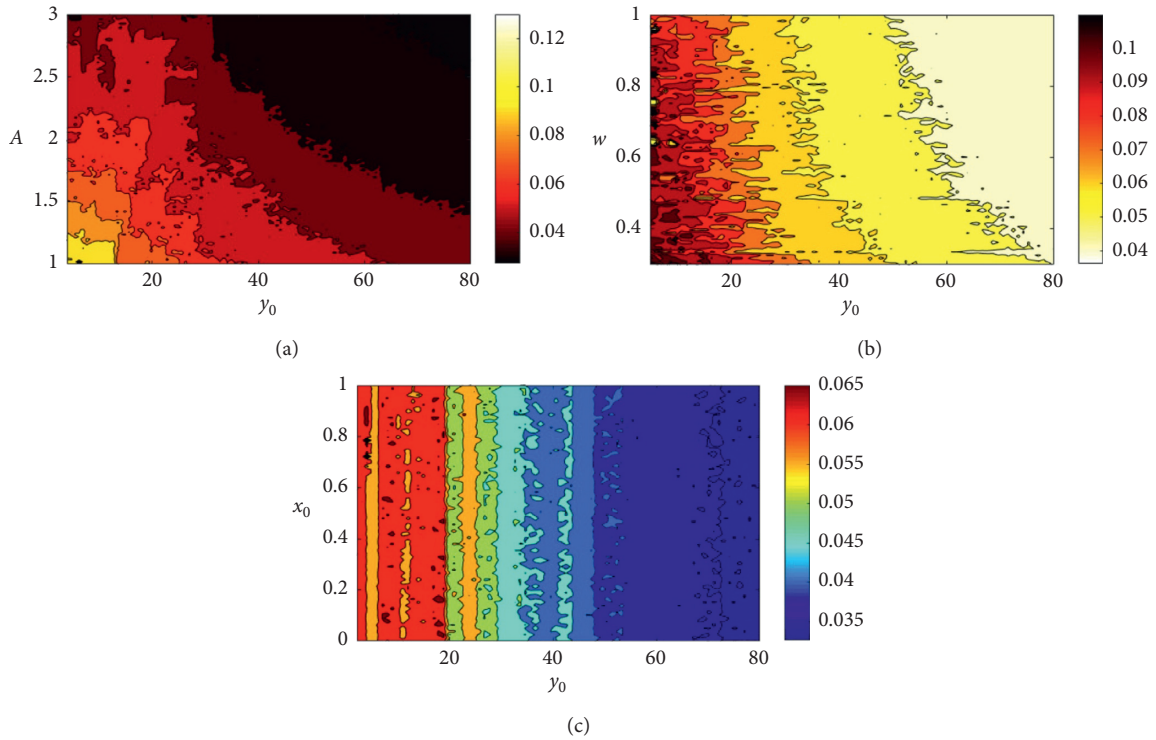

FIGURE 7: Complexity values of the system (equation (3)) calculated by SamEn. (a) $w = 0.5$, and the initial values are set $(0, y_0)$. (b) $A = 1$ and the initial values are set $(0.01, y_0)$. (c) $A = 2, w = 0.5$, and the initial values are set (x_0, y_0).

$$\text{SamEn}(m, r, N) = \theta^m(r) - \theta^{m+1}(r). \tag{9}$$

Now, we employ the SamEn algorithm for $m = 2$ and $r = 0.2 \times (\text{Standard Deviation})$ to evaluate the complexity of the multistability region of the megastable system (3). Figure 7(a) plots the SamEn values of the system when the parameter A and the initial value y_0 change. As can be observed in this figure, when $A = 1$, the system exhibits higher complexity values. The complexity values of the

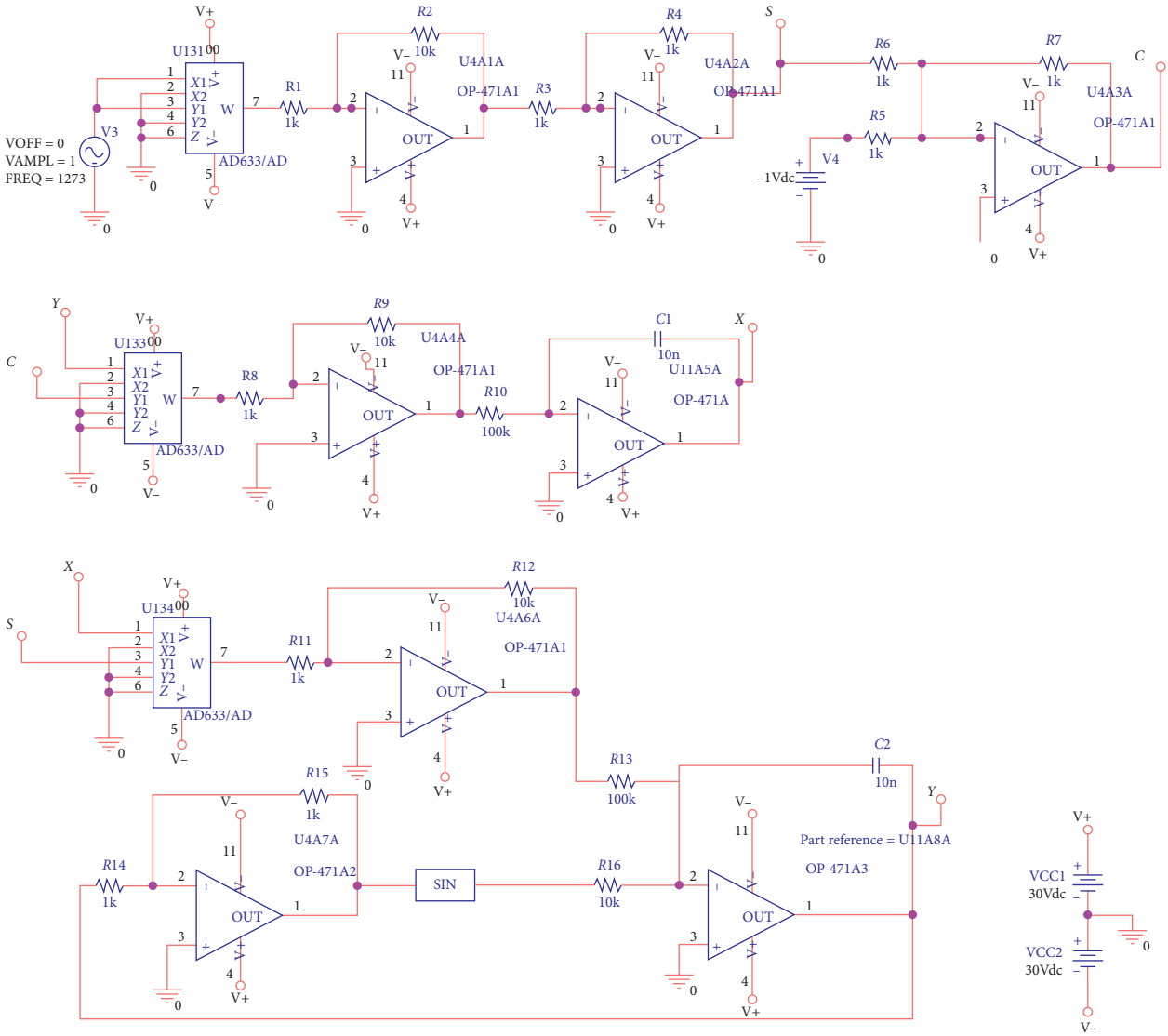

Figure 8: The circuit schematic of the introduced system (Pspice (version 9.1)). The elements values are chosen to represent the system when its parameters are considered $w = 0.8$ and $A = 1$. The system time is scaled $T = t/\alpha$ when $\alpha = (R = 10K\Omega) \times (C = 10\text{nF}) = 10000$.

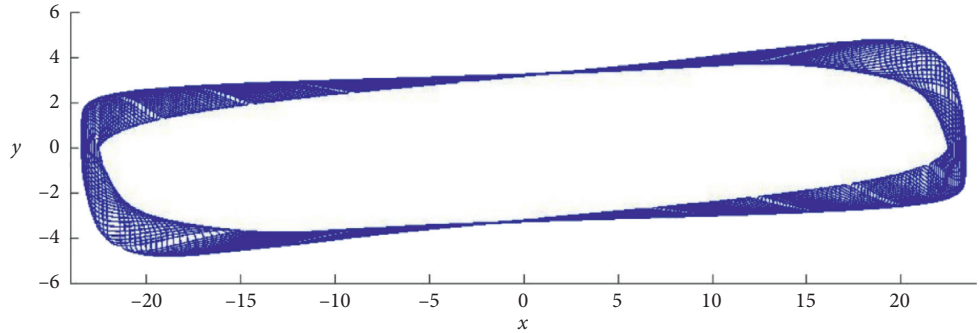

(a)

Figure 9: Continued.

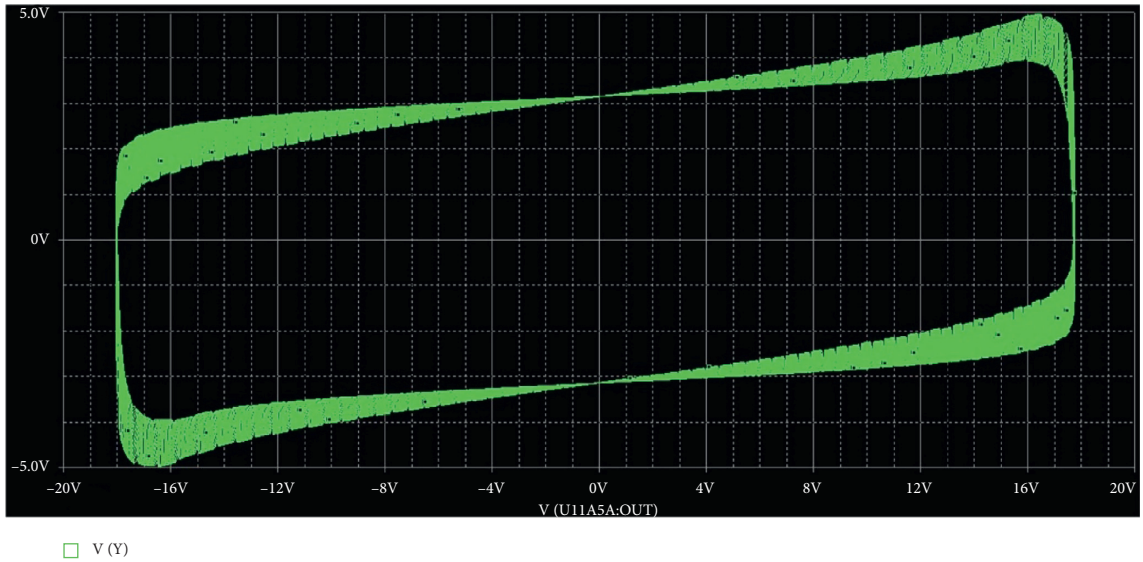

(b)

Figure 9: The phase portrait of the simulated circuit. (a) The phase space of the system when $w = 0.8$ and $A = 1$ (simulated with Matlab 2020). (b) The result of the simulated circuit (Pspice, version 9.1).

system begin decreasing by increasing the value of A. Furthermore, Figure 7(b) shows the SamEn values for a range of w and y_0. This figure demonstrates that the lower complexity values appear when the initial value (y_0) increases. However, Figure 7(a) is also demonstrated this behavior.

To further visualize the system's complexity performance for a particular set of parameters, Figure 7(c) depicts its SamEn values when both initial values (y_0 and x_0) change. This figure shows the complexity values of the system decrease when (y_0) increases.

5. Circuit Design

The analog circuit of the introduced forced system is simulated in this part. The circuit is designed using simple elements such as resistors, capacitors, and Op-Amps (Figure 8). To generate $\cos^2(wt)$ and $\sin^2(wt)$, an AC voltage source is used. AD633/AD is used to generate the second power of the AC voltage source. Considering AD633/AD multiply its outputs to 0.1, the circuit of Op-Amp (U4A1A) (considering $R1 = 1\text{k}$ and $R2 = 10\text{k}$) is used for compensation. In the same way, Op_Amp (U4A4A) and Op-Amp (U4A6A) are used to compensate for the 0.1 coefficient of AD633/AD. Time is rescaled so that $T = t/\alpha$ when $\alpha = (R = 10\text{K}\Omega) \times (C = 10\text{nF}) = 10000$ is assumed. The equations of the implicated circuit are written as follows:

$$\begin{aligned}
\cos^2(w\alpha T) &= \left(\frac{R7}{R5}\right)1 - \frac{R7}{R6}\left(\frac{R2R4}{R1R3}\left(0.1\ \sin^2(w\alpha T)y\right)\right),\\
\frac{\mathrm{d}x}{\mathrm{d}(\alpha T)} &= -\frac{1}{R10C1}\left(\frac{R9}{R8}\right)\left(0.1\ \cos^2(w\alpha T)y\right),\\
\frac{\mathrm{d}y}{\mathrm{d}(\alpha T)} &= \frac{1}{R16C2}\left(\frac{R12}{R11}0.1\ \sin^2(w\alpha T)x\right) + \frac{1}{R16C2}\sin\left(\frac{R15}{R14}y\right).
\end{aligned} \tag{10}$$

When x and y represent the outputs of the Op-Amps U11A5A and U11A8A, respectively. The values of the elements are selected as follows: $R1 = 1K\Omega$, $R2 = 1K\Omega$, $R3 = 1K\Omega$, $R4 = 1K\Omega$, $R5 = 1K\Omega$, $R6 = 1K\Omega$, $R7 = 1K\Omega$, $R8 = 1K\Omega$, $R9 = 1K\Omega$, $R10 = 1K\Omega$, $R11 = 1K\Omega$, $R12 = 1K\Omega$, $R13 = 1K\Omega$, $R14 = 1K\Omega$, $R15 = 1K\Omega$, $R16 = 1K\Omega$, $C1 = 1\text{nF}$, and $C2 = 1\text{KF}$. For $w = 0.8$ the frequency of AC voltage is considered $(w = 0.8) \times (\alpha = 10000)/2\pi \approx 1273$. The system phase space simulated by Matlab for $w = 0.8$ and $A = 1$ is shown in Figure 9(a). Considering Figure 2, these parameters are chosen so that the system has a chaotic behavior. For the mentioned set of parameters, the circuit

shown in Figure 8 is implicated in Pspice software (version 9.1). The result of the simulated circuit is demonstrated in Figure 9(b).

6. Conclusion

Considering recent interests in introducing new strange attractors, this paper introduced a new method to force oscillatory coupling terms of an oscillator. This method, which was named blinking forcing, considers oscillatory coefficients for oscillatory terms. The method was implicated on the simplest megastable system. The megastable forced dynamic could generate chaotic, torus, and limit cycle trajectories in its different attractors without changing its parameters. Complexity simulation analysis has demonstrated that these coexisting attractors exhibit different complexity values as the initial conditions vary. Besides, its *"picture frame"* like strange attractors can be considered a new topology that has not been proposed until yet, according to the authors' best knowledge. It is proposed that the introduced blinking method of forcing oscillatory terms is to be applied and studied on the other oscillators in the next research studies.

Data Availability

The data used to support the findings of the study are available within the article.

Conflicts of Interest

The authors declare that they have no conflicts of interest.

Acknowledgments

This work was partially funded by Center for Nonlinear Systems, Chennai Institute of Technology, India vide funding no. CIT/CNS/2021/RD/007.

References

[1] F. Nazarimehr and J. C. Sprott, "Investigating chaotic attractor of the simplest chaotic system with a line of equilibria," *The European Physical Journal Special Topics*, vol. 229, no. 6-7, pp. 1289–1297, 2020.

[2] Z. Faghani, F. Nazarimehr, S. Jafari, and J. C. Sprott, "Simple chaotic systems with specific analytical solutions," *International Journal of Bifurcation and Chaos*, vol. 29, no. 9, Article ID 1950116, 2019.

[3] G. A. Leonov and N. V. Kuznetsov, "Hidden attractors in dynamical systems. from hidden oscillations in hilbert-Kolmogorov, aizerman, and kalman problems to hidden chaotic attractor in chua circuits," *International Journal of Bifurcation and Chaos*, vol. 23, no. 1, Article ID 1330002, 2013.

[4] V.-T. Pham, S. Jafari, C. Volos, X. Wang, and S. M. R. H. Golpayegani, "Is that really hidden? The presence of complex fixed-points in chaotic flows with no equilibria," *International Journal of Bifurcation and Chaos*, vol. 24, no. 11, Article ID 1450146, 2014.

[5] Z. Wei, I. Moroz, J. Sprott, A. Akgul, and W. Zhang, "Hidden hyperchaos and electronic circuit application in a 5D self-exciting homopolar disc dynamo," *Chaos: An Interdisciplinary Journal of Nonlinear Science*, vol. 27, Article ID 033101, 2017.

[6] J. C. Sprott and B. Munmuangsaen, "Comment on "A hidden chaotic attractor in the classical Lorenz system"," *Chaos, Solitons & Fractals*, vol. 113, pp. 261-262, 2018.

[7] M. Molaie, S. Jafari, J. C. Sprott, and S. M. R. H. Golpayegani, "Simple chaotic flows with one stable equilibrium," *International Journal of Bifurcation and Chaos*, vol. 23, no. 11, Article ID 1350188, 2013.

[8] S. Jafari and J. C. Sprott, "Simple chaotic flows with a line equilibrium," *Chaos, Solitons & Fractals*, vol. 57, pp. 79–84, 2013.

[9] S. Jafari, J. C. Sprott, V.-T. Pham, C. Volos, and C. Li, "Simple chaotic 3D flows with surfaces of equilibria," *Nonlinear Dynamics*, vol. 86, no. 2, pp. 1349–1358, 2016.

[10] G. A. Leonov, N. V. Kuznetsov, M. A. Kiseleva, E. P. Solovyeva, and A. M. Zaretskiy, "Hidden oscillations in mathematical model of drilling system actuated by induction motor with a wound rotor," *Nonlinear Dynamics*, vol. 77, no. 1-2, pp. 277–288, 2014.

[11] K. Sun and J. C. Sprott, "Periodically forced chaotic system with signum nonlinearity," *International Journal of Bifurcation and Chaos*, vol. 20, no. 5, pp. 1499–1507, 2010.

[12] B. Van der Pol, "On "relaxation-oscillations"," *The London, Edinburgh, and Dublin Philosophical Magazine and Journal of Science*, vol. 2, no. 11, pp. 978–992, 1926.

[13] B. Hernández-Galván, J. López-Rentería, B. Aguirre-Hernández, and G. Fernández-Anaya, "Robust stability in discrete control systems via linear controllers with single and delayed time," *Mathematical Problems in Engineering*, vol. 2018, Article ID 3674628, 15 pages, 2018.

[14] E. Zambrano-Serrano, J. M. Muñoz-Pacheco, and E. Campos-Cantón, "Chaos generation in fractional-order switched systems and its digital implementation," *AEU - International Journal of Electronics and Communications*, vol. 79, pp. 43–52, 2017.

[15] N. R. Cazarez-Castro, M. Odreman-Vera, S. L. Cardenas-Maciel, H. Echavarria-Heras, and C. Leal-Ramírez, "Fuzzy differential equations as a tool for teaching uncertainty in engineering and science," *Computación Y Sistemas*, vol. 22, 2018.

[16] C. Li, J. C. Sprott, T. Kapitaniak, and T. Lu, "Infinite lattice of hyperchaotic strange attractors," *Chaos, Solitons & Fractals*, vol. 109, pp. 76–82, 2018.

[17] J. R. Pulido-Luna, J. A. López-Rentería, and N. R. Cazarez-Castro, "Design of a nonhomogeneous nonlinear synchronizer and its implementation in reconfigurable hardware," *Mathematical and Computational Applications*, vol. 25, no. 3, p. 51, 2020.

[18] D. A. Prousalis, C. K. Volos, B. Bao, E. Meletlidou, I. N. Stouboulos, and I. M. Kyprianidis, "Extreme multistability in a hyperjerk memristive system with hidden attractors," in *Recent Advances in Chaotic Systems and Synchronization*Elsevier, Amsterdam, Netherlands, 2019.

[19] D. Prousalis, C. Volos, I. Stouboulos, I. Kyprianidis, and D. Frantzeskakis, "An extended study of extreme multistability in a memristive circuit," in *Proceedings of the 2017 Panhellenic Conference on Electronics and Telecommunications (PACET). IEEE, 2017*, pp. 1–4, Volos, Greece, May 2017.

[20] B. Pradhan, S. Mukherjee, A. Saha, H. Natiq, and S. Banerjee, "Multistability and chaotic scenario in a quantum pair-ion plasma," *Zeitschrift für Naturforschung A*, vol. 76, no. 2, pp. 109–119, 2021.

[21] Y. Zhang and G. Luo, "Multistability of a three-degree-of-freedom vibro-impact system," *Communications in Nonlinear Science and Numerical Simulation*, vol. 57, pp. 331–341, 2018.
[22] M. Chen, M. Sun, B. Bao, H. Wu, Q. Xu, and J. Wang, "Controlling extreme multistability of memristor emulator-based dynamical circuit in flux-charge domain," *Nonlinear Dynamics*, vol. 91, no. 2, pp. 1395–1412, 2018.
[23] V. T. Pham, D. S. Ali, N. M. G. Al-Saidi, K. Rajagopal, F. E. Alsaadi, and S. Jafari, "A novel mega-stable chaotic circuit," *Radioengineering*, vol. 29, no. 1, pp. 140–146, 2020.
[24] M. A. Rahim, H. Natiq, N. Fataf, and S. Banerjee, "Dynamics of a new hyperchaotic system and multistability," *The European Physical Journal Plus*, vol. 134, pp. 1–9, 2019.
[25] E. Jiménez-López, J. S. González Salas, L. J. Ontañón-García, E. Campos-Cantón, and A. N. Pisarchik, "Generalized multistable structure via chaotic synchronization and preservation of scrolls," *Journal of the Franklin Institute*, vol. 350, no. 10, pp. 2853–2866, 2013.
[26] A. Pisarchik, R. Jaimes-Reátegui, C. Rodríguez-Flores, J. García-López, G. Huerta-Cuellar, and F. Martín-Pasquín, "Secure chaotic communication based on extreme multistability," *Journal of the Franklin Institute*, vol. 358, no. 4, pp. 2561–2575, 2021.
[27] U. Feudel, A. N. Pisarchik, and K. Showalter, "Multistability and tipping: from mathematics and physics to climate and brain—minireview and preface to the focus issue," *Chaos: An Interdisciplinary Journal of Nonlinear Science*, vol. 28, Article ID 033501, 2018.
[28] W. J. Sanders, "The topology of chaos: alice in stretch and squeezeland," *The Mathematics Teacher*, vol. 96, p. 218, 2003.
[29] C. Li, W. Hu, J. C. Sprott, and X. Wang, "Multistability in symmetric chaotic systems," *The European Physical Journal Special Topics*, vol. 224, no. 8, pp. 1493–1506, 2015.
[30] H. Natiq, M. R. Kamel Ariffin, M. A. Asbullah, Z. Mahad, and M. Najah, "Enhancing chaos complexity of a plasma model through power input with desirable random features," *Entropy*, vol. 23, p. 48, 2021.
[31] E.-C. Díaz-González, B. Aguirre-Hernández, J. A. López-Rentería, E. Campos-Cantón, and C. A. Loredo-Villalobos, "Stability and multiscroll attractors of control systems via the abscissa," *Mathematical Problems in Engineering*, vol. 2017, Article ID 6743734, 19 pages, 2017.
[32] E. C. Díaz-González, J.-A. López-Rentería, E. Campos-Cantón, and B. Aguirre-Hernández, "Maximal unstable dissipative interval to preserve multi-scroll attractors via multi-saturated functions," *Journal of Nonlinear Science*, vol. 26, no. 6, pp. 1833–1850, 2016.
[33] B. Aguirre-Hernández, E. Campos-Cantón, J. A. López-Renteria, and E. C. Díaz González, "A polynomial approach for generating a monoparametric family of chaotic attractors via switched linear systems," *Chaos, Solitons & Fractals*, vol. 71, pp. 100–106, 2015.
[34] G. Huerta-Cuellar, E. Jiménez-López, E. Campos-Cantón, and A. N. Pisarchik, "An approach to generate deterministic Brownian motion," *Communications in Nonlinear Science and Numerical Simulation*, vol. 19, no. 8, pp. 2740–2746, 2014.
[35] H. E. Gilardi-Velázquez and E. Campos-Cantón, "Nonclassical point of view of the brownian motion generation via fractional deterministic model," *International Journal of Modern Physics C*, vol. 29, no. 3, Article ID 1850020, 2018.
[36] J. C. Sprott, "Simplest dissipative chaotic flow," *Physics Letters A*, vol. 228, no. 4-5, pp. 271–274, 1997.
[37] H. Natiq, S. Banerjee, and M. R. M. Said, "Cosine chaotification technique to enhance chaos and complexity of discrete systems," *The European Physical Journal Special Topics*, vol. 228, no. 1, pp. 185–194, 2019.
[38] J. S. Richman and J. R. Moorman, "Physiological time-series analysis using approximate entropy and sample entropy," *American Journal of Physiology-Heart Circulatory Physiology*, vol. 278, pp. 2039–2049, 2000.
[39] H. Natiq, M. Said, M. Ariffin, S. He, L. Rondoni, and S. Banerjee, "Self-excited and hidden attractors in a novel chaotic system with complicated multistability," *The European Physical Journal Plus*, vol. 133, pp. 1–12, 2018.
[40] J. C. Sprott, "A new class of chaotic circuit," *Physics Letters A*, vol. 266, pp. 19–23, 2000.
[41] G. D. Leutcho, S. Jafari, I. I. Hamarash, J. Kengne, Z. Tabekoueng Njitacke, and I. Hussain, "A new megastable nonlinear oscillator with infinite attractors," *Chaos, Solitons & Fractals*, vol. 134, Article ID 109703, 2020.
[42] E. Tlelo-Cuautle, A. Dalia Pano-Azucena, O. Guillén-Fernández, and A. Silva-Juárez, "Analog implementations of fractional-order chaotic systems," in *Analog/Digital Implementation of Fractional Order Chaotic Circuits and Applications*Springer, Berlin, Germany, 2020.
[43] E. Tlelo-Cuautle, A. Dalia Pano-Azucena, O. Guillén-Fernández, and A. Silva-Juárez, "Integer and fractional-order chaotic circuits and systems," in *Analog/Digital Implementation of Fractional Order Chaotic Circuits and Applications*Springer, Berlin, Germany, 2020.
[44] A. Silva-Juárez, E. Tlelo-Cuautle, L. G. De la Fraga, and R. Li, "FPAA-based implementation of fractional-order chaotic oscillators using first-order active filter blocks," *Journal of Advanced Research*, vol. 25, pp. 77–85, 2020.
[45] E. Tlelo-Cuautle, A. D. Pano-Azucena, O. Guillén-Fernández, and A. Silva-Juárez, *Analog/digital Implementation of Fractional Order Chaotic Circuits and Applications*, Springer, Berlin, Germany, 2020.
[46] V. Carbajal-Gómez, E. Tlelo-Cuautle, R. Trejo-Guerra, C. Sánchez-López, and J. Munoz-Pacheco, "Experimental synchronization of multiscroll chaotic attractors using current-feedback operational amplifiers," *Nonlinear Science Letters B: Chaos, Fractal Synchronization*, vol. 1, pp. 37–42, 2011.
[47] H. Chen, S. He, A. D. Pano Azucena et al., "A multistable chaotic jerk system with coexisting and hidden attractors: dynamical and complexity analysis, FPGA-based realization, and chaos stabilization using a robust controller," *Symmetry*, vol. 12, no. 4, p. 569, 2020.
[48] A. Sambas, S. Vaidyanathan, E. Tlelo-Cuautle et al., "A novel chaotic system with two circles of equilibrium points: multistability, electronic circuit and FPGA realization," *Electronics*, vol. 8, no. 11, p. 1211, 2019.
[49] A. Sambas, S. Vaidyanathan, E. Tlelo-Cuautle et al., "A 3-D multi-stable system with a peanut-shaped equilibrium curve: circuit design, FPGA realization, and an application to image encryption," *IEEE Access*, vol. 8, pp. 137116–137132, 2020.
[50] O. Guillen-Fernandez, A. Silva-Juarez, A. Melendez-Cano, J. C. Nunez-Perez, and E. Tlelo-Cuautle, "On the FPGA-based implementation of the synchronization of chaotic oscillators in master-slave topology*," 2019.
[51] A. Pano-Azucena, E. Tlelo-Cuautle, S. Tan, B. Ovilla-Martinez, and L. De la Fraga, "FPGA-based implementation of a multilayer perceptron suitable for chaotic time series prediction," *Technologies*, vol. 6, no. 4, p. 90, 2018.
[52] E. Tlelo-Cuautle, J. D. Díaz-Muñoz, A. M. González-Zapata et al., "Chaotic image encryption using hopfield and

hindmarsh-rose neurons implemented on FPGA," *Sensors*, vol. 20, no. 5, p. 1326, 2020.

[53] E. Tlelo-Cuautle, O. Guillén-Fernández, J. De Jesus Rangel-Magdaleno, A. Melendez-Cano, J. C. Nuñez-Perez, and L. G. De la Fraga, "FPGA implementation of chaotic oscillators, their synchronization, and application to secure communications," in *Recent Advances in Chaotic Systems and Synchronization*, pp. 301–328, Elsevier, Amsterdam, Germany, 2019.

[54] E. Tlelo-Cuautle, A. Dalia Pano-Azucena, O. Guillén-Fernández, and A. Silva-Juárez, "Synchronization and applications of fractional-order chaotic systems," in *Analog/Digital Implementation of Fractional Order Chaotic Circuits and Applications*Springer, Berlin, Germany, 2020.

[55] S. Jafari, K. Rajagopal, T. Hayat, A. Alsaedi, and V.-T. Pham, "Simplest megastable chaotic oscillator," *International Journal of Bifurcation and Chaos*, vol. 29, no. 13, Article ID 1950187, 2019.

[56] J. C. Sprott, *Elegant Chaos: Algebraically Simple Chaotic Flows*, World Scientific, Singapore, 2010.

Hindawi
Complexity
Volume 2021, Article ID 5560538, 13 pages
https://doi.org/10.1155/2021/5560538

Research Article

A Stochastic Switched Epidemic Model with Two Epidemic Diseases

Amine El Koufi, Abdelkrim Bennar, and Noura Yousfi

Laboratory of Analysis, Modeling and Simulation (LAMS), Faculty of Sciences Ben M'sik, Hassan II University, P.O. Box 7955 Sidi Othman, Casablanca, Morocco

Correspondence should be addressed to Amine El Koufi; elkoufiamine1@gmail.com

Received 4 February 2021; Revised 2 March 2021; Accepted 5 March 2021; Published 25 March 2021

Academic Editor: Eric Campos

In this paper, we study a stochastic epidemic model with double epidemics which includes white noise and telegraph noise modeled by Markovian switching. Sufficient conditions for the extinction and persistence of the diseases are established. In the end, some numerical simulations are presented to demonstrate our analytical results.

1. Introduction

Compartmental models represent an important mathematical tool to describe the spread of infectious diseases [1–6]. A mathematical model that describes the spread of infectious diseases currently known as the SIR model divides the population into three classes, the sensitive S, infectious I, and recovered R, and was firstly developed by Kermack and Mckendrick [7] in 1927. To take into account the case of recovered individuals who lose their immunity and return to the susceptible compartment, we use SIRS epidemic models investigated by many scientists (see, for example, [8–10]). In classic SIRS epidemic models, the disease caused by one virus but in the real world, there are certain diseases to which the population is infected with two or more viruses (see [11–14]). Zhao et al. [15] established the following SIRS model describing the dynamics of two viruses (see Figure 1):

$$\begin{cases} S'(t) = \mu - \beta_1 S(t) I_1(t) - \beta_2 S(t) I_2(t) - \mu S(t) + \delta R(t), \\ I_1'(t) = \beta_1 S(t) I_1(t) - (\mu + \gamma_1) I_1(t), \\ I_2'(t) = \beta_2 S(t) I_2(t) - (\mu + \gamma_2) I_2(t), \\ R'(t) = \gamma_1 I_1(t) + \gamma_2 I_2(t) - (\mu + \delta) R(t), \end{cases} \tag{1}$$

where $S(t)$ denotes the number of susceptible individuals at time t, $I_1(t)$ and $I_2(t)$ are, respectively, the numbers of infected individuals with virus A and virus B, $R(t)$ denotes the number of removed individuals at time, the parameters β_1 and β_2 are the disease transmission coefficient with virus A and virus B, respectively, μ represents the birth rate of the population and the natural death rate of the population, γ_1 and γ_2 are the recovery rates of infectious individuals with virus A and with virus B, and δ is the lost immunity rate.

However, the biological systems are necessarily touched via the environmental noise, which can present an additional degree of realism compared with their corresponding deterministic models. Thus, it is an important component in an ecosystem. Consequently, many works existing in the literature studied the effects of white noise on epidemic models (see, for example, [16–18]). El Fatini et al. [19] studied a stochastic epidemic model. They assumed that environmental perturbations are of the white noise type. They showed the existence and the uniqueness of the solution of their proposed model. They established sufficient conditions for extinction by constructing some suitable Lyapunov function. And they showed sufficient conditions for the persistence of the disease under some conditions on parameters of the model. Liu et al. [20] investigated the dynamical behavior of a higher-order stochastically perturbed SIRI epidemic model with relapse and media coverage. They showed sufficient measures for the existence and uniqueness of an ergodic stationary distribution of their stochastic model by constructing a suitable Lyapunov function. And

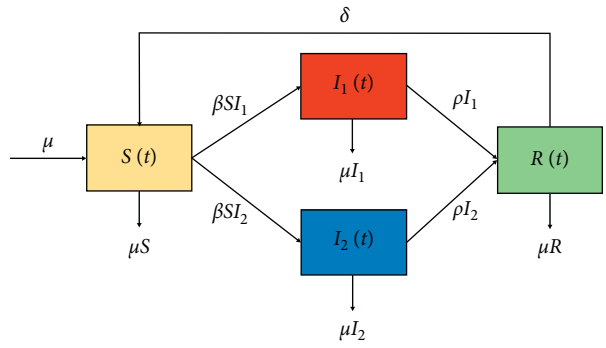

Figure 1: The compartmental diagram for the SIRS model with two epidemic diseases.

they obtained sufficient conditions for the elimination of the infectious disease. Tang et al. [21] investigated the threshold of a class of the stochastic SIRS epidemic model with with nonlinear incidence, which determines the extinction and persistence of the disease. In [22], Qi et al. investigated the dynamics of a nonautonomous stochastic SIS epidemic model with nonlinear incidence rate and double epidemic. Rajasekar and Pitchaimani [23] have formulated the following stochastic SIRS model with two viruses:

$$\begin{cases} \mathrm{d}S(t) = \left[\mu - \beta_1 S(t) I_1(t) - \beta_2 S(t) I_2(t) - \mu S(t) + \delta R(t)\right]\mathrm{d}t + \sigma_1 S(t)\mathrm{d}B_1(t), \\ \mathrm{d}I_1(t) = \left[\beta_1 S(t) I_1(t) - (\mu + \gamma_1) I_1(t)\right]\mathrm{d}t + \sigma_2 I_1(t)\mathrm{d}B_2(t), \\ \mathrm{d}I_2(t) = \left[\beta_2 S(t) I_2(t) - (\mu + \gamma_2) I_2(t)\right]\mathrm{d}t + \sigma_3 I_2(t)\mathrm{d}B_3(t), \\ \mathrm{d}R(t) = \left[\gamma_1 I_1(t) + \gamma_2 I_2(t) - (\mu + \delta) R(t)\right]\mathrm{d}t + \sigma_4 R(t)\mathrm{d}B_4(t), \end{cases} \tag{2}$$

where $B_i(t)$ for $i = 1, 2, 3, 4$ are independent standard Brownian motions which are defined on a complete probability space $(\Omega, \mathcal{F}, \mathbb{P})$ with filtration $\{\mathcal{F}_t\}_{t\geq 0}$ satisfying the usual conditions and σ_i^2 for $i = 1, 2, 3, 4$ denote the intensity of the white noise.

On the other hand, the white noise cannot express the phenomena that the population may submit sudden catastrophic collisions in nature. The telegraph noise can be illustrated as a switching between two or more regimes of environment, which differ by factors such as nutrition or socio-cultural factors [24–26]. In fact, switching between environmental regimes is frequently memoryless and the waiting time for the next switching follows the exponential distribution [27]. So, the regime switching can be modeled by a continuous-time Markov chain $\{r(t)\}_{t\geq 0}$ taking values in a finite-state space $\mathbb{S} = \{1, \ldots, m\}$. Many works have introduced Markov process into their models. For example, in [28], Zhang and Peng addressed a stochastic cholera epidemic model with vaccination. They presented the threshold of a stochastic cholera epidemic model which determines the extinction of the disease and the existence of a unique ergodic stationary distribution. Wang et al. [29] discussed the asymptotic properties of the solution of a stochastic SIRS epidemic model with Beddington–DeAngelis incidence rate and Markovian switching. They proved that the proposed model is stochastically asymptotically stable in the large. In addition, they presented threshold values and conditions which determine disease extinction and persistence. In [30], Li et al. proposed a stochastic SIRS model with vaccination and regime switching. They proved sufficient conditions for the extinction and the existence of the stationary distribution of the population. Motivated by the above facts, in this work, we will initially include telegraph noise into stochastic model (1) to obtain a more realistic model. Then, the following stochastic white and telegraphic noise perturbations on the diseases transmission coefficient are assumed:

$$\begin{aligned} \beta_1 \mathrm{d}t &\longrightarrow \beta_1(r(t))\mathrm{d}t + \sigma_1(r(t))\mathrm{d}B_1(t), \\ \beta_2 \mathrm{d}t &\longrightarrow \beta_2(r(t))\mathrm{d}t + \sigma_2(r(t))\mathrm{d}B_2(t). \end{aligned} \tag{3}$$

Then, the stochastic SIRS epidemic model with two viruses (1) can be expressed as the following stochastic system under regime switching:

$$\begin{cases} \mathrm{d}S(t) = [\mu(r(t)) - \beta_1(r(t))S(t)I_1(t) - \beta_2(r(t))S(t)I_2(t) - \mu(r(t))S(t) \\ \qquad +\delta(r(t))R(t)]\mathrm{d}t - \sigma_1(r(t))S(t)I_1(t)\mathrm{d}B_1(t) - \sigma_2(r(t))S(t)I_2(t)\mathrm{d}B_2(t), \\ \mathrm{d}I_1(t) = [\beta_1(r(t))(t)I_1(t) - (\mu(r(t)) + \gamma_1(r(t)))I_1(t)]\mathrm{d}t \\ \qquad +\sigma_1(r(t))S(t)I_1(t)\mathrm{d}B_1(t), \\ \mathrm{d}I_2(t) = [\beta_2(r(t))S(t)I_2(t) - (\mu(r(t)) + \gamma_2(r(t)))I_2(t)]\mathrm{d}t \\ \qquad +\sigma_2(r(t))S(t)I_2(t)\mathrm{d}B_2(t), \\ \mathrm{d}R(t) = \gamma_1(r(t))I_1(t) + \gamma_2(r(t))I_2(t) - (\mu(r(t)) + \delta(r(t)))R(t). \end{cases} \tag{4}$$

This article proposes a stochastic SIRS epidemic model with regime switching and double epidemic hypothesis. Our main purpose is to investigate the effect of the white and telegraph noises on the spread dynamics of the disease in the population. The rest of the paper is as follows. In Section 3, we show the existence and uniqueness of a global positive solution to system (4). In Sections 4 and 5, we study the existence of a stochastic threshold for the extinction and the persistence in mean of the disease. In last section, we present some numerical simulations to demonstrate our main theoretical results.

2. Existence and Uniqueness of the Nonnegative Solution

Throughout this paper, we let $(\Omega, \mathscr{F}, \{\mathscr{F}_t\}_{t\geq 0}, \mathbb{P})$ be a complete probability space with a filtration $\{\mathscr{F}_t\}_{t\geq 0}$ satisfying the usual conditions (i.e., it is increasing and right continuous while $\mathscr{F}_0$ contains all $\mathbb{P}$-null sets). Let $\{r(t)\}_{t\geq 0}$ be a right-continuous Markov chain on the probability space $(\Omega, \mathscr{F}, \{\mathscr{F}_t\}_{t\geq 0}, \mathbb{P})$ taking values in a finite-state space $\mathbb{S} = \{1, 2, \ldots, m\}$ with the generator $\Phi = (\phi_{uv})_{1\leq u,v\leq N}$ given, for $\delta > 0$, by

$$P(r(t+\delta) = v | r(t) = u) = \begin{cases} \phi_{uv}\delta + o(\delta), & \text{if } u \neq v, \\ 1 + \phi_{uu}\delta + o(\delta), & \text{if } u = v. \end{cases} \tag{5}$$

Here, ϕ_{uv} is the transition rate from u to v and $\phi_{uv} \geq 0$ if $u \neq v$, while

$$\phi_{uu} = -\sum_{u\neq v} \phi_{uv}. \tag{6}$$

Suppose that the Markov chain $r(t)$ is independent of the Brownian motion $B(\cdot)$ and it is irreducible. Under this condition, the Markov chain has a unique stationary distribution $\pi = (\pi_1, \ldots, \pi_N)$, which can be determined by solving the linear equation $\pi\Phi = 0$, subject to $\sum_{i=1}^{N} \pi_i = 1$, and $\pi_i > 0$, $\forall i \in \mathbb{S}$. Thereafter, for any vector $h = (h(1), \ldots, h(N))^T$, let $\widehat{h} = \min_{i\in\mathbb{M}}\{h(i)\}$ and $\check{h} = \max_{i\in\mathbb{M}}\{h(i)\}$.

We consider the following stochastic system:

$$\mathrm{d}\vartheta(t) = f(t, \vartheta(t), r(t))\mathrm{d}t + g(t, \vartheta(t), r(t))\mathrm{d}B(t), \quad (*) \tag{7}$$

where $B(t)$ is a d-dimensional standard Wiener process defined on a complete probability space $(\Omega, \mathscr{F}, \{\mathscr{F}_t\}_{t\geq 0}, \mathbb{P})$.

Denoted by $C^{1,2}(\mathbb{R}^d \times \mathbb{S}; \mathbb{R}_+)$, the family of all nonnegative functions $\mathscr{Q}$ is defined on $\mathbb{R}^d \times \mathbb{S}$ such that they are continuously twice differentiable in ϑ. The operator $\mathscr{L}$ associated with $(*)$ is defined as follows:

$$\begin{aligned} \mathscr{L}\mathscr{Q}(\vartheta, i) &= \mathscr{Q}_t(t, \vartheta, i) + \mathscr{Q}_\vartheta(t, \vartheta, i) f(t, \vartheta, i) \\ &\quad + \frac{1}{2} g^T(t, \vartheta, i)\mathscr{Q}_{\vartheta,\vartheta}(t, \vartheta, i) g(t, \vartheta, i) \\ &\quad + \sum_{j\in\mathbb{S}} \phi_{ij}\mathscr{Q}(t, \vartheta, j), \end{aligned} \tag{8}$$

where $\mathscr{Q}_\vartheta$ and $\mathscr{Q}_{\vartheta,\vartheta}$ represent the gradient and Hessian of $\mathscr{Q}$ and T is the transpose of a matrix.

By Itô's formula, if $\mathscr{Q}$ defined on $\mathbb{R}^d \times \mathbb{S}$, we have

$$\mathrm{d}\mathscr{Q}(\vartheta(t), i) = \mathscr{L}\mathscr{Q}(\vartheta(t), i)\mathrm{d}t + \mathscr{Q}_\vartheta(\vartheta(t), i) g(\vartheta(t), i)\mathrm{d}B(t). \tag{9}$$

The total population in system (4) verifies the following equation:

$$\begin{aligned} &\mathrm{d}\big(S(t) + I_1(t) + I_2(t) + R(t)\big) \\ &\qquad = \big[\mu - \mu\big(S(t) + I_1(t) + I_2(t) + R(t)\big)\big]\mathrm{d}t. \end{aligned} \tag{10}$$

Thus,

$$\begin{aligned} &S(t) + I_1(t) + I_2(t) + R(t) \\ &\quad = 1 + \big(S(0) + I_1(0) + I_2(0) + R(0) - 1\big)e^{-\mu(r(t))t}, \quad \text{for all } t \geq 0. \end{aligned} \tag{11}$$

Since, for $X(0) \in \mathbb{D}$, we have

$$S(t) + I_1(t) + I_2(t) + R(t) = 1, \quad \text{for all } t \geq 0 \text{ a.s.} \tag{12}$$

Let

$$\mathbb{D} = \big\{\big(S + I_1 + I_2 + R\big) \in \mathbb{R}_+^4 \colon S + I_1 + I_2 + R = 1\big\}. \tag{13}$$

By using the same method as in [31, 32], we can easily prove the following theorem.

Theorem 1. *Let $X(0) = (S(0), I_1(0), I_2(0), R(0)) \in \mathbb{D}$, then there is a unique solution $(S(t), I_1(t), I_2(t), R(t))$ to system (4) on $t \geq 0$, and the solution will remain in $\mathbb{D}$ with probability 1.*

Firstly, we define the following expressions which we use to determine the extinction of epidemics:

$$\sum_{i=1}^{m}\pi_i D_i = \sum_{i=1}^{m}\pi_i\left(-\sigma_1^2(i)+\beta_1(i)-(\mu(i)+\gamma_1(i))\right),$$
$$\sum_{i=1}^{m}\pi_i A_i = \sum_{i=1}^{m}\pi_i\left(-\sigma_2^2(i)+\beta_2(i)-(\mu(i)+\gamma_2(i))\right). \tag{14}$$

3. Extinction

This section is consecrated to give sufficient conditions so that the epidemics die out. According to [33], we have the following lemma.

Lemma 1. *Suppose that there exists a function* $U(u,i)\in C^{1,2}(\mathbb{R}^3\times\mathbb{S};\mathbb{R}_+)$ *and* $\rho(u)\in(\mathbb{R}^3\times;\mathbb{R}_+)$ *disappears only at* E_0 *such that*

$$\mathscr{L}U(u,i)\le -\rho(u),\quad \text{for all } (u,i)\in\mathbb{R}^3\times\mathbb{S},$$
$$\lim_{|x|\longrightarrow\infty}\inf_{j\in\mathcal{S}}U(u,i)=\infty. \tag{15}$$

Then, the equilibrium E_0 of system (4) is globally asymptotically stable in probability.

By Lemma 1, we identify the conditions for stochastic asymptotic stability of the disease-free equilibrium which are presented by the following theorem.

Theorem 2. *If* $\beta_2(i)\ge\sigma_2^2(i)$ *and* $\beta_1(i)\ge\sigma_1^2(i)$ *for all* $i\in\mathbb{S}$, *and*

$$\sum_{i=1}^{m}\pi_i D_i<0,$$
$$\sum_{i=1}^{m}\pi_i A_i<0, \tag{16}$$

then the disease-free equilibrium E_0 *is globally stochastically asymptotically stable on* $\mathbb{D}$.

Proof. We consider the following Lyapunov function:

$$\mathscr{H}(S,I,R,i)=m_1(1-S)^2+(\eta+\omega_i)I_1^{(1/\eta)}+(\theta+\varpi_i)I_2^{(1/\theta)}+m_2R^2,\quad \text{for all } i\in\mathbb{S}, \tag{17}$$

where m_1, m_2, η, and θ are real positive constants to be determined later. By Itô's formula, we calculate $\mathscr{L}\mathscr{H}$ as follows:

$$\begin{aligned}
\mathscr{L}\mathscr{H} &= -2m_1(1-S)\left[\mu-\mu S-\beta_1 SI_1-\beta_2 SI_2+\delta R\right]+m_1\sigma_1^2S^2I_1^2\\
&\quad+m_2\sigma_2^2S^2I_2^2+\frac{1}{\eta}(\eta+\omega_i)I_1^{(1/\eta)}\left[\beta_1 S-(\mu+\gamma_1)\right]\\
&\quad+\frac{1}{2\eta}\left(\frac{1}{\eta}-1\right)(\eta+\omega_i)\sigma_1^2S^2I_1^{(1/\eta)}\\
&\quad+\frac{1}{\theta}(\theta+\varpi_i)I_2^{(1/\theta)}\left[\beta_2 S-(\mu+\gamma_2)\right]+\frac{1}{2\theta}\left(\frac{1}{\theta}-1\right)(\theta+\omega_i)\sigma_2^2S^2I_2^{(1/\theta)}\\
&\quad+2m_2R\left[\gamma_1I_1+\gamma_2I_2-(\mu+\delta)R\right]+\sum_{k\ne i,k\in\mathbb{S}}\phi_{ik}(\omega_k-\omega_i+\varpi_k-\varpi_i)\\
&=-2m_1(1-S)^2+2m_1\beta_1SI_1(1-S)+2m_1\beta_2SI_2(1-S)\\
&\quad-2m_1\delta(1-S)R+m_1\sigma_1S^2I_1^2+m_1\sigma_2S^2I_2^2+\frac{1}{\eta}(\eta+\omega_i)\beta_1I_1^{(1/\eta)}S\\
&\quad-\frac{1}{\eta}(\eta+\omega_i)(\mu+\gamma_1)I_1^{(1/\eta)}+\frac{1}{2\eta}\left(\frac{1}{\eta}-1\right)(\eta+\omega_i)\sigma_1^2S^2I_1^{(1/\eta)}\\
&\quad+\frac{1}{\theta}(\theta+\varpi_i)\beta_2I_2^{(1/\theta)}S-\frac{1}{\theta}(\theta+\varpi_i)(\mu+\gamma_2)I_2^{(1/\theta)}\\
&\quad+\frac{1}{2\theta}\left(\frac{1}{\theta}-1\right)(\theta+\omega_i)\sigma_2^2S^2I_2^{(1/\theta)}+m_2\gamma_1RI_1+m_2\gamma_2RI_2-m_2(\mu+\delta)R^2\\
&\quad+I_1^{(1/\eta)}\sum_{k\ne i,k\in\mathbb{S}}\phi_{ik}(\omega_k-\omega_i)+I_2^{(1/\theta)}\sum_{k\ne i,k\in\mathbb{S}}\phi_{ik}(\varpi_k-\varpi_i).
\end{aligned} \tag{18}$$

Using the fact that $I \le 1 - S$ and $S, I \in \mathbb{D}$, we obtain

$$\begin{aligned}\mathscr{L}\mathscr{H} \le & -2m_1(1-S)^2 + 2m_1\beta_1 I_1^{(1/\eta)} + 2m_1\beta_2 I_2^{(1/\theta)} + m_1\sigma_1^2 I_1^{(1/\eta)} + m_1\sigma_2^2 I_2^{(1/\theta)} \\ & + \frac{1}{\eta}(\eta+\omega_i)\beta_1 I_1^{(1/\eta)} S - \frac{1}{\eta}(\eta+\omega_i)(\mu+\gamma_1) I_1^{(1/\eta)} \\ & + \frac{1}{2\eta}\left(\frac{1}{\eta}-1\right)(\eta+\omega_i)\sigma_1^2 S^2 I^{(1/\eta)} + \frac{1}{\theta}(\theta+\varpi_i)\beta_2 I_2^{(1/\theta)} S \\ & - \frac{1}{\theta}(\theta+\varpi_i)(\mu+\gamma_2) I_2^{(1/\theta)} + \frac{1}{2\theta}\left(\frac{1}{\theta}-1\right)(\theta+\omega_i)\sigma_2^2 S^2 I_2^{(1/\theta)} \\ & + (m_2\gamma_1 - m_1\delta) R I_1 + (m_2\gamma_2 - m_1\delta) R I_2 - m_2(\mu+\delta) R^2 \\ & + I_1^{(1/\eta)} \sum_{k\neq i, k\in\mathbb{S}} \phi_{ik}(\omega_k - \omega_i) + I_2^{(1/\theta)} \sum_{k\neq i, k\in\mathbb{S}} \phi_{ik}(\varpi_k - \varpi_i),\end{aligned} \tag{19}$$

for all η and $\theta \ge 1$. Since we can choose $m_2 < \min_{i\in\mathbb{S}}\{(m_1\delta(i)/\gamma_1(i)), (m_1\delta(i)/\gamma_2(i))\}$, we obtain

$$\begin{aligned}\mathscr{L}\mathscr{H} \le & -2m_1(1-S)^2 - m_2(\mu+\delta)R^2 + \frac{(\eta+\omega_i)}{\eta} I_1^{(1/\eta)}\left[\frac{\eta m_1}{(\eta+\omega_i)}\left(\sigma_1^2 + 2\beta_1\right)\right. \\ & \left. -(\mu+\gamma_1) + \frac{1}{2\eta}\sigma_1^2 + \beta_1 S - \sigma_1^2 S^2 + \frac{\eta}{(\eta+\omega_i}\sum_{k\neq i, k\in\mathbb{S}} \phi_{ik}(\omega_k - \omega_i)\right] \\ & + \frac{(\theta+\omega_i)}{\theta} I_2^{(1/\theta)}\left[\frac{\theta m_1}{(\theta+\omega_i)}\left(\sigma_2^2 + 2\beta_2\right) - (\mu+\gamma_2) + \frac{1}{2\theta}\sigma_2^2 + \beta_2 S\right. \\ & \left. -\sigma_2^2 S^2 + \frac{\theta}{(\theta+\varpi_i)}\sum_{k\neq i, k\in\mathbb{S}} \phi_{ik}(\varpi_k - \varpi_i)\right] \\ =: & -2m_1(1-S)^2 - m_2(\mu+\delta)R^2 + \frac{(\eta+\omega_i)}{\eta} I_1^{(1/\eta)}\left[\frac{\eta m_1}{(\eta+\omega_i)}\left(\sigma_1^2 + 2\beta_1\right)\right. \\ & \left. +\frac{1}{2\eta}\sigma_1^2 + f_i(S) + \frac{\eta}{(\eta+\omega_i)}\sum_{k\neq i, k\in\mathbb{S}} \phi_{ik}(\omega_k - \omega_i)\right] \\ & + \frac{(\theta+\omega_i)}{\theta} I_2^{(1/\theta)}\left[\frac{\theta m_1}{(\theta+\omega_i)}\left(\sigma_2^2 + 2\beta_2\right) + \frac{1}{2\theta}\sigma_2^2 + g_i(S)\right. \\ & \left. +\frac{\theta}{(\theta+\varpi_i)}\sum_{k\neq i, k\in\mathbb{S}} \phi_{ik}(\varpi_k - \varpi_i)\right],\end{aligned} \tag{20}$$

where $f_i(x) = -\sigma_1^2(i)x^2 + \beta_1(i)x - (\mu(i) + \gamma_1(i))$ and $g_i(x) = -\sigma_2^2(i)x^2 + \beta_2(i)x - (\mu(i) + \gamma_2(i))$. Note that the functions $f_i(x)$ and $g_i(x)$ are all increasing on $(0, 1)$, which means

$$\begin{aligned} f_i(x) &\le f_i(1) =: D_i, \\ g_i(x) &\le g_i(1) =: A_i, \end{aligned} \tag{21}$$

then

$$\begin{aligned}\mathscr{L}\mathscr{H} \le & -2m_1(1-S)^2 - m_2(\mu+\delta)R^2 + \frac{(\eta+\omega_i)}{\eta} I_1^{(1/\eta)}\left[\frac{\eta m_1}{(\eta+\omega_i)}\left(\sigma_1^2+2\beta_1\right)\right. \\ & \left. + \frac{1}{2\eta}\sigma_1^2 + D_i + \frac{\eta}{(\eta+\omega_i)}\sum_{k\neq i,k\in\mathbb{S}}\phi_{ik}(\omega_k-\omega_i)\right] \\ & + \frac{(\theta+\varpi_i)}{\theta} I_2^{(1/\theta)}\left[\frac{\theta m_1}{(\theta+\varpi_i)}\left(\sigma_2^2+2\beta_2\right) + \frac{1}{2\theta}\sigma_2^2 + A_i\right. \\ & \left. + \frac{\theta}{(\theta+\varpi_i)}\sum_{k\neq i,k\in\mathbb{S}}\phi_{ik}(\varpi_k-\varpi_i)\right].\end{aligned} \tag{22}$$

Since the generator matrix Φ is irreducible, then for $D = (D_1, \ldots, D_m)^T$, there exists $\Xi = (\omega_1, \ldots, \omega_m)^T$ solution of the Poisson system:

$$\Phi\Xi = -D + \left(\sum_{i=1}^{m}\pi_i D_i\right)\vec{E}. \tag{23}$$

And for $A = (A_1, \ldots, A_m)^T$, there exists $\Theta = (\varpi_1, \ldots, \varpi_m)^T$ solution of the Poisson system:

$$\Phi\Theta = -A + \left(\sum_{i=1}^{m}\pi_i A_i\right)\vec{E}, \tag{24}$$

where $\vec{E}$ denotes the column vector with all its entries equal to 1.

Substituting (23) and (24) in (22), we get

$$\begin{aligned}\mathscr{L}\mathscr{H} \le & -2m_1(1-S)^2 - m_2(\mu+\delta)R^2 + \frac{(\eta+\omega_i)}{\eta} I_1^{(1/\eta)}\left[\frac{\eta m_1}{(\eta+\omega_i)}\left(\sigma_1^2+2\beta_1\right)\right. \\ & \left. + \frac{1}{2\eta}\sigma_1^2 + \frac{\eta}{(\eta+\omega_i)}\left(D_i - \sum_{i=1}^{m}\pi_i D_i\right) + \sum_{i=1}^{m}\pi_i D_i\right] \\ & + \frac{(\theta+\varpi_i)}{\theta} I_2^{(1/\theta)}\left[\frac{\theta m_1}{(\theta+\varpi_i)}\left(\sigma_2^2+2\beta_2\right) + \frac{1}{2\theta}\sigma_2^2\right. \\ & \left. + \frac{\theta}{(\theta+\varpi_i)}\left(A_i - \sum_{i=1}^{m}\pi_i A_i\right) + \sum_{i=1}^{m}\pi_i A_i\right].\end{aligned} \tag{25}$$

Choosing η_0 and θ_0, such that

$$\begin{aligned} C_1 &=: \max_{i\in\mathbb{S}}\left\{\frac{\sigma_1^2}{2\eta_0} + \frac{\eta_0}{(\eta_0+\omega_i)}\left(D_i - \sum_{i=1}^{m}\pi_i D_i\right) + \sum_{i=1}^{m}\pi_i D_i\right\} < 0, \\ C_2 &:= \max_{i\in\mathbb{S}}\left\{\frac{\sigma_2^2}{2\theta_0} + \frac{\theta_0}{(\theta_0+\varpi_i)}\left(A_i - \sum_{i=1}^{m}\pi_i A_i\right) + \sum_{i=1}^{m}\pi_i A_i\right\} < 0.\end{aligned} \tag{26}$$

Since we choose $\eta > \max\{-\omega_i, \eta_0, 1\}$ and $\theta > \max\{-\varpi_i, \theta_0, 1\}$ such that

$$\begin{aligned} m_1 < \min\Bigg\{ & -\frac{\eta + \min\omega_i}{\eta\left(\max\sigma_1^2 + 2\max\beta_1\right)} \times C_1, \\ & -\frac{\theta + \min\varpi_i}{\theta\left(\max\sigma_2^2 + 2\max\beta_2\right)} \times C_2\Bigg\}.\end{aligned} \tag{27}$$

According to Lemma 1, the proof is completed.

Theorem 3. *Let $(S(t), I_1(t), I_2(t), R(t))$ be the solution of system (4), then for any given initial value $(S(0), I_1(0), I_2(0), R(0)) \in \mathbb{D}$, model (4) has the following property:*

$$\begin{aligned}\lim_{t\longrightarrow\longrightarrow\infty}\sup & \frac{1}{t}\ln(1-S+I_1+I_2+R) \\ & \le \sum_{i=1}^{m}\pi_i\left(\frac{\beta_1^2(i)-\mu(i)\sigma_1^2(i)}{2\sigma_1^2(i)} + \frac{\beta_2^2(i)-\mu(i)\sigma_2^2(i)}{2\sigma_2^2(i)}\right), \quad \text{a.s.}\end{aligned} \tag{28}$$

If

$$\sum_{i=1}^{m}\pi_i\left(\frac{\beta_1^2(i)-\mu(i)\sigma_1^2(i)}{2\sigma_1^2(i)} + \frac{\beta_2^2(i)-\mu(i)\sigma_2^2(i)}{2\sigma_2^2(i)}\right) < 0 \tag{29}$$

holds, then the disease-free E_0 is almost surely exponentially stable in $\mathbb{D}$. Namely, the diseases die out with probability one.

Proof. Consider the following function:

$$\mathscr{G}(S, I_1, I_2, R, i) = \ln(1 - S + I_1 + I_2 + R). \tag{30}$$

By Itô's formula, we obtain

$$\begin{aligned} \mathrm{d}\mathscr{G} = {} & \frac{1}{1 - S + I_1 + I_2 + R}\left[-\mu(r)(1 - S) - \mu(r)I_1 - \mu(r)I_2\right. \\ & \left. -(\mu(r) + 2\delta(r))(r)R + 2\beta_1(r)SI_1 + 2\beta_2(r)SI_2\right]\mathrm{d}t \\ & - 2\sigma_1^2(r)\left(\frac{SI_1}{1 - S + I_1 + I_2 + R}\right)^2 \mathrm{d}t - 2\sigma_2^2(r)\left(\frac{SI_2}{1 - S + I_1 + I_2 + R}\right)^2 \mathrm{d}t \\ & + \frac{2\sigma_1(r)SI_1}{1 - S + I_1 + I_2 + R}\mathrm{d}B_1 + \frac{2\sigma_2(r)SI_2}{1 - S + I_1 + I_2 + R}\mathrm{d}B_2. \end{aligned} \tag{31}$$

Note that

$$\frac{1}{(1 - S + I_1 + I_2 + R)}\left[-\mu(r)(1 - S) - \mu(r)I_1 - \mu I_2 - (\mu(r) + 2\delta(r))R\right] \leq -\mu(r). \tag{32}$$

Thus, we have

$$\begin{aligned} d\mathscr{G} \leq {} & \left(-2\sigma_1(r)\left(\frac{SI}{1 - S + I_1 + I_2 + R} - \frac{\beta_1(r)}{2\sigma_1^2(r)}\right) + \frac{\beta_1^2(r)}{2\sigma_1^2(r)} - \frac{\mu(r)}{2}\right)dt \\ & + \left(-2\sigma_2(r)\left(\frac{SI}{1 - S + I_1 + I_2 + R} - \frac{\beta_2(r)}{2\sigma_2^2(r)}\right) + \frac{\beta_2^2(r)}{2\sigma_2^2(r)} - \frac{\mu(r)}{2}\right)dt \\ & + \frac{2\sigma_1(r)SI_1}{1 - S + I_1 + I_2 + R}dB_1 + \frac{2\sigma_2(r)SI_2}{1 - S + I_1 + I_2 + R}dB_2. \\ \leq {} & \left[\frac{\beta_1^2(r) - \mu(r)\sigma_1^2(r)}{2\sigma_1^2(r)} + \frac{\beta_2^2(r) - \mu(r)\sigma_2^2(r)}{2\sigma_2^2(r)}\right]dt + \frac{2\sigma_1(r)SI_1}{1 - S + I_1 + I_2 + R}dB_1 \\ & + \frac{2\sigma_2(r)SI_2}{1 - S + I_1 + I_2 + R}dB_2. \end{aligned} \tag{33}$$

Integrating both sides of (33) from 0 to t and dividing by t, we get

$$\begin{aligned}\frac{\mathscr{G}(t)}{t} \leq & \frac{\mathscr{G}(0)}{t} \\ & + \frac{1}{t}\int_0^t \left(\frac{\beta_1^2(r(u)) - \mu(r(u))\sigma_1^2(r(u))}{2\sigma_1^2(r(u))} + \frac{\beta_2^2(r(u)) - \mu(r(u))\sigma_2^2(r(u))}{2\sigma_2^2(r(u))}\right)\mathrm{d}u \\ & + \frac{1}{t}\int_0^t \frac{2\sigma_1(r(u))S(u)I_1(u)}{1 - S(u) + I_1(u) + I_2(u) + R(u)}\,\mathrm{d}B_1(u) \\ & + \frac{1}{t}\int_0^t \frac{2\sigma_2(r(u))S(u)I_2(u)}{1 - S(u) + I_1(u) + I_2(u) + R(u)}\,\mathrm{d}B_2(u).\end{aligned} \tag{34}$$

Let $F_i(t) = \int_0^t ((2\sigma_i(r)S(u)I_i(u))/(1 - S(u) + I_1(u) + I_2(u) + R(u)))\mathrm{d}B_i(u)$ $(i = 1, 2)$, then

$$\begin{aligned}&\langle F_i(t), F_i(t)\rangle \\ &= \int_0^t \left(\frac{2\sigma_i(r(u))S(u)I_i(u)}{1 - S(u) + I_1(u) + I_2(u) + R(u)}\right)^2 \mathrm{d}u \leq 4\breve{\sigma}_i, \quad t < \infty.\end{aligned} \tag{35}$$

Then, by strong law of large numbers, we obtain

$$\lim_{t\longrightarrow\infty} \frac{F_i(t)}{t} = 0, \quad \text{a.s.} \tag{36}$$

By the ergodic theory of the Markov chain, we can obtain

$$\begin{aligned}&\limsup_{t\longrightarrow\longrightarrow\infty} \frac{1}{t}\int_0^t \left(\frac{\beta_1^2(r(u)) - \mu(r(u))\sigma_1^2(r(u))}{2\sigma_1^2(r(u))} + \frac{\beta_2^2(r(u)) - \mu(r(u))\sigma_2^2(r(u))}{2\sigma_2^2(r(u))}\right)\mathrm{d}u \\ &\leq \sum_{i=1}^m \pi_i \left(\frac{\beta_1^2(i) - \mu(i)\sigma_1^2(i)}{2\sigma_1^2(i)} + \frac{\beta_2^2(i) - \mu(i)\sigma_2^2(i)}{2\sigma_2^2(i)}\right), \quad \text{a.s.}\end{aligned} \tag{37}$$

Hence, if $\sum_{i=1}^m \pi_i(((\beta_1^2(i) - \mu(i)\sigma_1^2(i))/2\sigma_1^2(i)) + ((\beta_2^2(i) - \mu(i)\sigma_2^2(i))/2\sigma_2^2(i))) < 0$, then the disease-free E_0 is almost surely exponentially stable in $\mathbb{D}$.

4. Persistence

In this section, we explain sufficient conditions for the persistence of two epidemics.

We define $\langle h\rangle_t = (1/t)\int_0^t h(u)\mathrm{d}u$ if h is an integrable function on $[0, +\infty)$.

Definition 1. System (4) is said to be persistent in the mean, if

$$\liminf_{t\longrightarrow\infty} \frac{1}{t}\int_0^t I(u)\mathrm{d}u > 0, \quad \text{a.s.} \tag{38}$$

Let

$$R_0^s = \sum_{i=0}^m \pi_i \left(2\mu(i) + \gamma_1(i) + \gamma_2(i) + \frac{\sigma_1(i)}{2} + \frac{\sigma_2(i)}{2} - k_1(i)\mu(i)\right). \tag{39}$$

Theorem 4. *Let $(S(t), I_1(t), I_2(t), R(t))$ be the solution of model (4). If $R_0^s > 0$, then*

$$\begin{aligned}&\liminf_{t\longrightarrow\infty} \langle I_1 + I_2\rangle_t \geq I^*, \\ &\liminf_{t\longrightarrow\infty} \langle R\rangle_t \geq \frac{\min\{\widehat{\gamma}_1, \widehat{\gamma}_2\}}{\breve{\mu} + \breve{\delta}} I^*, \\ &\liminf_{t\longrightarrow\infty} \langle 1 - S\rangle_t \geq \left(\frac{\breve{\mu} + \breve{\delta} + \min\{\widehat{\gamma}_1, \widehat{\gamma}_2\}}{\breve{\mu} + \breve{\delta}}\right) I^*,\end{aligned} \tag{40}$$

where $I^* = (R_0^s/\overline{D})$ with $\overline{D}$ is positive constant.

Proof. By system (4), one can obtain that

$$\begin{aligned}\mathscr{L}(-\ln I_1) &= -\beta_1(i)S + \mu(i) + \gamma_1(i) + \frac{\sigma_1^2(i)}{2}S^2, \\ \mathscr{L}(-\ln I_2) &= -\beta_2(i)S + \mu(i) + \gamma_2(i) + \frac{\sigma_2^2(i)}{2}S^2.\end{aligned} \tag{41}$$

Moreover,

$$\begin{aligned}\mathscr{L}(S+I_1+I_2) &= \mu(i)-\mu(i)S-(\mu(i)+\gamma_1(i))\\ &\quad I_1-(\mu(i)+\gamma_2(i))I_2+\delta(i)R,\\ \mathscr{L}R &= \gamma_1(i)I_1+\gamma_2(i)I_2-(\mu(i)+\delta(i))R.\end{aligned} \tag{42}$$

So, we consider the Lyapunov function $\mathscr{T}$ defined on $\mathbb{D}$ by

$$\begin{aligned}\mathscr{T}(S,I_1,I_2,i) = &-\ln I_1-\ln I_2\\ &-k_1(i)(S+I_1+I_2)-k_2(i)R-v(i),\end{aligned} \tag{43}$$

where $(k_1(i),k_2(i))^T$ is the unique positive solution of the following system:

$$\begin{aligned}&\beta_1(i)+\beta_2(i)-k_1(i)\mu(i)+\sum_{l=1}^{m}\phi_{il}k_1(l)=0,\\ &k_1(i)\delta(i)-k_2(i)(\mu(i)+\delta(i))+\sum_{l=1}^{m}\phi_{il}k_2(l)=0.\end{aligned} \tag{44}$$

Using Itô's formula, one can get that

$$\begin{aligned}\mathrm{d}\mathscr{T} = &\mathscr{L}\mathscr{T}\,\mathrm{d}t-[\sigma_1(i)S+k_1(i)SI_1]\mathrm{d}B_1(t)\\ &-[\sigma_2(i)S+k_2(i)SI_2]\mathrm{d}B_2(t),\end{aligned} \tag{45}$$

where

$$\begin{aligned}\mathscr{L}\mathscr{T} = &-\beta_1 S+\mu(i)+\gamma_1(i)+\frac{\sigma_1^2(i)}{2}S^2-\beta_2(i)S+\mu(i)+\gamma_2(i)+\frac{\sigma_2^2(i)}{2}S^2\\ &-k_1(i)[\mu(i)-\mu(i)S-(\mu(i)+\gamma_1(i))I_1-(\mu(i)+\gamma_2(i))I_2+\delta(i)R]\\ &-k_2(i)[\gamma_1(i)I_1+\gamma_2(i)I_2-(\mu(i)+\delta(i))R]-\sum_{l=1}^{m}\phi_{il}k_1(l)(S+I_1+I_2)\\ &-\sum_{l=1}^{m}\phi_{il}k_2(l)R-\sum_{l=1}^{m}\phi_{il}v(l).\end{aligned} \tag{46}$$

Using the fact that $S\in(0,1)$, we deduce that

$$\begin{aligned}\mathscr{L}\mathscr{T} \le &2\mu(i)+\gamma_1(i)+\gamma_2(i)+\frac{\sigma_1^2(i)}{2}+\frac{\sigma_2^2(i)}{2}-k_1(i)\mu(i)-\sum_{l=1}^{m}\phi_{il}v(l)\\ &-\left[\beta_1(i)+\beta_2(i)-k_1(i)\mu(i)+\sum_{l=1}^{m}\phi_{il}k_1(l)\right]S\\ &-\left[k_1(i)\delta(i)-k_2(i)(\mu(i)+\delta(i))+\sum_{l=1}^{m}\phi_{il}k_2(l)\right]R\\ &+\left[k_1(i)(\mu(i)+\gamma_1(i))-k_2(i)\gamma_1(i)-\sum_{l=1}^{m}\phi_{il}k_1(l)\right]I_1\\ &+\left[k_1(i)(\mu(i)+\gamma_2(i))-k_2(i)\gamma_2(i)+\sum_{l=1}^{m}\phi_{il}k_1(l)\right]I_2.\end{aligned} \tag{47}$$

From (44), we get that

$$\begin{aligned}\mathscr{L}\mathscr{T} \le{}& 2\mu(i)+\gamma_1(i)+\gamma_2(i)+\frac{\sigma_1^2(i)}{2}+\frac{\sigma_2^2(i)}{2}-k_1(i)\mu(i)-\sum_{l=1}^{m}\phi_{il}\upsilon(l)\\&+\left[\beta_1(i)+\beta_2(i)+k_1(i)\gamma_1(i)\right]I_1+\left[\beta_1(i)+\beta_2(i)+k_1(i)\gamma_2(i)\right]I_2.\end{aligned}\tag{48}$$

In addition, we also have

$$\begin{aligned}\mathscr{L}\mathscr{T} &\le 2\mu(i)+\gamma_1(i)+\gamma_2(i)+\frac{\sigma_1^2(i)}{2}+\frac{\sigma_2^2(i)}{2}-k_1(i)\mu(i)-\sum_{l=1}^{m}\phi_{il}\upsilon(l)\\&\quad+\left[\check{\beta}_1+\check{\beta}_2+\check{k}_1\check{\gamma}_1\right]I_1+\left[\check{\beta}_1+\check{\beta}_2+\check{k}_1\check{\gamma}_2\right]I_2\\&\le 2\mu(i)+\gamma_1(i)+\gamma_2(i)+\frac{\sigma_1^2(i)}{2}+\frac{\sigma_2^2(i)}{2}-k_1(i)\mu(i)-\sum_{l=1}^{m}\phi_{il}\upsilon(l)\,\phi_{il}\upsilon(l)+\overline{D}\left(I_1+I_2\right),\\&\quad+\overline{D}\left(I_1+I_2\right)\\&\coloneqq -R_0(i)-\sum_{l=1}^{m}\end{aligned}\tag{49}$$

where

$$\overline{D}=\max\left\{\check{\beta}_1+\check{\beta}_2+\check{k}_1\check{\gamma}_1,\check{\beta}_1+\check{\beta}_2+\check{k}_1\check{\gamma}_2\right\}.\tag{50}$$

Since the generator matrix Φ is irreducible, then for $R_0=(R_0(1),\ldots,R_0(m))^T$, there exists $\Upsilon=(\upsilon(1),\ldots,\upsilon(m))^T$ solution of the Poisson system:

$$\Phi\Upsilon=-R_0+\left(\sum_{i=1}^{m}\pi_i R_0(i)\right)\begin{pmatrix}1\\1\\\cdot\\\cdot\\1\end{pmatrix},\tag{51}$$

which implies that

$$\mathscr{L}\mathscr{T}\le -R_0^s+\overline{D}\left(I_1+I_2\right).\tag{52}$$

Integrating (45) from 0 to t and dividing by t on both sides, we obtain

$$\frac{\mathscr{T}(t)}{t}\le\frac{\mathscr{T}(0)}{t}-R_0^s+\overline{D}\langle I_1+I_2\rangle_t-\frac{M_1(t)}{t}-\frac{M_2(t)}{t},\tag{53}$$

where $M_j(t)=\sigma_j(i)S\mathrm{d}B_j(t)$ (for $j=1,2$) is a continuous martingale with $M(0)=0$ and its quadratic variation is as follows:

$$\langle M_j(t),M_j(t)\rangle=\int_0^t\left(\sigma_j(i)S(u)\right)^2\mathrm{d}u\le\left(\check{\sigma}_j\right)^2t.\tag{54}$$

Thus, the strong law of large number for local martingales [27] implies that

$$\lim_{t\longrightarrow\infty}\frac{M_j(t)}{t}=0,\quad\text{a.s.}\tag{55}$$

Since $(S,I_1,I_1,R)\in\mathbb{D}$, we can derive

$$\begin{aligned}\mathscr{T}\left(S,I_1,I_2,i\right)&=-\ln I_1-\ln I_2-k_1(i)\left(S+I_1+I_2\right)\\&\quad-k_2(i)R-\upsilon(i)\ge-\check{k}_1-\check{k}_2-\check{\upsilon}\coloneqq C.\end{aligned}\tag{56}$$

Taking the superior limit on both sides of (45) and combining with (52), (55), and (56), we deduce that

$$\liminf_{t\longrightarrow\infty}\langle I_1+I_2\rangle_t\ge\frac{R_0^s}{\overline{D}}\coloneqq I^*,\quad\text{a.s.}\tag{57}$$

Integrating the third equation of (4) and dividing both sides by t, we have

$$\langle R\rangle_t\ge\frac{\min\{\widehat{\gamma}_1,\widehat{\gamma}_2\}}{(\check{\mu}+\check{\delta})}\langle I_1+I_2\rangle_t-\frac{R(t)-R(0)}{(\widehat{\mu}+\widehat{\delta})t}.\tag{58}$$

Since $\lim_{t\longrightarrow\infty}((R(t)-R(0))/t)=0$ and using (57), we get

$$\liminf_{t\longrightarrow\infty}\langle R\rangle_t\ge\frac{\min\{\widehat{\gamma}_1,\widehat{\gamma}_2\}}{\check{\mu}+\check{\delta}}I^*.\tag{59}$$

Furthermore, it follows by $1-S=I+R$ that

Table 1: Parameter values used in numerical simulations.

States	Coefficients							
	μ	β_1	β_2	δ	γ_1	γ_2	σ_1	σ_2
1	0.25	0.5	0.6	0.5	0.4	0.3	0.2	0.1
2	0.3	0.6	0.4	0.4	0.2	0.4	0.12	0.2

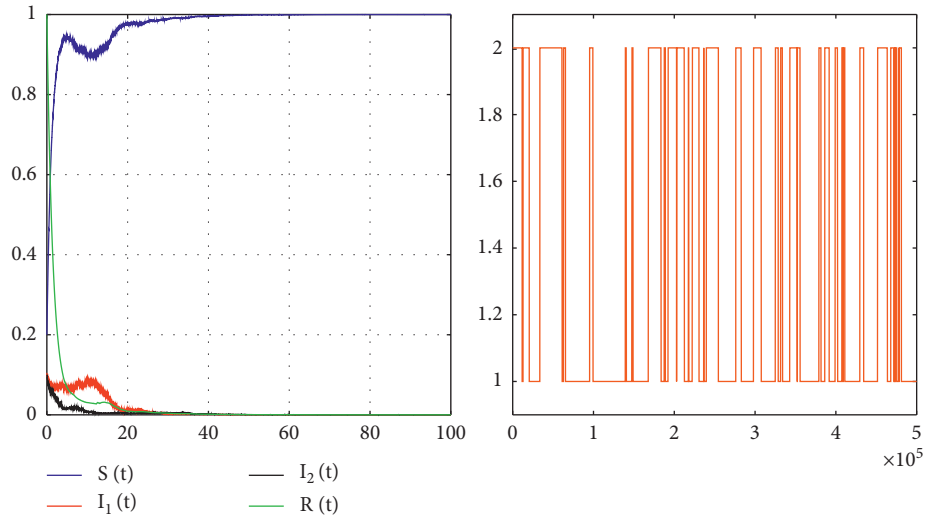

Figure 2: Sample paths of $S(t)$ in blue, $I_1(t)$ in red, $I_2(t)$ in black, $R(t)$ in green, and $r(t)$ in brown in Example 1.

Table 2: Parameter values used in numerical simulations.

States	Coefficients							
	μ	β_1	β_2	δ	γ_1	γ_2	σ_1	σ_2
1	0.01	0.9	0.8	0.4	0.2	0.3	0.6	0.8
2	0.01	0.8	0.8	0.4	0.3	0.2	0.7	0.7

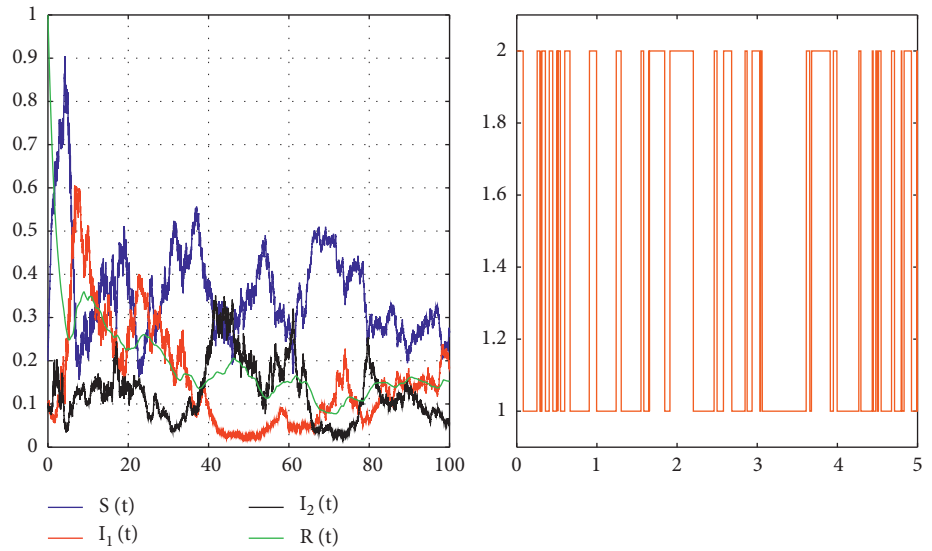

Figure 3: Sample paths of $S(t)$ in blue, $I_1(t)$ in red, $I_2(t)$ in black, $R(t)$ in green, and $r(t)$ in brown in Example 1.

$$\liminf_{t\longrightarrow\infty}\langle 1-S\rangle_t \geq \left(\frac{\breve{\mu}+\breve{\delta}+\min\{\widehat{\gamma}_1,\widehat{\gamma}_2\}}{\breve{\mu}+\breve{\delta}}\right)I^*. \tag{60}$$

This completes the proof.

5. Simulation

In the following, we give numerical simulations to illustrate the main theoretical results.

Example 1. We consider the Markov chain $(r(t))_{t\geq 0}$ taking values in $\mathbb{S}=\{1,2\}$, with generator defined by the following:

$$\Phi=\begin{pmatrix}-1 & 1\\ 2 & -2\end{pmatrix}. \tag{61}$$

The parameter values of (4) are presented in Table 1.

Exact computations supply us $\sum_{i=1}^{2}\pi_i D_j=-0.0352$ and $\sum_{i=1}^{2}\pi_i A_j=-0.0467$. Consequently, by Theorem 2, the disease-free equilibrium E_0 is globally stochastically asymptotically stable on $\mathbb{D}$. Figure 2 confirms this result.

Example 2. In this example, we use the parameter values given in Table 2 and the Markov chain used in Example 1. By simply computing, we obtain $R_0^s>0$. Theorem 4 shows that the two epidemics persist in the population. Figure 3 confirms this result.

6. Conclusion

This paper investigates a stochastic switched epidemic model with double epidemic diseases and cure rate affected with a composite of environmental perturbations modeled by white and color noises. We established conditions for extinction and persistence of diseases.

The theoretical result given in this paper shows that the stationary distribution of Markov chain $r(t)$ controls the propagation of the epidemic in the population. To know, if the Markov chain $r(t)$ takes the values which lead to find that $\sum_{i=1}^{m}\pi_i D_i<0$ and $\sum_{i=1}^{m}\pi_i A_i<0$, then the epidemic diseases die out. We have given numerical simulations in order to support and illustrate the main results of this paper.

In this perspective, we prepare to include Lévy noises into epidemic models (4) to describe the effect of sudden and dangerous phenomena such as pandemic, tsunami, and volcano.

Data Availability

The data were curated by the authors and are available upon request.

Conflicts of Interest

The authors declare that they have no conflicts of interest.

References

[1] R. M. Anderson, B. Anderson, and R. M. May, *Infectious Diseases of Humans: Dynamics and Control*, Oxford University Press, Oxford, UK, 1992.

[2] C. V. De-Leon, "On the global stability of SIS, SIR and SIRS epidemic models with standard incidence," *Chaos, Solitons & Fractals*, vol. 44, no. 12, pp. 1106–1110, 2011.

[3] X. Jin, S. Jin, and D. Gao, "Mathematical analysis of the ross-MacDonald model with quarantine," *Bulletin of Mathematical Biology*, vol. 82, no. 4, 2020.

[4] C. Tian, Q. Zhang, and L. Zhang, "Global stability in a networked SIR epidemic model," *Applied Mathematics Letters*, vol. 107, Article ID 106444, 2020.

[5] L. Zhao, Z.-C. Wang, and S. Ruan, "Dynamics of a time-periodic two-strain SIS epidemic model with diffusion and latent period," *Nonlinear Analysis: Real World Applications*, vol. 51, Article ID 102966, 2020.

[6] R. K. Upadhyay, A. K. Pal, S. Kumari, and P. Roy, "Dynamics of an SEIR epidemic model with nonlinear incidence and treatment rates," *Nonlinear Dynamics*, vol. 96, no. 4, pp. 2351–2368, 2019.

[7] W. O. Kermack and A. G. McKendrick, "A contribution to the mathematical theory of epidemics," *Proceedings of the Royal Society of London. Series A, Containing Papers of a Mathematical and Physical Character*, vol. 115, no. 772, pp. 700–721, 1927.

[8] L. Xiang, Y. Zhang, and J. Huang, "Stability analysis of a discrete SIRS epidemic model with vaccination," *Journal of Difference Equations and Applications*, vol. 26, no. 3, pp. 309–327, 2020.

[9] M. Lu, J. Huang, S. Ruan, and P. Yu, "Bifurcation analysis of an SIRS epidemic model with a generalized nonmonotone and saturated incidence rate," *Journal of Differential Equations*, vol. 267, no. 3, pp. 1859–1898, 2019.

[10] S. Han, C. Lei, and X. Zhang, "Qualitative analysis on a diffusive SIRS epidemic model with standard incidence infection mechanism," *Zeitschrift für angewandte Mathematik und Physik*, vol. 71, no. 6, pp. 1–23, 2020.

[11] X.-z. Meng, "Stability of a novel stochastic epidemic model with double epidemic hypothesis," *Applied Mathematics and Computation*, vol. 217, no. 2, pp. 506–515, 2010.

[12] X. Meng, S. Zhao, T. Feng, and T. Zhang, "Dynamics of a novel nonlinear stochastic SIS epidemic model with double epidemic hypothesis," *Journal of Mathematical Analysis and Applications*, vol. 433, no. 1, pp. 227–242, 2016.

[13] A. Miao, X. Wang, T. Zhang, W. Wang, and B. S. A. Pradeep, "Dynamical analysis of a stochastic SIS epidemic model with nonlinear incidence rate and double epidemic hypothesis," *Advances in Difference Equations*, vol. 2017, no. 1, Article ID 226, 2017.

[14] A. El Koufi, M. Naim, A. Bennar, and N. Yousfi, "Stability analysis of a stochastic SIS model with double epidemic hypothesis and specific nonlinear incidence rate," *Communications in Mathematical Biology and Neuroscience*, vol. 2018, 2018.

[15] J. Zhao, L. Wang, and Z. Han, "Stability analysis of two new SIRS models with two viruses," *International Journal of Computer Mathematics*, vol. 95, no. 10, pp. 2026–2035, 2018.

[16] X. B. Zhang, H. F. Huo, H. Xiang, Q. Shi, and D. Li, "The threshold of a stochastic SIQS epidemic model," *Physica A: Statistical Mechanics and Its Applications*, vol. 482, pp. 362–374, 2014.

[17] A. El Koufi, J. Adnani, A. Bennar, and N. Yousfi, "Analysis of a stochastic SIR model with vaccination and nonlinear incidence rate," *International Journal of Differential Equations*, vol. 2019, Article ID 9275051, 9 pages, 2019.

[18] Y. Chen, B. Wen, and Z. Teng, "The global dynamics for a stochastic SIS epidemic model with isolation," *Physica A: Statistical Mechanics and Its Applications*, vol. 492, pp. 1604–1624, 2018.

[19] M. El Fatini, A. Lahrouz, R. Pettersson, A. Settati, and R. Taki, "Stochastic stability and instability of an epidemic model with relapse," *Applied Mathematics and Computation*, vol. 316, pp. 326–341, 2018.

[20] Q. Liu, D. Jiang, T. Hayat, A. Alsaedi, and B. Ahmad, "Dynamical behavior of a higher order stochastically perturbed SIRI epidemic model with relapse and media coverage," *Chaos, Solitons & Fractals*, vol. 139, Article ID 110013, 2020.

[21] T. Tang, Z. Teng, and Z. Li, "Threshold behavior in a class of stochastic SIRS epidemic models with nonlinear incidence," *Stochastic Analysis and Applications*, vol. 33, no. 6, pp. 994–1019, 2015.

[22] H. Qi, L. Liu, and X. Meng, "Dynamics of a nonautonomous stochastic sis epidemic model with double epidemic hypothesis," *Complexity*, vol. 2017, Article ID 4861391, 14 pages, 2017.

[23] S. P. Rajasekar and M. Pitchaimani, "Qualitative analysis of stochastically perturbed SIRS epidemic model with two viruses," *Chaos, Solitons & Fractals*, vol. 118, pp. 207–221, 2019.

[24] M. Slatkin, "The dynamics of a population in a Markovian environment," *Ecology*, vol. 59, no. 2, pp. 249–256, 1978.

[25] M. Liu, X. He, and J. Yu, "Dynamics of a stochastic regime-switching predator-prey model with harvesting and distributed delays," *Nonlinear Analysis: Hybrid Systems*, vol. 28, pp. 87–104, 2018.

[26] X. Yu, S. Yuan, and T. Zhang, "Persistence and ergodicity of a stochastic single species model with Allee effect under regime switching," *Communications in Nonlinear Science and Numerical Simulation*, vol. 59, pp. 359–374, 2018.

[27] X. Mao and C. Yuan, *Stochastic Differential Equations with Markovian Switching*, Imperial College Press, London, UK, 2006.

[28] X. Zhang and H. Peng, "Stationary distribution of a stochastic cholera epidemic model with vaccination under regime switching," *Applied Mathematics Letters*, vol. 102, Article ID 106095, 2020.

[29] S. Wang, Y. Peng, and F. Wang, "Stability and asymptotic behavior of a regime-switching SIRS model with beddington-DeAngelis incidence rate," *Mathematical Problems in Engineering*, vol. 2020, Article ID 7181939, 12 pages, 2020.

[30] X. Li, X. Li, and Q. Zhang, "Time to extinction and stationary distribution of a stochastic susceptible-infected-recovered-susceptible model with vaccination under Markov switching," *Mathematical Population Studies*, vol. 27, no. 4, pp. 259–274, 2020.

[31] A. El Koufi, A. Bennar, and N. Yousfi, "Dynamics of a stochastic SIRS epidemic model with regime switching and specific functional response," *Discrete Dynamics in Nature and Society*, vol. 2020, Article ID 5898456, 13 pages, 2020.

[32] X. Mao, G. Marion, and E. Renshaw, "Environmental Brownian noise suppresses explosions in population dynamics," *Stochastic Processes and Their Applications*, vol. 97, no. 1, pp. 95–110, 2002.

[33] C. Yuan and X. Mao, "Robust stability and controllability of stochastic differential delay equations with Markovian switching," *Automatica*, vol. 40, no. 3, pp. 343–354, 2004.